TRACKING THE ULTRAFAST PHOTOPHYSICAL EVENTS IN ALL INORGANIC METAL HALIDE PEROVSKITES THROUGH TRANSIENT ABSORPTION SPECTROSCOPY

GURPREET KAUR

A thesis submitted for the partial fulfilment of

the degree of Doctor of Philosophy

Institute of Nano Science and Technology

Knowledge city, Sector 81, SAS Nagar, Manauli PO, Mohali

140306, Punjab, India.

Indian Institute of Science Education and Research, Mohali

Knowledge city, Sector 81, SAS Nagar, Manauli PO, Mohali

140306, Punjab, India.

March, 2023

Declaration

The work presented in this thesis has been carried out by me under the guidance of Prof. Deepa Ghosh and Prof. Hirendra N.Ghosh at Institute of Nano Science and Technology, Mohali. This work has not been submitted in part or in full for a degree, a diploma, or a fellowship to any other university or institute. Whenever contributions of others are involved, every effort is made to indicate this clearly, with due acknowledgement of collaborative research and discussions. This thesis is a bona fide record of original work done by me and all sources listed within have been detailed in the bibliography.

GURPREET KAUR

In my capacity as the supervisor of the candidate's thesis work, I certify that the above statements by the candidate are true to the best of my knowledge.

Prof. Hirendra N.Ghosh
(Co-Supervisor)

Prof. Deepa Ghosh
(Supervisor)

Table of contents

Contents	Page No.
Acknowledgements……	i-v
List of Acronyms……	vi-vii
Abstract……	viii-ix
List of figures……..	x-xx
List of tables……	xxi
Thesis Overview……..	xxii-xxv
Chapter 1 Introduction	**(1-36)**
1.1 Perovskites*:* "A look back in time"…….	1-3
1.2 Nanostructures and Quantum confinement……..	3-5
1.3 Halide Perovskite vs. the conventional semiconductor nanocrystals	5-8
1.4 Metal Halide Perovskites……..	8
1.4.1 The Structural Considerations……..	8-12
1.4.2 The all inorganic alkali metal halide perovskites…….....	12
1.4.2.1 Lead (Pb) based perovskites - $APbX_3$…….	12-14
1.4.2.2 Lead free perovskites – ABX_3, where B is any suitable Divalent cation other than Pb^{2+}……	14
A. Isovalent replacement	14-15
B. Heterovalent replacement	15-16
1.5 Photophysical processes that take place in Metal Halide Perovskites subsequent to photoexcitation……...	16-18
1.6 Intervalley scattering……..……	18
1.7 Factors affecting the carrier cooling rates in Metal Halide Perovskites	19
1.7.1 Hot Phonon Bottleneck effect (HPB effect)…….	19
1.7.2 Auger heating……...	19-21
1.7.3 Polaron formation…….....	21-23
1.8 Phonon dynamics- the interplay of lattice vibrations……...	23-24
1.9 Coherent phonon generation…….	24-25
1.10 Silent modes and Hyper-Raman Scattering (HRS)……...	25-26
1.11 References…….	26-35

Chapter 2 Experimental Section **(37-98)**

2.1 Hot injection methodology for the synthesis of halide perovskites….. 37-40

2.2 Synthesis procedures……..... 40

2.2.1 Synthesis of $CsPbBr_3$ NCs, Cs_4PbBr_6 NCs and $CsPbBr_3$/ Cs_4PbBr_6 core @shell NCs …….. 41-42

2.2.2 Synthesis of PbS QDs…….. 42

2.2.3 Synthesis of Cs_2SnI_6 NCs……. 42-43

2.3 Steady state material characterization tools…….. 43

2.3.1 X-Ray Diffraction (XRD)……. 43-45

2.3.2 Transmission Electron Microscopy (TEM)…….. 45-50

2.3.3 Steady state absorption spectroscopy (UV-Vis-NIR)…….. 50-52

2.3.4 Steady state Photoluminescence/ fluorescence spectroscopy..… 52-54

2.4 Time Correlated Single Photon Counting (TCSPC) / Time Resolved Photoluminescence (TRPL) studies…… 54-57

2.5 Transient absorption (TA) spectroscopy…… 57-60

2.5.1 Generation of ultrashort pulses……..... 60

2.5.1.1 Q-Switching……. 60-63

2.5.1.2 Mode-locking……..... 63-66

2.5.2 Construction of a femtosecond laser…… 66-67

2.5.2.1 Seed laser or also known as “Femtosecond oscillator”….. 67-68

2.5.2.2 Pump laser……... 68

2.5.2.3 Chirped pulse amplifier- regenerative amplifier (regn) & a stretcher/compressor module……. 68-69

A. Stretcher unit……. 69-70

B. Pulse picker…… 70-71

C. Regenerative Amplifier/Gain medium……... 71-72

D. Compressive unit…… 72-73

2.5.2.4 Tuning the wavelength- non-linear effects- generation Of the “pump” beam…… 73

A. Harmonic generation…….. 73-75

B. Sum Frequency, Difference Frequency and Optical Parametric Generation……... 75-77

C. White Light Continuum (WLC) Generation…….. 77

2.5.3 Experimental Setup established in our lab…… 77-80

2.5.3.1 Transient Absorption spectrometer- “Helios Fire”…….. 80-81
2.5.3.2 Surface Xplorer™ software……. 81-82
2.5.3.3 Decrypting the spectral signatures observed in the TA data 82-83
2.6 Terahertz (THz) time-domain spectroscopy…….. 84-86
2.6.1 Experimental setup in our lab……... 86-88
2.6.2 Data collection and analysis……. 89
2.7 References……. 89-97
Chapter 3 Polaron Mediated Slow Carrier Cooling in Type-1 3D/0D $CsPbBr_3$@Cs_4PbBr_6 Core- Shell Perovskite System (99-120)
3.1 Motivation and Background…….. 100-101
3.2 Results and discussion……... 101
3.2.1 Steady state optical, crystallographic & morphological studies 101-103
3.2.2 Time resolved PL measurements……..... 103
3.2.3 Ultrafast Transient Absorption measurements……..... 103-104
3.2.3.1 Upon near band gap excitation (480 nm)……..... 104-107
3.2.3.2 Far above band gap excitation (300 nm)……. 107-110
3.3.3.3 Hot carrier cooling dynamics……..... 110-113
3.2.3.4 Polaron formation…… 113-115
3.3 Summary…… 115-116
3.4 References……. 116-120
Chapter 4 Temperature Dependent Interplay of Polaron formation and Hot Carrier Cooling Dynamics in $CsPbBr_3$ Nanocrystals: Role of Carrier-Phonon Coupling Strength (121-140)
4.1 Motivation and Background……..... 122-123
4.2 Results and discussion……... 123
4.2.1 Sample preparation…… 123
4.2.2 Steady state optical absorption & crystallographic studies…….. 123-124
4.2.3 Temperature dependent Photoluminescence studies…… 124-126
4.2.4 Temperature dependent TA measurements…….. 126-127
4.2.4.1 Influence of temperature on carrier relaxation and Polaron formation…… 128-134
4.2.4.2 Temperature dependent biexciton dynamics……... 134-135
4.3 Summary…… 135-136
4.4 References…….. 136-140

Chapter 5 Unravelling the Underlying Hot Carrier Transfer and Relaxation Pathways in Type -1 $CsPbBr_3$–PbS System (141-160)

5.1 Motivation and Background…….. 142-143

5.2 Results and discussion……... 143

5.2.1 Preliminary crystallographic and morphological studies……. 143-145

5.2.2 Steady state optical studies- Absorption and PL…….. 145-147

5.2.3 Femtosecond Transient Absorption studies…….. 148

5.2.3.1 300 nm excitation……..... 148-152

5.2.3.2 480 nm excitation…… 152-155

5.2.3.3 620 nm excitation……..... 155-156

5.3 Summary…… 156-157

5.4 References…….…… 157-160

Chapter 6 Mapping the Real-Time Vibrational Infrastructure of Cs_2SnI_6 Nanocrystals through Coherent Phonon dynamics (161-190)

6.1 Motivation and Background…….. 162-163

6.2 Results and discussion……... 164

6.2.1 Primary characterisation of Cs_2SnI_6 DP NCs…… 164

6.2.1.1 Crystallographic studies (X-Ray Diffraction (XRD)) and Morphological investigations (Transmission Electron Microscopy (TEM))……. 164-165

6.2.1.2 Steady State optical studies…….. 165

6.2.2 Vibrational information from resonant TA dynamics…….. 165-169

6.2.2.1 Estimation of the Raman active F_{2g} mode……..... 169-170

6.2.2.2 Estimation of the Raman and IR inactive F_{1g} mode…… 170-171

6.2.3 Coherent phonon generation mechanisms in Cs_2SnI_6 NCs…….. 171-173

6.2.4 Origin of the 61cm^{-1} mode…… 173-177

6.2.5 Inherent anharmonicity in the lattice and the combination modes 177-178

6.2.6 Temperature dependent investigations……. 178-180

6.3 Summary…… 181

6.4 References…….. 181-188

Chapter 7 Ultrafast Glimpses of the Excitation Energy-Dependent Exciton Dynamics and Charge Carrier Mobility in Cs_2SnI_6 Nanocrystals (189-218)

7.1 Motivation and Background……..... 190-192

7.2 Results and discussion……... 192

7.2.1 Preliminary morphological and steady state optical studies…… 192-193
7.2.2 Theoretical findings……. 193-196
7.2.3 Positioning of band edge levels from experimental analysis…... 196-197
7.2.4 Transient absorption deductions…….. 197
7.2.4.1 Spectral analysis…….. 197-203
7.2.4.2 Temporal analysis…… 203-210
7.2.5 Carrier mobility measurements…… 210-212
7.3 Summary…… 212-213
7.4 References……. 213-217
Chapter 8 Conclusions and Future Outlook (219-224)
8.1 Conclusions……... 219-223
8.2 Future Outlook……... 223-224

List of Publications included in the thesis……. xxvi
List of other Published works (other than that included in the thesis)..... xxvi-xxviii
Permissions from Journals for reuse of content in thesis…… xxix-xxxii
Conferences Attended/Oral and Poster presentations…… xxxiii

Acknowledgements

"No One Can Whistle A Symphony, It Takes An Orchestra to Play It."

- H.E. Luccock.

On both intellectual and scientific level, this PhD journey has been a period of intensive learning for me. I am eternally thankful to many people who played critical roles in the realisation of my thesis. My dissertation may though appear to be a testament to my scientific path but is in actual a joint effort of all these people who helped me along the road and kept me sane. First of all, I would thank the **Almighty** for helping me through. Throughout all the trying times of finishing my dissertation, he has offered me unwavering support.

When deciding on a PhD programme, the one factor that supersedes all others is the choice of the PhD supervisor. I am glad to confess that I consider myself quite fortunate in this aspect. **Prof. H.N. Ghosh** is a prolific researcher in his field, and after working with him, I can see why he is regarded as a doyen in ultrafast spectroscopy. He is so into work and so enthusiastic about it that I guess by being a part of his life we, his students, are either directly or indirectly imprinted with the same mindset. As my PhD guide, he has contributed in various aspects, but one of the most significant one has been to spark my interest in spectroscopy and lasers. To be honest, I have to admit that I was never much fascinated by lasers before I joined the laboratory back in the year 2017. But now as I am about to leave this laboratory I realise how engrossed in this topic I have become that it is impossible for me to ever turn back. He gave me the freedom to choose my study area in accordance with my interest which I believe is crucial for building necessary confidence in the budding researchers and fostering independent thinking. Another thing about **Prof. H.N. Ghosh** is that he is so vibrant and vivacious in person that he stays confident and optimistic at all times, including moments of emotional turmoil. This is a pretty hard trait to imbibe and I guess only a handful of people possess it. His capability to capitulate his audience very easily during the presentations is worth to be pointed out and I hope that in the coming times I will be able to instil this art in myself. Supportiveness and availability are two qualities that PhD students respect most in their supervisors, and Prof. H. N. Ghosh thrives in both aspects. Besides patiently mentoring me throughout, he also always had my back. He has always been prompt in every work he has taken up. I greatly value the fact that, even after moving back to BARC this year, he didn't allow the distance to hinder the communication in any way or have any impact on the work. Infact, we never sensed his absence because he constantly took time out of his hectic schedule at BARC to get in touch with us.

The other thing I admire in him the most is that he is very friendly and quite approachable, may it be any time of day and no matter how much busy he is. Not just his PhD students, but other people as well, can attest to this. In addition to being a scientific mentor, on the personal front he has a deep appreciation for the fact that a student's life extends much beyond obtaining a PhD degree which most people fail to understand. He very clearly recognises that the working pattern of each student and keeping in mind the best interest of every student, allows them to work in line with it. There were moments when I used to become lethargic, at those instances he gave me the necessary push and challenged me to strive harder. If I look back today through my PhD journey, I believe that no one else could have played a finer role as my PhD advisor than him. Thank you **Prof. H.N. Ghosh** for everything!!! You've given me a lot of strength with your belief in me and encouraging remarks. You have my gratitude forever, and I wish you success in all of your endeavours in the future and good health.

I would also extend my thanks to **Prof. Deepa Ghosh** for her steadfast support in her role as a supervisor after Prof. H. N. Ghosh rejoined BARC. Since I only had a little time left on my tenure after that, we didn't get to connect that much. From what little engagement I've had with her so far, I've found her to be pretty helpful and cooperative. No matter what, she always extended a kind helping hand to each of us in the lab. She helped us counter all the issues in every respect, very smoothly and timely and provided the apt solutions.

In order to maintain the pace of the work and maintain tranquilly, which go hand in hand with each other, a healthy lab culture is one of the key requirements throughout a PhD candidate's term. Cheers of applaud to the entire Ultrafast & Terahertz spectroscopy group- **Tanmay Goswami, Nandan Ghorai, Ayushi Shukla, Arshdeep Kaur Sohal, Himanshu Bhatt, Ramchandra Saha (my first ever junior), Manvi Sachdeva, Nitika Kharbanda, Vikas Nain, Dr. K. Justice Babu and Dr. Samresh Samanta** for making the work atmosphere so cheerful, upbeat, and conducive. I consider myself really fortunate to have such a lovely bundle of labmates who evolved to be my family and have become an integral part of my life. I'll miss not seeing them every day. For the assistance you have provided both related to the lab or otherwise, I owe many of you a debt of appreciation. A particular mention ought to be made for **Tanmay Goswami,** my lab partner and friend. We both joined the lab together the same day, and when I reflect back on those early days when I struggled to fit in, I see that he played a crucial part in my determination to persevere in the face of all the challenges. I don't even remember how it transpired, but he turned into one of my closest friends I had ever come across. There is actually no enough amount of thanks for the support and encouragement he provided me throughout this long and bumpy journey of five years both in and outside the

lab. He had a major role in my ability to see things through to the conclusion. He gave me the strength to keep going even when I felt like giving up and always kept me sane through my challenging times. Having someone like him to rely on, encouraged me to take numerous chances that I would not have otherwise considered. I also owe him a great deal of gratitude for transforming me from an individual who used to be always obsessed with work into one who values both fun and learning. In all of his future endeavours, I wish that may fate always be on his side, assisting him in achieving whatever is best for him, and I hope he achieves great heights he so well deserves.

Ayushi Shukla and **Himanshu Bhatt**, my friends-juniors, need special credit for standing out as an incredible source of support. All of it—the get-togethers, the birthday bashes, the movie times, the 3B2 trips, the tea breaks, the backpacked trips, even the planning that went into them—I thoroughly enjoyed and I owe it all to you people. **Ayushi** not only lent me a helping hand in the lab but also in life outside. I will always treasure the days when I had to work late into the night and despite anything she was always there for me and used to accompany me. Her unfallen support in literally everything I believe drove things much easier for me. In my opinion, we were a terrific team. I realised this especially when we had frustrating periods while aligning Terahertz, I believe it was only because we were supported by one another that we were able to succeed. Not only this, but she also had a major role in lightening up my mood even in those moments when things turned out to be bit disappointing. I also want to convey my gratitude to our Post-Doc **Dr. K. Justice Babu** who deserves the credit for being a great mentor, a supportive senior and a friend to me throughout. He is the one who introduced me to the perovskite field in the first place. I've learnt a lot from him at work (especially the synthesis) and also in life (through his poetry and on board quotes about Zindagi!!). I will remember him for all the tasty South Indian cuisines he cooked for us, the epic coffee and the deadly ginger tea. My **Mahila Mandal** team- **Manvi (our leader), Nitika, Arshdeep and Ayushi** thank you all for the exclusive girls' only enjoyable outings.

I would also like to thank my seniors, our alumini who motivated and helped me during my initial days. I would like to extend my thanks to **Dr. Sourav Maity** for answering my each and every question both scientific and beyond that crossed my mind. I would also like to thank **Dr. Jayanta Dana** and **Dr. Sourav Maity** who acquainted me with ultrafast lasers and introduced me to the "ultrafast encylcopedia". I recall **Dr. Radhamanohar** pushing me to do synthesis since during the just initial days I used to be reluctant to carry out synthesis being a physics student. It is the joint venture of all these three Post-Docs that I started taking interest in synthesis and I really owe this to three of them. I cannot recollect the moment when I started

getting along and sharing a bond with them. Also, thanks to the pro tips shared by them, I was able to go through this tedious process of PhD. **Dr. Dharmendra Yadav** taught me a lot but his commitment to his work and care for others are the two things I will always treasure the most. I also want to thank **Dr. Sachin Rondiya, Dr.Somen Mondal, Dr. Palwinder Singh and Dr. Inderjeet Singh** for guiding me scientifically and for the pep-talks they gave me when I most needed them.

I also want to extend my warm thanks to my PhD monitoring committee members **Dr. Kiran S.Hazra** and **Dr. Dipankar Mandal** for always sparing out their valuable time for the yearly assessments and providing me with constructive suggestions. I would also want to thank them for their cooperation in all aspects. I would also like to convey my gratitude to the faculty members that I had the chance to work with as a result of our collaborative efforts: **Prof. Umesh Waghmare, Prof. Goutam De, Prof. Kanishka Biswas, Dr. Ranjani Viswanatha and Dr. Suvankar Chakraverty**. The concepts exchanged with them and their students during the collaborative projects, in my opinion, has widened my knowledge and viewpoint outside of my primary study area, which I feel will be helpful to me in the future. I owe a great deal to **Anamika Kumari, Arijit Sinha, Koyendrila Debnath, Saptarshi Chakraborty, Tapasvini and Manisha Samanta** in this regard.

I also want to express my gratitude to our laser engineers- **Arun Kumar P R (Laser Science Services (I) Pvt. Ltd.), Arunkumar Singh (Trokut Solutions Pvt. Ltd.) and M. Sajjanam Morrison (Laser spectra services)** for their prompt assistance, which contributed to the efficient operation of our laser systems- "the heart of my PhD".

I am grateful to INST for providing the financial and instrumental support during my PhD. Besides this, I owe a debt of gratitude to the INST community as a whole, which has been contributory in making my stay at this place both joyful and productive and in introducing me to so many fantastic individuals. I am really grateful to all the friends and academic colleagues who have either consciously or unconsciously pushed me in the direction of my objective. Even on the gloomier days, you people have enlivened and lightened my time at INST. Here, I'd like to highlight a few special names: **Mujeeb** (who used to drag me for outings in an effort to cheer me up whenever I felt low)**, Shaifali**, **Mamta** (my T-mate), **Neha, Gaurav,** and **Avinash.** I would also want to acknowledge everyone who assisted me, whether directly or indirectly, while working or staying at INST: **Rohit Varshaney, Atikur sir, Anirban sir, Khalid sir, Ankush di, Naimat sir, Arpana, Vibhav, Baljeet, Ashwinder, Sanchita, Anjana, Praveen sir, Neha, Gagan, Parry, Rimple, Aakriti, Manju, Krishna sir, Asmita, Raveena, and Neethu**. Without an efficiently working administrative staff, getting the work done timely and

smoothly would have been challenging. For this, I would like to commend the great administrative team of both INST and IISER Mohali.

I owe a great deal to my friends from school and from university for always keeping in touch, taking time out of their busy schedule to talk and meet which refreshed my spirits: **Gonika, Shailza, Anisha, Amrit, Jyoti, Shivani, Meenakshi, Sonia, Abhishek, Jasmine and Chaman.** "**Sonali Kakkar and Bharat Thakur**" are two of my most favourite buddies whom I wish to specially acknowledge. It was back during the Postgrad days at Panjab University when I first met **Sonali** and at the wink of eye, we turned out to be best friends. Then later when she also joined here at INST alongwith me, it was only because of her that INST from the very beginning felt like a home to me because I knew despite anything I will always have a support besides me. She made me realise that having your best friend by your side during the most tiring times makes it an easy ride. **Bharat**, my friend since school has been literally been there for me always. There is not even a single time I can remember when I needed help and he was not available. He always stood by my side. He is in true terms a gem of a person.

Without acknowledging my life's most fundamental vitality, my family, whose tireless efforts, sacrifices and endurance made this journey possible, this acknowledgment would be incomplete. I've been blessed with a wonderful family who has been there for me at every step of my life, including my PhD. I whole-heartedly thank my **Mumma and Papa** for always believing in me and having faith in my ability to succeed. Their blessings have kept me going so far. I cannot really thank them for shaping me into the person I am today. Anything I do to make up for what they did for me so that I may achieve my objectives will be less. A heartfelt credit to **my little sister** for always motivating me to seize every amazing chance that came my way and for having faith in me despite all the uncertainties I had to confront. I would like to thank her for being such a special person throughout my life to whom I could turn to in all moments of happiness and sorrow. No matter how much low I may feel, she makes every effort to lift my spirits with our sibling inside fun. A big thanks to her for being a blessing in disguise of a sibling to me.

Gurpreet Kaur

INST, Mohali

List of Acronyms

PSC	Perovskite Solar Cell
MHP	Metal Halide Perovskite
PCE	PhotoConversion Efficiency
UV	Ultraviolet
PV	Photovoltaic
PL	Photoluminescence
HC	Hot Carrier
HPB	Hot Phonon Bottleneck
VB	Valence Band
CB	Conduction Band
E_g	Energy band gap/Energy gap
VBM	Valence Band Maxima
CBM	Conduction Band Minima
TA	Transient Absorption
IR	Infrared
DECP	Displacive Excitation of Coherent Phonons
ISRS	Impulsive Stimulated Resonant Scattering
PNC	Perovskite Nanocrystal
LARP	Ligand-Assisted Reprecipitation method
QD	Quantum Dot
AIP	All Inorganic Perovskite
ODE	1- Octadecene
OA	Oleic Acid
OAm	Oleylamine
RBF	Round Bottom Flask
N_2	Nitrogen
O_2	Oxygen
NIR	Near Infrared
EM	Electromagnetic
TA	Transient Absorption
SHG	Second Harmonic Generation
KLM	Kerr Lens Mode-locking

CW	Continuous Wave
CPA	Chirp Pulse Amplification
THP	Thin Film Polariser
SDG	Synchronization and Delay Generator
GVD	Group Velocity Dispersion
CP	Circularly Polarised
SFG	Sum Frequency Generation
DFG	Difference Frequency Generation
NLC	Non-Linear Crystal
WP	Wave Plate
OPG	Optical Parametric Generation
OPA	Optical Parametric Amplification
WLG	White Light Generator
THz	Terahertz
GSB	Ground State Bleach

Abstract

By virtue of their unique and unparalleled properties, perovskites have taken centre stage of the present research evolving around the quest for renewable sources of energy. It all started back in the year 2013 when metal halide perovskites (MHPs) made their first debut in the photovoltaic (PV) research world by showcasing an impressive Photo-Conversion Efficiency. Since then there has been no turning back; infact there has been a commendable hike in these numbers and lately these figures have skyrocketed to 31.25 % in case of organic-inorganic perovskite based tandem cells. All this may be attributed to their unique properties like defect tolerance, relaxed carrier cooling, large diffusion lengths etc. to name a few. However, the situation is different with the all-inorganic MHPs since their status in the PV business is not very spectacular and the resultant PCEs lag behind their hybrid counterparts. Despite this, the all-inorganic MHPs are still chosen over hybrid ones because of their greater stability and long-term consistency. It is moreover anticipated that these materials may attain their theoretically projected device efficiency limitations provided the necessary efforts are made to unleash them from their shortcomings. There are two strategies that can be followed for improvising the performance of any device. The first one relies on optimising the device structure and the second one is based on understanding the sequence of the photophysical events that occur in the functional layer subsequent to photoexcitation. In the present thesis, we have embraced this later approach. We have analysed the underlying behaviour of the photogenerated species to advance our previously held knowledge of the light-induced response of some of the all-inorganic MHP systems by taking assistance of transient absorption (TA) spectroscopy. A broad range of parameters significantly impact the charge carrier cooling process adopted by the charge carriers. Speaking particularly about MHPs, this carrier cooling rate is known to be quite decelerated in these structures, which is pretty beneficial from the perspective of PV applications. Here in this dissertation, we have attempted to modulate the existing cooling rate in $CsPbBr_3$ which is a very well established and promising lead based MHP system by providing an envelope of highly polar Cs_4PbBr_6 over it. In addition to facilitating Type-1 band alignment, this type of architecture also promotes polaron formation, which retards down the carrier relaxation process. Then in another study, we have also deciphered the temperature dependent interplay of the process of polaron formation and carrier cooling in $CsPbBr_3$ nanocrystals (NCs). Whenever any device is subjected to operation, it is exposed to variations in external temperature. Therefore for steering the device performance, it is crucial to

comprehend how these underlying competing processes behave at different temperatures. Besides this, studies conducted at low temperatures provide deeper understanding of the otherwise complicated photo-physical phenomena that are challenging to study at normal temperature due to increased system entropy brought on by substantial phonon disorder. Further we also executed an excitation energy dependent study for understanding the transfer pathways adopted by charge carriers in a composite system comprising of $CsPbBr_3$ and the low band gap PbS. This particular heterosystem is an established phototransistor functional layer. Here, we figured that the charge carrier transfer paths chosen are substantially influenced by the density of the states into which the charge carriers are originally injected in addition to the energy offset. Cs_2SnI_6 is the one of the most appropriate and promising alternative of lead based MHPs and it has also showcased some impressive efficiency numbers. Nevertheless, despite this, most of its photophysical aspects—both phonon-based and excitonic—have not yet been adequately addressed. Here in one of our investigations by deciphering the coherent phonon dynamics, we have furnished a full-fledged portrait of the phonon infrastructure constituting Cs_2SnI_6 lattice. Along with realising the process of coherent phonon generation and decay, we also discovered the silent and low frequency modes that are often unresolved in traditional frequency domain techniques. Moreover, through the pump and temperature dependent investigations, we have also provided a qualitative idea of the carrier-phonon strength prevailing in Cs_2SnI_6. In another venture we have unleashed the exciton dynamics play role in the photophysical behaviour of Cs_2SnI_6 by executing pump dependent TA studies. Here, we encountered unusually slow decay of the high excitons and discovered that their dynamics are entangled with that of the low energy excitonic species through intervalley scattering and phonon absorption processes. Further through effective mobility measurements, in Cs_2SnI_6 the hot carriers are found to exhibit higher mobility than the cold carriers. Given this high mobility of the hot carriers and the gradual decay of the high energy excitons, Cs_2SnI_6 is suggested as a potential material for hot carrier solar cells.

List of figures

1.1 The graph based on Clarivate Analytics data depicting the year-by-year citation history of the first publication on PSCs by Kojima and Miyaska…….. **[2]**

1.2 The major divisions into which perovskite systems can be classified…… **[3]**

1.3 Figure contains schematic representations illustrating the contours of the density of states (DOS) for bulk, 2D, 1D, and 0D materials…… **[5]**

1.4 Schematic representation of the electronic band structures of two frequently encountered semiconductors: **(A)** the traditional defect-tolerant systems (II-VI, III-V); **(B)** a model defect-tolerant architecture; here σ stands for the bonding orbital and σ* for the anti-bonding orbital; **(C)** A concise illustration of bonding in a $APbX_3$ structure portraying the defect tolerance…… **[7]**

1.5 (**A)** Graphical portrayal of the existence of the hole manifold in ordinary semiconductors, which causes the hot holes in these systems—which have been heated up through energy transfer—to rapidly lose their energy through phonon emissions. (**B)** Perovskite structures on the other hand lack a hole manifold due to the symmetrical distribution of the electronic states in both VB and CB. Therefore, even if Auger type energy transfer re-excites the holes in the VB, due to the low density of electronic states there is an intrinsic phonon bottleneck that eventually slows down the carrier cooling process…… **[8]**

1.6 Characteristic structure of a standard cubic 3D perovskite; red spheres represent the A cation and light green sphere depicts the B cation which forms the octahedral network with the X – anions (blue spheres)……. **[9]**

1.7 The tolerance factor-octahedral factor (t-μ) map for few halide perovskite compounds…….. **[10]**

1.8 The positioning of the defect states stemming from halide vacancies in the $CsPbX_3$ systems……... **[11]**

1.9 Various variants of metal halide perovskites: (**A)** Prototypical cubic structure of ABX_3 perovskites, **(B)** Tetragonal and **(C)** octahedral perovskite structures obtained as a consequence of octahedral tilting, (**D)** Vacant A-site BX_3 perovskites (**E),(F)** Ordered perovskites of the type- A_2BCX_6 and $A_2B(I)B(II)X_6$ respectively; Vacancy ordered perovskites of the type (**G)** $A_2B[V]X_6$ and (**H)** $A_3B_2[V]X_9$……..... **[14]**

1.10 Various processes that take place subsequent to photoexcitation as described in the text described schematically by the distribution of the carriers in the VB and CB.. **[16]**

1.11 The upsides and downsides of the various structural designs of lead free perovskites obtained as a result of isovalent and heterovalent replacement…….. **[17]**

1.12 Illustration of both degenerate and non-degenerate intervalley scattering processes in any arbitrary multivalley band structure……. **[18]**

1.13 Schematic illustrating the process of hot phonon bottleneck effect and Auger heating; the energy released during the recombination of the electron hole pair (1-1') is transferred to the electron 2 in the conduction band and hence it is excited to higher excited state (denoted as 2')…… **[20]**

1.14 Pictorial illustration of the process of polaron formation in any polar semiconductor system. The dark pink spheres depict the initial positions of the positive lattice ions before photoexcitation, while light purple spheres show the displaced positive ions following the irradiation process; similar denotation for the negative ions has been made by using yellow spheres. After being hit by the pump pulse, the negative ions lying along the trajectory of the propagating electrons are pushed away and those which are positively charged are drawn in. As a result, the lattice begins to deform dynamically all along the motion of the charge carrier. By acting on the otherwise free electron (forming a polaron), the resulting self-induced polarisation cloud modifies the carrier's ordinary physical characteristics. Only the electron polaron has been used here to illustrate the scenario for the purpose of simplicity, however there are also hole polarons……... **[22]**

1.15 Resultant modes obtained as a consequence of addition of coherent and inocoherent phonons……... **[25]**

2.1 Systematic hypothetical representation of the evolution of atomic concentration in a traditional LaMer mechanism during the three phases of reaction (LaMer and Dinegar, 1950)……... **[39]**

2.2 Typical Hot injection synthesis setup for the synthesis of AMX_3 perovskite nanocrystals…… **[39]**

2.3 **(A)** Diffraction of incident X-rays by a crystal and Bragg's law. **(B)** Schematic illustration of goniometer assembly in a typical XRD setup…….. **[44]**

2.4 The different potential processes that may occur when a thin sample is struck by a highly accelerated electron beam……..... **[46]**

2.5 Basic configuration depicting the typical components of a Transmission Electron Microscope (TEM)…… **[48]**

2.6 Schematic illustrating the basic optical setup of a steady state absorption spectrometer…… **[52]**

2.7 Basic configuration of a fluorometer…….. **[54]**

2.8 Fundamental architecture of a TCSPC system demonstrating its basic building blocks…….. **[56]**

2.9 Schematic depicting the fundamental strategy of a pump-probe experimental setup. The pump beam excites the sample, and any pump induced changes in sample absorption are subsequently examined by the probe beam, which is incident on the sample at an adjustable delay relative to the pump beam (Δt)……... **[59]**

2.10 Schematic in the upper panel illustrates the Q switching technique employing an electro-optic modulator (Pockels cell or Kerr cell). The figure in the lower panel depicts the formation of the giant pulses as a result of Q-switching…….. **[62]**

2.11 (**A)** Random modes in a laser cavity (**B)** Modes sharing identical phases, (**C)** The resulting electric field intensity obtained from the superposition of randomly phased modes (Figure A) (some curves are ascending and others are descending near the cavity's entry) and the six phase aligned modes depicted in Figure (**B, D)**. Pulses resulting from the superposition of 4, 8 and 60 modes depicting that the pulse width goes down as the number of modes involved are increased……... **[64]**

2.12 **(A)** Kerr effect induced self-focusing of a Gaussian beam. **(B)** Mode-locking in a cavity employing Kerr medium functioning as a focusing lens: in the continuous wave (CW) mode of operation or when the modes are not aligned in phase, self-focusing is not practical, as a result such light beams are rejected by the aperture. Such beams thus experience high cavity losses and do not participate in lasing. On the other hand, mode-locked pulses experience self-focusing due to Kerr effect and thus can pass through the spatial aperture for amplification…… **[66]**

2.13 Layout of the Chirped Pulse Amplifier unit……... **[69]**

2.14 The two different forms of dispersions that incident light encounters when it travels through an optical medium are shown schematically……..... **[70]**

2.15 Schematic illustrating the components constituting the REGEN unit (Pulse Picker assembly and gain medium)……... **[73]**

2.16 Photon picture showing the harmonic generation while taking into account the conservation of energy and momentum throughout the generation process. Such processes can take place both collinearly and non- collinearly provided both the energy

and momentum are conserved. **(A)** The process of SHG when the incoming waves are incident collinearly on the crystal. **(B)** The non-linear method of SHG where the incoming waves enter at an angle to one another and the second harmonic that results is oriented halfway between the directions of the incident waves. **(C)** Sum frequency method for harmonic generation, mixing an incoming fundamental with its second harmonic. The vector sum of these incident frequencies determines the direction of the sum frequency generated signal (For explanation sake, a fundamental and a second harmonic has been presented here as the incident waves, however these incoming waves can be any order harmonics of the fundamental)……..... **[74]**

2.17 **(A)** The generalised process of Sum Frequency Generation where two incoming frequencies upon being incident on a NLC yield a resultant photon whose frequency is the sum of the incident photon frequencies. **(B)** Photon picture of the Difference Frequency Generation process where the output frequency at the disposal of the NLC is the difference of the incident frequencies. **(C)** depicts the process of optical parametric generation where the NLC divides a "Pump" photon into two distinct frequency photons, the one with higher frequency is called "SIGNAL" and the one carrying lower frequency is called "IDLER"……. **[75]**

2.18 Optical Parametric Amplification: a pump photon and a "SIGNAL" photon which is actually the output from the OPG stage are incident together on a NLC. The "SIGNAL" photon is amplified as it gains energy at the cost of the energy of the pump and an IDLER photon is also produced along…… **[76]**

2.19 Layout of OPERA Solo showing the several steps the incident beam takes to produce the desired frequency at the output port. (BRM – Beam Routing Mirror, MTEL – Optical Mirror Telescope, BS – Beam Splitter, DM – Dichroic Mirror, NC1 & NC2 – Non-linear Crystals (adjustable angles for achieving perfect phase matching condition-software controlled), BB – Beam Blocker, DP – Brewster Plate (result in adjustable delay- software controlled), IM – Idler Mirror (placed in position only if IDLER or its second harmonic/sum frequency has to extracted at the output))…….... **[78]**

2.20 The sketch providing a summary of the ultrafast setup that we employed for the research projects included in this dissertation……... **[81]**

2.21 **(A)** Possible origins of the pump probe signals: Ground State Bleaching, Stimulated emission and Excited state Absorption. **(B)** The different ways they are manifested in the TA spectral data…… **[83]**

2.22 The region of the EM spectrum where the THz radiation lies and the frequencies corresponding to the rotational, vibrational and electronic transitions…….. **[84]**

2.23 Simple layout of the Newport built Terahertz Time Domain spectrometer used in the present dissertation…… **[87]**

3.1 **(A)** High Resolution TEM images of (a, d) $CsPbBr_3$, (b, e) Cs_4PbBr_6 and (c, f) $CsPbBr_3$@Cs_4PbBr_6 core-shell NCs. **(B)** Powder XRD patterns of the deposited films of (a) $CsPbBr_3$, (b) Cs_4PbBr_6 and (c) $CsPbBr_3$@ Cs_4PbBr_6 core-shell NCs. **(C)** Steady state optical absorption spectra of (a) $CsPbBr_3$, (b) Cs_4PbBr_6 and (c) $CsPbBr_3$@ Cs_4PbBr_6 core-shell NCs. **(D)** Typical UV-vis absorption (black line) and the corresponding steady state PL emission spectra (red line) for the same concentration of NCs depicting a Stokes' shift (Δ_S) of ~30 meV (inset: Corresponding Time-resolved PL decay curves of (a) $CsPbBr_3$@ Cs_4PbBr_6 NCs (τ_{av}=8 ns) and (b) $CsPbBr_3$ (τ_{av}=12 ns)…… **[102]**

3.2 **(A, B)** Representative pseudo colored plots for $CsPbBr_3$ and $CsPbBr_3$@ Cs_4PbBr_6 core-shell NC systems respectively under just above the band gap excitation (λ_{ex} = 480 nm). **(C, D)** Comparative kinetic traces for both the systems probed at probe wavelength λ = 525 nm (positive band) and probe wavelength λ = 514 nm (bleach band) respectively……. **[104]**

3.3 **(A)** De-convoluted absorption spectra of $CsPbBr_3$ NCs showing the separated excitonic contribution from the continuum states contribution. **(B)** Early time (0.3 ps) TA spectra of $CsPbBr_3$ NC matches with the second derivative of steady state absorption for $CsPbBr_3$ (Inset) which clearly represents the biexciton induced Stark effect in the TA spectra……. **[106]**

3.4 **(A, B**) Representative pseudo color plots depicting the extremely slow hot carrier cooling for $CsPbBr_3$ and $CsPbBr_3$@Cs_4PbBr_6 core-shell NC systems respectively under far above band gap energy excitation (λ_{ex} = 300 nm, ~ 4.1 eV). **(C, D)** Comparative kinetic traces for probe wavelength λ = 525 nm (positive band) and probe wavelength λ = 514 nm (bleach band) respectively……... **[107]**

3.5 **(A)** The band energy alignment in $CsPbBr_3$@Cs_4PbBr_6 NCs showing the various probable processes can undergo on above band gap excitation. **(B)** Schematic representation of Burstein-Moss effect depicting the wideness of the energy band gap with different charge carrier density. (blue spheres represent the valence band electrons which upon photoexcitation move to the conduction band (red spheres) leaving behind the holes (vacant sites))……... **[109]**

3.6 **(A), (D)** Normalised TA spectra under non-resonant pump excitation (300 nm) for varying probe delays (from 0.5 to 2.2 ps), the dashed boxes drawn show the high energy tail region over which Maxwell Boltzmann fitting has been done for $CsPbBr_3$@Cs_4PbBr_6 core-shell, $CsPbBr_3$ NCs respectively. **(B), (E)** show the magnified high energy tail region which have been fitted using Maxwell Boltzmann fitting to extract the T_e values. **(C), (F)** The corresponding temporal evolution of the carrier temperature T_e…… **[112]**

3.7 Normalized photo induced absorption kinetics of the (a) $CsPbBr_3$ and (b) $CsPbBr_3$ @Cs_4PbBr_6 core-shell NCs probed at 550 nm during early time scale (the black solid lines gives the best fit eligible for the corresponding kinetic traces)**.** The electron covered by the phonon cloud implicates the polaron formation followed by the polaron decay in correspondence to the approximate time scale for the events…….. **[114]**

4.1 **(A)** Absorption spectrum of the $CsPbBr_3$ NCs deposited over the glass substrate via spin coating. **(B)** Powder X-Ray Diffraction pattern for the as deposited $CsPbBr_3$ film……..... **[124]**

4.2 **(A)** Normalised temperature dependent PL plots for $CsPbBr_3$ NC film. **(B)** The quantitative shift in the peak maxima and the altered PL linewidth tracked as a function of temperature, representing the two sections of the probed temperature region over which the different couplings dominate distinctly (Regime 1 (5 K-200 K), Regime 2 (200 K-300 K))……..... **[125]**

4.3 The deconvoluted non- Lorentzian PL spectrum (5 K) presenting the contribution from the two Gaussian peaks coming up from the bound exciton and the free exciton. **[126]**

4.4 **(A) - (E)** The TA spectra spanning a wide range of temperatures, from 300 K to 5 K under 3.54 eV pump excitation.A supplementary low energy feature, which is completely missing around 300 K markedly emerges at cryogenic temperatures. **(F)**The normalized TA dynamical responses illustrated by probing the kinetics at the position of the free excitonic bleach……..... **[127]**

4.5 Field Emission Scanning Electron Microscopy (FE-SEM) images of the as-deposited $CsPbBr_3$ NCs over the glass substrate, showing the uniformity of the thickness of the deposited film…….. **[130]**

4.6 **(A)** Schematic representation of two competitive processes namely, polaron formation and hot carrier cooling, deciding the eventual governing relaxation mechanism *w.r.t* different temperatures. **(B)** The low energy positive signal maxima (620 nm, 2.0 eV) for the entire range of investigated temperatures (normalised)…….. **[131]**

4.7 **(A), (C)** Characteristic TA spectra traces normalized at the position of maximum amplitude of bleach for 300 K, 5 K plotted for the early probe delay time scales (0.4 ps to 2.3 ps), the marked region (dashed boxes drawn) signify the high energy section opted for carrying on the Maxwell-Boltzmann fitting to pull out the carrier temperature values (T_c). **(B), (D)** plots represent the temporal progression of T_c for extreme ends of the investigated temperatures 300 K, 5 K. **(E)** Relative plots for T_c normalized at 0.4 ps, illustrating the difference in the various relaxation trails embarked upon by the HC. **(F)** Relative biexcitonic dynamics (~2.34 eV), showing the distinction in the formation and decay dynamics as a function of temperature (Normalised)……..... **[133]**

5.1 Powder XRD data for **(A)** $CsPbBr_3$ NCs and **(B)**PbS QDs deposited on glass film.[**144]**

5.2 High Resolution Transmission Electron Microscopy (HR-TEM) images of **(A, B)** $CsPbBr_3$ NCs and **(C, D, E)** PbS QDs dispersed in Toluene……..... **[145]**

5.3 **(A)** Steady state optical absorption spectra for the pure $CsPbBr_3$ NCs, PbS QDs and their resultant composite colloidal mixture ($CsPbBr_3$ + PbS); The corresponding PL data illustrates the quenching of PL intensity in the composite system monitored at the emission position of $CsPbBr_3$. **(B)** in the case of far band gap excitation (w.r.t $CsPbBr_3$)- 300 nm and **(C)** for near band gap excitation- 480 nm). **(D)** Simultaneous increment in the PL intensity probed in the NIR region at the position of PbS emission peak potraying a transfer of charge carriers from $CsPbBr_3$ towards PbS states under 300 nm excitation and **(E)** 480 nm excitation. **(F)** Schematic illustration depicting the difference in the density of electronic states encountered in the composite system when excited using different excitation wavelengths……. [**147]**

5.4 Representative Transient Absorption spectra for (**A)** $CsPbBr_3$ NCs in the visible regime; (**B)** PbS QDs in NIR regime; (**C)** $CsPbBr_3$-PbS NC composite in visible; and (**D)** $CsPbBr_3$-PbS NC composite in the NIR regime; (**E)** Normalised bleach kinetics for PbS NCs ((a), probe wavelength = 955 nm) and $CsPbBr_3$-PbS NC composite ((b), probe wavelength = 962 nm); (**F)** Normalised bleach kinetics for $CsPbBr_3$- NCs (c) and $CsPbBr_3$-PbS NC composite (d) probed at visible bleach maxima (504 nm). The data presented here are for the samples after exciting at 300 nm…….... [**149]**

5.5 TA spectra for (**A)** $CsPbBr_3$NCs in the visible regime; (**B)** PbS QDs in NIR region; (**C)** $CsPbBr_3$–PbS composite in NIR region; (**D)** $CsPbBr_3$–PbS composite in NIR region; (**E)** Normalised bleach kinetics at 503 nm for (a) pure $CsPbBr_3$ NCs and (b) $CsPbBr_3$–PbS composite; (**F)** Normalised bleach kinetics at 955 nm/976 nm for (c) pure $CsPbBr_3$ NCs and (d) $CsPbBr_3$–PbS composite; after exciting the samples at 480 nm. [**153]**

5.6 Representative Transient Absorption (TA) spectral maps under 620 nm excitation for (**A)** $CsPbBr_3$-PbS NCs in the visible probe region. (**B)** PbS QDs in the NIR regime; (**C)** $CsPbBr_3$-PbS NC composite in the NIR regime. (**D)** Comparative normalized TA kinetics at NIR bleach position for (a) PbS QDs probing at 945 nm; and (b) $CsPbBr_3$-PbS NC composite probing at 960 nm); (**E)** TA kinetics for $CsPbBr_3$-PbS NC composite at 540 nm. **(F)** Schematic illustration of the processes taking place when the $CsPbBr_3$-PbS composite sample is excited at 620 nm…….. **[155]**

6.1 XRD pattern for the synthesised Cs_2SnI_6 NCs spin-coated over glass substrate (the black lines represent the standard XRD pattern of Fm-3m Cs_2SnI_6……. **[164]**

6.2 **(A)** Large area TEM image of the synthesised pristine Cs_2SnI_6 NCs **(B)** High Resolution (HR)-TEM image…….. **[165]**

6.3 **(A)** Steady state optical absorption spectra for Cs_2SnI_6 NCs and (**B)** the corresponding photoluminescence (PL) spectra. (Excitation energy= 2eV)…….. **[165]**

6.4 (**A)** Schematic representation of the pump-probe technique employed for data acquisition, (**B)** Pseudo-colour 2D contour representation for the TA response recorded upon photo-excitation of Cs_2SnI_6 NCs (pump energy = 2 eV), (**C)** The corresponding TA spectral traces for selected delay times, (**D)** Resultant kinetics monitored at specific probe energies (1.77 eV, 1.83 eV) illustrating the periodic modulations due to coherent phonon generation superimposed over the carrier dynamics. The oscillations perceived in the TA data at two different probe energies are in phase ($\Delta\varphi = 0^0$) indicating that the oscillations are an outcome of amplitude modulation……..... **[166]**

6.5 **(A)** Extracted residual oscillations with a typical time period of "0.26 ps" after subtracting the exponential decay behaviour from the TA trace**, (B)** Power spectrum obtained after Fast Fourier transforming these residual oscillations revealing the distinct phonon modes feasible in Cs_2SnI_6…….. **[168]**

6.6 **(A)** Schematic illustration of ISRS mechanism displaying the induction of coherent lattice motions in the ground electronic state. Such translational motions in turn trigger vibrational wavepackets with their maxima around the equilibrium position and are thus manifested as oscillations in the vicinity of the normal mode coordinate. **(B)** For DECP strategy, the G.S wavepacket as a consequence of photoexcitation is initially projected into higher excited electronic state, where later this wavepacket begins to oscillate around a point different from the equilibrium position…….. **[171]**

6.7 **(A-D)** TA kinetic traces for Cs_2SnI_6 NCs obtained while irradiating the samples with different photogenerated charge carrier densities (2 eV pump) at the position of

excitonic bleach and **(E)** Intensity dependent plots depicting the linear increment of the coherent phonon amplitude with increasing photogenerated charge carrier density…….. **[173]**

6.8 **(A)** FFT Power spectra generated upon Fourier transforming the residual oscillations for three different pump excitations. **(B-D)** Phase angle analysis for the different modes under these different excitation conditions (monitored at three distinct probe energies: 1.74 eV, 1.78 eV, 1.82 eV)…….. **[175]**

6.9 Power spectrum obtained as a consequence of fast fourier transforming the oscillatory TA data acquired using extremely intense 2eV pump pulses (Laser power :1mW) displaying the mode at 67cm^{-1} (silent mode) to stand out of all the other modes... **[176]**

6.10 **(A-C)** Transient spectral plots for Cs_2SnI_6 acquired upon cooling the lattice down to cryogenic temperatures (5 K – 200 K) for 2eV pump excitation, (**D)** Corresponding residual oscillations demonstrating no phonon softening over the investigated temperature range. **(E)** FFT power spectra plotted for cryogenic temperatures, displaying no possible structural distortion as a function of lattice temperature….. **[180]**

7.1 **(A)** 3D model for the $Fm\bar{3}m$ crystal structure of Cs_2SnI_6. **(B)** HR-TEM image of the synthesized Cs_2SnI_6 DP NCs; Steady state optical properties. **(C)** Optical absorption spectrum along with the de-convoluted fits (Inset shows the photograph of the prepared sample). **(D)** Corresponding photoluminescence spectrum of the dispersed samples (Inset displays the sample illuminated with UV radiation)……. **[192]**

7.2 **(A)** Band structure of Cs_2SnI_6 in $Fm\bar{3}m$ phase calculated with hybrid functional HSE06 revealing that Cs_2SnI_6 is a semiconductor with a direct band gap of 1.03 eV at Γ point of the Brillouin zone, **(B)** Tauc plot used for the estimation of the energy band gap (E_g), obtained from steady-state absorption keeping in consideration that Cs_2SnI_6 is a direct band gap material, **(C)** the electronic transition dipole moment (TDM) between the KS states is shown along the high-symmetry path which shows the transition probability of electrons across the high symmetry path in the Brillouin zone; Our estimated optical absorption spectra (with HSE06) are shown in **(D)**, which qualitatively agrees with the experimental one. We have assigned transitions (shown in **(A)** by pink arrows) corresponding to the peaks in absorption spectra, inset is showing expanded transitions in energy range 2.0 eV to 3.0 eV. We find states lying –2 eV deep in VBM also contributing to peaks in the absorption spectra (denoted as E_D)…… **[194]**

7.3 **(A)** UPS plot in the high binding energy regime employed for the estimation of E_f from the secondary cutoff energy. The zoomed region shows the linear extrapolation of the low energy region of the plot yielding "$E_v - E_f$", **(B)** The band level diagram displaying the band levels of Cs_2SnI_6 after summarising the collective results obtained from the UPS investigations and Tauc plot…… **[197]**

7.4 TA spectral responses acquired in the UV domain upon exciting the Cs_2SnI_6 NCs with **(A-C)** pump energies adequate to directly populate the exciton "B", **(D-F)** pump energies less than that required for the direct excitation of exciton "B"…… **[199]**

7.5 TA spectral responses recorded in the visible probe region upon exciting the Cs_2SnI_6 NCs with different pump energies…….. **[200]**

7.6 Schematic representation illustrating that how the IV scattering process results in the formation of "C" exciton from the charge carriers initially injected into the electronic states lying in the L valley above the threshold excitonic transition "B". These $E > E_B$ excitations can be further sub-categorised into two domains: (I) depicts the excitations with pump energies $E_C > E >> E_B$ (the region denoted by E_L^{High} - high energy electronic states lying at L site situated far from the band edge of B-exciton) (II) the region described as E_L^{Low} refers to relatively low energy electronic states lying at L site close to the B- exciton edge. In the former situation when the charge carriers are injected into sufficiently high energy electronic states (E_L^{High}), the situation is quite simple as IV scattering is practical. However in the later situation, when the photon energy E is just above the threshold required for the formation of B-exciton , *i.e.* E_L^{Low} and the charge carriers are injected into relatively lower energy electronic states, there is an energy offset (ΔE) involved that needs to be surpassed for IV scattering processes to take place. This offset seen by the injected charge carriers can be circumvented in two ways: by absorption of the emitted phonons (III) or by the absorption of the probe (IV)… **[202]**

7.7 Transient bleach profiles for Cs_2SnI_6 NCs irradiated with different pump energies. **(A)** C-exciton dynamics showing the difference in the bleach rise time under different color pumps. **(B)** Bleach dynamics for B-exciton under varied excitations. **(C)** Schematic depicting the pump dependent contribution of phonon absorption processes in the formation of B exciton (2.74 eV bleach). For 2 eV pump, due to the existence of large energy offset (0.74 eV), the photogenerated carriers take long time to advance from the initially excited state to the B-exciton band edge because they require to absorb a significant number of phonons to beat this energy barrier (T_1); however, for higher energy pump like 2.58 eV, this offset is relatively reduced (0.16 eV) so relatively less

number of phonons are required to counter this mismatch, resulting in the faster formation of B-exciton (T_2). **(D)** Comparative kinetics displaying the difference in the bleach growth times of A- exciton with pump energies varying between 4 eV and 2 eV…… **[204]**

7.8 **(A-E)** Normalised kinetic traces comparing the time dependent behaviour of the three excitons dominating the photo-physics of Cs_2SnI_6 under different pumps. The probe energies corresponding to monitored electronic transitions have been denoted by the nomenclature adopted throughout this writing, **(F)** Schematic portrayal of the most probable processes involved in the formation and decay of these excitons (I- IVS mechanism involved in the formation of C exciton from B exciton, II- decay of C exciton through A exciton at Γ valley, III- intraband relaxation of the hot carriers at Γ point (A-exciton formation), IV-decay of B-exciton through radiative recombination, V- phonon absorption by the excited carriers in the Γ valley for the formation of B exciton, VI- decay of B exciton through A exciton, VII- phonon absorption by the charge carriers injected into the low energy electronic states to reach the high energy levels……... **[208]**

7.9 **(A)** THz-TDS waveform transmitted through air, quartz and Cs_2SnI_6 spincoated over quartz substrate **(B)** Effective mobility plots depicting the difference in trends for the rise in the mobility observed under two distinct types of pump excitations: far above band gap excitation (2.95 eV pump) and close to band gap (2 eV) excitation. **[212]**

List of tables

Table 3.1 Kinetics fitting parameters for $CsPbBr_3$ and $CsPbBr_3@Cs_4PbBr_6$ core-shell systems dispersed in n-hexane after exciting the samples at 480 nm…… **[107]**

Table 3.2 Kinetics fitting parameters for $CsPbBr_3$ and $CsPbBr_3@Cs_4PbBr_6$ core-shell systems dispersed in n-hexane after exciting the samples at 300 nm……. **[110]**

Table 4.1 Kinetic Fitting parameters for the probe monitored at the bleach position for $CsPbBr_3$ NCs deposited over a glass substrate under a pump excitation of 3.54 eV (The values in the brackets in the table indicate the respective weightages for the time constants mentioned)…… **[128]**

Table 4.2 Kinetic Fitting parameters for the probe monitored at the biexciton position (2.34eV)…… **[135]**

Table 5.1 Kinetic fitting parameters for the probe monitored at the bleach position (probe wavelength (WL) mentioned in bracket) for pure $CsPbBr_3$, pure PbS and $CsPbBr_3$ – PbS composite NCs under a pump excitation of 300 nm…… **[150]**

Table 5.2 Kinetic fitting parameters for the probe monitored at the bleach position (probe wavelength (WL) mentioned in bracket) for pure $CsPbBr_3$, pure PbS and $CsPbBr_3$ – PbS composite NCs under a pump excitation of 480 nm…… **[154]**

Table 5.3 Kinetic fitting parameters for the probe monitored at the bleach position (probe wavelength (WL) mentioned in bracket) for pure PbS and $CsPbBr_3$ – PbS composite NCs under a pump excitation of 620 nm……. **[156]**

Table 6.1 Assigning the origin to the various observed modes (2 eV pump excitation, (Intensity- 100 μW))…… **[178]**

Table 7.1 Fitting parameters for A exciton bleach growth dynamics……. **[206]**

Table 7.2 Time constants obtained upon multi exponential fitting of the signal growth and decay profiles for different excitons under different energy pump excitations…… **[209]**

Thesis overview

The present thesis is based on comprehensively examining the lesser known fundamental photophysics and the ultrafast excited state occurrences in both lead based and lead free all-inorganic MHPs as well their heterostructures. For serving this goal, femtosecond TA spectroscopy has been deployed as a valuable asset. Because of the ultrashort pulsewidths, the time scales that may be analysed with this method typically vary from a few femtoseconds (fs) to nanoseconds (ns). In this way by leveraging the advantages of TA spectroscopy, we have attempted to track down the transient response of the photogenerated entities such as charge carriers, excitons, and other quasi-particles that form and decay across these time scales in our systems of interest. Besides this, we have also probed some of the MHP systems at cryogenic temperatures to better understand the phonon aided phenomena which ultimately drive the carrier dynamics by mitigating the thermal complications that otherwise interfere at room temperature. In essence, the central theme of this thesis is the investigation of the time dependent evolution of the photophysics guiding the prospective materials that make up the functional layers of solar panels or other optoelectronic devices. We believe that a deeper comprehension of them could result in the design of optoelectronic devices with even higher efficiency. The thesis has been organised in the following framework:

❒ ***The chapter 1*** commences with a brief history of perovskites, their advancement over time, and the parameters that define their structural viability. Narrowing down of this wide class of materials to metal halide perovskites, we have then presented an overview of the all-inorganic perovskites and their further sub-categories like vacancy ordered derivatives etc. This chapter then further addresses the numerous processes that take place in a perovskite material right after photoexcitation and pays diligence on introducing the various factors like phonon bottleneck effect, polaron formation etc. that are pivotal to charge carrier cooling in MHPs. Herein the concept of lattice vibrations and the phonon modes, which indirectly control the carrier cooling, has also been contextualised in addition to the revelations about the charge carrier relaxation processes.

❒ ***The chapter 2*** seeks to address the synthesis strategies deployed for the halide perovskite NC systems examined in this thesis work as well as the key experimental techniques employed for their subsequent characterisation, detailing the theory underpinning each approach and the precise setups used. The as-synthesised NCs have been characterised using a variety of experimental approaches, which may be majorly categorised into two sections:

steady state characterisation techniques and time resolved methods. Probing the excited state in semiconductors requires ultrafast excitation instruments as well as detection devices capable of capturing signals linked to the excited state within the relevant time scale. Given that the primary subject of this dissertation is to comprehend such excited state photophysical characteristics of the various perovskite structures, transient absorption spectroscopy can be considered as the ideal tool for the job. Therefore, we have paid special emphasis on the explanation of its experimental setup.

❒ Slow carrier cooling is advantageous for PV applications and if strategically harnessed, can assist in achieving high PCEs. ***The chapter 3*** is designed with an aim to further retard the carrier relaxation rate in the prototypical $CsPbBr_3$ system which is already known to exhibit slow cooling. For accomplishing this aim, we provided an envelope of highly polar Cs_4PbBr_6 over $CsPbBr_3$ core (Type 1 structure) and found that as per our anticipation the carrier cooling dynamics demonstrated by this core-shell configuration is much retarded than the pristine $CsPbBr_3$. Further upon examining the dynamics of the low energy region, we discovered that the Type-1 architecture is not the only factor contributing to the delayed carrier cooling observed here; polaron formation is also equally liable. The mobility of the carriers that are photo-generated in the shell is fairly low due to the formation of polarons in the highly polar Cs_4PbBr_6 lattice. Even though these carriers are native to the Cs_4PbBr_6 shell, they eventually relax at the $CsPbBr_3$ band edges, which delays the cooling of the carriers even further, as shown by the kinetics probed at the $CsPbBr_3$ bleach position.

❒ ***The chapter 4*** which is based on temperature-dependent investigations, executed for $CsPbBr_3$ revealed that while the carrier cooling dynamics are rather sluggish at 300 K, they are seen to be expedited when the lattice temperature is gradually lowered to 5 K. We identified the cause of such accelerated kinetics to be the inability of $CsPbBr_3$ lattice to sustain the polarons at low temperatures because of the absence of longitudinal optical (LO) phonons. However, due to the abundance of LO phonons at temperatures in the proximity of 300 K, the indulgence of polaron brought on by strong carrier-LO phonon coupling in the carrier cooling process manifests as slow kinetics at temperatures close to 300 K. Since the devices while in operation are subjected to various temperature settings, this prior understanding of the hot carriers' typical behaviour may be utilised to optimise the performance of $CsPbBr_3$ based device.

❒ Apart from the utility in PV domain, $CsPbBr_3$ employed in conjunction with PbS in a composite system is known to function as a highly sensitive, broadband photodetector. The ***chapter 5*** has been designed to explore the underlying hot carrier relaxation and transfer strategies within the $CsPbBr_3$−PbS heterostructure. For this intent, we vigilantly chose a set of different excitation energies. While exciting with high energy photons (300 nm) and comparing the bleach growth kinetics, we found the transfer of the hot carriers in this Type-1 heterostructure to be bi-directional since the bleach growth dynamics are noticed to be quite decelerated in contrast to those monitored for the pure NCs. However, there is a drastic variation observed when the composite is excited close to the band edge. The probe dynamics in such instance of near band gap excitation (480 nm), suggests that unlike the hot carriers, the cold carriers on the other hand tend to opt for only one way transfer of carriers, that is, from $CsPbBr_3$ to PbS energy states. Such a detailed knowledge of carrier relaxation and transfer mechanisms can prove utterly advantageous for the design and further improvement in the performance of any sort of photo electronic devices employing $CsPbBr_3$−PbS colloidal hetero-structure.

❒ ***The chapter 6*** is based on the inspection of lead free Cs_2SnI_6 system which is a competing contender for the lead containing perovskite systems and has also shown promising results. Despite this, virtually little is known for this system. Employing TA spectroscopy, we have attempted to portray a real time picture of its phonon structure and identify the modes that were yet not assigned an origin particularly, the low frequency silent modes which are overlooked by the conventional spectroscopies. Additionally, we looked at the unified framework of displacive excitation and impulsive scattering to examine the generation mechanism of the low symmetry modes observable in the frequency domain as well as the fully symmetric coherent phonon mode "A_{1g}" that is manifested as strong oscillations in the time domain data for Cs_2SnI_6. The excitation pump phase analysis and intensity-dependent TA measurements provide strong backing. Furthermore, we conducted temperature-dependent investigations, which when combined with the pump-dependent experiments, shed light on the degree of carrier-phonon coupling. We firmly believe that all this important information regarding phonon modes and how they couple with the photogenerated carriers may be applied to enhance the performance of Cs_2SnI_6-based devices in near future.

❒ Unlike the preceding study that examined the phonon dynamics***, the chapter 7,*** which is also based on Cs_2SnI_6, focuses on investigation of its exciton dynamics. The positioning of

the excitons in its Brillouin zone is first ascertained through the theoretical findings. Subsequent to these assignments, we deployed TA spectroscopy to examine the temporal evolution of these excitons and found the decay of the high energy exciton to be quite delayed. Surprisingly, the formation of high energy excitons is still observed even when the incoming photon energy is insufficient. The rationale for this result, we observed, is that the generation and decay processes of these excitons are entangled and are mediated by intervalley scattering mechanisms. In conclusion, our findings suggest that Cs_2SnI_6 might be a promising candidate in hot carrier-based solar cell systems that need delayed decay of high energy excitons.

❒ The final chapter, **Chapter 8** recapitulates the results of the study conducted in this thesis and offers a prognosis for potential future advancements that might build on this work.

Chapter 1

Introduction

1.1 Perovskites: "*A look back in time*"

Long back in 1839, a scientist hailing from Germany named Gustav Rose while exploring the Urals during his expedition to Russia, came across a new calcium titanate ($CaTiO_3$)-based mineral. He named this newly discovered mineral as "perovskite", as a homage to the Russian mineralogist Lev von Perovski (1792–1856).[1]

Years passed and it was then roughly half century later in 1893 when H.L. Wells and collaborators while working in a war unit at Yale University prepared the very first synthetic cesium and lead based halide perovskites known today.[2] Their crystal structure however was not yet known at that time. Later, in 1950, CHR. KN. MØller while working at the Royal Veterinary and Agricultural College in Denmark did a pioneering task by investigating their structure.[3] During the same era, numerous oxide perovskites were also discovered and synthesised which found their utility in a variety of applications. After a while in 1978 then the first organic-inorganic halide perovskite was synthesised by Dieter Weber, and later in 1994, due to its outstanding performance in opto-electronic devices, first demonstrated by IBM researchers, it drew enormous interest from the research community.[4] Furthermore, in the year 1999, oxide perovskite materials made their debut in the photovoltaic (PV) industry.[5] But when the halide perovskites were used as the absorber layer in PV devices (2009) and displayed impressive photoconversion efficiency (PCE) close to 3.8%, the start of a new exciting millennium was marked.[6] Since then, these figures have continued to rise (at present- 31.25%, as per the National Renewable Energy Laboratory (NREL) records accessed on 26.9.22) and are presently giving the traditional solar light absorber layers a competitive edge.[7] The citation records of the first paper published on perovskite solar cells (PSCs) by Miyasaka and group reflect that even the number of studies on PSCs has increased rapidly over the last decade **(Figure 1.1)**.[8]

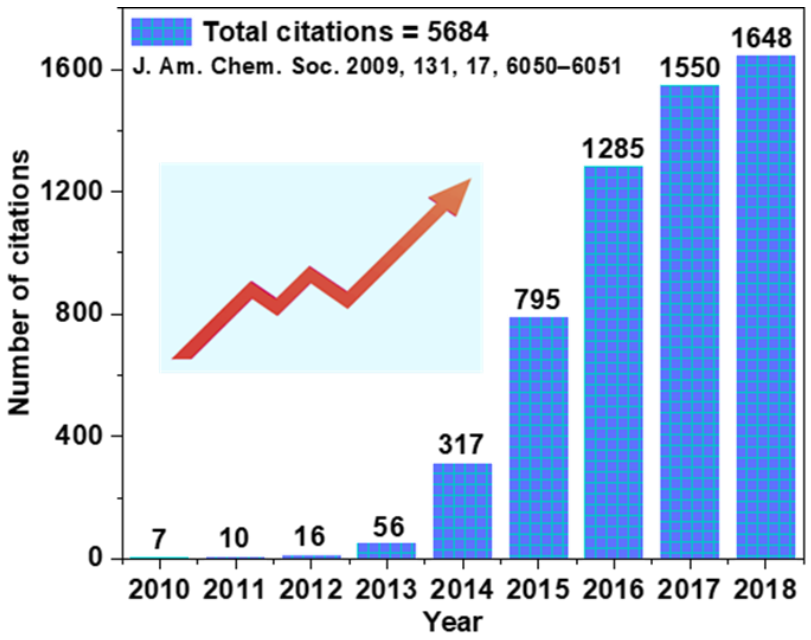

Figure 1.1 The graph based on Clarivate Analytics data depicting the year-by-year citation history of the first publication on PSCs by Kojima and Miyaska. "Reprinted (adapted) with permission from ref. {8}. Copyright {2009} American Chemical Society."

Up until this point, we have only mentioned the halide and oxide perovskites that are relatively more explored **(Figure 1.2).** But aside from these, there are many other systems that have structures similar to $CaTiO_3$. Perovskite materials are thus one of the most abundant and significant structural classes, exhibiting a wide range of intriguing properties depending on the atoms or molecules that comprise their structure. Ferroelectrics, piezoelectrics, thermoelectrics, photovoltaics, photodetectors, phototransistors and optoelectronics etc. are just a few of the application domains where these materials come handy.[9–12] But when the focus is specifically on light-based devices, metal halide perovskites (MHPS) are the ones that pique the research community's interest. The reason that MHPs thrive in this application domain is that they exhibit all those excellent properties that are the prerequisites for such applications, predominantly the optical band gap, slow carrier cooling, defect tolerance etc. (discussed in detail in later sections).

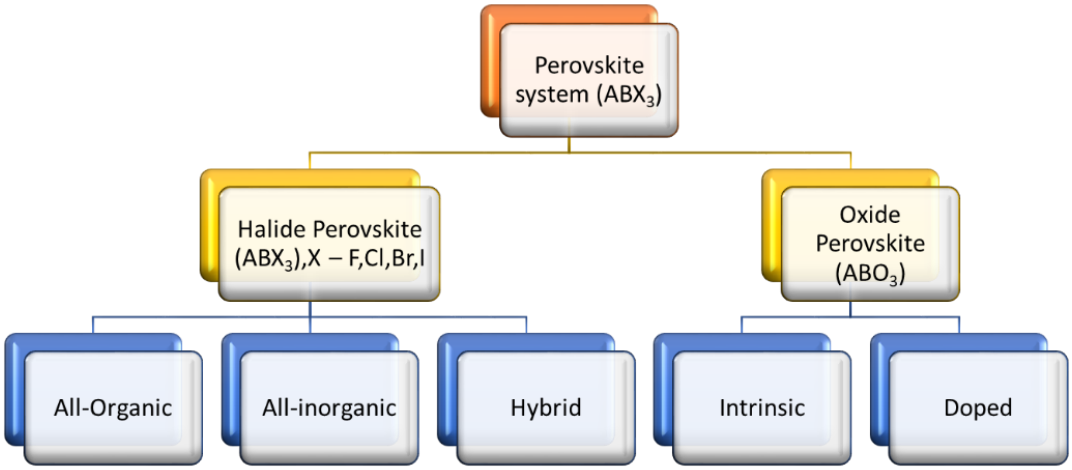

Figure 1.2 The major divisions into which perovskite systems can be classified.

1.2 Nanostructures and Quantum confinement

Anytime a semiconducting system is irradiated, the incoming photon energy absorption may stimulate an electron in its valence band (VB) and promote it to the conduction band (CB), leaving a hole behind. In certain situations, these electrons and holes bind together as a pair in a constricted state, which is referred to as an exciton. This bound state can be considered equivalent to a hydrogen-like system, therefore Bohr radius approximation may be used to estimate the separation distance between its constituent entities. Exciton Bohr radius ($a_{exciton}$) is the term that is usually adopted to describe this crucial equilibrium distance and it may be quantitatively represented as: [13,14]

$$a_{exciton} = \frac{ma_0}{\mu}\varepsilon \qquad \textbf{Eq. 1.1}$$

Here, a_0 is Hydrogen atom Bohr radius, μ is the reduced mass, m is the electron mass and ε is the permittivity.

Starting with a macroscopic material (say "bulk"), if its dimensions are significantly shrunk to the point that at least one of them is smaller than natural length scale of the exciton "$a_{exciton}$" designated for that material, quantum effects become operative. The wavefunctions associated with the charge carriers become restricted as per the particle's physical dimensions and the material is referred to be "quantum-confined".[15–17] **Eq. 1.1** makes it abundantly evident that a material's quantum confinement threshold is dictated by the quantum mechanical characteristics of its electrons and holes, making it unique to that material.

Unlike with the bulk materials, where electronic energy levels are continuous, low dimensional structures exhibit discreteness in their energy states.[18,19] This may be understood by recalling that bands in bulk matter emerge from a larger ensemble of atoms and molecules,

merging their many neighbouring energy levels which leads to such continuum of states. For the nanostructure systems, things are substantially different. The number of overlapping orbitals or energy levels reduces as the particle size approaches the nano scale, where each particle is made up of merely a small number of atoms or molecules, and therefore, the states are discrete.[18,20,21] Moreover, since the band width is lower in the latter case, the energy band gap (E_g) of the nano-dimensioned materials is higher than the bulk counterparts and this gap widens even more with further decrement in the size of the particle.[22–24] The most remarkable thing about the quantum confined structures is that they retain their bulk crystalline properties while also displaying substantial size dependence of their properties due to the prevalence of quantum confinement. In this manner, low-dimensional nanostructures link the bulk and molecular domains, opening up new avenues for utilising the material's intrinsic properties but with an added advantage of modifying the intrinsic properties by merely changing the particle size. As opposed to bulk systems, nanostructures offer a number of advantages, including improved absorption coefficient, extended excited state lifetime, sluggish carrier cooling (due to the presence of certain energy gap between two consecutive energy states), tuneable band gaps, etc. to name a few.[25–28] Due to their highly customizable optical and electronic properties, quantum structures are more appealing than bulk for usage in a variety of opto-electronic and photovoltaic applications.[15,21,29,30]

All nanomaterials may be categorised into three broad categories: zero dimensional (0D), one dimensional (1D), or two dimensional (2D) based on the number of dimensions in which the confined charge carrier has free degrees of motion. In the case of a quantum dot, the charged carrier's mobility is constrained in all three directions and there is no direction for free motion—0D; whereas in the case of a quantum wire, confinement is along two dimensions and there is only one direction also which the carriers can freely translate—1D. However, a quantum well can be labelled as a 2D material since the motion of the carriers in such architectures is restricted in merely one direction and thus, the charge carriers have two available directions of free motion. **Figure 1.3** shows the variations in density of states for all the variously constrained systems, from bulk to quantum dots.

A second criterion for classifying these structures, in addition to the dimensionality aspect is the extent of confinement. As a result, the nanostructures may be divided into three separate domains: weak, strong, or intermediately confined depending on the size of the synthesised particle (R), the exciton Bohr radius and the effective radius of each carrier in that particular system (a_h and a_e).[31] The confinement is considered to be i) 'strong' when the size of the particle is smaller than all these three parameters i.e. $R < a_h, a_e, a_{exciton}$ ii) 'weak' if the

particle outsizes the exciton Bohr radius i.e. R > $a_{exciton}$ but also R < a_h, a_e iii) 'intermediate' when R~ $a_{exciton}$ and simultaneously a_h < R < a_e or a_e < R < a_h;.[32,33]

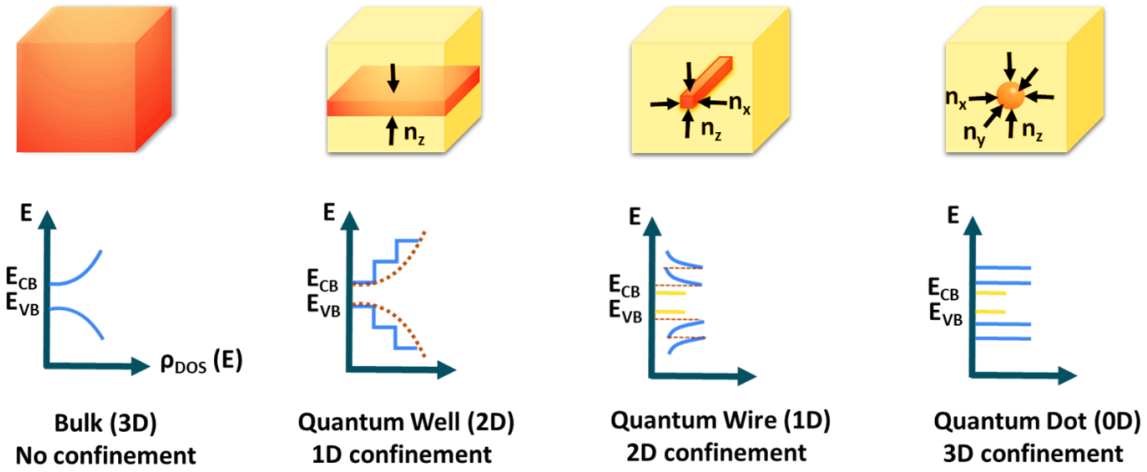

Figure 1.3 Figure contains schematic representations illustrating the contours of the density of states (DOS) for bulk, 2D, 1D, and 0D materials.

1.3 Halide Perovskite vs. the conventional semiconductor nanocrystals

While silicon or other conventional semiconductor-based PVs took far longer to achieve equal efficiencies, halide perovskites did it in just over 10 years. This can be linked to several advantageous characteristics associated with the halide perovskite structure. The II-VI or III-V metal chalcogenide systems, such as CdTe, CdS, PbS, etc., that have long been utilised as functional layers in optoelectronic and PV devices, are basically what we refer to when we talk about the archetypal semiconductor nanocrystals (NCs) or quantum dots (QDs). The emission wavelengths of such structures can be readily tuned by changing the particle size, but the emerging class of perovskite NC systems give us far **more precise tuning** choices that go well beyond what is possible with these typical NCs.[34,35] This is entirely due to the fact that the manipulation of the chemical composition of perovskite NCs controls their emission as opposed to conventional NCs, for which the emission is sensitive to and reliant on individual particle size. A halide anion-exchange reaction can alter the emission wavelength post-synthesis in addition to adjusting the reaction temperature (and eventually, nanocrystal size) during synthesis.[36,37] Moreover, compared to conventional semiconductor NCs, the emission from perovskite NCs is also **relatively purer**. Another unique feature that distinguishes halide perovskite NCs particularly the lead based ones from ordinary semiconductor NCs is their

defect tolerance due to the strategic positioning of the dominant defect states in their band structure. It is intriguing to note that although these materials have a comparable density of defect states as the conventional NCs, yet due to the positioning of the defect sites either in the bands themselves or extremely close to the band edges, non-radiative recombination of the charge carriers is impeded, thus producing a counterintuitively high photoluminescence (PL).[38,39] Furthermore, the capture cross sections of these traps is also lower. However this degree of tolerance is a strong function of the Stoichiometry of the synthesized material and the synthesis environment. On the contrary, it is unfeasible for conventional NCs to achieve such high magnitudes of PL intensity; instead, core-shell structures for conventional NCs must be developed, in which the non-radiative centres resulting from the surface imperfections of the core are passivated by the shell material. The answer to this distinct behaviour lies in the nature of the orbitals that constitute the VB and CB of $APbX_3$ perovskites. For the ordinary NCs, the VB states are predominantly built from the bonding orbitals, whereas the anti-bonding orbitals constitute the CB states **(Figure 1.4 A)**.[40] Therefore, the surface defect states that are usually non-bonding in nature reside in the mid-gap region between the Valence Band Maxima (VBM) and Conduction Band Minima (CBM).[41–43] Lead based Perovskite NCs, however, do not adhere to this. In these systems, anti-bonding orbitals are believed to make up both the VB (hybridisation of Pb (ns) and X (np) orbitals) and CB states (hybridisation of Pb(np) and X(np) orbitals) **(Figure 1.4 B,C)**. Therefore owing to the lack of bonding/anti-bonding interactions in these structures, it is extremely unusual for the non-bonding surface states arising from anion vacancies to reside in the area between VBM and CBM, rather they tend to lay very close to the band edges (shallow traps-lying within the thermal activation range).[44,45] This is especially true for the case of lead-based systems alone and not the other analogues due to the specific relativistic corrections that apply to Pb more effectively, which widen the CB in these structures and drop the CBM below the Pb(np) atomic orbitals.[46]

The most fascinating and alluring part of perovskites, specifically the MHPs, despite the fact that they have a number of exotic features, is their intrinsically **delayed carrier cooling rates.** [47,48] High conversion efficiencies are often known to be hindered by a dominant loss channel of hot carrier cooling.[49,50] Thermodynamic calculations nevertheless predict that efficiencies close to 67% can be achieved in single junction solar cells if the high energy carriers can be strategically extracted.[51] This can be made feasible by deploying systems that have a gradual cooling of the carriers, giving enough time for the retrieval of these carriers before they cool down. In perovskites, the underlying reason for the delayed carrier cooling is

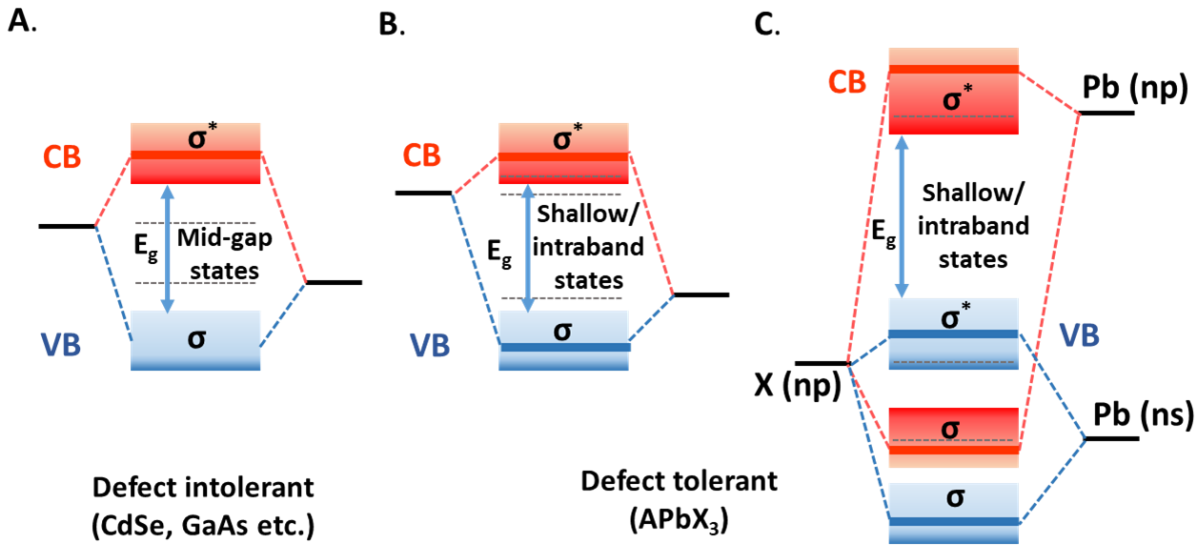

Figure 1.4 Schematic representation of the electronic band structures of two frequently encountered semiconductors: **(A)** the traditional defect-tolerant systems (II-VI, III-V). **(B)** a model defect-tolerant architecture; here σ stands for the bonding orbital and σ* for the anti-bonding orbital. **(C)** A concise illustration of bonding in a $APbX_3$ structure portraying the defect tolerance. "Reprinted (adapted) with permission from ref. {41}. Copyright {2015}, Materials Research Society."

the lack of the hole manifold which assists in maintaining the inherent phonon bottleneck (because of the requirement of larger number of phonons to bridge the energy gap) as opposed to quantum-confined conventional II- VI semiconductors **(Figure 1.5)**. These phonons are just another quasi-particles and are a quanta of lattice vibrations. Because hole and electron effective masses are identical in these systems, there is no major Auger type energy transfer activity in these systems, which might cause speedy energy dissipation.[52,53] of all these factors, research into metal halide perovskites is booming, driven by the materials' potential for usage in third-generation PVs and optoelectronics.[54] In addition to these applications, Lead halide perovskites have been effectively employed in a variety of different devices, including optically pumped lasers, transistors, water splitting cells, and photo-detectors etc.

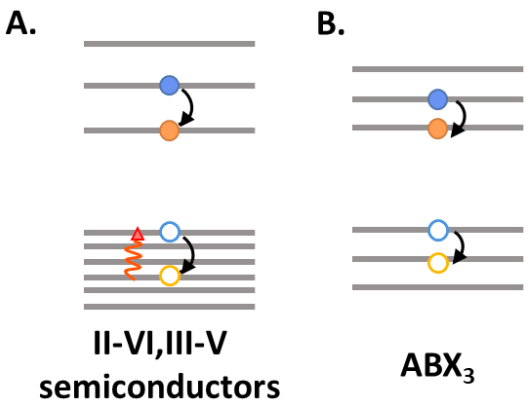

Figure 1.5 (**A)** Graphical portrayal of the existence of the hole manifold in ordinary semiconductors, which causes the hot holes in these systems—which have been heated up through energy transfer—to rapidly lose their energy through phonon emissions. (**B)** Perovskite structures on the other hand lack a hole manifold due to the symmetrical distribution of the electronic states in both VB and CB. Therefore, even if Auger type energy transfer re-excites the holes in the VB, due to the low density of electronic states there is an intrinsic phonon bottleneck that eventually slows down the carrier cooling process.

1.4 Metal Halide Perovskites

1.4.1 The Structural Considerations

The family of 3D MHPs can be described by the standard chemical formula used for the description of any perovskite structure- ABX_3, where A is any monovalent organic/inorganic cation, B is a divalent metal cation and X is a halogen anion. In any perfect cubic perovskite geometry, the arrangement of the ions is in such a manner that the bigger sized cation A forms a twelve-fold cuboctahedral coordination and cation B forms 6-fold octahedral coordination with anion X, resulting in a 3D framework of corner-sharing BX_6 octahedra **(Figure 1.6)**. Based on the nature of A-site cation, MHPs can be categorised into two groups of materials. The system is classified as an all-inorganic alkali MHP if the A-site is constituted by Cs or Rb cation and the B-site is occupied by a divalent metal ion (Pb^{2+}, Sn^{2+}). On the other hand, those MHP structures which have their A-site occupied by organic cations (methylammonium (MA) - CH_3NH_3, formamidinium (FA) - $CH(NH_2)_2$, or both) and the B-cation is a divalent metal ion, fall under the category of hybrid MHPs. There is however one more situation, when the A-site is occupied by organic cations (methylammonium (MA), formamidinium (FA), or their mixture) and the B-site is also inhabitated by an organic cation- NH_4^+. Such systems are classified as purely organic perovskites and do not belong to the MHP family.[55]

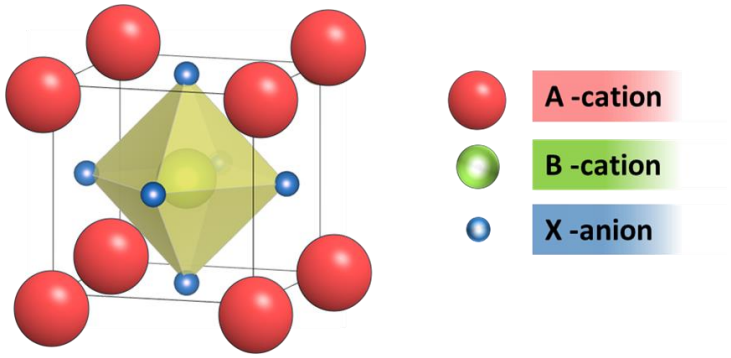

Figure 1.6 Characteristic structure of a standard cubic 3D perovskite; red spheres represent the A cation and light green sphere depicts the B cation which forms the octahedral network with the X – anions (blue spheres).

Although it may appear from the structural formula that there are indefinite possible structures, yet there are some geometric constraints owing to which an ABX_3 type halide perovskite cannot be formed by just any combination of A^+, B^{2+}, and X^-. For the existence of a stable MHP crystal structure, there are specific requirements that must be met. The structural integrity of any perovskite material is assessed by the evaluation of two basic empirical parameters: The Goldschmidt tolerance factor (t) and the octahedral factor (μ) which are defined as:[56,57]

$$t = \frac{R_A + R_X}{\sqrt{2}(R_B + R_X)} \qquad \textbf{Eq.1.2}$$

$$\mu = \frac{R_B}{R_X} \qquad \textbf{Eq.1.3}$$

These equations clearly implicate that ions of various sizes and affinities lead to perovskite structures with different tolerance levels. For the stable ideal cubic perovskites, this "t" is close to unity. In fact, all tolerance factor values in the range of 0.81 to 1.11 are regarded as empirically favourable for the existence of ideal 3D perovskite structures. But in instances when the tolerance factor falls beyond these limits, the structures adapt lower dimensional or non-perovskite frameworks with different types of BX_6 octahedra sharing. The other parameter "μ" which is often called as the octahedral factor **(Eq.1.3)** defines the stability of the octahedral and its value ranges from 0.442 to 0.895.[58,59] Several variants of the conventional MHP structure, and thus of ABX_3 stoichiometry, have been realised since their very introduction.

Tolerance factor together with the octahedral factor can be mapped to obtain 't-μ' plots which may be used to gain a qualitative understanding of the stability of a perovskite structure **(Figure 1.7)**. These maps assert that the only compounds that are stable in the ideal cubic 3D perovskite structure are those that are around the blue boundaryline. Infact this stability extends

further to even the other compounds illustrated by the red spots (decomposition energy ΔH_D >0) but in such situation 3D cubic phase is not the stable structure. Regarding the compounds designated as "black spots" (decomposition energy ΔH_D <0), because they are located in the instability area, they fail to crystallise in stable perovskite structures.

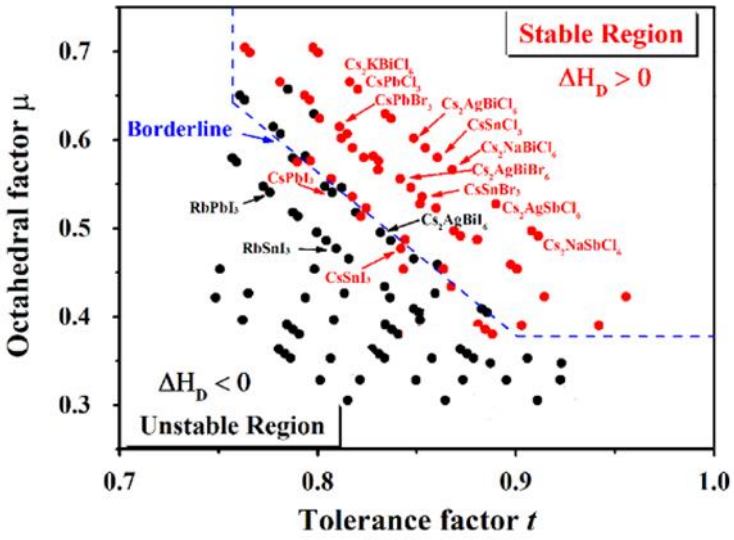

Figure 1.7 The tolerance factor-octahedral factor (t-μ) map for few halide perovskite compounds. "Reprinted (adapted) with permission from ref. {59}. Copyright {2017} American Chemical Society."

Natural perovskite minerals are limited in number, but synthetic perovskites can have elemental compositions from across the entire periodic table. Such diversity in perovskite structures makes this class an intriguing topic of study. As already stated amongst all the perovskite classes, MHPs are those perovskite structures which are the most compelling when it comes to harnessing the light energy. To be even more specific, the heavier halide MHPs (X- Cl, Br, I) are the candidates that attract attention for such application domains, including not only those with the ABX_3 framework but also their variants, both hybrid and inorganic.

Figure 1.8 depicts the different possible variants of MHPs. Majority of the all-inorganic MHPs do not crystallise in the pure cubic ABX_3 perovskite crystal structure (eg. $CsPbBr_3$, $CsPbCl_3$). They instead exhibit a distorted lattice that results in hettotype structures. All of this is due to the tilting of the individual octahedra caused by the size differences between the building ions A, B, and X which lead to these distortions.[60] The 3D perovskite structure is however still maintained despite these distortions, which result in structures with lower crystal symmetry, either orthorhombic or tetragonal. In both the standard cubic and distorted perovskite structures (ABX_3), owing to the fact that the A site cation is monovalent and B site cation is divalent, the charge on the X anion is straightforwardly balanced.

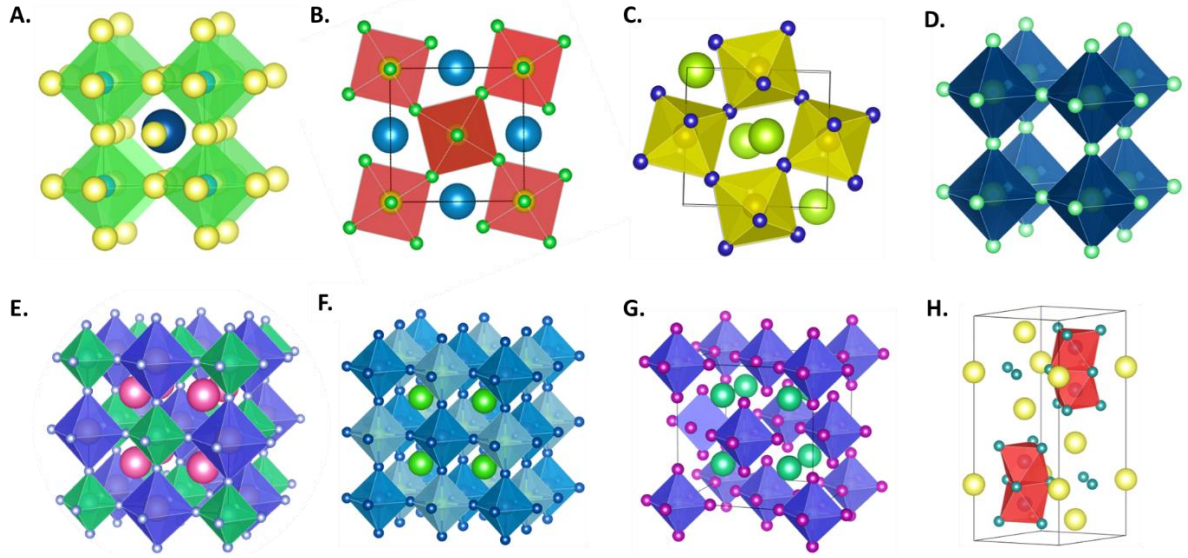

Figure 1.8 Various variants of metal halide perovskites: (**A)** Prototypical cubic structure of ABX_3 perovskites, **(B)** Tetragonal and **(C)** octahedral perovskite structures obtained as a consequence of octahedral tilting, (**D)** Vacant A-site BX_3 perovskites (**E),(F)** Ordered perovskites of the type- A_2BCX_6 and $A_2B(I)B(II)X_6$ respectively; Vacancy ordered perovskites of the type (**G)** $A_2B\square X_6$ and (**H)** $A_3B_2\square X_9$.

Nevertheless, this is not so simple in case of the variant stochiometries like double perovskites, vacancy ordered etc. These variants are fundamentally the derivatives of the standard perovskite structure and can be obtained from the ABX_3 stoichiometry by simply removing the A cation or by replacing the A and/or B cations completely or partially (ordering). In situations when the A and B site cations are substituted by a combination of cations (two or even more, the cations may or may not be derived from the same element) with different valence states but with an overall neutral charge balance, the resultant structures we obtain are referred to as double/quadruple perovskites (structural formula- A_2BCX_6, $A_2B(I)B(II)X_6$) - ordered crystal structures. Lead free perovskites like $Cs_2AgBiBr_6$ fall under this category. Other times, structures deviating significantly from the ABX_3 stoichiometry are obtained when the A and B sites are either entirely or partially vacant. Situations in which A-site is completely unoccupied (A vacant BX_3 perovskites) occur only in fluorides ($\square BF_3$) and not in heavier halides. Similarly, A_3BX_6 cryolite structures (Na_3AlF_6) are another form of fluoride ordered perovskites where the cations that occupy the A sites occupy half of the B sites but such structures have so far never been associated with heavy halide MHPs. The other category, which also denotes the last subgroup of MHPs and is similar to ordered perovskites, is the one

in which the B-site cation positions are partially occupied by vacancies; this is also the basis for the name "vacancy ordered perovskites" for these structures. The $A_2B\square X_6$ group of vacancy-ordered perovskites where tetravalent cations (B(IV)) occupy half of the B-site positions, with the remaining positions being filled by the vacancies ❐ is among the most studied due to its potential characteristics.[60] Cs_2SnI_6, Cs_2TeI_6 etc. are some of the examples of these structures. However, if trivalent metal ions (B(III)) such as Sb^{3+} or Bi^{3+} occupy some of the B-site positions in place of B(IV) cations, then a reasonable ratio of 2:1 between the metal ions and vacancies for the occupancy of the B-sites must be maintained in order to attain the charge neutral balance. The resultant structures crystallise in the stoichiometry $A_3B_2\square X_9$ and the heavy metal compounds $Cs_3Sb_2I_9$ and $Cs_3Bi_2I_9$ for example are such systems. But unlike the previously described $A_2B\square X_6$ structures, these systems crystallise in two dimensional layers.

1.4.2 The all inorganic alkali metal halide perovskites

The nature of the A-site cation plays a pivotal role in determining the stability of a perovskite structure. Despite the fact that hybrid perovskite/Silicon tandem solar cells have shown record-breaking PCE of 31.25% (as per the National Renewable Energy Laboratory (NREL) records accessed on 26.9.22), the stability of such perovskite systems is a major barrier that obstructs their commercialization.[7] This limitation is a straightforward consequence of the fact that the performance of the perovskite-based devices with an organic cation at the A-site typically deteriorates over time due to structural inconsistency. Thus, it is this shortcoming that prevents hybrid or organic-inorganic perovskites from being deployed for other applications as well. On the other hand, all-inorganic MHPs exhibit durability and relatively consistent performance over extended periods of time, withstanding even the fluctuations in the ambient conditions.[61,62] Unfortunately, the PCE of the devices employing the all-inorganic perovskites is still lower than that of their organic-inorganic counterparts and considerably below the Shockley-Queisser limit derived for their bandgap. Therefore in order to fairly compete with the organic and hybrid perovskites, the all-inorganic members of the MHP family demand more extensive research.

1.4.2.1 Lead (Pb) based perovskites - $APbX_3$

As of now when it comes to all-inorganic 3D alkali MHPs, $CsPbX_3$ systems are the most popular and the most robust members of the class. This is owing to the smaller size of the Rubidium atom than Cesium atom as an effect of which the tolerance factor is overall lowered. This makes the perovskites housing Cesium cation at the A-site to be substantially more stable

than those with Rubidium cation.[63] $RbPbX_3$ structures infact fail to crystallise in a stable ABX_3 cubic perovskite lattice at room temperature. This is quite evident from the "t-μ" plots provided in **Figure 1.7**.[64–66] The family of Cs based MHPs encompasses three stable heavy halide systems namely $CsPbBr_3$, $CsPbCl_3$ and $CsPbI_3$. Amongst this trio, the lightest analogue, $CsPbCl_3$, is although stable **(Figure 1.7)** but not particularly useful for PV applications due to its large E_g (Ultraviolet (UV) range), which prevents it from capturing a large portion of the solar energy radiation (only 4% of the solar spectrum is contained in the UV domain ($\lambda < 400$ nm)). Also, because the production of defect states in $CsPbCl_3$ requires very little energy, this material has a high defect state density. These defects caused by the Chloride vacancies are positioned midway through the band gap because of which they function as charge carrier trapping sites **(Figure 1.9)**. On the other hand, the heaviest anion counterpart in its cubic phase *i.e.* α- $CsPbI_3$ (E_g of other phases is incompatible) is unquestionably the most compelling due to its optimal band gap (1.73 eV), which allows it to capture almost all range of photons from incident solar radiation (spanning from UV to Infrared (IR)). Furthermore despite the fact that it also houses high density of defects, the electronic band structure is quite defect tolerant or closest to defect immune, as suggested by the positioning of the defect states relative to the conduction band minima **(Figure 1.9)**. However, due to its vulnerability to moisture and oxygen, it degrades over time and complicates the investigative process. This behaviour is caused by the tolerance factor of α - $CsPbI_3$, which is 0.81, that is extremely near to the lowest limit defined for the persistence of stable perovskite structure. The perovskite system with Bromide ion at X- site *i.e.* $CsPbBr_3$ (tolerance factor ~ 0.824) however is both relatively robust in terms of air and moisture- stability and offers good absorption over the wavelengths contained in the solar radiation. In addition to this, the Bromide vacancies form shallow type defects (< 5 k_BT below the CBM). As a consequence, its electronic band structure is altered only mildly **(Figure 1.9)**. It has also demonstrated promising performance in PV devices with PCE close to 11%.[67] However, these figures are still relatively low in comparison to their hybrid counterparts.

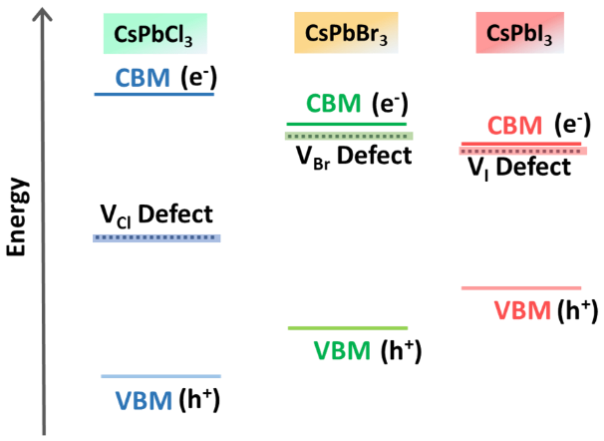

Figure 1.9 The positioning of the defect states stemming from halide vacancies in the $CsPbX_3$ systems.

1.4.2.2 Lead free perovskites - ABX_3, where B is any suitable divalent cation other than Pb^{2+}

Lead cation at the B-site is the most preferred choice for perovskite structure. Despite this, the growing toxicity concerns associated with lead leakage raise questions about the viability and commercial acceptance of lead-based products. To address this potential hazard of lead poisoning posed by lead-based MHPs, environment friendly alternatives are being explored. This search can be streamlined by taking note of some chemical design guidelines. The three key factors to consider altogether while looking for alternative elements are coordination, ionic radius and charge neutrality.[68] In light of this, the less toxic alternatives to Pb^{2+} can be provided by either the isovalent ions like Sn^{2+}, and Ge^{2+} or even the heterovalent elements like Sb^{3+} and Bi^{3+} etc. When lead is replaced with an isovalent cation, the genuine perovskite structure is preserved. This is because the charge is immediately balanced since the cation belongs to the same group as lead in the periodic table. But this is not the case with heterovalent substitutes. As a result, structural designs like B-cation split ($A_2B(I)B(III)X_3$), anion mixed ($AB(Ch, X)_3$; Ch is a chalcogenide anion and X is a halogen anion), and ordered vacancy frameworks ($A_3B_2\square X_9$, $A_2B\square X_6$) are obtained in the pursuit of charge neutrality in heterovalent replacements.

A. Isovalent replacement:

Among all the possible isovalent replacements, the group-14 element Sn(II) is the most apparent substitution for Pb. This is chiefly because of the close proximity of its ionic radius (Pb: 149pm, Sn: 135 pm) and alike ns^2 electronic configuration as Pb^{2+} which makes it possible to have perovskite structures with formula $CsSnX_3$ similar to their lead-based counterparts. In

particular, the bromide and iodide members of this family have an ideal band gap that enables optimum light absorption from direct solar energy. Utilizing $CsSnI_3$ as the absorber layer (E_g ~ 1.4 eV), a significant value of PCE ~ 8.05% has been achieved, and theoretically, optimised $CsSnI_3$-based PV devices are expected to have an efficiency close to 23%.[69,70] Despite the anticipation regarding stability drawable from the t- μ maps, it suffers from stability issues upon exposure to moisture and air because of the facile oxidation of Sn (II) to higher oxidation state Sn(IV).This over the time gradual degradation renders it ineffective for long term applications. Another possible substitute- Germanium is also a considerate option. $CsGeX_3$ structures, like their tin-based counterparts, have narrower band gaps than Pb systems, making them suitable for solar applications.[71,72] Nevertheless, owing to the fact that the ionic size of Ge (Ge^{2+}) is lower than both $Sn^{2+}$and Pb^{2+}, the stability issues associated with $CsGeX_3$ are even more pronounced than that related with the $CsSnX_3$ structures, resulting in accelerated oxidation of Ge^{2+} to Ge^{4+}. Furthermore, there are no commendable PCE numbers for PV devices reported till date (0.11%-2005 by Krishnamoorthy *et al.*) employing $CsGeX_3$ absorber layer which can be attributable to its rapid degradation.[73] In the event of isovalent replacement, there is another possibility besides the $CsBX_3$ structure. Divalent cations can also lead to the creation of the 2D morphology Cs_2BX_6 framework.

B. Heterovalent replacement:

As previously stated, heterovalent substitutions disrupt the real perovskite structure in order to compensate for charge neutrality. Even then not all the resultant structures necessarily comply with the primary prerequisites for a good PV material namely: stability and ideal band gap for maximal solar light absorption. The benefits and cons of all the lead free structures formed via isovalent and heterovalent substitution are schematically depicted and briefed in the **Figure 1.10** The classification above shows that none of the lead free structures produced via isovalent substitution are absolutely appropriate for the targeted optoelectronic and PV applications. Even among the alternatives obtained subsequent to heterovalent replacement, the vacancy ordered $A_2\square B(IV)X_6$ structures ($\square$-vacancy) are the only ones that meet the requirements for these applications. One such unique and promising member of this family of perovskites which realises all the desirable prerequisites is $Cs_2Sn\square I_6$ also simply referred to as "Cs_2SnI_6". The chloride and bromide analogues, however, are not apt due to their wider band gap. The Cs_2SnI_6 structure is essentially a defect derivative of $CsSnI_3$ obtained upon removal of half of the Sn atoms. At contrast to $CsSnI_3$, this structure has Sn in its maximum oxidation state, Sn^{4+}, hence there is no possibility of its oxidation and therefore is relatively stable. Its band gap is also

perfect for absorbing solar radiation (bulk band gap-1.3 eV to 1.6 eV depending upon its preparation), even more ideal than its well-known lead-based equivalent, $CsPbI_3$.[74,75] Utilizing Cs_2SnI_6 in PV devices, an exemplary PCE of more than 10% has already been attained.[76] Apart from being used as absorber layer, it has also been used as a hole transporting layer in dye sensitized solar cells. Meanwhile, similar structures but with cations like Ti^{4+}, Te^{4+} etc. in place of Sn^{4+} are also being explored in an effort to achieve obtaining high device efficiencies and consistent performance over extended time period.

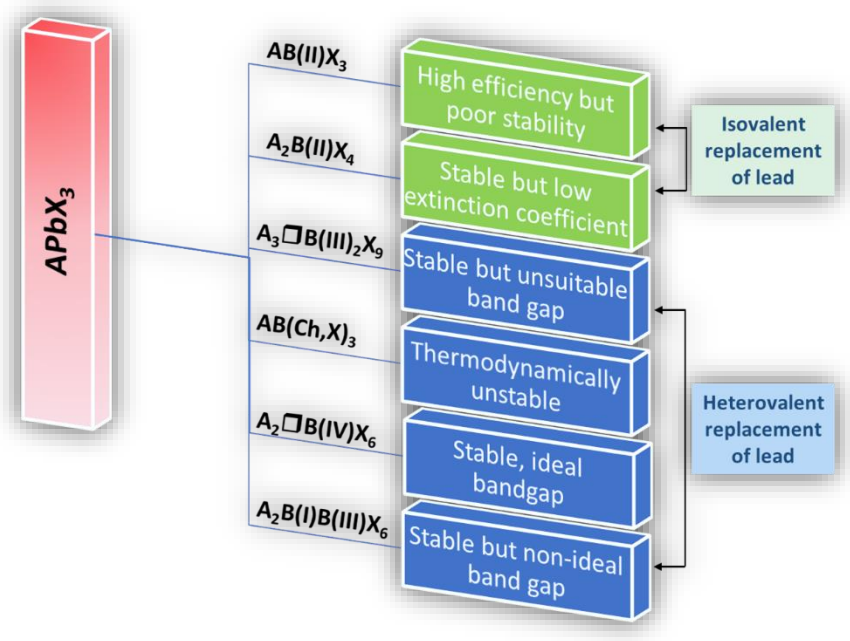

Figure 1.10 The upsides and downsides of the various structural designs of lead free perovskites obtained as a result of isovalent and heterovalent replacement.

1.5 Photophysical processes that take place in Metal Halide Perovskites (MHPs) subsequent to photoexcitation

Whenever a semiconductor system is incident with photons having an energy surplus than the E_g, the carriers, both electrons and holes are generated in the high energy electronic states. The temperature of such carriers is greater than the lattice temperature and therefore they are referred to as "hot carriers (HCs)" or "hot excitons". These hot species then eventually reach the band edge states but before that they undergo series of photophysical events that take place over a time span of a few femtoseconds or picoseconds.[77] Subsequent to photoexcitation (Process I), the prior thermal equilibrium of the system is perturbed (Process 0) and the injected charge carriers are all at different temperatures so they first thermalize among themselves through carrier-carrier scatterings (Process II). This process, known as carrier thermalization,

proceeds extremely quickly and often completes in a few femtoseconds. The HCs while thermalizing follow the Fermi-Dirac statistics. In the next step (Process III), the thermalized HCs then start equilibrating with the lattice after carrier thermalization, mostly through inelastic carrier-phonon interactions. This phase termed as "HC cooling" can actually be multi-stepped).[57] Conventionally it only involves the interaction of the HCs with the LO phonons which finishes off in a time span of 1 ps, but in polar materials with high dielectric constant just like perovskites, polaron formation can also step in (Process III). The polaron formation basically involves the interaction of the charge carriers with the lattice deformation that sets in as the carriers propagate through the lattice.[78] A polaron can be construed of as a quasiparticle made up of a charge carrier and the surrounding lattice, or in terms of phonon analogies, as a carrier dressed by phonon cloud. Until the surplus energies carried by the charge carriers are smaller than the LO phonon energy, carrier-LO phonon interactions persist. Then in the next step, the LO phonon undergo decay into low energy acoustic phonons or Transverse Optical (TO) Phonons (Process IV) which further decay over a time of few hundreds of picoseconds (Process V). The cold carriers after reaching the band edges then recombine with their counter carriers and this process usually lasts over long few nanoseconds time (Process VI).The sequence of the events that take place subsequent to photoexcitation are depicted in **Figure 1.11.**

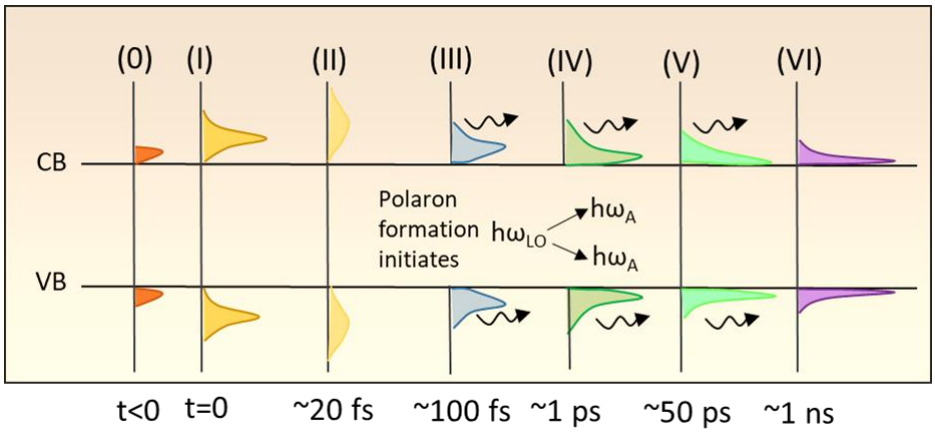

Figure 1.11 Various processes that take place subsequent to photoexcitation as described in the text described schematically by the distribution of the carriers in the VB and CB.

MHPs as already stated before, exhibit unusually slow carrier cooling capabilities which can prove essentially advantageous from the perspective of HC based solar cells. It all started in the year 2013 when initial findings of delayed HC cooling (~0.4 ps) in Methyl Ammonium Lead Iodide ($MAPbI_3$) polycrystalline thin films were published and since then there has been increasing interest in understanding and manipulating this unusual phenomena.[48] Such

investigations have been conducted employing transient absorption spectroscopy and other time resolved spectroscopic techniques which provide a profound opportunity of tracking really quick processes taking place in such short time scales. It should be emphasised, nonetheless, that the measured carrier cooling rate is highly correlated with the injected charge carrier density. This is particularly true given that many processes evolve in various ways based on the incident fluence, eventually having a variety of effects on the carrier relaxation process. Thus, when photoexcited with diverse carrier densities, the same MHP system can display various relaxation speeds.

1.6 Intervalley scattering

Besides opting for the conventional relaxation pathway of intravalley scattering, the charge carriers initially injected at band extrema adjacent to or at zone boundaries can also scatter from one valley to another in the multivalley band structure, whether degenerate in energy or not as depicted in **Figure 1.12**. This process of intervalley scattering just like the intravalley relaxation process is driven by the carrier-phonon interactions. The zone edge phonons, as opposed to the zone centred phonons which are incredibly effective in driving the intravalley transitions, are typically seen to be the ones responsible for the intervalley scattering process. Indeed, the process may frequently involve multiple zone-edge phonons, with the final involvement determined by the selection criteria established by group theory. This is due to the short-range nature of the intervalley carrier-phonon interactions, which is plainly satisfied by the zone edge phonons that are incapable of producing long-range electric fields.[79,80]

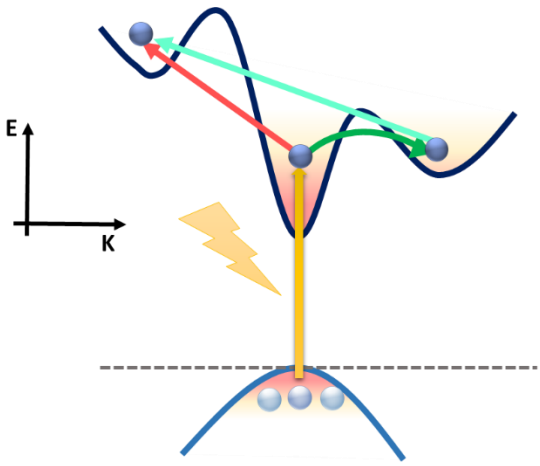

Figure 1.12 Illustration of both degenerate and non-degenerate intervalley scattering processes in any arbitrary multivalley band structure.

1.7 Factors affecting the carrier cooling rates in Metal Halide Perovskites

1.7.1 Hot Phonon Bottleneck effect (HPB effect)

When the injected charge carrier densities are sufficiently high, HPB effect is one of the two most established factors that are generally held liable for the retarded carrier cooling observed in MHPs. [81–83] The fundamental ground for such effect stems from the existence of a huge population of non-equilibrated LO phonons at such high fluences. This surplus LO phonon population retards the further emission of the LO phonons and leads to even reheating of the charge carriers inturn setting in a substantial delay in the carrier cooling process **(Figure 1.13)**.[84] The HPB effect is not just parameterized by the phonon lifetime (τ_{ph}) alone but is rather a manifestation of the complex competition between two contrary processes: decay rate of the LO phonons ($k_{ph} = 1/\tau_{ph}$) and carrier- LO phonon scattering rate ($k_{(e-/h+)-ph}$). The ultimate rate of HC cooling is thus guided by that process which proceeds as a faster rate [85]. Both of these parameters are although a strong function of the employed carrier density yet at moderate carrier densities- (n) < 10^{18} cm^{-3}, there is no significant contribution noticed from the HPB effect and also the HC cooling rate is observed to be independent of the injected flux. [86] Therefore it is only when the carrier densities are higher than 10^{18} cm^{-3}, HPB effect becomes effective. The HPB effect seen in MHPs is caused by a number of different reasons in addition to the increased LO phonon population. One of these reasons is that the Klemens channel mediated LO phonon decay (decay into two oppositely propagating Longitudinal Acoustic (LA) phonons) is generally not much efficient in MHPs owing to which the LO phonons usually opt for other less efficient decay routes like Ridley channel (decay of an LO phonon into a transverse optical (TO) phonon and an acoustic phonon mode, may be a Transverse Acoustic (TA) or LA mode).[87] On top of that, the density of states in the electronic structure of MHPs is also quite low which also is one of the aspects that results in bottleneck effect.[88] Therefore, the existence of low state density, a large population of non-equilibrated LO phonons, and the suppression of the effective Klemens channel work together to produce a strong PHB effect noticeable in MHPs particularly at high incident carrier densities.

1.7.2 Auger heating

Apart from the HPB effect, the multi-particle Auger heating phenomenon is equally significant in retarding the HC cooling rate when the incident charge carrier densities are sufficiently high

(>10^{18} cm^{-3}). This process basically involves the interband recombination of an electron-hole pair and the transfer of the subsequent energy to some other carrier which as a result of this

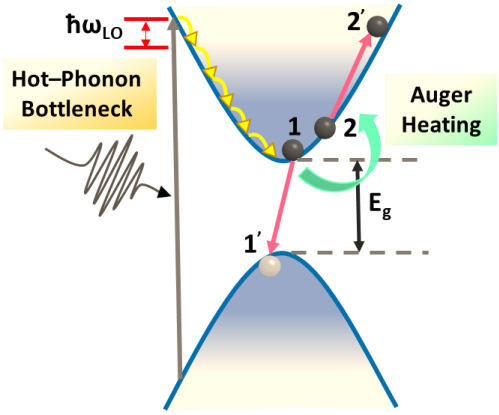

Figure 1.13 Schematic illustrating the process of hot phonon bottleneck effect and Auger heating; the energy released during the recombination of the electron hole pair (1-1') is transferred to the electron 2 in the conduction band and hence it is excited to higher excited state (denoted as 2').

transfer is excited to a further high energy electronic state **(Figure 1.13)**. However, there is another form of Auger process that is not covered here in this section: intraband Auger heating. The involvement of the Auger heating process in the overall observed HC cooling dynamics can be mathematically stated as:[84]

$$< \frac{dE}{dt} >_{(total)} = < \frac{dE}{dt} >_{(carrier-phonon)} + \; k_3 \, n^2 (E_g + E) \qquad \textbf{Eq.1.4}$$

$$\frac{dn}{dt} = \; -k_1 n - k_2 n^2 - k_3 n^3 \qquad \textbf{Eq.1.5}$$

Here in this kinetic equation **(Eq. 1.4)**, the term on the left hand side denotes the total energy loss rate and the first term on the right hand side refers to the contribution coming from the carrier-phonon coupling while the second term "k_3n^2 (E_g +E)" is related to Auger heating process (k_3 - three body Auger recombination coefficient).The term 'n' signifies the carrier concentration which itself varies as a function of time as depicted in **Eq.1.5** depending on the rates of the defect mediated monomolecular recombination (k_1) and free carrier based bimolecular recombination (k_2) events taking place in any given system. Furthermore, the **Eq.1.5** is clearly suggestive that this three body Auger process only bears significant contribution when 'n' is exceedingly high since at low values of 'n', the monomolecular (k_1) and bimolecular processes (k_2) take over. As per the Fermi Golden rule ($k_3 \propto \sqrt[2]{E_g} \exp(-\frac{m_e}{m_e+m_h} . \frac{E_g}{k_B T})$), the extent of the energy transferred during the Auger heating

process varies with the quantity "$E_g + E$" (here E_g stands for the energy band gap of the system) and this simply implies that the process of Auger heating is strongly reliant on the energy band gap of the system.[89] This is also the reason why particularly the iodide perovskites owing to their comparatively smaller E_g than their lighter halide analogues exhibit very strong Auger heating when the injected charge carrier densities are unusually high. Further contrasting the bulk systems with the nanostructures, it is usually observed that Auger heating is a more favourable process in the later cases because of the conservation of momentum and existence of better overlap between the electron and hole wavefunctions.[90]

The process of Auger heating undoubtedly seems beneficial as it brings in retardation in the carrier relaxation process however this deceleration in the carrier relaxation process is brought down at the cost of prevalent population of the injected charge carriers which is also simultaneously declined.[85] This information should thus be taken into account while creating any future devices.

In general, it is anticipated that the screening of the Coulomb potential provided by the large population of free carriers present at high fluences will slow the HC cooling process for any semiconductor system. The free carrier Coulomb screening effect in MHPs is much less than in ordinary semiconductors, and most critically, its contribution to delaying the carrier relaxation process has been determined to be negligible mechanism that might impact cooling rate is acoustic-phonon upconversion.[82,91,92] However, it has been found to be a very ineffective mechanism for Cs-based MHPs; hence, its involvement in the carrier relaxing process may also be categorically disregarded.

1.7.3 Polaron formation

Although the delayed HC cooling seen in MHPs at high fluences may be satisfactorily explained either through the process of auger heating or the HPB effect yet both these mechanisms become inapt at lower injected densities. One of the long-established explanations for the sluggish carrier cooling observed while working with low carrier densities is "polaron formation". Simply put, a polaron is a quasiparticle made up of a charge carrier and the phonon cloud dressing it **(Figure 1.14)**. The formation of this shallow bound state is apparently an outcome of the Coulombic interaction occurring between the charge carriers and the polarizable lattice. This explains why in contrast to the covalent semiconductors, the soft, ionic and polarizable systems just like MHPs which are an abode of large static dielectric constant and strong carrier-phonon coupling are more prone to polaron formation. [93–95] Besides this, it is well asserted that the scattering of the carriers with the optical phonons limits mobility in

HOIPs more significantly than their scattering with acoustic phonons.[96,97] The polaron theory initially formulated by Fröhlich, which was later expanded by Feynman, has traditionally been used to address this scattering of charge carriers with optical phonons. According to this theory, the extent of the carrier-LO phonon coupling is frequently characterised by the Fröhlich parameter $\alpha_{(e\text{-}ph)}$, which may be mathematically defined as follows: [94,98]

$$\alpha_{e-ph} = \frac{1}{2}\left(\frac{1}{\varepsilon_\infty} - \frac{1}{\varepsilon_0}\right)\frac{k_e e^2}{\hbar\omega_{LO}}\sqrt{\frac{2m^*\omega_{LO}}{\hbar}} \qquad \textbf{Eq.1.6}$$

where, ε_∞ and ε_0 are the high frequency and static dielectric constants respectively; ħ is Planck's constant, $\hbar\omega_{LO}$ is the LO phonon mode energy and m* stands for the effective mass of electron or hole.

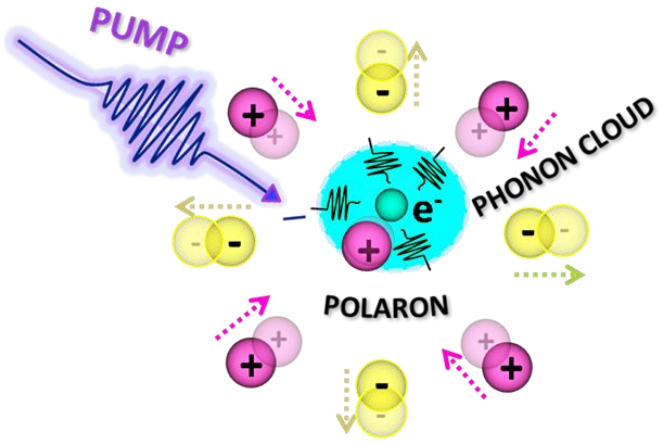

Figure 1.14 Pictorial illustration of the process of polaron formation in any polar semiconductor system. The dark pink spheres depict the initial positions of the positive lattice ions before photoexcitation, while light purple spheres show the displaced positive ions following the irradiation process; similar denotation for the negative ions has been made by using yellow spheres. After being hit by the pump pulse, the negative ions lying along the trajectory of the propagating electrons are pushed away and those which are positively charged are drawn in. As a result, the lattice begins to deform dynamically all along the motion of the charge carrier. By acting on the otherwise free electron (forming a polaron), the resulting self-induced polarisation cloud modifies the carrier's ordinary physical characteristics. Only the electron polaron has been used here to illustrate the scenario for the purpose of simplicity, however there are also hole polarons.[99] "Reprinted (adapted) with permission from ref.{99}. Copyright {2020} American Chemical Society."

Polaron formation is mostly considered relevant only at low fluences which is because at high injected carrier densities, the polaronic states rather tend to become unstable owing to the mutual repulsions existing between them. There are two ways to interpret the significant decrease in carrier relaxation rate that is seen as a result of polaron formation: i) the conception of polarons causes a substantial reduction in the effective Coulombic screening, which delays the scattering of dressed charge carriers with other species such as charge carriers, defects, etc., extending the carrier lifespan and diffusion length.[100–103] ii) Also, because of the dressing of the otherwise free carriers with phonon cloud, the effective carrier mobility is also reduced by a certain factor which also accounts for decelerated carrier relaxation.

The formation of the polaron is quite favoured over the bare charge carriers since it results in lowering of the system's total energy. Additionally, depending on how widely these polaronic states are dispersed among the unit cells and on the basis of the strength of carrier-phonon coupling, polarons may be categorised as large or small. Both these categories exhibit a divergent tendency with respect to the lattice temperature; while the small polarons exhibit higher mobility at high temperatures ($d\mu/dT > 0$), the large polarons exhibit the opposite behaviour ($d\mu/dT < 0$).[104] The polarons observed in lead based perovskites have been identified as intermediate to large ($\alpha \sim 1.1$ and 2.7).This is owing to the $d\mu/dT < 0$ trend noticed in the investigated range of temperatures in both their transport and spectroscopic investigations.[105] When comparing tin-based $ASnX_3$ systems to lead-based structures, the former are known to be less polaronic.[93] The hole and electron polarons are identical in kind and size because the bare-band effective masses in halide perovskites are more or less equal.

1.8 Phonon dynamics- the interplay of lattice vibrations

As hinted by the preceding section, the relaxation pathways followed by the charge carriers are indirectly guided by the phonon/lattice dynamics. All of this may be traced to the dynamic responsiveness of the lattice that directly influences the lattice polarizability and the dielectric environment (ε) surrounding the charge carriers. These polarizabilities not only steer the screening of Columbic interactions witnessed by the carriers among themselves which account for the excitonic strength (Exciton binding energy $E_B \propto 1/\varepsilon^2$) but also with the lattice (carrier-phonon coupling) that is decisive towards the carrier mobility.[106–110] In light of this, the lattice vibrational dynamics and its effect on the optical response is an engaging subject for any material and such knowledge is always useful for formulation of efficient and advanced devices. Furthermore if we contrast the different MHP systems, owing to their lighter masses tin-based perovskites sustain higher optical phonon frequencies than the lead-based perovskites

($\nu_{Sn\text{-}I} > \nu_{Pb\text{-}I}$).[111] Thus, it is anticipated that the contribution of lattice polarization in exciton screening should be noticeably larger in tin-based systems and the same is also encountered in the findings.[100,112] The literatures reported till date therefore clearly suggest that the ionic metal halide cage significantly contributes to the exciton screening in MHPs, but the polarisability of the A-site cation has not yet been found to make a sizable impact to carrier mobility.[113–115] For revealing the time-dependent response of the MHP systems subsequent to photoexcitation in the current thesis study, we have mostly exploited transient absorption (TA) spectroscopy. In addition to providing information on charge carrier dynamics, this method also enables the realisation of the coupling processes operating in the probed systems using a variety of methods, such as calculations using a two-temperature model and polarization-dependent investigations, among others. [115–117]

1.9 Coherent phonon generation

Every time an incident radiation strikes a system, lattice vibrations set in, but the emitting phonons are all arbitrarily orientated in phase with respect to one another, making the emission incoherent. But then there are certain instances when the pulsewidth of the deployed femtosecond laser is lesser or even comparable to the duration of a lattice vibration which makes it feasible to excite many modes of that particular lattice vibration with a high level of spatial and temporal coherence, resulting in the generation of what are known as coherent phonon modes **(Figure 1.15)**. In pump-probe techniques like TA spectroscopy, detection is very sensitive to any change in the refractive index of the probe pulse. We are able to see these collective and in-phase atomic displacements in real time thanks to the periodic variation in the refractive index of the probe pulse induced by such patterned emission. These coherent phonons are usually manifested as oscillations superimposed over the otherwise gathered transient responses in the differential spectroscopy measurements. The transformation of the oscillatory time-domain data into frequency domain builds a complete manifold of the phonon modes supported by the lattice and even gives a clear idea of the phonon-phonon and carrier-phonon couplings prevalent in the system through the pump energy dependent studies.[118] There are generally two theories that are adopted for explaining the mechanism of coherent phonon generation: Impulsive Stimulated Raman Scattering (ISRS) and Displacive Excitation of Coherent Phonons (DECP). It may though seem that all such information can be drawn from typical Raman spectroscopy but such techniques limit the information only to ground state phenomenon, while TA spectroscopy allows to venture the wavepacket dynamics in the excited state as well.[118] Besides this, the estimations of the carrier-phonon coupling obtained from

continuous wave methods are typically exaggerated.[119] The most notable benefit that gives time resolved approaches an edge over frequency domain techniques is the capacity to identify the low frequency and the silent phonon modes(inactive in both Raman and IR studies) which can't be resolved by standard frequency domain methods because of the symmetry constraints.

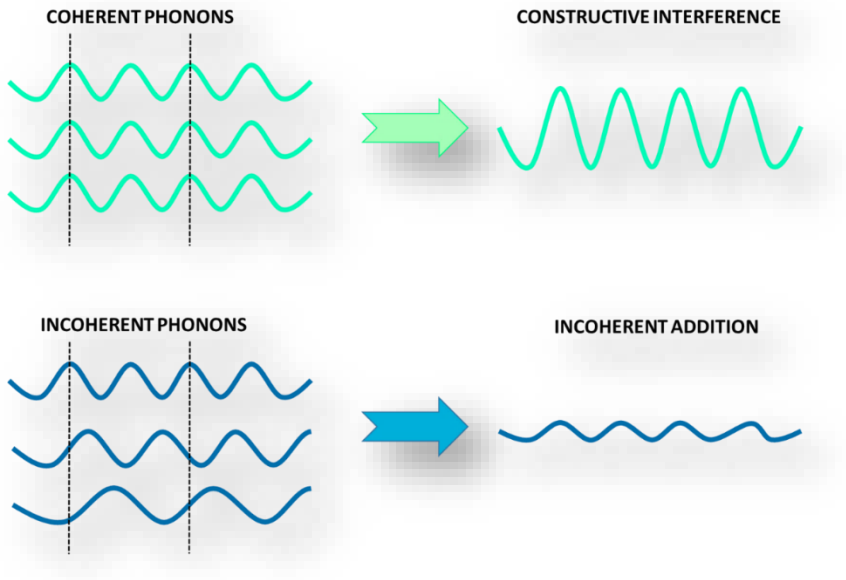

Figure 1.15 Resultant modes obtained as a consequence of addition of coherent and incoherent phonons.

1.10 Silent modes and Hyper-Raman Scattering (HRS)

Besides the phonon modes which are active either in Raman or IR spectroscopies, there exist some other phonon modes as well which remain inactive in both Raman and IR studies and thus are undetected in both these frequency domain techniques. Such modes are usually termed as the "silent modes". The necessary prerequisite for the observation of these modes is the existence of Hyper Raman Scattering (HRS). Unlike the change in polarisability and dipole moment during a lattice vibration which are responsible for the appearance of the phonon modes in Raman and IR studies respectively, it is the hyperpolarisability component that dictates the occurance of HRS. The dipole moment induced in any system by the incident electric Field E may be represented as follows:[120]

$$\mu = 4\pi\varepsilon_0 \left(\alpha \mathrm{E} + \frac{1}{2}(\beta E^2) + \frac{1}{6}(\gamma E^3) + \cdots\right) \qquad \textbf{Eq.1.7}$$

Here, α defines the input from Raman and Rayleigh scattering, whereas β and γ are the hyperpolarizabilty tensors that determine the contribution stemming from Hyper-Raman scattering. For typically used electric field strengths, only the first polarisability term *i.e.* α is often important, while terms β and γ have insignificant weights. In these scenarios, μ is a linear

function of E. However, these non-linear components take on a substantial role when the incident field intensity is increased.[121] Typically, continuous wave laser sources with output powers of a few tens or hundreds of mW are used in traditional Raman investigations. The transient absorption investigations, however, use femtosecond pulses, which have incredibly small pulse widths, indicating that the pulse energy is quite high. Because of this, the electric field magnitudes associated with these femtosecond lasers are far greater than those experienced with ordinary Raman lasers, enabling Hyper Raman scattering to occur in the system.

1.11 References

(1) Chakhmouradian, A. R.; Woodward, P. M. Celebrating 175 Years of Perovskite Research: A Tribute to Roger H. Mitchell. *Phys Chem Miner* **2014**, *41* (6), 387–391.

(2) Wells, H. L. Über Die Cäsium-Und Kalium-Bleihalogenide. *Zeitschrift für Anorg Chemie* **1893**, *3* (1), 195–210.

(3) MØLLER, C. H. R. K. N. A Phase Transition in Cæsium Plumbochloride. *Nature* **1957**, *180* (4593), 981–982.

(4) Weber, D. $CH_3NH_3PbX_3$, Ein Pb(II)-System Mit Kubischer Perowskitstruktur / $CH_3NH_3PbX_3$, a Pb(II)-System with Cubic Perovskite Structure. *Zeitschrift für Naturforsch B* **1978**, *33*, 1443–1445.

(5) Porta, P.; De Rossi, S.; Faticanti, M.; Minelli, G.; Pettiti, I.; Lisi, L.; Turco, M. Perovskite-Type Oxides: I. Structural, Magnetic, and Morphological Properties of $LaMn_{1-x}Cu_xO_3$ and $LaCo_{1-x}Cu_xO_3$ Solid Solutions with Large Surface Area. *J Solid State Chem* **1999**, *146* (2), 291–304.

(6) Kojima, A.; Teshima, K.; Shirai, Y.; Miyasaka, T. Organometal Halide Perovskites as Visible-Light Sensitizers for Photovoltaic Cells. *J Am Chem Soc* **2009**, *131* (17), 6050–6051.

(7) Liu, H.; Xiang, L.; Gao, P.; Wang, D.; Yang, J.; Chen, X.; Li, S.; Shi, Y.; Gao, F.; Zhang, Y. Improvement Strategies for Stability and Efficiency of Perovskite Solar Cells. *Nanomaterials*. 2022.

(8) Jena, A. K.; Kulkarni, A.; Miyasaka, T. Halide Perovskite Photovoltaics: Background, Status, and Future Prospects. *Chem Rev* **2019**, *119* (5), 3036–3103.

(9) Li, N.; Niu, X.; Li, L.; Wang, H.; Huang, Z.; Zhang, Y.; Chen, Y.; Zhang, X.; Zhu, C.; Zai, H.; et al. Liquid Medium Annealing for Fabricating Durable Perovskite Solar Cells with Improved Reproducibility. *Science* **2021**, *373* (6554), 561–567.

(10) Burschka, J.; Pellet, N.; Moon, S.J.; Humphry-Baker, R.; Gao, P.; Nazeeruddin, M. K.; Grätzel, M. Sequential Deposition as a Route to High-Performance Perovskite-Sensitized Solar Cells. *Nature* **2013**, *499* (7458), 316–319.

(11) Cho, H.; Jeong, S.H.; Park, M.H.; Kim, Y.H.; Wolf, C.; Lee, C.L.; Heo, J. H.; Sadhanala, A.; Myoung, N.; Yoo, S.; et al. Overcoming the Electroluminescence Efficiency Limitations of Perovskite Light-Emitting Diodes. *Science* **2015**, *350* (6265), 1222–1225.

(12) Zhou, H.; Chen, Q.; Li, G.; Luo, S.; Song, T.; Duan, H.-S.; Hong, Z.; You, J.; Liu, Y.; Yang, Y. Interface Engineering of Highly Efficient Perovskite Solar Cells. *Science* **2014**, *345* (6196), 542–546.

(13) Ashcroft, N. W.; Mermin, N. D. *Solid State Physics*; Saunders College Publishing: Fort Worth, 1976.

(14) Norris, D. J.; Bawendi, M. G. Measurement and Assignment of the Size-Dependent Optical Spectrum in CdSe Quantum Dots. *Phys Rev B* **1996**, *53* (24), 16338–16346.

(15) Brus, L. E. Electron–Electron and Electron-hole Interactions in Small Semiconductor Crystallites: The Size Dependence of the Lowest Excited Electronic State. *J Chem Phys* **1984**, *80* (9), 4403–4409.

(16) Kokanović, I.; Leontić, B.; Lukatela, J. Evidence for Electron - Electron Interaction and Localization Effects in the Magnetic Susceptibility of Hydrogen - Doped Zr-Ni Metallic Glass. *Solid State Commun* **1989**, *69* (5), 447–451.

(17) Scalbert, D.; Cernogora, J.; Mauger, A.; Guillaume, C. B. àla; Mycielski, A. Resonant Raman Scattering on Low Energy Excited States of Fe^{++} in $Cd_{1-X}Fe_xSe$. *Solid State Commun* **1989**, *69* (5), 453–456.

(18) Murray, C. B.; Kagan, C. R.; Bawendi, M. G. Synthesis and Characterization of Monodisperse Nanocrystals and Close-Packed Nanocrystal Assemblies. *Annu Rev Mater Sci* **2000**, *30* (1), 545–610.

(19) Banin, U.; Lee, C. J.; Guzelian, A. A.; Kadavanich, A. V; Alivisatos, A. P.; Jaskolski, W.; Bryant, G. W.; Efros, A. L.; Rosen, M. Size-Dependent Electronic Level Structure of InAs Nanocrystal Quantum Dots: Test of Multiband Effective Mass Theory. *J Chem Phys* **1998**, *109* (6), 2306–2309.

(20) Xia, J.B. Electronic Structures of Zero-Dimensional Quantum Wells. *Phys Rev B* **1989**, *40* (12), 8500–8507.

(21) Alivisatos, A. P. Semiconductor Clusters, Nanocrystals, and Quantum Dots. *Science* **1996**, *271* (5251), 933–937.

(22) Abdullah, B. J. Size Effect of Band Gap in Semiconductor Nanocrystals and

Nanostructures from Density Functional Theory within HSE06. *Mater Sci Semicond Process* **2022**, *137*, 106214.

(23) Li, L.; Hu, J.; Yang, W.; Alivisatos, A. P. Band Gap Variation of Size- and Shape-Controlled Colloidal CdSe Quantum Rods. *Nano Lett* **2001**, *1* (7), 349–351.

(24) Klimov, V. I. Mechanisms for Photogeneration and Recombination of Multiexcitons in Semiconductor Nanocrystals: Implications for Lasing and Solar Energy Conversion. *J Phys Chem B* **2006**, *110* (34), 16827–16845.

(25) Leatherdale, C. A.; Woo, W.K.; Mikulec, F. V; Bawendi, M. G. On the Absorption Cross Section of CdSe Nanocrystal Quantum Dots. *J Phys Chem B* **2002**, *106* (31), 7619–7622.

(26) Shim, M.; Guyot-Sionnest, P. Permanent Dipole Moment and Charges in Colloidal Semiconductor Quantum Dots. *J Chem Phys* **1999**, *111* (15), 6955–6964.

(27) Ma, X.; Mews, A.; Kipp, T. Determination of Electronic Energy Levels in Type-II CdTe-Core/CdSe-Shell and CdSe-Core/CdTe-Shell Nanocrystals by Cyclic Voltammetry and Optical Spectroscopy. *J Phys Chem C* **2013**, *117* (32), 16698–16708.

(28) Warburton, R. J.; Schulhauser, C.; Haft, D.; Schäflein, C.; Karrai, K.; Garcia, J. M.; Schoenfeld, W.; Petroff, P. M. Giant Permanent Dipole Moments of Excitons in Semiconductor Nanostructures. *Phys Rev B* **2002**, *65* (11), 113303.

(29) Edvinsson, T. Optical Quantum Confinement and Photocatalytic Properties in Two-, One- and Zero-Dimensional Nanostructures. *R Soc Open Sci* **2022**, *5* (9), 180387.

(30) Koch, U.; Fojtik, A.; Weller, H.; Henglein, A. Photochemistry of Semiconductor Colloids. Preparation of Extremely Small ZnO Particles, Fluorescence Phenomena and Size Quantization Effects. *Chem Phys Lett* **1985**, *122* (5), 507–510.

(31) Mohamed, W. A. A.; Abd El-Gawad, H.; Mekkey, S.; Galal, H.; Handal, H.; Mousa, H.; Labib, A. Quantum Dots Synthetization and Future Prospect Applications. **2021**, *10* (1), 1926–1940.

(32) Ramirez, H. Y.; Lin, C. H.; Chao, C. C.; Hsu, Y.; You, W. T.; Huang, S. Y.; Chen, Y. T.; Tseng, H. C.; Chang, W. H.; Lin, S. D.; et al. Optical Fine Structures of Highly Quantized InGaAs/GaAs Self-Assembled Quantum Dots. *Phys Rev B* **2010**, *81* (24), 245324.

(33) Efros, A. L.; Brus, L. E. Nanocrystal Quantum Dots: From Discovery to Modern Development. *ACS Nano* **2021**, *15* (4), 6192–6210.

(34) Protesescu, L.; Yakunin, S.; Bodnarchuk, M. I.; Krieg, F.; Caputo, R.; Hendon, C. H.; Yang, R. X.; Walsh, A.; Kovalenko, M. V. Nanocrystals of Cesium Lead Halide Perovskites ($CsPbX_3$, X = Cl, Br, and I): Novel Optoelectronic Materials Showing

Bright Emission with Wide Color Gamut. *Nano Lett* **2015**, *15* (6), 3692–3696.

(35) Bi, C.; Wang, S.; Wen, W.; Yuan, J.; Cao, G.; Tian, J. Room-Temperature Construction of Mixed-Halide Perovskite Quantum Dots with High Photoluminescence Quantum Yield. *J Phys Chem C* **2018**, *122* (9), 5151–5160.

(36) Nedelcu, G.; Protesescu, L.; Yakunin, S.; Bodnarchuk, M. I.; Grotevent, M. J.; Kovalenko, M. V. Fast Anion-Exchange in Highly Luminescent Nanocrystals of Cesium Lead Halide Perovskites ($CsPbX_3$, X = Cl, Br, I). *Nano Lett* **2015**, *15* (8), 5635–5640.

(37) Akkerman, Q. A.; D'Innocenzo, V.; Accornero, S.; Scarpellini, A.; Petrozza, A.; Prato, M.; Manna, L. Tuning the Optical Properties of Cesium Lead Halide Perovskite Nanocrystals by Anion Exchange Reactions. *J Am Chem Soc* **2015**, *137* (32), 10276–10281.

(38) Ye, J.; Byranvand, M. M.; Martínez, C. O.; Hoye, R. L. Z.; Saliba, M.; Polavarapu, L. Defect Passivation in Lead-Halide Perovskite Nanocrystals and Thin Films: Toward Efficient LEDs and Solar Cells. *Angew Chemie Int Ed* **2021**, *60* (40), 21636–21660.

(39) Brandt, R. E.; Poindexter, J. R.; Gorai, P.; Kurchin, R. C.; Hoye, R. L. Z.; Nienhaus, L.; Wilson, M. W. B.; Polizzotti, J. A.; Sereika, R.; Žaltauskas, R.; et al. Searching for "Defect-Tolerant" Photovoltaic Materials: Combined Theoretical and Experimental Screening. *Chem Mater* **2017**, *29* (11), 4667–4674.

(40) Zhang, S. B.; Wei, S.-H.; Zunger, A.; Katayama-Yoshida, H. Defect Physics of the $CuInSe_2$ Chalcopyrite Semiconductor. *Phys Rev B* **1998**, *57* (16), 9642–9656.

(41) Brandt, R. E.; Stevanović, V.; Ginley, D. S.; Buonassisi, T. Identifying Defect-Tolerant Semiconductors with High Minority-Carrier Lifetimes: Beyond Hybrid Lead Halide Perovskites. *MRS Commun* **2015**, *5* (2), 265–275.

(42) Zakutayev, A.; Caskey, C. M.; Fioretti, A. N.; Ginley, D. S.; Vidal, J.; Stevanovic, V.; Tea, E.; Lany, S. Defect Tolerant Semiconductors for Solar Energy Conversion. *J Phys Chem Lett* **2014**, *5* (7), 1117–1125.

(43) Brakkee, R.; Williams, R. M. Minimizing Defect States in Lead Halide Perovskite Solar Cell Materials. *Applied Sciences*. 2020.

(44) Guo, Y.; Wang, Q.; Saidi, W. A. Structural Stabilities and Electronic Properties of High-Angle Grain Boundaries in Perovskite Cesium Lead Halides. *J Phys Chem C* **2017**, *121* (3), 1715–1722.

(45) Kang, J.; Wang, L.-W. High Defect Tolerance in Lead Halide Perovskite $CsPbBr_3$. *J Phys Chem Lett* **2017**, *8* (2), 489–493.

(46) Umari, P.; Mosconi, E.; De Angelis, F. Relativistic GW Calculations on $CH_3NH_3PbI_3$

and $CH_3NH_3SnI_3$ Perovskites for Solar Cell Applications. *Sci Rep* **2014**, *4* (1), 4467.

(47) Sum, T. C.; Mathews, N.; Xing, G.; Lim, S. S.; Chong, W. K.; Giovanni, D.; Dewi, H. A. Spectral Features and Charge Dynamics of Lead Halide Perovskites: Origins and Interpretations. *Acc Chem Res* **2016**, *49* (2), 294–302.

(48) Xing, G.; Mathews, N.; Sun, S.; Lim, S. S.; Lam, Y. M.; Grätzel, M.; Mhaisalkar, S.; Sum, T. C. Long-Range Balanced Electron- and Hole-Transport Lengths in Organic-Inorganic $CH_3NH_3PbI_3$. *Science* **2013**, *342* (6156), 344 LP – 347.

(49) Green, M. A. Third Generation Photovoltaics: Ultra-High Conversion Efficiency at Low Cost. *Prog Photovoltaics Res Appl* **2001**, *9* (2), 123–135.

(50) Green, M. A. Third Generation Photovoltaics : Advanced Solar Energy Conversion; 2006.

(51) Ross, R. T.; Nozik, A. J. Efficiency of Hot-carrier Solar Energy Converters. *J Appl Phys* **1982**, *53* (5), 3813–3818.

(52) Li, M.; Fu, J.; Xu, Q.; Sum, T. C. Slow Hot-Carrier Cooling in Halide Perovskites: Prospects for Hot-Carrier Solar Cells. *Adv Mater* **2019**, *31* (47), 1802486.

(53) Li, Y.; Lai, R.; Luo, X.; Liu, X.; Ding, T.; Lu, X.; Wu, K. On the Absence of a Phonon Bottleneck in Strongly Confined $CsPbBr_3$ Perovskite Nanocrystals. *Chem Sci* **2019**, *10* (23), 5983–5989.

(54) Iqbal, M. A. Materials for Photovoltaics: Overview, Generations, Recent Advancements and Future Prospects; Malik, M., Ed.; IntechOpen: Rijeka, 2022; p Ch. 2.

(55) Stoddart, A. Purely Organic Perovskites. *Nat Rev Mater* **2018**, *3* (8), 226.

(56) Fu, Y.; Hautzinger, M. P.; Luo, Z.; Wang, F.; Pan, D.; Aristov, M. M.; Guzei, I. A.; Pan, A.; Zhu, X.; Jin, S. Incorporating Large A Cations into Lead Iodide Perovskite Cages: Relaxed Goldschmidt Tolerance Factor and Impact on Exciton–Phonon Interaction. *ACS Cent Sci* **2019**, *5* (8), 1377–1386.

(57) Chen, K.; Barker, A. J.; Morgan, F. L. C.; Halpert, J. E.; Hodgkiss, J. M. Effect of Carrier Thermalization Dynamics on Light Emission and Amplification in Organometal Halide Perovskites. *J Phys Chem Lett* **2015**, *6* (1), 153–158.

(58) Mohapatra, A.; Kar, M. R.; Bhaumik, S. Recent Progress and Prospects on Metal Halide Perovskite Nanocrystals as Color Converters in the Fabrication of White Light-Emitting Diodes. *Front Electron Mater* **2022**, *2*.

(59) Sun, Q.; Yin, W.J. Thermodynamic Stability Trend of Cubic Perovskites. *J Am Chem Soc* **2017**, *139* (42), 14905–14908.

(60) Akkerman, Q. A.; Manna, L. What Defines a Halide Perovskite? *ACS Energy Lett* **2020**,

604–610.

(61) Zhang, W.; Eperon, G. E.; Snaith, H. J. Metal Halide Perovskites for Energy Applications. *Nat Energy* **2016**, *1* (6), 16048.

(62) Zhou, Y.; Zhao, Y. Chemical Stability and Instability of Inorganic Halide Perovskites. *Energy Environ Sci* **2019**, *12* (5), 1495–1511.

(63) Xiao, J.W.; Liang, Y.; Zhang, S.; Zhao, Y.; Li, Y.; Chen, Q. Stabilizing $RbPbBr_3$ Perovskite Nanocrystals through Cs^+ Substitution. *Chem-A Eur J* **2019**, *25* (10), 2597–2603.

(64) Linaburg, M. R.; McClure, E. T.; Majher, J. D.; Woodward, P. M. $Cs_{1-X}Rb_xPbCl_3$ and $Cs_{1-X}Rb_xPbBr_3$ Solid Solutions: Understanding Octahedral Tilting in Lead Halide Perovskites. *Chem Mater* **2017**, *29* (8), 3507–3514.

(65) Hu, Y.; Aygüler, M. F.; Petrus, M. L.; Bein, T.; Docampo, P. Impact of Rubidium and Cesium Cations on the Moisture Stability of Multiple-Cation Mixed-Halide Perovskites. *ACS Energy Lett* **2017**, *2* (10), 2212–2218.

(66) Kovalenko, E. N.; Yunakova, O. N.; Yunakov, N. N. Exciton Spectra of $Cs_{1-X}Rb_xPbCl_3$ Solid Solution Thin Films. *Low Temp Phys* **2019**, *45* (10), 1122–1126.

(67) Ullah, S.; Wang, J.; Yang, P.; Liu, L.; Yang, S.E.; Xia, T.; Guo, H.; Chen, Y. All-Inorganic $CsPbBr_3$ Perovskite: A Promising Choice for Photovoltaics. *Mater Adv* **2021**, *2* (2), 646–683.

(68) Filip, M. R.; Liu, X.; Miglio, A.; Hautier, G.; Giustino, F. Phase Diagrams and Stability of Lead-Free Halide Double Perovskites $Cs_2BB'X_6$: B = Sb and Bi, B′ = Cu, Ag, and Au, and X = Cl, Br, and I. *J Phys Chem C* **2018**, *122* (1), 158–170.

(69) Ban, H.; Nakajima, T.; Liu, Z.; Yu, H.; Sun, Q.; Dai, L.; Shen, Y.; Zhang, X.-L.; Zhu, J.; Chen, P.; et al. Over 8% Efficient $CsSnI_3$-Based Mesoporous Perovskite Solar Cells Enabled by Two-Step Thermal Annealing and Surface Cationic Coordination Dual Treatment. *J Mater Chem A* **2022**, *10* (7), 3642–3649.

(70) Wu, B.; Zhou, Y.; Xing, G.; Xu, Q.; Garces, H. F.; Solanki, A.; Goh, T. W.; Padture, N. P.; Sum, T. C. Long Minority-Carrier Diffusion Length and Low Surface-Recombination Velocity in Inorganic Lead-Free $CsSnI_3$ Perovskite Crystal for Solar Cells. *Adv Funct Mater* **2017**, *27* (7), 1604818.

(71) Idrissi, S.; Ziti, S.; Labrim, H.; Bahmad, L. Band Gaps of the Solar Perovskites Photovoltaic $CsXCl_3$ (X=Sn, Pb or Ge). *Mater Sci Semicond Process* **2021**, *122,* 105484.

(72) Ming, W.; Shi, H.; Du, M.H. Large Dielectric Constant, High Acceptor Density, and Deep Electron Traps in Perovskite Solar Cell Material $CsGeI_3$. *J Mater Chem A* **2016**, *4*

(36), 13852–13858.

(73) Krishnamoorthy, T.; Ding, H.; Yan, C.; Leong, W. L.; Baikie, T.; Zhang, Z.; Sherburne, M.; Li, S.; Asta, M.; Mathews, N.; et al. Lead-Free Germanium Iodide Perovskite Materials for Photovoltaic Applications. *J Mater Chem A* **2015**, *3* (47), 23829–23832.

(74) Qiu, X.; Cao, B.; Yuan, S.; Chen, X.; Qiu, Z.; Jiang, Y.; Ye, Q.; Wang, H.; Zeng, H.; Liu, J.; et al. From Unstable $CsSnI_3$ to Air-Stable Cs_2SnI_6: A Lead-Free Perovskite Solar Cell Light Absorber with Bandgap of 1.48eV and High Absorption Coefficient. *Sol Energy Mater Sol Cells* **2017**, *159*, 227–234.

(75) Saparov, B.; Sun, J.-P.; Meng, W.; Xiao, Z.; Duan, H.-S.; Gunawan, O.; Shin, D.; Hill, I. G.; Yan, Y.; Mitzi, D. B. Thin-Film Deposition and Characterization of a Sn-Deficient Perovskite Derivative Cs_2SnI_6. *Chem Mater* **2016**, *28* (7), 2315–2322.

(76) Lee, B.; Ezhumalai, Y.; Lee, W.; Chen, M.-C.; Yeh, C.Y.; Marks, T. J.; Chang, R. P. H. Cs_2SnI_6-Encapsulated Multidye-Sensitized All-Solid-State Solar Cells. *ACS Appl Mater Interfaces* **2019**, *11* (24), 21424–21434.

(77) König, D.; Casalenuovo, K.; Takeda, Y.; Conibeer, G.; Guillemoles, J. F.; Patterson, R.; Huang, L. M.; Green, M. A. Hot Carrier Solar Cells: Principles, Materials and Design. *Phys E Low-dimensional Syst Nanostructures* **2010**, *42* (10), 2862–2866.

(78) The Principal Quasi-Particles in Material Physics. In *Solid-State Physics for Electronics*; 2009; pp 335–383.

(79) Yu, P. Y.; Cardona, M. Vibrational Properties of Semiconductors, and Electron-Phonon Interactions BT - Fundamentals of Semiconductors: Physics and Materials Properties; Yu, P. Y., Cardona, M., Eds.; Springer Berlin Heidelberg: Berlin, Heidelberg, 2010; pp 107–158.

(80) Suzuura, H.; Ando, T. Electron Lifetime Due to Optical-Phonon Scattering in a Graphene Sheet. *J Phys Conf Ser* **2009**, *150* (2), 22080.

(81) Prabhu, S. S.; Vengurlekar, A. S. Hot-Carrier Energy-Loss Rates in Alloy Semiconductors. *Phys Rev B* **1996**, *53* (12), 7815–7818.

(82) Prabhu, S. S.; Vengurlekar, A. S.; Roy, S. K.; Shah, J. Nonequilibrium Dynamics of Hot Carriers and Hot Phonons in CdSe and GaAs. *Phys Rev B* **1995**, *51* (20), 14233–14246.

(83) Choi, C. K.; Kwon, Y. H.; Krasinski, J. S.; Park, G. H.; Setlur, G.; Song, J. J.; Chang, Y. C. Ultrafast Carrier Dynamics in a Highly Excited GaN Epilayer. *Phys Rev B* **2001**, *63* (11), 115315.

(84) Burgos-Caminal, A.; Moreno-Naranjo, J. M.; Willauer, A. R.; Paraecattil, A. A.; Ajdarzadeh, A.; Moser, J.E. Hot Carrier Mobility Dynamics Unravel Competing Sub-

Ps Cooling Processes in Lead Halide Perovskites. J. Phys. Chem. C **2021**, 125, 1, 98–106

(85) Fu, J.; Xu, Q.; Han, G.; Wu, B.; Huan, C. H. A.; Leek, M. L.; Sum, T. C. Hot Carrier Cooling Mechanisms in Halide Perovskites. *Nat Commun* **2017**, *8* (1), 1300.

(86) Mukhanov, V. F. Quantum Theory of Gauge Invariant Cosmological Perturbations. *Sov Phys JETP* **1988**, *67*, 1297–1302.

(87) Klemens, P. G. Anharmonic Decay of Optical Phonons. *Phys Rev* **1966**, *148* (2), 845–848.

(88) Kawai, H.; Giorgi, G.; Marini, A.; Yamashita, K. The Mechanism of Slow Hot-Hole Cooling in Lead-Iodide Perovskite: First-Principles Calculation on Carrier Lifetime from Electron–Phonon Interaction. *Nano Lett* **2015**, *15* (5), 3103–3108.

(89) Haug, A. Auger Recombination in Direct-Gap Semiconductors: Band-Structure Effects. *J Phys C Solid State Phys* **1983**, *16* (21), 4159–4172.

(90) Achermann, M.; Bartko, A. P.; Hollingsworth, J. A.; Klimov, V. I. The Effect of Auger Heating on Intraband Carrier Relaxation in Semiconductor Quantum Rods. *Nat Phys* **2006**, *2* (8), 557–561.

(91) Fu, J.; Xu, Q.; Han, G.; Wu, B.; Huan, C. H. A.; Leek, M. L.; Sum, T. C. Author Correction: Hot Carrier Cooling Mechanisms in Halide Perovskites. *Nat Commun* **2018**, *9* (1), 238.

(92) Yoffa, E. J. Screening of Hot-Carrier Relaxation in Highly Photoexcited Semiconductors. *Phys Rev B* **1981**, *23* (4), 1909–1919.

(93) Frost, J. M. Calculating Polaron Mobility in Halide Perovskites. *Phys Rev B* **2017**, *96* (19), 195202.

(94) Feynman, R. P. Slow Electrons in a Polar Crystal. *Phys Rev* **1955**, *97* (3), 660–665.

(95) Lifshitz, E. M. LEV DAVIDOVICH LANDAU (1908–1968). *Sov Phys Uspekhi* **1969**, *12* (1), 135–145.

(96) Filippetti, A.; Mattoni, A.; Caddeo, C.; Saba, M. I.; Delugas, P. Low Electron-Polar Optical Phonon Scattering as a Fundamental Aspect of Carrier Mobility in Methylammonium Lead Halide $CH_3NH_3PbI_3$ Perovskites. *Phys. Chem. Chem. Phys.* **2016**, *18* (22), 15352–15362.

(97) Wright, A. D.; Verdi, C.; Milot, R. L.; Eperon, G. E.; Pérez-Osorio, M. A.; Snaith, H. J.; Giustino, F.; Johnston, M. B.; Herz, L. M. Electron–Phonon Coupling in Hybrid Lead Halide Perovskites. *Nat Commun* **2016**, *7* (1), 11755.

(98) Fröhlich, H. Electrons in Lattice Fields. *Adv Phys* **1954**, *3* (11), 325–361.

(99) Kaur, G.; Ghosh, H. N. Hot Carrier Relaxation in $CsPbBr_3$-Based Perovskites: A Polaron Perspective. *J Phys Chem Lett* **2020**, *11* (20), 8765–8776.

(100) Frost, J. M.; Whalley, L. D.; Walsh, A. Slow Cooling of Hot Polarons in Halide Perovskite Solar Cells. *ACS Energy Lett* **2017**, *2* (12), 2647–2652.

(101) Neukirch, A. J.; Nie, W.; Blancon, J.C.; Appavoo, K.; Tsai, H.; Sfeir, M. Y.; Katan, C.; Pedesseau, L.; Even, J.; Crochet, J. J.; et al. Polaron Stabilization by Cooperative Lattice Distortion and Cation Rotations in Hybrid Perovskite Materials. *Nano Lett* **2016**, *16* (6), 3809–3816.

(102) Ivanovska, T.; Dionigi, C.; Mosconi, E.; De Angelis, F.; Liscio, F.; Morandi, V.; Ruani, G. Long-Lived Photoinduced Polarons in Organohalide Perovskites. *J Phys Chem Lett* **2017**, *8* (13), 3081–3086.

(103) Zhu, X.-Y.; Podzorov, V. Charge Carriers in Hybrid Organic–Inorganic Lead Halide Perovskites Might Be Protected as Large Polarons. *J Phys Chem Lett* **2015**, *6* (23), 4758–4761.

(104) Dykman, M. I.; Rashba, E. I. The Roots of Polaron Theory. *Phys Today* **2015**, *68* (4), 10–11.

(105) Miyata, K.; Atallah, T. L.; Zhu, X.Y. Lead Halide Perovskites: Crystal-Liquid Duality, Phonon Glass Electron Crystals, and Large Polaron Formation. *Sci Adv* **2017**, *3* (10), e1701469.

(106) Claus Klingshirn. *Semiconductor Optics Advanced Texts in Physics*; 2005.

(107) Emin, D. *Polarons*; Cambridge University Press, 2012.

(108) Wooten, F. Optical Properties Measurement Techniques Solar Energy Materials Special Issue. *Sol Energy Mater* **1989**, *18* (3–4), 231.

(109) Fox, M. Optical Properties of Solids. *Am J Phys* **2002**, *70* (12), 1269–1270.

(110) Herz, L. M. Charge-Carrier Dynamics in Organic-Inorganic Metal Halide Perovskites. *Annu Rev Phys Chem* **2016**, *67*, 65–89.

(111) He, Y.; Galli, G. Perovskites for Solar Thermoelectric Applications: A First Principle Study of $CH_3NH_3AI_3$ (A = Pb and Sn). *Chem Mater* **2014**, *26* (18), 5394–5400.

(112) Verma, S. D.; Gu, Q.; Sadhanala, A.; Venugopalan, V.; Rao, A. Slow Carrier Cooling in Hybrid Pb-Sn Halide Perovskites. *ACS Energy Lett* **2019**, *4* (3), 736–740.

(113) Rehman, W.; McMeekin, D. P.; Patel, J. B.; Milot, R. L.; Johnston, M. B.; Snaith, H. J.; Herz, L. M. Photovoltaic Mixed-Cation Lead Mixed-Halide Perovskites: Links between Crystallinity, Photo-Stability and Electronic Properties. *Energy Environ Sci* **2017**, *10* (1), 361–369.

(114) Herz, L. M. Charge-Carrier Mobilities in Metal Halide Perovskites: Fundamental Mechanisms and Limits. *ACS Energy Lett* **2017**, *2* (7), 1539–1548.

(115) Kulbak, M.; Cahen, D.; Hodes, G. How Important Is the Organic Part of Lead Halide Perovskite Photovoltaic Cells? Efficient $CsPbBr_3$ Cells. *J Phys Chem Lett* **2015**, *6* (13), 2452–2456.

(116) Ahmed, S.; Rui, W.; Altaf, F.; Khan, J.; Bocchetta, P.; Zhang, H. Ultrafast Studies of $ZrTe_3$ by Transient Absorption Spectrometer. *Materials (Basel)* **2022**, *15* (15).

(117) Dyakonova, N.; Karandashev, S. A.; Levinshtein, M. E.; Matveev, B. A.; Remennyi, M. A. Low Frequency Noise in Reverse Biased P-*InAsSbP*/n-*InAs* Infrared Photodiodes. *Semicond Sci Technol* **2018**, *34* (1), 15013.

(118) Norimatsu, K.; Hada, M.; Yamamoto, S.; Sasagawa, T.; Kitajima, M.; Kayanuma, Y.; Nakamura, K. G. Dynamics of All the Raman-Active Coherent Phonons in Sb_2Te_3 Revealed via Transient Reflectivity. *J Appl Phys* **2015**, *117* (14), 143102.

(119) Sagar, D. M.; Cooney, R. R.; Sewall, S. L.; Dias, E. A.; Barsan, M. M.; Butler, I. S.; Kambhampati, P. Size Dependent, State-Resolved Studies of Exciton-Phonon Couplings in Strongly Confined Semiconductor Quantum Dots. *Phys Rev B* **2008**, *77* (23), 235321.

(120) Long, D. A.; Stanton, L.; Linnett, J. W. Studies of Nonlinear Phenomena - I. Theory of the Hyper Raman Effect. *Proc R Soc London A Math Phys Sci* **1970**, *318* (1535), 441–457.

(121) Dickens, P. G.; Whittingham, M. S. The Tungsten Bronzes and Related Compounds. *Q Rev Chem Soc* **1968**, *22* (1), 30–44.

Chapter 2

Experimental section

2.1 Hot injection methodology for the synthesis of halide perovskites

It is well acknowledged that the synthetic pathway chosen for the preparation of HP NCs has a significant impact on their characteristics, notably their optical quality. The way the surface bonds terminate and the stoichiometric ratio of the ions making up the perovskite structure are the fundamental causes accountable for this diversity.[1–3] For the synthesis of PNCs, there are indeed a variety of well-established methods that may be used, all of which can be broadly divided into two categories: "top-down" and "bottom-up". However, the processes referred to as top-down routes such as ball milling and chemical exfoliation etc., that involve the fragmentation of macroscopic solids result in NCs which suffer from high density of surface defect states and therefore are not much compelling.[4,5] In contrast, the bottom-up synthesis routes which involve reactions in either liquid phase or gas phase with the initial precursors as molecules or ions are much more promising and are thus more often used. Furthermore among these routes, the liquid phase synthesis, particularly the HI method is considered as the most effective for producing high quality NCs.[6,7]

In principal, the contemporary method of HI which was first discovered by Alivisatos and Bawendi et al. to produce CdS, CdSe QDs etc. is essentially based on LaMer and Dinegar's work which reveals the manner in which the formation of highly dispersed colloidal NCs is a function of fast nucleation and the subsequent regulated expansion of the pre-existing nuclei.[8–10] As per Lamer's model, the entire process of NC formation can be categorised into three primary stages **(Figure 2.1)**: I) Generation: The first phase involves the generation of soluble atoms in solution; II) Self-nucleation: This next stage marks the commencement of the nucleation phase where due to the atomic concentration exceeding the critical supersatuation level ($C_{min}^{nucleation}$), the energy barrier for nucleation is surpassed. Therefore, as a result of burst nucleation, the atoms now begin to form clusters; III) Growth: Following nucleation, there is an obvious reduction in the atomic concentration and when it drops below $C_{min}^{nucleation}$ but is

still greater than the saturation concentration C_s, growth process begins where the smaller nuclei grow into larger ones mediated through diffusion process.

The process of HI fundamentally involves the quick injection of organometallic reagents into a heated solvent in order to produce homogenous nuclei.[9,11] As a measure to inhibit the resultant QDs from clumping together, the reaction solution employed in this procedure besides the precursor and high boiling point solvent contains surfactant molecules/ligands. Alkylphosphine and alkylphosphine oxides, long-chain carboxylic acids (such as oleic acid), and long-chain amines (e.g., oleylamine) are some of the ligands that are routinely deployed for this purpose. Subsequent to the completion of the nucleation process, size-focusing effect comes into play when the solution undergoes a homogenous development of the QDs wherein the growth rate for the bigger QDs is slower than the relatively small QDs **(Figure 2.1)**. Then, as the development progresses, Ostwald ripening unfolds, which involves the growth of the bigger QDs and simultaneous dissolution of the smaller QDs owing to their higher chemical potential.[12] The mean size of the particle then continues to increase with concurrent decrement in the particle concentration until the point of saturation is reached. Since the HI route allows the isolation of the nucleation step from the growth stage, this approach is particularly successful at providing a high degree of control over the particle size and their uniform size distribution. Further, this synthesis method renders it possible to design QDs of different sizes by merely adjusting the reactant temperature, surfactant ratio, and the duration of the reaction.

In context of perovskites, the first ever successful attempt to synthesise $MAPbBr_3$ NCs using a solution-based colloidal method was reported at the end of 2013 by Schmidt et.al when they obtained a PLQY of ~ 20% for the as-synthesised NCs.[13] It was then two years later, in 2015, when Protesescu and coworkers successfully synthesised mono-disperse $CsPbX_3$ (X= Cl, Br, I) NCs with PLQY close to 90% by adopting the conventional HI synthesis method frequently deployed for the preparation of conventional colloidal QDs such as CdS, PbS.[14] However other than the HI methodology, there also exist other liquid phase strategies like LARP and solvothermal synthesis for producing the MHP NCs which are also often employed.[3]

These later mentioned synthesis routes undoubtedly yield good quality and luminous NCs but in comparison to the considerably more efficient high-temperature hot-injection approach, the resultant products obtained from these procedures suffer from huge density of surface defects and are usually poly-disperse. This is owing to the fact that halide perovskite NCs have quick reaction and nucleation kinetics and in these one pot or heat-up procedures, the reaction time cannot be regulated adequately to avert size broadening and shape dispersion,

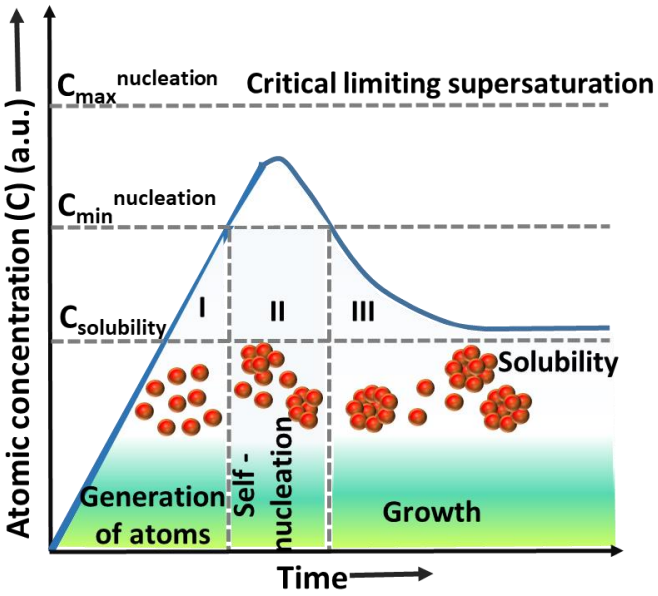

Figure 2.1 Systematic hypothetical representation of the evolution of atomic concentration in a traditional LaMer mechanism during the three phases of reaction (LaMer and Dinegar, 1950).

so these are rarely employed. In order words, till date the best known approach for producing high quality and mono-dispersed PNCs is the standard two-step HI method and its further modified versions. We therefore opted for the HI route of synthesis for the preparation of all the inorganic NC systems investigated in this present thesis work.

Among all AIPs, the structures containing Cesium ($CsPbX_3$) as the A-site cation are the most extensively researched. There are two fundamental phases involved in the HI synthesis of these $CsPbX_3$ NCs. The preliminary stage includes making Cs-oleate, and the second stage

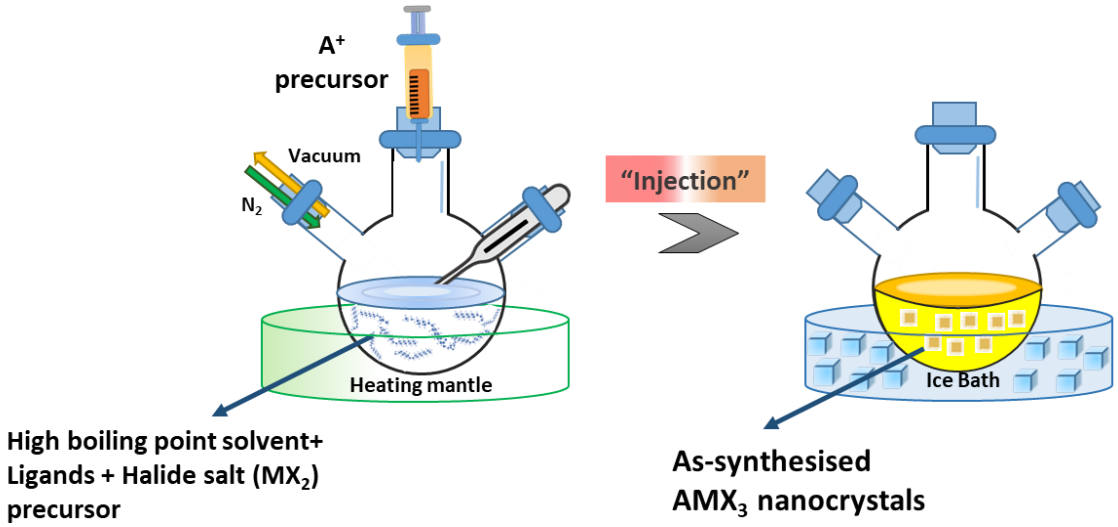

Figure 2.2 Typical Hot injection synthesis setup for the synthesis of AMX_3 perovskite nanocrystals.

requires making a Pb (II)-halide-based precursor into which a suitable amount of the former solution is quickly injected. Considering the nature of the underlying ionic metathesis mechanism, which accounts for their extraordinarily rapid nucleation and growth kinetics, with the growth happening in around 1-3 seconds, the reaction flask is then submerged in a cold bath to yield $CsPbX_3$ NCs. Further by altering the halide precursors (Cl to I), the obtained NCs can be tweeked to have a band gap varying over a wide range (410- 700 nm). The underlying reaction that drives the process can be explained as follows:[15]

- $2Cs\text{-oleate} + 3PbX_2 \Rightarrow 2CsPbX_3 + Pb(oleate)_2$

Following the ground-breaking success attained in the synthesis of all inorganic lead-based perovskites in 2015, a year later, HI technique was also deployed for the synthesis of lead-free perovskites. The pioneering work in this regard was reported independently by two research groups. BÖhm and co-workers successfully synthesized $CsSnX_3$ NCs by injecting a solution prepared by the dissolution of SnX_2 salts in TOP into a heated solution comprising of Cs_2CO_3, OA and OAm maintained at 170°C.[16] Along the similar timeframe, by using the tetravalent salt SnI_4, Wang and colleagues synthesized another tin-based perovskite with a higher oxidation state of tin (Sn^{4+}), which is also significantly more stable than the Sn^{2+} based system. [17]

2.2 Synthesis procedures

"The chemicals required for all the synthesis undertaken in this dissertation work were utilised just as purchased from Sigma Aldrich, without any prior purification."

Chemicals used:

Cesium Carbonate (Cs_2CO_3, 99 % trace metals basis) and Lead (II) Bromide ($PbBr_2$, 99.99 % trace metals basis), Zinc Bromide ($ZnBr_2$, ≥ 98%) Lead (II) Oxide (PbO), bis (trimethylsilyl) Sulphide (TMS), Tin (IV) Iodide (SnI_4)

Capping agents:

Oleylamine (OLA, tech, 70 %) and oleic acid (OA, tech, 90%)

Solvents and reagents:

1-Octadecence (ODE, tech, 90%), Tri-n-OctylPhosphine (TOP), Tert- butanol (AR grade) and n-hexane

2.2.1 Synthesis of $CsPbBr_3$ NCs, Cs_4PbBr_6 NCs and $CsPbBr_3/Cs_4PbBr_6$ core @ shell NCs

❒ **Preparation of Cesium-Oleate (Cs-Oleate)**

In a three neck RBF, 1.25 mmol of Cs_2CO_3 was added along with 20 mL solution of ODE and 1 mL of OA. The mixture was then magnetically agitated while the solution was alternately degassed and purged with N_2, and the reaction temperature was maintained at 120 °C. The entire procedure was performed numerous times to be sure there was no moisture or oxygen left in the flask that may degrade the sample. Following this, the temperature was elevated to 150°C in order to facilitate the complete dissolution of Cs_2CO_3 with the reaction mixture being continuously purged with N_2. When Cs_2CO_3 dissolves completely, it means that Cs-Oleate has successfully formed. The temperature of Cs- Oleate must always be kept above 100° C before it is used to synthesise NCs.

⇒ **Synthesis of $CsPbBr_3$ NCs:**

We executed the synthesis of $CsPbBr_3$ NCs following the well-known synthesis approach reported by Kovalenko and colleagues after incorporating a few minor changes.[18] In a 25 mL three neck RBF, 0.188 mmol of $PbBr_2$, 5 mL of ODE, and 0.5 mL each of OA and OAm were loaded while being stirred continuously under vacuum at 120 °C and alternately purged with N_2. The temperature was then raised to 160° C, and 0.4 mL of the already-prepared Cs- Oleate solution was injected swiftly. Subsequent to injection, the reaction solution was then cooled to room temperature with ice cold bath. The unreacted precursors were then removed by centrifuging the crude solution. After centrifuging, the supernatant was removed, and the resulting NCs were dispersed in hexane.

⇒ **Synthesis of $CsPbBr_3/Cs_4PbBr_6$ core@shell NCs:**

Without any additional processing, freshly synthesised CsPbBr3 NCs were employed as the seed solution. We adhered to a previously documented synthesis report for the formation of the core/shell structures after incorporating minor changes in the methodology.[19] 0.1 mM of $ZnBr_2$ was now added to the seed solution, and the mixture was then agitated for 30 minutes at 60 °C while under vacuum, followed by 10 min of N_2 purging. Following this, the reaction temperature was elevated to 80 °C in N_2 environment, and 1.6 mL of Cs- Oleate was quickly introduced into the mixture. After a time lapse of 10s, the solution temperature was brought down to room temperature using an ice bath. The crude product was centrifuged at 8000 rpm

for 5 minutes to extract the NCs. After discarding the supernatant, the precipitate that contained the NCs was then redispersed in hexane.

⇒ **Synthesis of Cs_4PbBr_6 NCs:**

Cs_4PbBr_6 NCs were synthesized by mixing 0.188 mmol of $PbBr_2$, 5 mL of ODE, 0.5 mL of both OA and OLA in a 25 mL 3-neck round bottomed flask. After mixing, the solution was then continuously stirred in vacuum for 30 min at 120 °C. Following degassing, the flask was then purged with N_2 for 5 min. This was repeated three times in succession. Then the temperature was reduced to 80°C and 1.6 mL of pre-heated Cs- Oleate solution was swiftly injected into this mixture. Immediately upon injection, within 10s, the reaction mixture was cooled with the aid of ice bath.

2.2.2 Synthesis of PbS QDs

The synthesis of PbS QDs was undertaken following the previously reported procedure by Tang *et al.* 2 mmol PbO,20 mL ODE alongwith 2 mL of OA were loaded together in a 50 mL three neck RBF.[20] Then this reaction mixture was maintained at 100°C while being degassed for one hour and later it was purged with N_2.Degassing and N_2 purging is repeated several times in succession with an aim to completely remove any moisture content or O_2 present in the flask. Solution turned colourless from the initial yellow colour which is indicative of the successful formation of Pb- Oleate.

To prepare the sulphur precursor solution, in a 25 mL RBF, 0.2 mL TMS, 1mL OA and 10 mL ODE were added and stirred vigorously under inert conditions. This as-prepared TMS solution, which is a highly reactive Sulphur source was injected into the Pb- Oleate solution at 120°C. As soon as this solution is injected, the otherwise colourless solution transforms into brown, suggesting the successful formation of PbS QDs. To enable the growth of the QDs, the reaction was left to stir at 120°C.The obtained product containing the QDs was then centrifuged thrice after precipitating it with a 1:1 mixture of methanol and acetone and the finally obtained QDs were dispersed in n-hexane for further usage.

2.2.3 Synthesis of Cs_2SnI_6 NCs

We followed similar strategy for the synthesis of Cs_2SnI_6 as that followed by Wang *et al.* but with slight modifications.[17] The precursors, 0.18 mmol of SnI_4, 0.5 mL each of OA and OAm, and 7 mL of ODE were first loaded into a 50 mL RBF. Following that, this reaction mixture was heated to 120 °C while being continuously degassed and N_2 purged. After heating this mixture for almost an hour, the temperature was then raised to 210°C and upon doing so the

solution's colour changed from yellow to dark transparent crimson. After reaching the desired temperature, 0.4mL of the pre-heated Cs- Oleate was added to the reaction mixture. Orange coloration that appears shortly after injection denotes the successful formation of Cs_2SnI_6 NCs. 10 seconds later, the reaction was quenched by cooling it with an ice bath. The final product underwent two rounds of centrifugation to remove any unreacted precursors, and the remaining precipitate was then dissolved in n-hexane for further characterization and experimental use.

2.3 Steady state material characterization tools

This segment provides an overview of all steady state material characterisation methods utilised to acquire the data for this thesis.

2.3.1 X-Ray Diffraction (XRD)

This approach includes exposing materials to X-rays and then measuring the intensities and dispersion angles of the scattered photons to derive the structural and composition information for any given system.

Principle: It is typically observed that whenever a periodic structure is struck with an electromagnetic (EM) radiation having a wavelength equivalent to the length of the geometric variations of the structure, diffraction effects usually set in. Interestingly, the interatomic spacings encountered in crystal systems are of the order of a few Angstroms, which equate to X-ray wavelengths. In this way, the lattice planes can behave analogous to diffraction gratings and furthermore in the case when the waves impinge at the glancing angle, the planes can disperse the spherical wave-fronts in a specular manner, just like reflection by a mirror. In light of this, it stands to reason that when crystalline and molecular structures are subjected to X-rays, phenomena like destructive and constructive interference should be imminent. The conditions of interference are governed by the well-known "Bragg's equation," formulated by William Henry Bragg and William Lawrence Bragg. It should be further noted that the atomic arrays constituting the crystals can function as scatterers for the incoming X-rays in both elastic and inelastic ways. But only the elastic and coherent scattering mode is responsible for the diffraction effects; the inelastic/incoherent scattering just intensifies the noise.

Bragg's law: Consider that there are two waves 1 and 2, travelling in phase, incident on atoms "A" and "B" positioned in two separate parallel-oriented lattice planes of a crystal **(Figure 2.3 A)**. The interplanar distance between the neighbouring planes is "d" and the angle of incidence is "θ". For the incident waves to be reflected from the atomic surface, they must strike the atom

at an angle equal to the glancing angle; in that case the angle of reflection will automatically be θ. As is clearly seen in the figure, there is a difference in the path lengths transvered by the two waves. The beam 2 has to travel an extra path of length "AO+ OB". In order that these waves still remain in phase even after being reflected by the atoms and interfere constructively, the path difference between the two waves should be integral times their wavelength.[21,22] Geometrically, it follows that this extra path length equals 2dsinθ. Therefore, Bragg's condition for constructive interference can be expressed as[23,24]

$$n\lambda = 2d\sin\theta \qquad \textbf{Eq.2.1}$$

This constructive interference is manifested as high intensity peaks perceivable at certain angles in the X-ray diffractogram, which can directly reveal the interplanar spacings, thus assisting in identification of the crystal structure for any given system. In addition to structural information, composition-related information may also be retrieved. This is a consequence of the fact that the scattered intensity from a given atom is influenced by its electron density and, hence the atomic number. Even more, with the aid of the Scherrer formula, by looking into the width of the peaks, we can even get a rough estimation of the crystallite size and the strain in the crystal.

$$\tau = \frac{k\lambda}{\beta \cos\theta} \qquad \textbf{Eq.2.2}$$

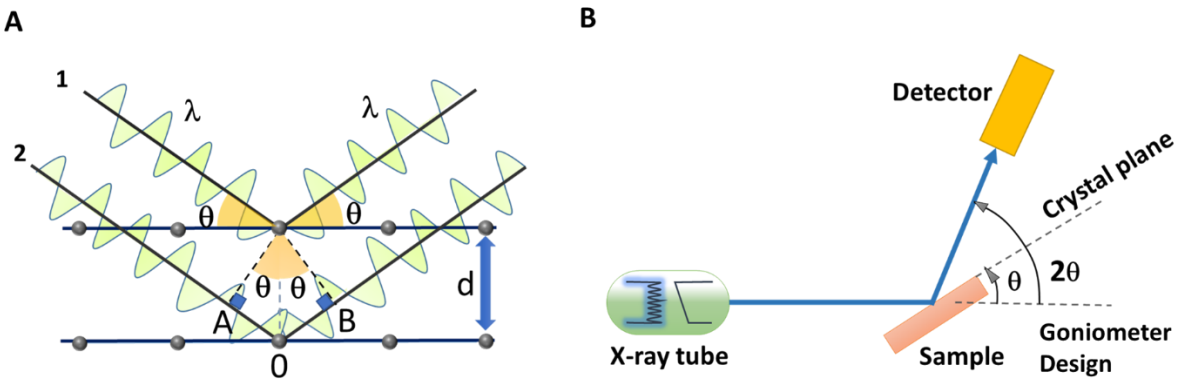

Figure 2.3 (A) Diffraction of incident X-rays by a crystal and Bragg's law. **(B)** Schematic illustration of goniometer assembly in a typical XRD setup.

Experimental setup:

A typical X-ray diffractometer setup consists of an assembly of three basic elements: an X-ray source, a goniometer and a detector **(Figure 2.3 B)**. The source is often a cathode ray tube, which generates electrons when the filament is heated, and by the application of appropriate biasing, these electrons are then driven towards the anode and bombarded on its surface, which

is essentially the target source for X-ray emission.[24–27] Characteristic X-ray spectra are generated when the electrons striking the anode surface carry enough energy to displace the inner shell electrons of the target material constituting the anode. This threshold for ejection is however undoubtedly different depending on the anode material. Therefore, the emitted X-ray spectra are unique to the target substance (Cu, Fe, Mo, Cr). The imminent X-ray spectra are made up of multiple components with the most prevalent among these as K_α and K_β. K_α is further made up of $K_{\alpha1}$ and $K_{\alpha2}$ and out of these two, the component $K_{\alpha1}$ has a slightly smaller wavelength and is twice as intense as $K_{\alpha2}$. Because only monochromatic wavelength is required for diffraction, either foils or crystal monochromators are used to filter out the other unwanted components.[28] Among all the target materials, copper is the most popular and most employed with Cu K_α = 1.5418 Å. The radiation is collimated before being directed towards the material. The intensity of the reflected X-rays is measured while both the sample and detector are rotated. The results are recorded and processed by a detector, which transforms the collected signal to a count rate, which is then sent to a device such as a computer monitor.

X-ray diffractometers are conventionally built following the goniometer design. This ensures that, for every angle θ by which the sample holder rotates in the direction of the incident X-ray beam, the detector which is mounted on an arm for the collection of the diffracted rays also moves by twice that angle (2θ) **(Figure 2.3 B)**. For data collection, XRD scans are typically programmed to run between 5 and 80 degrees.

The XRD patterns featured in the present thesis have been collected using Bruker D8 advance diffractometer utilising Cu K_α radiation (λ= 1.5418 Å), operating at an accelerating voltage of 40kV and 25 mA current. The scans were primarily acquired in a range of 5°- 80° with the sweep rate maintained as $0.005°s^{-1}$. The samples were prepared by spin-coating the as-prepared NCs on glass substrates. The acquired diffractograms were compared with the database for powder diffraction files (PDF) maintained by International Centre for Diffraction Data (ICDD) (formerly, Joint Commission on Powder Diffraction Standards (JCPDS)) for the determination of the crystal structure.

2.3.2 Transmission Electron Microscopy (TEM)

TEM instrument works on the same basic optical principles as a light microscope, except instead of light, it employs electrons and in place of conventional glass lenses, it uses magnetic lenses. Furthermore since electrons have a considerably shorter de broglie wavelength than photons of light, pictures taken with TEM instrument are far more detailed and resolved than those taken with a light microscope (over two million times

higher magnification than the ordinary optical microscope). In this way, by delivering greatly magnified pictures, TEM offers the minutest features of the specimens, sometimes even down to the level of the atoms that make them up, and therefore provide easy characterization of their morphology, composition and structure.

Principle: A standard TEM apparatus operates by the transmission of a highly accelerated electron beam across the sample resulting in a variety of interactions that may be used to gather a wide range of information about the sample. After being bombarded by a high-intensity electron beam, the sample's atoms, acting as scatterers, often cause several sorts of scattering processes. Characteristic X-ray emission, backscattering of electrons, inelastic and elastic scattering, secondary electron emission etc. are few of these phenomenon. [29–31] However, when discussing typical TEM imaging (bright field, *i.e.* the most commonly employed mode of imaging in TEM), the only electrons that are of relevance to us are those in the forward scattered beam, which pass through the material essentially undeviated (limited within 5° along the direct beam) **(Figure 2.4)** . The samples used in TEM imaging should be fairly thin for the same reason; otherwise, other types of scattering mechanisms, notably backscattering processes, may predominate. Undoubtedly, such remaining scattering processes are also equally significant but for other forms of electron microscopy.

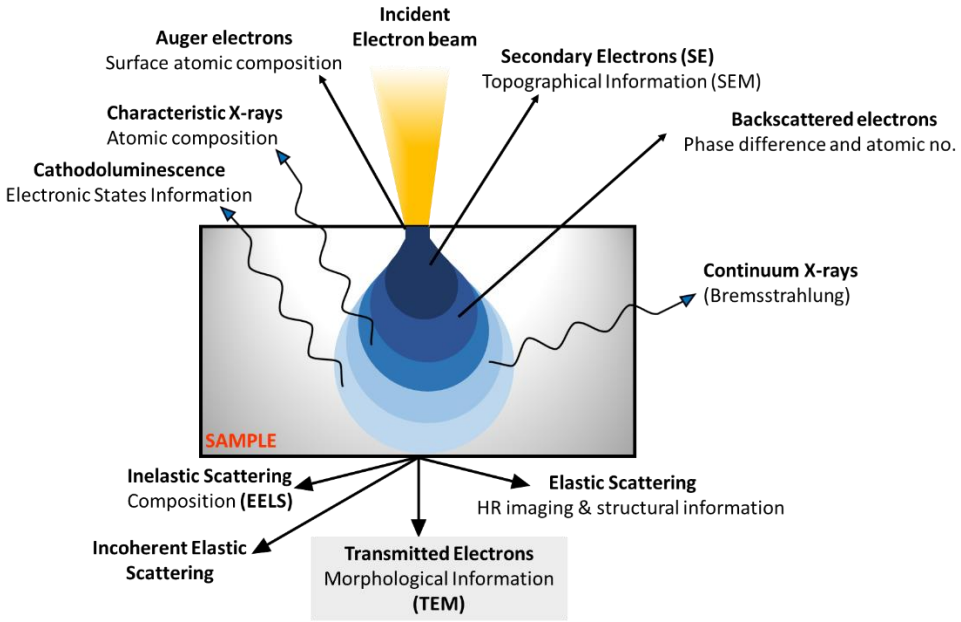

Figure 2.4 The different potential processes that may occur when a thin sample is struck by a highly accelerated electron beam.

Equation governing the resolution of the TEM instrument: The diffraction limited theoretical resolution (d) reported by Abbe for the traditional light microscope may be adjusted

and applied to the TEM with the aid of de Broglie's formula.[32] Combining Abbe's equation ($d = \frac{0.612*\lambda}{n\ sin\alpha}$, where λ is the wavelength of the employed radiation, n is the refractive index of the medium between the lens and the source of radiation, α is the half aperture angle measured in radians) with the de Broglie hypothesis and adding certain assumptions, such as n =1 and α~ 0.01, which is frequently the case with TEM, results in the expression $d = \frac{0.753*\lambda}{\alpha\sqrt{V}}$. This equation clearly shows that the resolution of the TEM equipment is an inverse function of the accelerating voltage V. That explains the rationale that how by using high accelerating voltage (typically 120 kV for organic samples and 200 kV for inorganic materials) while operating TEM, such fine resolutions on the atomic scale may be attained.

Instrumental setup: The first ever TEM instrument was built by Ernst Ruska and Max Knolls in the year 1931. A typical TEM instrument is made up of three crucial parts that are each assigned a certain purpose:[33–35] 1) An electron gun that is a source of the electron beam and a condenser lens system that directs this beam further onto the specimen, 2) then there is the image producing assembly which includes the objective lens, portable specimen stage, intermediate lens and finally the projector lens: the function of these components is to concentrate electrons travelling through the specimen to create a true, greatly magnified picture, 3) following this, there is an image recording assembly which transforms an electron picture into a form that can be perceived the human eye. A digital camera for long-term archiving and a fluorescent screen for seeing and focusing the image make up the usual image-recording system. The schematic potraying the basic setup of a TEM instrument is shown in the **Figure 2.5**. Besides this, a vacuum environment must exist throughout the whole course of the electron beam because of the tiny dimensions of electrons, which makes it easy for air or other gas molecules to deflect them. This is accomplished by deploying a number of various vacuum pumps, as well as their related valves and gauges.

1. **Electron gun and the condenser lens system**: The four fundamental components that constitute an electron gun are - a cathode, a biasing circuit, Wehnelt cap, and an extraction anode. Usually a tungsten filament (now rarely used), or a single crystal of lanthanum hexaboride (LaB_6) most commonly used nowadays) which are based on the principle of thermionic emission serve as the emission source or cathode. The other popular categories are field emission (fine tungsten needles) and Schottky electron guns. Field emission sources

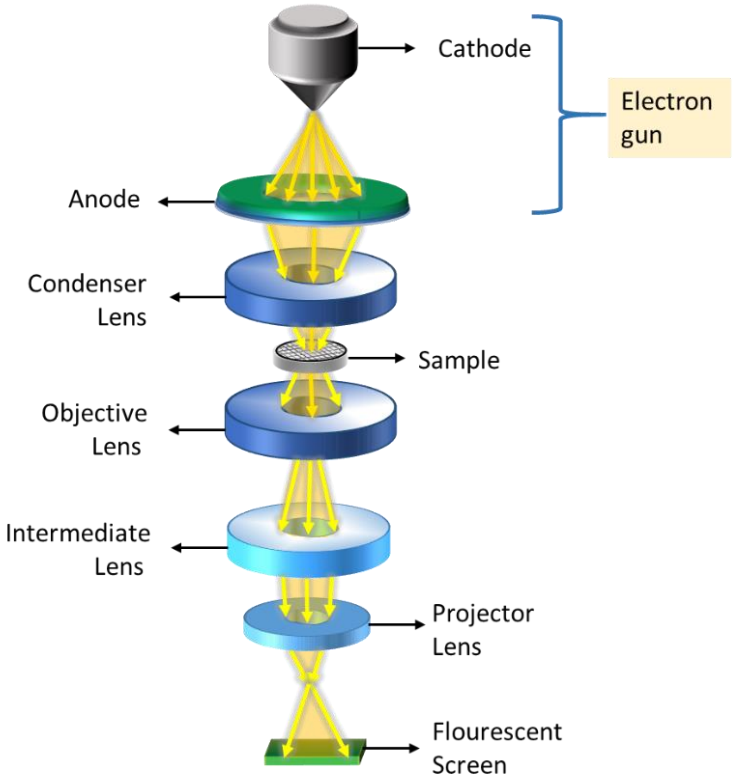

Figure 2.5 Basic configuration depicting the typical components of a Transmission Electron Microscope (TEM).

are although better than the thermionic emission based sources since they are source of monochromatic electrons in contrast to the later which generate less monochromatic electrons but are more delicate and costly. The cathode is maintained at a high negative voltage equal to the set accelerating voltage. It is enclosed inside a control grid known as Wehnelt cylinder or Wehnelt cap which is again supplied with a small negative biasing in order to have a controllable and narrow electron beam. The accelerated electrons emitted from the cathode thus are in this way converged to a crossover point positioned somewhere between the Wehnelt and the other electrode i.e. the anode that is another essential component of the electron gun. The anode is shaped in the form of disc with a hole in its centre and is grounded in order to attract the emitted electrons. The electrons that leave the cathode surface are then directed toward it by the administration of a steady and suitable voltage.

The specimen is loaded in the region of the condenser lens optics assembly. The condenser lens' system situated between the electron gun and the specimen then regulates the brightness and angular aperture of the beam emanating from the anode. The condenser aperture limits this beam, keeps high angle electrons out and also takes care of the spherical abberation. Despite the fact that a single lens can concentrate the beam onto the target, twin condensers are more usually utilised. The first lens, which is significantly more powerful, creates the reduced

image of the source, which is then projected onto the specimen by the second lens. This arrangement is more flexible and it efficiently utilises the space between the electron gun and the specimen stage since this configuration allows the adjustment of the first lens to a significant amount to regulate how much the source's image shrinks (and thus, on how much area of the specimen the light falls).

2. **Image producing assembly:** The sample to be examined is put in the specimen holder, which is mounted in the vicinity of the objective lens. The objective lens has a modest focal length and its primary function is to form a legitimate, intermediately magnified picture of the specimen which is further magnified by the projector lens. Better contrast in the image is made possible by the objective aperture. To provide a wider range of magnification and to offer a bigger overall magnification without correspondingly lengthening the physical column of the microscope, modern instruments include two projector lenses, one of which is referred to as the intermediate lens. The ultimate magnification (M) achievable upon exiting the projector lens can be expressed as: $M = M_{Obj} \times M_{Int} \times M_{Proj}$. For picture stability and brightness, the device normally displays a final magnification on the screen of 1,000–250,000.

3. **Image recording assembly:** This section of the instrument basically serves two purposes: image detection (display) as well as its recording. The type of detector that needs to be employed and its positioning inside the TEM instrument are both dependent on the mode of imaging we are seeking. For instance, for conventional TEM imaging that basically maps the distributions of electron intensities, the forward scattered electron beam is projected onto a fluorescent screen and underneath the screen in the viewing chamber are placed the detectors which are exposed only upon the elevating of the screen. Scintillator-photomultiplier tubes and semiconductor detectors are the most frequency deployed detectors for this mode of imaging. The signal collected by the detector is then transformed into digital format and is propagated further by the dedicated electronics for display on cathode ray tubes or monitor screens. Similarly, depending on the sort of underlying scattering processes being considered, the associated pre-installed detectors—scintillation-photomultiplier tubes, semiconductor detectors, or charge coupled detectors (CCDs)—are activated for the appropriate imaging modes. (Scanning Transmission Electron Microscopy (STEM), Electron Energy Loss Spectroscopy (EELS), Energy Dispersive Spectroscopy (EDS) etc.).[32]

JEM 2100 from JEOL was utilised *in this thesis* to capture the TEM images and gather morphological data for the as-prepared NCs. It makes use of LaB_6 as the electron gun and enables the achievement of extremely high TEM resolution (0.19 nm). Although it may be

operated at a variety of accelerating voltages from 80 kV to 200 kV, we have chosen 200 kV for our investigations. There are two basic justifications for this choice of operating voltage: i) it allows for improved resolution in line with Abbe's equation and (ii) The use of such high accelerating voltage is safe because all of the samples under investigation are inorganic and do not deteriorate when subjected to high energy electron radiation. The samples were prepared by drop-casting the diluted dispersions of the as-prepared NCs on Holey Carbon Films on 300 Mesh Copper Grids.

2.3.3 Steady state absorption spectroscopy (UV-Vis-NIR)

This approach is extremely useful for establishing the ground state features of the material under investigation, such as its absorption coefficient and the intrinsic nature of its band gap.

Principle: Absorption is one of the various processes that takes place as a consequence of interaction of radiation with matter. The underlying principle of this absorption spectroscopy method is that any given material may absorb light and undergo electronic transitions that excite its electrons from their ground state to higher excited states.[36–38] The outcome of this process is the generation of a unique, material-specific spectra. An optical spectrometer basically gives a quantitative estimate of a material's absorption/transmission by keeping track of the wavelengths at which absorption/transmission takes place as well as the extent of absorption/transmission at each wavelength. Most commonly, the obtained spectrum is presented as a graph of absorbance (A) vs wavelength, because of this, it is known as the absorption spectrum. Furthermore, the terminology for this specific technique derives from the fact that it includes the incidence of light in the UV to NIR regime of the spectrum and the subsequent analysis of absorption in the same domain.

Beer Lambert's law is known to serve as the key guideline for determining the absorption capabilities of a material and forms the basis of absorption spectroscopy.[39–41] If we denote the intensity of incoming monochromatic light on the sample as I_0 and the intensity of transmitted light after passing through the sample as I, then the absorbance of the material can be defined as

$$A = \log\left(\frac{I_0}{I}\right) \qquad \textbf{Eq.2.3}$$

The Beer-Lambert law establishes that this absorbance is linearly related to the concentration of the material (c), its molar absorption (ε) coefficient and path length transversed by light (l) and this can be mathematically expressed through the relation.

$$A = \varepsilon cl \qquad \textbf{Eq.2.4}$$

The molar absorption coefficient ε is characteristic to any material and depends strongly on the incident wavelength. Therefore, it is a gauge of its effectivity as an absorber at any given wavelength of light.

Instrumental setup: The UV-Vis spectrophotometer comes in a variety of forms, but in order to comprehend its functionality, let's first look at its major parts **(Figure 2.6)**. First and foremost, a reliable source that can emit light over a variety of wavelengths is necessary for this light-based method. It is typical to employ a single xenon lamp as a light source for both UV and visible wavelength domains. Nevertheless, compared to tungsten and halogen lamps, xenon lamps are more expensive and less stable. Therefore, a deuterium arc lamp is the typical source of UV light for devices that require two lamps; in such cases, tungsten or halogen lamps are frequently used for scans in the visible light region. Then the next step demands the segregation of desirable wavelengths from the entire continuum depending on the requirement. For this reason, owing to their versatility, monochromators based on diffraction gratings or prisms are often utilised; although in some circumstances, other types of filters or even monochromators in combination with these filters may also be deployed. The light then passes through the samples after going via these wavelength selections. Executing the scan for the reference sample (also referred to as "blank"), which is essentially a cuvette filled with the same solvent as the one in which the sample is dispersed, is crucial for all measurements. Later, the instrument automatically utilises this reference signal to account for any solvent effects on the absorption measurements and provides the absolute absorbance of the sample. A detector is then utilised to transform the transmitted light into a discernible electrical signal after it has passed through the sample. The detectors employed are often built using semiconductors or photoelectric coatings.

In this thesis work, we employed Shimadzu make UV-2600 spectrometer with operating range as 190 nm to 1100 nm and light sources-Deuterium lamp and halogen lamp for acquiring the absorption data in the UV- Visible domain. Cary 5000 UV-VIS-NIR spectrophotometer from Agilent with operating range – 175 nm-3300 nm and light sources- Tungsten halogen visible and deuterium arc UV was used for the collection of data in the NIR region. This extended photometric range to 3300 nm is made possible by the use of PbSmart technology which are based on PbS detectors.

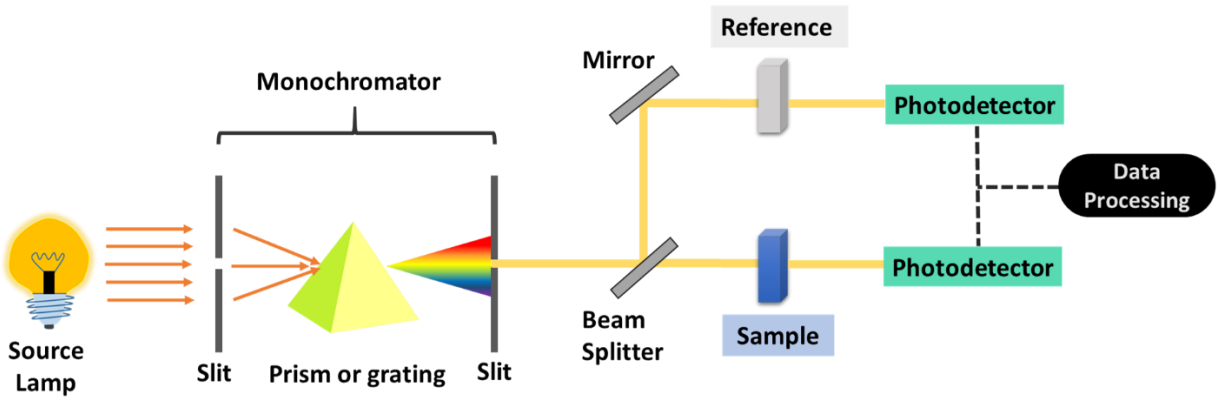

Figure 2.6 Schematic illustrating the basic optical setup of a steady state absorption spectrometer.

2.3.4 Steady state Photoluminescence/fluorescence spectroscopy

It is an important tool for obtaining a comprehensive idea of the quality of the synthesised material, charge transfer or energy transfer processes prevailing in a system, presence of defect states, nature of the band gap etc.

Principle: Any substance that is exposed to light and makes electronic transition from its ground state to an excited electronic state is bound to release this excess energy sooner or later in order to return back to its ground state, either radiatively or non-radiatively.[42,43] The radiative mode of relaxation which is mediated through the emission of photons is termed as PL. The Frank Condon principle plays a key role, and the charge carriers are frequently stimulated into the high energy vibrational levels of the excited states. As a result, they must relax down to the lowest vibrational level of the excited state before adopting radiative recombination. This justifies the rationale behind the typical red shift noticed in the PL emission *w.r.t* the lowest energy peak in the absorption spectrum (Stokes' shift). There are two further sub-categories of PL processes that may be classified based on their spontaneity of occurrence: fluorescence and phosphorescence; the former is spontaneous, while the latter is long-lived. PL spectroscopy, which is essentially a complimentary technique to absorption spectroscopy, is based on the examination of a material's PL emission.

The parameter referred to as PL Quantum Yield (PLQY) (Φ) is frequently used to evaluate how well a material emits the absorbed photons through fluorescence or, occasionally, phosphorescence ($N_{emitted}/N_{absorbed}$). It is basically a relative measure of the radiative (k_r) and the non-radiative emission rate constants (k_{nr}) and is mathematically expressed as: [43]

$$\Phi = \frac{k_r}{k_r + k_{nr}} \qquad \textbf{Eq.2.5}$$

A typical way of stating PLQY is in percentage terms although it is actually quantified on a scale from 0 to 1.0. When a process has a quantum yield of 1.0 (100%) it means that every photon that is absorbed causes an emission of a subsequent photon or in other words, the non-radiative emission rate constants are substantially less than those for the radiative channel. However, when working with unidentified samples, the PLQY (Φ_S) is expressed in terms of a previously identified, highly emissive fluorophore reference (Φ_r) using the following equation:

$$\Phi_s = \Phi_r \frac{I_S}{I_r} \frac{OD_r}{OD_s} \frac{\eta_S^2}{\eta_r^2} \qquad \textbf{Eq.2.6}$$

Here, I_s and I_r are the area under the PL curves for the sample and reference respectively, OD implies their optical densities at the excitation wavelength and η denotes the refractive indices of their respective solvents.

Instrumental setup: Terms such as "fluorometer" and "spectrofluorometer" are used interchangeably while referring to the instrument designated to measure PL. Although the design of a fluorometer might differ from instrument to instrument, there are several common elements that make up the basic arrangement of each fluorometer configuration: a steady light source, a monochromator assembly for the selection of the excitation wavelength, a sample holder, an emission monochromator, and a detector with low noise to signal ratio **(Figure 2.7)**. For the execution of steady state PL measurements, it is essentially required to have a constant excitation source. A robust, continuous xenon lamp is frequently deployed for this, since it serves as a source of intense, brilliant white light with a wide wavelength range encompassing the UV domain from 230 nm to near infrared region of the EM spectrum. Following this, an excitation monochromator is installed in the trajectory of light for selecting the appropriate wavelength as per requirement for the excitation of the sample. This segment resembles the construction of the steady state absorption spectrometer's first section, which has been previously covered. To choose light of a certain wavelength and dismiss the remainder of the spectrum, the monochomator employs a combination of diffraction gratings which rotate and determine the central wavelength that is to be propagated further and slits which determine the bandpass of the excitation wavelengths. The output beam from the excitation monochromator is then directed towards the sample, which causes the sample to emit photons as a result of radiative de-excitation. The emitted light is then passed through another set of monochromator (emission monochromator) which permits the passage of only the relevant emission wavelength and excludes the rest of the excitation light. The detector, which is often a photomultiplier tube, then collects the light from the emission monochromator at the very end and the data collected is then processed further.

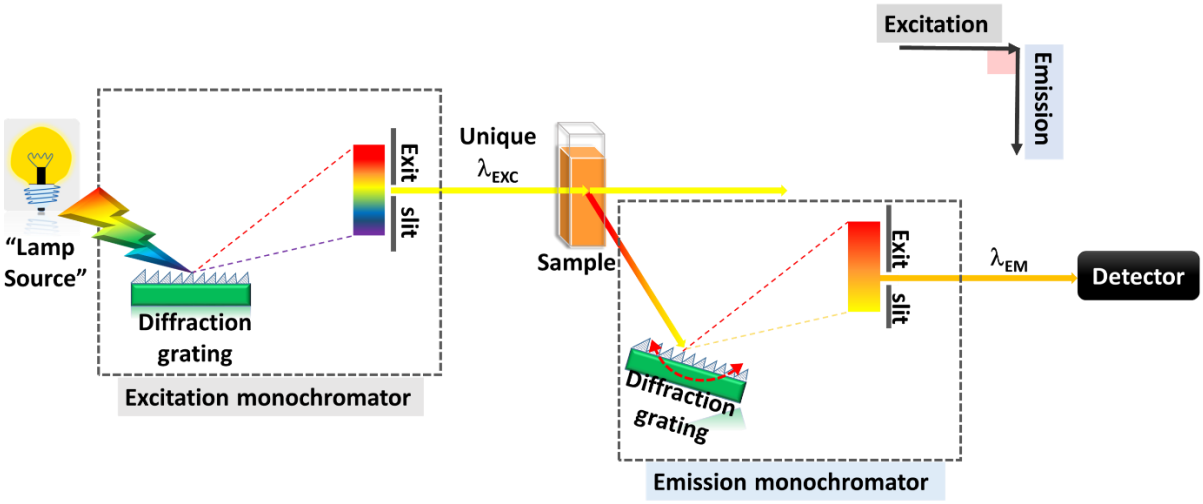

Figure 2.7 Basic configuration of a fluorometer.

The radiation emitted from the sample scatters in all directions. Therefore, unlike the steady state absorption instrument, in the PL spectroscopy setup, the detector is not positioned in line with the source to prevent the unnecessary incidence of the high intensity excitation wavelength on the detector. Furthermore, as the excitation wavelength and the emission wavelength may be fairly close to one another, there may be a chance of overlap between the two excitation and emission signals. The detector is therefore often positioned at a 90° angle to the incident beam in order to avoid this and to benefit from the fact that emission occurs in all directions.

We have deployed Edinburgh FS5 spectrofluorometer for the PL measurements undertaken in this thesis. It uses a 150 W CW Ozone-free xenon arc lamp as its light source. This fluorometer allows the samples to be stimulated at wavelengths ranging from 230 nm to 1000 nm, and the monitoring of resulting emission in a range between 200 nm and 870 nm. The emission detector is a Photomultiplier PMT-900 with a spectral range of 200 nm to 900 nm and is based on a single photon counting detection mechanism.

2.4 Time Correlated Single Photon Counting (TCSPC) / Time Resolved Photoluminescence (TRPL) studies

TRPL spectroscopy, also known as TCSPC, is essentially an extended form of PL spectroscopy. In fact, these time-dependent examinations allow us to further examine the dynamical trends of the emissive transitions for any particular material of interest, in contrast to steady state PL spectroscopy which only provides static insights into them. In this way by tracking down the PL decay dynamics, information on the radiative and non-

radiative recombination rates and thereby the lifetime of the emissive transitions may be gathered. Additionally, the recorded kinetics can also shed light on processes such as charge transfer, energy transfer, formation of traps in the system and the ensuing carrier trapping mechanisms.

The main objective of this thesis, as stated before, is to investigate the early time events, such as carrier relaxation and recombination, occurring subsequent to photoexcitation in different perovskite NC systems. Therefore transient absorption methods (described comprehensively in later sections) and TRPL studies are the two possibilities that spring to mind as the ideal tools for this goal. Speaking specifically of the radiative mode of recombination that leads to the PL process, we require a precise and accurate method to calculate PL lifetimes that typically range from a few picoseconds to a hundreds of nanoseconds or even more. These PL lifetimes cannot be measured using TA spectroscopy because covering this entire time range in such systems would require a long translation stage (10 - 15 m) which is impractical. Therefore, the only practically viable option is TRPL/TCSPC. This spectroscopic technique is based on an ingenious approach that utilises electronics and a tactical strategy to go above the inherent temporal resolution enforced by the electronics. [44–48]

Principle: The fundamentals of TCSPC lie in the detection of single photons emitted from a sample and the assessment of their arrival timings relative to a reference signal which is typically a pulsed source of light.[49,50]

In a typical TRPL experiment, the samples are excited using a high repetition rate pulsed laser source. In case if any single photon emission from the sample is detected, its arrival time is then correlated with the laser pulse. The electronics then gauge the interval between the excitation and emission events. TCSPC electronics can simply be considered analogous to a quick stopwatch having two inputs, one marked by the excitation event (START) and another by emission event (STOP). The START signal pulse twitches the clock, while the STOP signal pulse stops it. The successful completion of each such START-STOP signal sequence is manifested as an increment in the memory box of a histogram which has its x-axis defined by the different time durations it takes for the completion of the various START-STOP sequences. The pulsed laser has a repetition rate that is substantially higher than the rate at which photons are detected. However for various statistical reasons, it is vital to ensure that just one photon activity is recognised for each light flash. Any failure to implement this leads to multi-photon activities causing erroneous results, normally referred to as "pulse-pile up issue" in the literature which results in a certain instrument dead time.

A single excitation-emission cycle measurement, however, will not produce reliable data. As a result, million iterations of these START-STOP iterations are required. In this way, a histogram with respect to time, representing the temporal development of the PL intensity of the subject material is charted from these distinct sets of counts monitored for varying lengths of time.

Instrumental setup: Any typical TCSPC system is constituted by the following essential elements: a pulsed laser light source, a device to regulate the timing, single photon detector, and a monochromator **(Figure 2.8)**. For the choice of the desired emission wavelength at which the dynamics needs to be probed, the detector and monochromator are linked. [51,52]

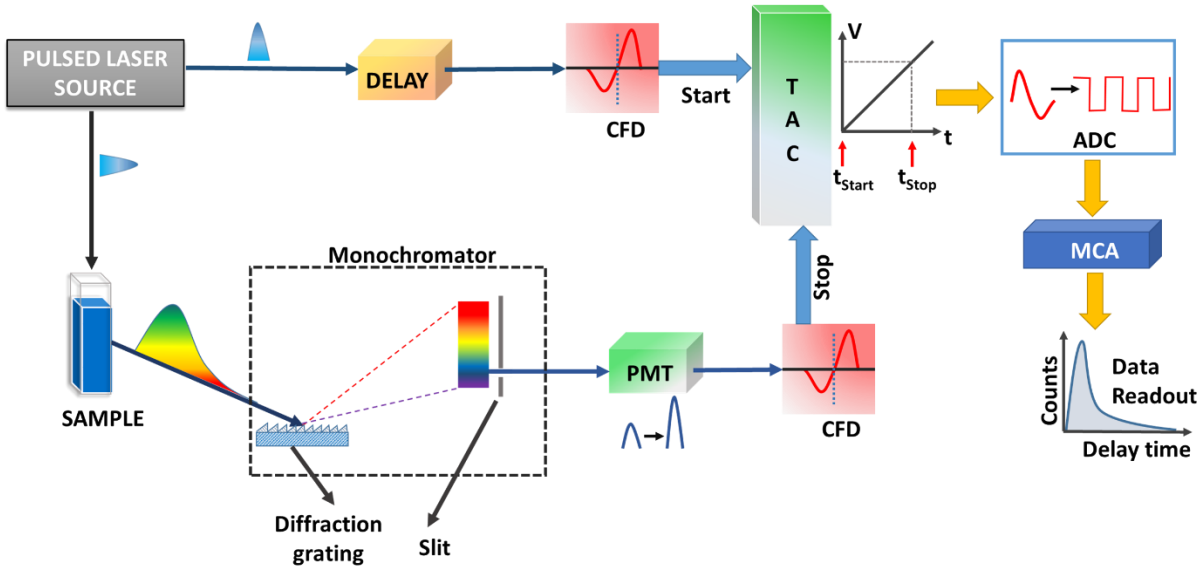

Figure 2.8 Fundamental architecture of a TCSPC system demonstrating its basic building blocks.

***Functioning of the timing device*:** The timing devices are further build-up from different components: Constant Fraction Discriminators (CFD), Time-to-Amplitude Converters (TAC), Analogue to Digital Converters (ADC), and Multi-Channel Analyser (MCA). Upon the detection of a single photon emission event, the TCSPC timing device goes through a series of events: the electronic signal generated in the detector unit is routed into the CFD, whose sole task is to commence a voltage ramp in the TAC module. The arrival of the START signal pulse commences the charging of the TAC's capacitor, which continues until the STOP signal pulse arrives at its input. The STOP signal comes from the laser source which acts as the synchronisation trigger. Once the signal has reached its maximum level, the capacitor is drained through the resistance, and the voltage across the resistance (ΔV) is then recorded. To put it

another way, the larger the charge accumulated on the capacitor suggests that longer is the charging period, which is a consequence of the larger gap between the detection of a single photon and the initial arrival of the trigger signal.

The voltage is then converted into time (t) via the ADC. This process is repeated several times and by keeping a record of how often a specific t happens, frequency vs. t is plotted. To categorize the values, the ADC delivers the data to memory. The MCA on the computer receives this digital signal and the count is then stored in an address dedicated to the frequency, which is subsequently displayed in the form of a histogram. This action is continued until one channel reaches a specific amount of counts, which is often 10,000. Since this strategy is quite statistical so in order to enhance accuracy, the preset stop count is chosen to be this high. The fundamental idea behind this method is that the excited state decay and fluorescence decay have shapes that are similar to the histogram.

TRPL measurements in this thesis were performed utilising a Deltaflex Modular Fluorescence Lifetime System (HORIBA Scientific) which is a turn-key spectrofluorometer with a typical 90° layout, designed to measure the excited state lifetimes, ranging from 1 ns to over 1 s. Depending upon the requirement, interchangeable nanoLED range sources can be employed,: pulsed LED sources are used to generate nanosecond pulses and pulsed laser diodes sources to generate picosecond pulses. The typical wavelengths which we have used for our studies are 280 nm and 402 nm. 280 nm excitation source is basically pulsed LED source and it has a pulse width (Instrument Response Function (IRF)) of < 1ns while the 402 nm wavelength source is pulsed laser diode and has a pulse width (IRF) of < 200 ps. It makes use of a Picosecond Photon Detection (PPD) module, which is a single, small device that houses all the required electronics, including a pre-amplifier, CFD, photomultiplier tube (PMT), and an appropriate power supply.

2.5 Transient absorption (TA) spectroscopy

Since its inception, this method has proved to be a precious asset for accessing the dynamic information concerning the temporal evolution of population through the electronic states that follows photoexcitation.[53] **Through the careful analysis of the spectral and kinetic traces, it presents an outline of the typical transient behaviour of the photogenerated species such as free charge carriers, bound species like excitons etc., charge transfer states and other qausi-particles like polarons, trions etc. to name a few. The average range of time scales which can be examined using this technique usually stretch from few nanoseconds to femtoseconds. Due to such high resolution, this**

technique covers specifics on the formation, decay, trapping- detrapping of these species as well as the various underlying relaxation or transfer processes or even the lattice vibrational dynamics etc. which usually occur on these fast time scales. As these inferences fairly align with the thesis's objectives, so we have used this technique comprehensively to unravel the complex photo-physical aspects of the systems under study.

In essence, TA spectroscopy is an upgraded form of absorption spectroscopy. Rather than measuring absorbance/transmission as in archetypal steady-state studies, the changes in these parameters are tracked here. Furthermore, this method does not require that the samples be necessarily fluorescent, unlike TCSPC, which also enables the investigation of the early time dynamics. TA spectroscopy not only allows the examination of even the non-luminescent samples but also in more precise and more advanced ultrafast time scales.[54]

Principle: In addition to the wavelength of the incident light, the population difference between the ground state and the excited state associated with the relevant transition also affects the absorption coefficient term in the Beer Lambert's equation. This population difference isn't a constant metric; instead, it changes over time based on the lifetime of the involved states. The transition coefficient is indeed an inversely proportional function of the spontaneous lifetime of the excited states.[55,56] But the lifetimes associated with these states are usually quite brief and in majority of the situations similar to those which prevail during steady state absorption spectroscopy, the incident light's strength is insufficient. Therefore, there is no appreciable depletion in the ground state population that can be detected by traditional steady state spectroscopic methods.

On the other hand, TA spectroscopy uses intense and temporally confined femtosecond laser pulses, making it possible to track even minute and extremely rapid changes in the ground state population.[57] Basically, an experimental setup needs a certain time resolution to follow ultrafast occurrences. For the equipment to be effective, a component must change more quickly (or at least as quickly) than the process being studied.[58,59] This resolution in TA spectroscopy comes from the use of femtosecond lasers. Despite the fact that there are numerous techniques to do transient absorption spectroscopy using ultrafast lasers, they are all essentially versions of the pump-probe technique. Two ultrashort laser beams are required for functioning in the most simple variant; the one with higher power "pump", initially perturbs the sample alters the otherwise prevalent population difference, diminishes the absorption coefficient of the related transition and leaves it in a non-equilibrium state by exciting a major

portion of the population to a higher energy level. To reveal these pump induced changes in the optical absorption, then a low-intensity "probe" laser delayed with respect to the pump pulse by time "Δt" is delivered through the sample using the delay line stage.[60–62] The simplified pictorial representation of the pump-probe technique is provided in **Figure 2.9**. The change in absorption is analysed based on the difference between the probe light's absorption in the absence of the pump and in its presence ⇒ ΔA (probe) $=\Delta A_{PUMP\ ON} - \Delta A_{PUMP\ OFF}$.[63–65]

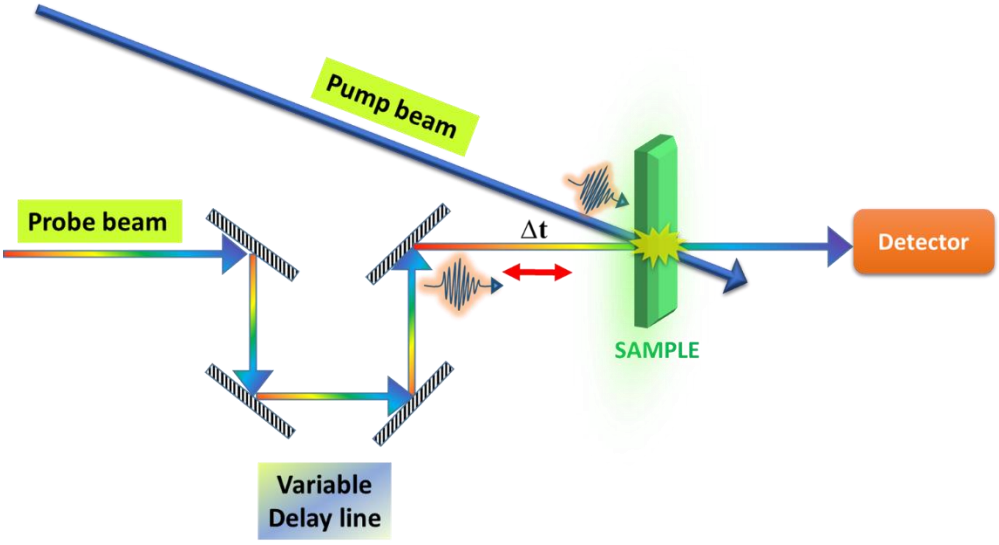

Figure 2.9 Schematic depicting the fundamental strategy of a pump-probe experimental setup. The pump beam excites the sample, and any pump induced changes in sample absorption are subsequently examined by the probe beam, which is incident on the sample at an adjustable delay relative to the pump beam (Δt).

This condition is achieved by chopping the pump pulse at a certain frequency. The entire procedure is then repeated numerous times with a series of different pump and probe pulse delay times (Δt) by using the optical delay line. In most cases both these pulsed beams have their origin from a common source of generation for instance, a mode locked laser and a beam splitter which separates the primary laser's output into two beams with different powers. Through the use of pump probe TA spectroscopy, we may infer the spontaneous lifetime of the electronic levels as well as other transient effects, enabling us to construct a picture of the dynamics of the electronic levels. Rather than focusing on one transition alone, we need to observe the effect of photoexcitation over the entire spectrum. It is impractical to accomplish this goal using monochromatic probes. Nevetherless, supercontinuum generation of white light probe which can be obtained following the nonlinear optics approach, helps in getting around this restriction.

The origin of femtosecond lasers which form the backbone of this TA spectroscopy technique may be traced back to early 1980s'.[66–68] The primary element that constitute these laser systems are femtosecond oscillators, which are the generation source of modest energy (nJ) and high repetition rate pulses (seed pulses) (often MHz to tens of GHz), with their output wavelengths centred mostly at the red and infrared region of the EM spectrum. With the aid of suitable amplification systems, these moderate energy pulses are then further amplified, their repetition rates are decreased, and by deploying non-linear phenomenon, a variety of desired wavelengths can be generated.[57,69,70]

2.5.1 Generation of ultrashort pulses

To produce any pulsed light beam with ultrashort widths, one can essentially use two primary methods: 1) Q-switching, which produces high energy pulses with pulsewidths of a few nanoseconds,[71] and 2) Mode -locking, which also produces high energy pulses but with pulsewidths that are relatively shorter in their spans—in the femtosecond range.[72]

2.5.1.1 Q-Switching

A well-known method for producing highly intense laser pulses (often referred to as "giant pulses") with a typical duration of a few nanoseconds is Q-switching or variable attenuation. To achieve this, the incident light beam is subjected to varying losses as it passes through the laser cavity. This method's name infact derives from the variable quality factors (Q-factor) of the laser cavity that result from differences in the losses it encounters. Simply described, a laser cavity consists of an active gain medium that undergoes population inversion, the mechanism that causes lasing, and is surrounded on both sides by cavity mirrors (one of them is totally reflecting and the other is semi-transparent-output coupler).[73] It can be considered analogous to an amplifier with positive feedback, with either a part or whole of its output returned and fed as the input again. However, when there are cavity losses prevalent in the resonator cavity, the light beam that has passed through the gain medium does not return, and there is no progressive feedback which is crucial for lasing to take place. Such a situation enables the development of a very large inverted population in the gain medium provided that the pumping rate is high enough, exciting a huge number of the ground state atoms to the metastable excited states. The next time the cavity losses are turned off *i.e.* when the gain medium is saturated with ample energy and the light beam after propagating through the gain medium is made to reflect back from the end mirror and is fed back, the Q-factor of the cavity increases and lasing sets in and the intracavity light is permitted to outflow.[74,75] Following the fact that the build-up

of population inversion in the active gain medium when the cavity losses are turned on is so powerful, the output laser radiation is enormously high and its growth is extremely instantaneous. Such high intensity of the pulses is the reason behind the label "giant pulse". Similarly, the decay of these pulses is also rapid since the built-up inversion falloffs rapidly while generating extremely powerful radiation.

Techniques for achieving Q-switching

There are several approaches employable for Q-switching. They can be divided into two major categories based on whether or not an external control is required: active Q-switching and passive Q-switching.[76]

The most commonly used passive variable cavity loss components employed in the laser cavities are saturable absorbers. In essence, saturable absorbers are those optical constituents that, depending on the strength of the incident light beams, offer a range of absorption losses. When the intensity of the incident light is very high, the loss of the saturable absorber is minimised, making it transparent to the incident light and vice versa.[77]

For active Q-switching, electro-optic and acousto-optic modulators are the most commonly employed components. Even between them, the more popular and the fastest switching ones are the electro-optic Pockels cell modulators. Pockels cells are basically electro-optic crystals that rely on Pockels effect for their operation and show linear variations in their refractive index when subjected to external voltage or electric field (~ 4 kV- 6kV voltage).[78] The materials which are usually employed for their construction are Potassium dihydrogen Phosphate (KDP) and lithium niobate ($LiNbO_3$). Such crystals are normally isotropic in the absence of any external voltage and the linearly polarised light entering into the crystal propagates without changing its state of polarisation. However under the application of voltage, there is birefringence induced in the optical medium along the crystal's optical axis and the light leaving the crystal during this duration has its polarisation state altered **(Figure 2.10)**. Furthermore, as the operation of these modulators strongly rely on the rotation of the polarisation of the incident light, so for application as Q-switches it is crucial to ensure that the laser operates only for one particular polarisation. For this purpose, the Pockels cell are either employed in conjunction with a linear polarising element placed separately in the cavity or the gain medium is provided with Brewster angles. When there is an externally applied voltage across the Pockels cell, the cell rotates the polarisation of the incident light by 45°. Following its reflection from the high reflectivity mirror, this linearly polarised light travels in the opposite direction and undergoes a second 45° polarisation rotation as it returns through the cell. Since

now the light output has its polarisation rotated by 90° *i.e.* crossed w.r.t. the polariser axis, the polariser blocks it and thus there is high cavity loss. However, when there is no applied voltage, there is no such rotation of the polarisation therefore the polariser allows the passage of the light beam towards the gain medium resulting in lasing of giant pulses.

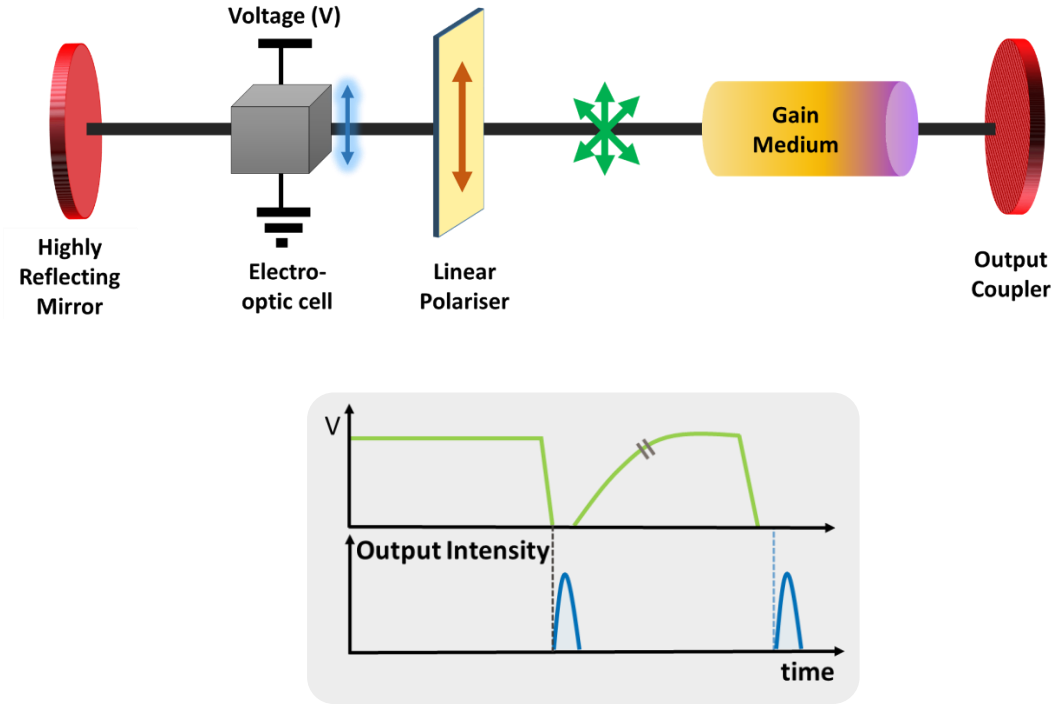

i) **Voltage ON :** Each time the beam travels through the electro-optic cell, its polarisation state is rotated by 45°.Therefore there is a total rotation by 90 degrees in one round trip.This results in crossing of the beam's polarisation with respect to the linear polarizer, forcing it to reflect from the cavity and causing significant cavity loss.

ii) **Voltage OFF :** The cell doesn't induce any change in the polarisation state of the incident beam, so it passes as it is, experiencing no cavity loss.

Figure 2.10 Schematic in the upper panel illustrates the Q switching technique employing an electro-optic modulator (Pockels cell or Kerr cell). The figure in the lower panel depicts the formation of the giant pulses as a result of Q-switching.

To distinguish this technique from the likewise used approach which in addition to this configuration employs a quarter waveplate ("ON-Q switching"), this technique is termed as "OFF- Q switching". There is also i.e. "ON Q-switching" where when there is no voltage applied across the Pockels cell, there is no lasing and vice versa. Thus, Pockels cell are nothing but voltage-controlled waveplates. In this manner, a fast shutter with the ability to "open" and "close" in nanoseconds can be made by using a Pockels cell in conjunction with a polarizer to switch between no optical rotation and 90° rotation. Kerr cell is another electro-optic modulator

which can be used instead of Pockels cell however owing to the requirement of higher voltage for obtaining desirable results, Pockels cell is more preferred. The arrangement of an electro-optic modulator inside the resonant cavity and the formation of the giant pulses is shown in **Figure 2.10**.

2.5.1.2 Mode-locking

Q-switching although provides us with intense and short pulse, however, the technique is limited to the nanoseconds regime only. For the situations where even more narrow pulses are demanded (femtoseconds), mode-locking comes to rescue. The fundamental ideology behind the implementation of this method is to impose a stable phase relationship between the longitudinal modes of the laser's resonant cavity. A laser cavity as already mentioned is nothing but a gaining medium enclosed inside two mirrors.[79] Light being a wave, when it hits the cavity mirrors, it bounces back, interferes with itself both constructively and destructively. This results in the generation of standing waves, also referred to as longitudinal modes.

No laser is ideal enough to produce monochromatic wavelengths, rather they are a source of a range wavelengths/modes or a finite bandwidth.[80] Typically, there is no fixed relationship between any of these modes; instead, each mode oscillates independently of the others. This can be paralleled to an ensemble of separate, independently emitting lasers, each of which has a slightly different light frequency. In case when the modes supported by the laser cavity with distinct frequencies and random phases are added up, the outcome is randomly distributed electric field and intensity in the time domain or is a beating pattern. However on the other hand, when the modes are all added together in phase, or when they have the same phase at the same spatial position, they interfere constructively at periodic intervals resulting in an intense recurring pulsed output rather than a random or averaged output **(Figure 2.11 A, B, C)**. The obtained output in such case is called "Phase-locked" or "mode-locked".[81]

The separation between the two consecutive pulses "Δt_{sep}" and the pulse width "Δt_p" are the two main parameters that characterise a mode-locked pulse.

$$\Delta t_{sep} = \frac{2\eta d}{c} \qquad \textbf{Eq.2.7}$$

$$\Delta t_p = \frac{1}{\Delta \nu N} = \frac{1}{\text{Gain bandwidth}} \qquad \textbf{Eq.2.8}$$

Here d is the intracavity distance, η is the refractive index of the gain medium constituting the laser cavity, c is the speed of light, Δν is the separation between two closely emitted frequencies.

These equations imply that the duration of any mode-locked pulse depends directly on the number of modes supported by the laser cavity. Also, greater the bandwidth of a laser gain

medium *i.e.* more the number of modes that add up together, shorter is the width of the obtained mode-locked pulse **(Figure 2.11 D)**.

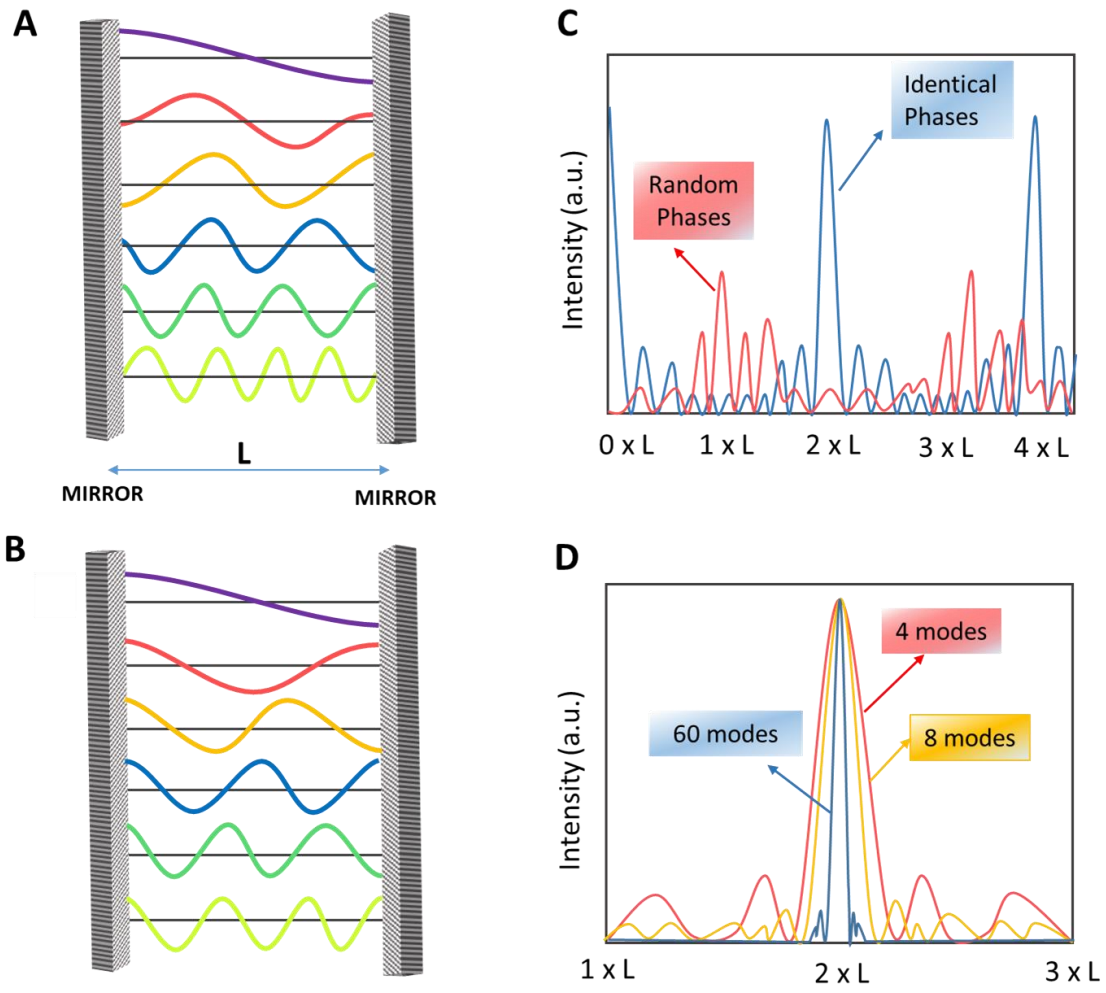

Figure 2.11 (**A)** Random modes in a laser cavity (**B)** Modes sharing identical phases, (**C)** The resulting electric field intensity obtained from the superposition of randomly phased modes (Figure A) (some curves are ascending and others are descending near the cavity's entry) and the six phase aligned modes depicted in Figure (**B, D).** Pulses resulting from the superposition of 4, 8 and 60 modes depicting that the pulse width goes down as the number of modes involved are increased.

The pulse's shape, however, is another element that affects the duration of the pulse. By taking into account this shape factor, the minimum pulse width for lasers producing Gaussian-shaped pulses is given as

$$\Delta t_p = \frac{0.441}{\text{Gain bandwidth}} \qquad \textbf{Eq.2.9}$$

Techniques for achieving Mode-locking

Similar to Q-switching, there are two categories of mode locking techniques for lasers: active and passive.[82,83] Utilizing an external signal to cause an intracavity light modulation is typical

of active methods. Passive techniques rely on simply placing something into the laser cavity that causes the light to self-modulate rather than using an external signal. The gist is that when the laser operates in random mode phases regime, a component that dampens the lasing action (raises cavity losses) must be added to the laser cavity, much like a Q-switched laser.

On the other hand, when the phases of various modes (fortuitously) sync, this component ought to promote lasing. The most common and straightforward mode-locking technique among all is Kerr lens mode-locking (KLM) that makes use of an electro-optic modulator in the cavity.

❒ **Kerr lens mode-locking:** This mode-locking technique utilises the non-linear optical Kerr effect. In optics, Kerr effect also known as the quadratic electro-optic (QEO) effect, describes a refractive index change induced in a medium in the presence of a modulating electric field provided by the light beam itself. In contrast to the Pockels effect which varies linearly with the electric field, the refractive index change induced in the Kerr effect is directly proportional to the square of the electric field, in other words linearly proportional to incident intensity I.[84–86] The intensity dependency of the refractive index "n" can be expressed as

$$n = n_0 + n_2 I \qquad \textbf{Eq.2.10}$$

Here, n_0 is the linear refractive index and n_2 is the second order non-linear refractive index. Since the order of magnitude of n_2 is generally very small, therefore for causing any significant modulations in "n", high light beam intensities are essential.

The light beam deployed in any laser system is Gaussian shaped in the direction normal to the direction of propagation implying that the intensity of the beam is more at the center and it decays gradually towards the edges. As a consequence, when such a beam passes through a medium capable of exhibiting Kerr effect, the refractive index becomes higher at the center than at the edges. The medium thus illustrates a profile analogous to a focusing optics, enabling it to function as a self-focusing lens **(Figure 2.12 A)**. Since, the pre-requisite for Kerr effect to take place is that the incident intensity should be immensely high, it is much more efficient when the light is pulsed rather than being spread over time. To put it another way, even with the same amount of light incident, self-focusing will be stronger when the modes are aligned in phase, or mode-locked, than when there is no such phase aligning, or when output is analogous to that from a CW laser. Now if an aperture is inserted in the path of the beam, only

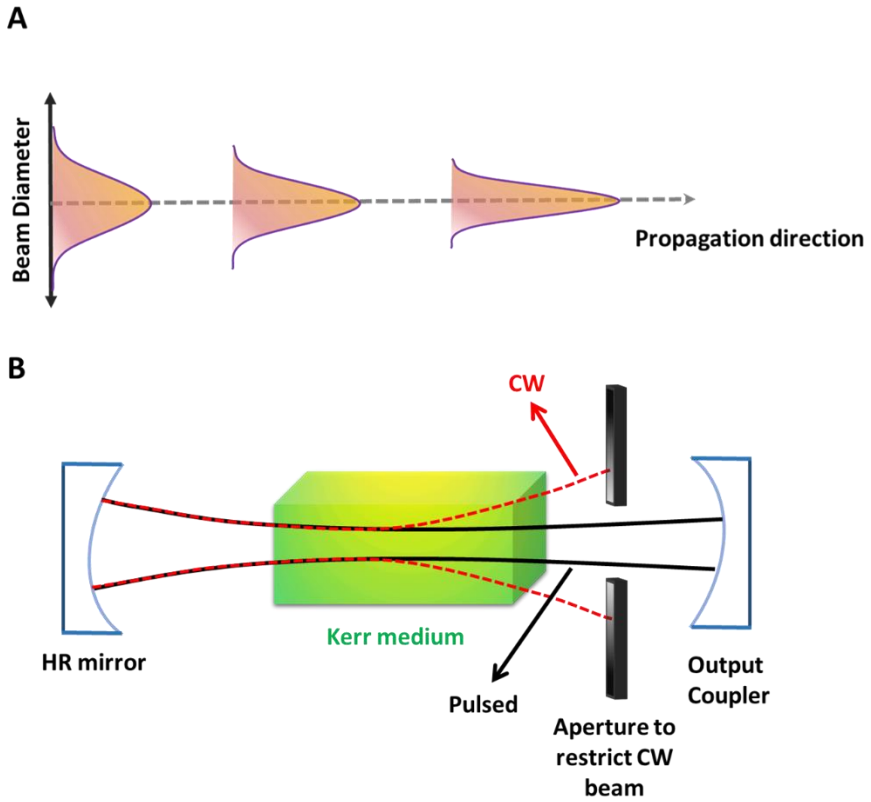

Figure 2.12 (A) Kerr effect induced self-focusing of a Gaussian beam, **(B)** Mode-locking in a cavity employing Kerr medium functioning as a focusing lens: in the continuous wave (CW) mode of operation or when the modes are not aligned in phase, self-focusing is not practical, as a result such light beams are rejected by the aperture. Such beams thus experience high cavity losses and do not participate in lasing. On the other hand, mode-locked pulses experience self-focusing due to Kerr effect and thus can pass through the spatial aperture for amplification.

the focused beam will be able to make way through it and travel into the cavity for amplification**(Figure 2.12 B)**.[85,86] The light beam obtained from the interference of the randomly phased modes due to the incapability to undergo self-focusing will however be rejected by the aperture, resulting in cavity losses. This strategy thus allows a natural selection of only phase locked modes.

2.5.2 Construction of a femtosecond laser

It might appear that the pulsed outputs from the aforementioned techniques would be adequate for studying the time-dependent processes caused by light. However, because these strategies deliver extremely high repetition rates, small bandwidths, and low pulse energies, it is impractical to use them directly for drawing spectroscopic conclusions. Following the results of these techniques, non-linear effect-based strategies can be used to address all of these

shortcomings. In light of this, any typical femtosecond laser system assembly is constructed from three crucial fragments that are chiefly based on these two above-mentioned approaches of attaining ultrashort pulse durations and the strategic use of non-linear phenomena.

- *seed laser*
- *pump laser*
- *a Chirped Pulse amplifier*

In the present thesis, the femtosecond laser system which we have employed is the "Astrella Ultrafast Laser system"- which is an integrated assembly of femtosecond oscillator and regenerative amplifier from Coherent Inc. This system operates by employing both Mode-locking and Q-switching techniques in conjunction. The details of each module of the laser system, as well as their underlying principles, are addressed here.

2.5.2.1 *SEED laser or also known as "FEMTOSECOND OSCILLATOR"*

As the name implies, the goal of the seed laser is simply to generate seed pulses, which after being subjected to the necessary modifications are obtained at the main laser system's output. These pulses suffer from various shortfalls that prevent their direct employment in the spectroscopic techniques, so to render them suitable they are modulated in line with the requirements. The Astrella system uses Vitara-T of the Coherent Vitara^{TM} family as the seed laser. This unit primarily consists of a CW diode laser (optically pumped semiconductor laser (OPSL) technology based-Verdi-G series, operating at 5W) pumping a Titanium-Sapphire (Ti^{3+} ions doped Al_2O_3) oscillator cavity. The usual output of this Verdi-G series laser is though in the NIR region centered at 1064 nm however, by enabling the process of intracavity second harmonic generation (SHG), it is made to deliver frequency doubled 532 nm visible light output. This intracavity frequency doubling is achieved using Lithium Triborate crystal (LBO) which is maintained at 323°F. Such a conversion is necessary because Ti^{3+}-Sapphire oscillator cavity can only be pumped with wavelengths lying in this domain (514 nm- 532 nm). The output of this unit are ultrafast pulses that are mode-locked (per pulse energy~ nJ, mode-locked pulse power~ 500 mW) with a tunable wavelength range 750-860 nm (maximum gain at 800 nm), a bandwidth ranging from 30 nm to 125 nm, uncompressed pulse width < 20 fs and a horizontal polarisation. The repetition rate of the obtained mode-locked pulses is 80MHz, which implies a time difference of 12.5 ns between the successive pulses. Ti^{3+}-Sapphire is specifically chosen as the gain medium for two main reasons: i) It is highly compelling due to its large bandwidth (wider than any other rare-earth doped gain media), which guarantees the generation of extremely brief pulses; ii) This medium inherently exhibits the Kerr effect,

therefore mode-locking doesn't require an additional intracavity component.[87] This output is then directed to the regenerative amplifier for the pulse narrowing and amplification. All of these seed laser's tasks are handled by the Vitara controller, which employs some critical electronics that serve as diagnostic accessories for the seed laser and aid in mode-locking initialization.

2.5.2.2 *PUMP laser*

The role of the pump laser is basically to help achieve the population inversion by pumping more and more number of atoms lying in the ground state of the gain medium to reach the excited states. The Astrella assembly houses "Revolution laser" from Coherent Inc. to serve as the pump laser. The Revolution module further consists of a diode pumped Q-switched laser (Neodymium doped Yttrium Lithium Fluoride, Nd: YLF) together with a second harmonic generator. The output of this unit is 527 nm and the obtained pulses have a repetition rate of 1kHz. The typical power delivered per pulse by this module is ~ 40mJ/pulse with a pulsewidth of < 150 ns. Thus, the Revolution pump laser provides the appropriate pulse energy to overcome the lasing threshold for the Ti^{3+}: Sapphire cavity serving as the gain medium in the regenerative amplifier assembly (discussed in the next section). Another reason for selecting Revolution as the pump laser is that its output wavelength is also the most appropriate, given that Ti^{3+}: Sapphire cavities are known to perform best at these wavelengths.

2.5.2.3 *CHIRPED PULSE AMPLIFIER- Regenerative amplifier (REGN) & A stretcher/compressor module*

The pulsed output from the seed laser is quite low in energy. The main function of this unit is thus to amplify this low power mode-locked output it receives from the seed laser (nJ → mJ per pulse) and also bring down their repetition rate (MHz to kHz). Although these pulses have a low per pulse power, the peak power they carry because of their strong temporal confinement is sufficient to damage the optical components mounted in the amplifier cavity. As a result, the pulses are stretched out in time using the stretcher module, which aids in a concurrent decrease in peak power before being transmitted to the specific amplifier assembly.[88] This module functions on the technique of Chirped Pulse Amplification (CPA) **(Figure 2.13)**. The sequence of events that take place in this unit can be summarised in the following steps:

- ✓ In the first stage, the mode-locked pulses (width~ few fs) from the femtosecond oscillator/seed laser (VITARA) are extended in time by deploying the *stretcher unit*, increasing their pulse lengths from a few fs to hundreds of picoseconds.

- ✓ Then for every 8000 pulses delivered by the oscillator, only one pulse is picked up by the *pulse picker*.
- ✓ The pulse is then injected into the gain medium where it is amplified (REGN).
- ✓ The amplified pulse is then finally compressed back in time to few femtoseconds by passing through the *compressor unit* and is coupled to the output window.

As indicated by the involvement of multiple steps, apart from the gain medium, which is the core of the Chirped Pulsed amplifier assembly, there are also the following additional units encased in this assembly that make use of various non-linear optical phenomena.

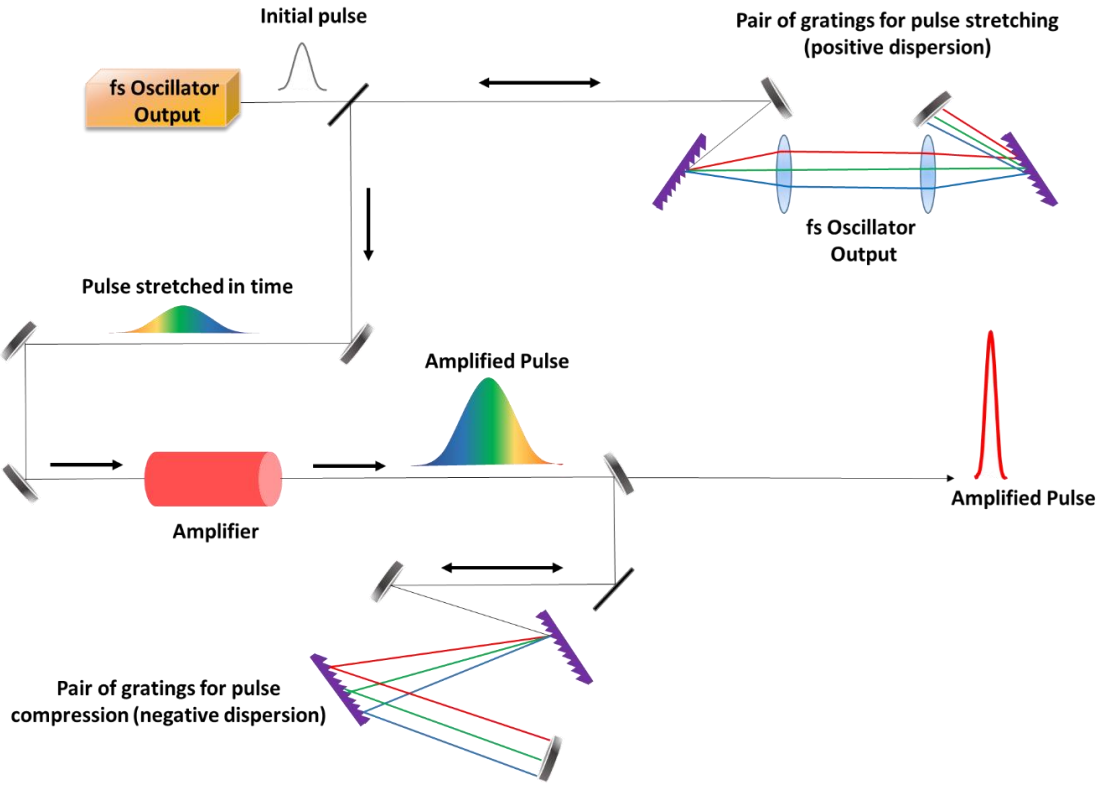

Figure 2.13 Layout of the Chirped Pulse Amplifier unit.

A. Stretcher unit: Before making their way into the amplifier gain medium, the output pulses from the seed laser are chirped and temporally stretched to longer durations by using powerful dispersive components referred to as pulse stretchers, which are most frequently a diffraction grating pair or even a long fibre.[89] These units basically harness the principle of Group Velocity Dispersion (GVD).

GVD: The various spectral components that make up a pulsed beam of light do not propagate at the same pace when made to travel through the optical components. As a result they incur different temporal delays depending on their wavelengths and ultimately segregate out. This temporal rearrangement, sometimes referred to as a "chirp," causes an extension in the pulse duration and this entire phenomenon is called GVD. By strategical alignment of the dispersive elements such as a diffraction grating pair alongwith the other optical elements, two types of GVD processes—positive and negative can be obtained.[57,90,91] While positive GVD ascertains that the bluer frequencies i.e. the small wavelengths have to travel longer distances than the red frequencies or the longer wavelengths (because small wavelengths travel faster), the negative GVD follows the contrary.

To be more precise, the stretcher unit's operation is predicated on the positive GVD which extends the femtosecond width seed pulses to picosecond domain. It is possible to achieve considerable stretching using a variety of methods, including pairs of diffraction gratings, volume Bragg gratings, and fibre Bragg gratings, etc.

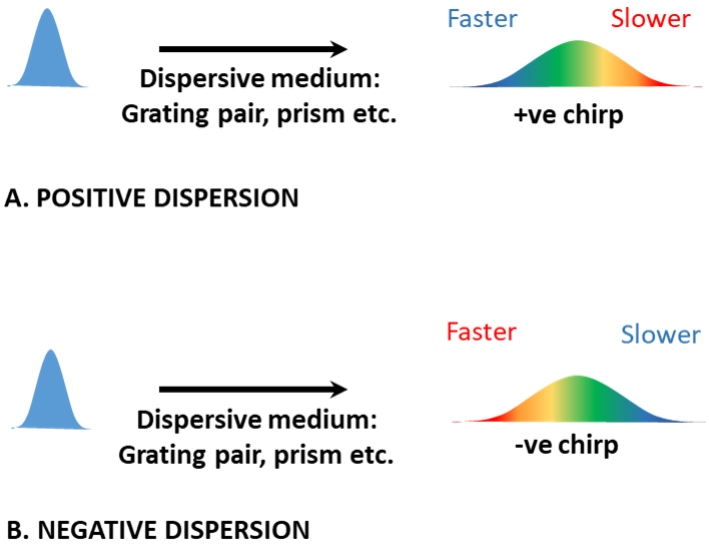

Figure 2.14 The two different forms of dispersions that incident light encounters when it travels through an optical medium are shown schematically.

B. Pulse picker: In order to ensure desired amplification and repetition rate of the output pulse train, it is necessary to have a proper timing in between the arrival of the 80 MHz mode-locked seed pulses and the Q-switched pump pulse train (1kHz). Only the usage of rapid response electronics can contribute to achieving this goal. This function is carried out by the Synchronization and Delay Generator (SDG) Elite in the Astrella system, which controls the switching of the Pockels cell at the appropriate moment. Its operation must be extremely precise or it may produce multiple undesirable output pulses. There are two Pockels cells

devoted for this function (Pockels cell 1 (PC1), Pockels cell 2(PC2)).The PC1 admits the pulse into the resonator cavity. To assure that only one pulse is allowed to enter into the cavity, the Pockels cells should every time be switched at the same time as the seed pulses. This is done by triggering the PC1 by the radio frequency provided by the mode-locker of the seed laser. PC2 then decides the ejection of the pulse out of the resonator cavity after being amplified by the desire amount. This is guaranteed by adding a delay of roughly 200 ns w.r.t the switching of PC1. The triggers to these Pockels cells are provided by the delay adjustments on the timing electronics. Pockels cell are employed in conjunction with thin film polariser (THP) for the desired injection and ejection of the incident pulses.

C. Regenerative Amplifier/Gain medium: The pulses selected by the pulse picker are then injected into the Ti^{3+}: Sapphire cavity which serves as the gain medium for the Regenerative Amplifier and amplifies the injected pulse by many orders (amplification factor > 10^6) by making several round trips in the laser cavity.[74,92,93] The population inversion which is necessary for the lasing of this medium is built by the intense pump pulses obtained from Revolution. Since the amplification obtained in a single pass through the laser medium is quite incredibly small, multiple passes are assured.

Operation of the Pockels cell

Prior to understanding the pulse selecting procedure, it is crucial to be aware of the following functions:

Signification of incidence at Brewster's angle:- If a light pulse with horizontal polarisation is incident at any medium at Brewster's angle, it will be reflected by its surface. In case, the incident pulse has vertical polarisation, it will be propagated into the medium;

Quarter-wave plate (λ/4):- it transforms a linearly polarised light to circularly polarised (CP) light.[91] To begin with, the horizontally polarised seed pulse coming from the stretcher unit is incident on the gain medium at Brewster's angle. As a result, it propagates in the direction of the PC1 rather than into the active medium. **Figure 2.15** provides the optical arrangement of the REGN that demonstrates the incident pulse's propagation to comprehend the function of the pulse picker. Due to the PC1 being off at the moment, the light pulse passes through it without any change in its polarisation state. However, because of the λ/4 plate, which it must pass through twice (once directly and once after reflection from mirror M1), its polarisation is turned by 90 degrees. Now that the pulse's polarisation state is vertical, it moves through the gain medium and experiences an energy amplification. If PC2 is likewise off at that time, the pulse exiting the amplifier will immediately travel through the THP, strike the mirror, and

reflect back to the observer. Since it is still vertically polarised, the pulse transmits through the gain medium once more and amplifies. Further there can be two possibilities: i) If PC1 is still OFF, the beam undergoes one more 90° rotation of polarisation and becomes horizontally polarised. In that case pulse is then reflected from the point A and rejected. ii) However if PC1 is now turned ON and the voltage applied is such that it functions as a λ/4 plate, there is in total 4 x λ/4 change in polarisation (2 times λ/4 change coming from the λ/4 plate and 2 times from PC1 functioning as λ/4 plate) which actually implies that the polarisation state of the pulse is unaffected. The polarisation is still vertical so the beam can again undergo amplification. When there is sufficient amplification achieved, the appropriate voltage is applied across PC2 to function as a λ/4. So the beam while passing through it twice (once direct and once after reflection from M2) has its polarisation changed by 90°, *i.e.* it becomes horizontally polarised and is thus reflected from the surface of the gain medium into the compressor unit.

D. Compressor unit: The amplified pulses that are obtained at the output of the REGN have widths that are spread out over a picosecond time period.[94] They are therefore temporally compressed to a duration similar to the input pulse width by passing through the compressor unit. This unit removes the chirp and limit their widths to femtosecond scale. For this reason, reverse effect as to what governs the stretcher unit is demanded in the compressor unit. In this opposing dispersion element, the lower wavelengths are forced to travel shorter routes than the higher wavelengths (negative GVD) in order to compensate for the positive GVD that the pulses went through before the gain stage.

The resultant pulse train which is obtained at the disposal of the pulse compressor is the final output which is utilised further for spectroscopy. The obtained output has the following optical parameters: central wavelength of 800 nm (range: 780 nm-820 nm), repetition rate of 1 kHz, pulse width ~ 35 fs and 5mJ energy/pulse.

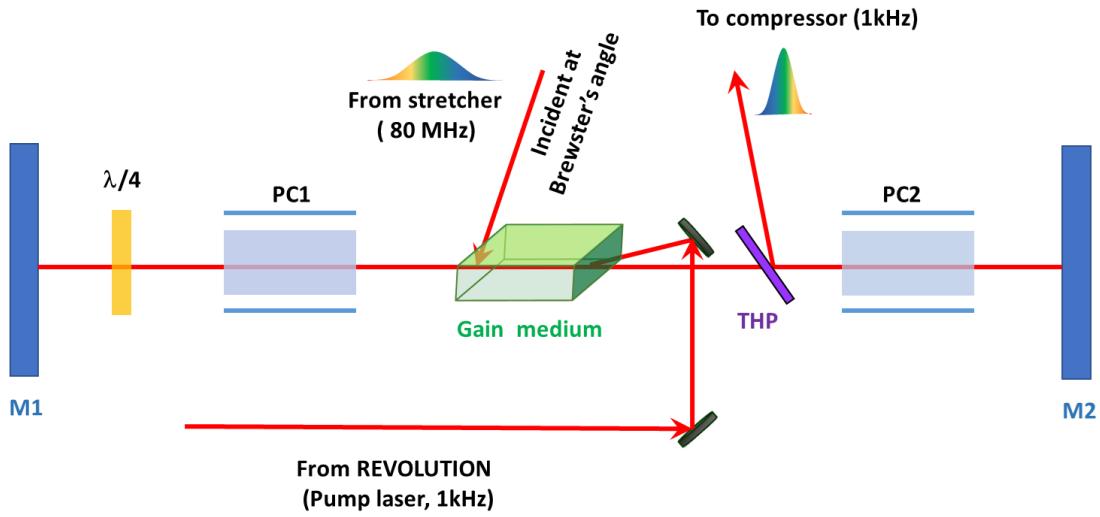

Figure 2.15 Schematic illustrating the components constituting the REGEN unit (Pulse Picker assembly and gain medium).

In TA spectroscopy, as already mentioned two different intensity beams ("pump" and "probe") are required, so the output is split into two divisions accordingly using the beam splitter. While the pump beam needs to be monochromatic, the probe beam is a white light continuum.

2.5.2.4 Tuning the wavelength- non-linear effects- generation of the "pump" beam

A. Harmonic generation

The output light beam delivered by the Astrella laser system is typically centred at 800 nm. However, in order to study the distinct systems which absorb light outside this range, we need to have access to wide range of wavelengths. Such tuning of wavelength can be achieved by exploiting the non-linear effects.[95–97] The easiest way to accomplish this is exploiting the phenomenon of harmonic generation. For any material, the relation between its polarisation (P) and the applied electric field strength E can be expressed in terms of a power series:

$$P = \varepsilon_0 (\chi^{(1)}E + \chi^{(2)}E^2 + \chi^{(3)}E^3 + \cdots) \qquad \textbf{Eq.2.11}$$

Here, $\chi^{(n)}$ stands for the nth order dielectric susceptibility of the material and ε_0 is the permittivity of vacuum. Furthermore, since light is an EM wave, so its electric field can be expressed as:

$$E = E_0 e^{i(kz-\omega t)} \qquad \textbf{Eq.2.12}$$

In the generally encountered cases, since the employed electric fields are quite weak, so only the first term in **Eq.2.11** is the significant one. Substituting the expression for E **(Eq.2.12)** into **Eq.2.11** indicates that in such cases, the material is capable of producing only a single frequency 'ω'. However, when the materials are subjected to immensely high electric field strengths, the second term in the **Eq.2.11** ($P \propto e^{2i\,(kz-\,\omega t)}$) also becomes relevant, implying that the material gives a substantial output at 2ω frequency. In this manner, by employing higher electric fields, further higher harmonics of the incident light frequency can be generated. These harmonics while propagating through a medium can interact among themselves or with the fundamental, resulting in either sum of the incoming frequencies (Sum Frequency Generation- SFG) or their difference (Difference Frequency Generation- DFG) **(Figure 2.16)**.

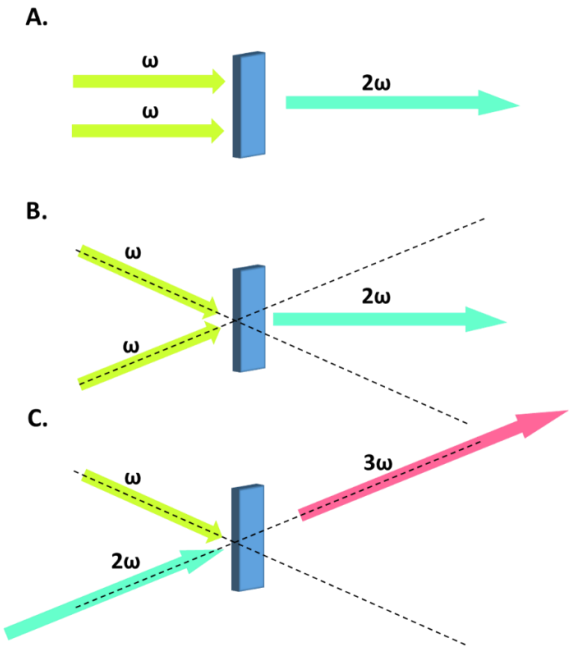

Figure 2.16 Photon picture showing the harmonic generation while taking into account the conservation of energy and momentum throughout the generation process. Such processes can take place both collinearly and non- collinearly provided both the energy and momentum are conserved. **(A)** The process of SHG when the incoming waves are incident collinearly on the crystal. **(B)** The non-linear method of SHG where the incoming waves enter at an angle to one another and the second harmonic that results is oriented halfway between the directions of the incident waves. **(C)** Sum frequency method for harmonic generation, mixing an incoming fundamental with its second harmonic. The vector sum of these incident frequencies determines the direction of the sum frequency generated signal (For explanation sake, a fundamental and a second harmonic has been presented here as the incident waves, however these incoming waves can be any order harmonics of the fundamental).

In addition to the constraints set by conservation of energy and momentum, the generation of the harmonics demands one more necessary prerequisite- fulfilment of the phase matching condition. This implies that the beam incident on the medium and the one generated should travel with the same phase velocity within the medium. In other words, the refractive index for both should be equal.

For crystals exhibiting inversion symmetry, $\chi^{(2)}$ is zero. Therefore, isotropic materials can straightaway be ruled out from being the candidates for SHG, but they can still produce higher order harmonics. β- Barium Borate (BBO) which is an anisotropic crystal is the most commonly employed medium for harmonic generation owing its two attributes- high damage threshold and extraordinarily high $\chi^{(2)}$ thus facilitating easy and efficient harmonic generation.[98,99]

B. Sum Frequency, Difference Frequency and Optical Parametric Generation

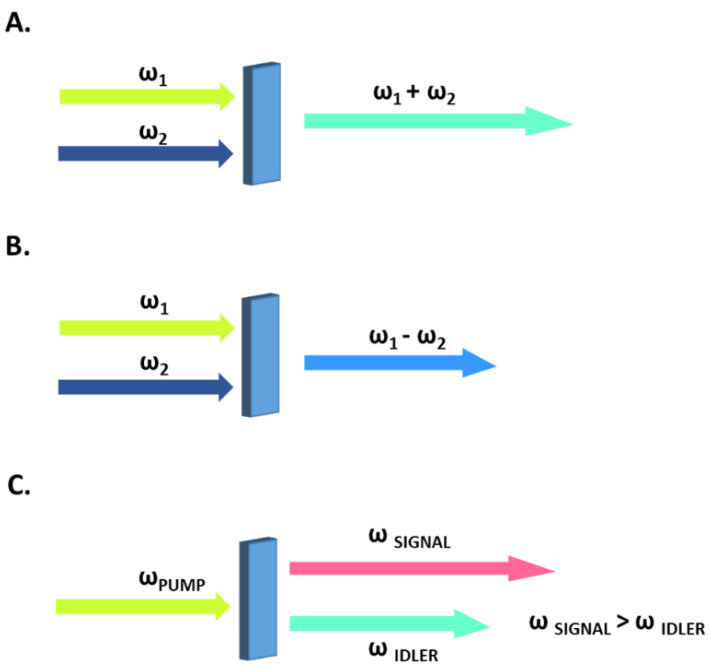

Figure 2.17 (A) The generalised process of Sum Frequency Generation where two incoming frequencies upon being incident on a NLC yield a resultant photon whose frequency is the sum of the incident photon frequencies. **(B)** Photon picture of the Difference Frequency Generation process where the output frequency at the disposal of the NLC is the difference of the incident frequencies. **(C)** depicts the process of optical parametric generation where the NLC divides a "Pump" photon into two distinct frequency photons, the one with higher frequency is called "SIGNAL" and the one carrying lower frequency is called "IDLER".

The process of harmonic generation undoubtedly extends the range of otherwise accessible wavelengths but this strategy restricts us merely to the generation of harmonics. However, if the process of SFG and DFG is implemented employing two different frequencies ω_1 and ω_2 (not harmonics of each other), much wider range of frequencies besides the harmonics can be generated. Talking in terms of photon perspective, while for SFG, a higher frequency photon ω_3 ($\omega_1 + \omega_2 \rightarrow \omega_3$) is generated by adding up two lower frequency photons (ω_1 and ω_2) (SHG- a special case of SFG), in case of DFG (or also called Parametric Down Conversion), a single photon is obtained from the difference of the incident of incident frequencies ($\omega_1 - \omega_2 \rightarrow \omega_3$) **(Figure 2.17 A, B)**.

Apart from SFG and DFG, there is another process called Optical Parametric Generation (OPG) which involves the destruction of the incoming photon (usually called "pump" (ω_P)) with simultaneous creation of two outgoing photons ($\omega_P \rightarrow \omega_S + \omega_I$) **(Figure 2.17 C)**. The photon generated with higher frequency is referred to as "SIGNAL" (ω_S) and the other with lower frequency is known as the "IDLER" (ω_I). The frequency of these idler and signal photons generated as a consequence of OPG is highly influenced by the phase matching condition, which in turn is influenced by the angle formed by the incident pump beam with the crystal optical axis.

Unfortunately, the OPG approach suffers from a significant downside since the output pulses are extremely low in energy and lack directionality. This issue is alleviated by employing the process of Optical Parametric Amplification (OPA) that requires the inclusion of an extra stage based on DFG immediately after the OPG step **(Figure 2.18)**.[100]

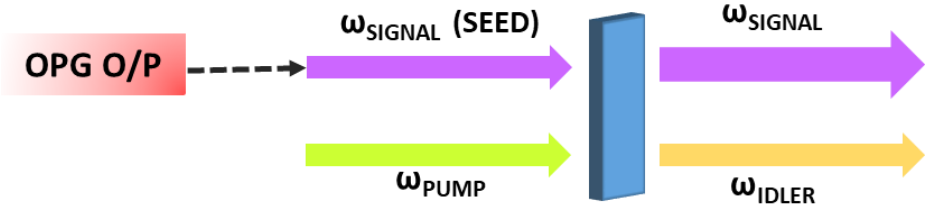

Figure 2.18 Optical Parametric Amplification: a pump photon and a "SIGNAL" photon which is actually the output from the OPG stage are incident together on a NLC. The "SIGNAL" photon is amplified as it gains energy at the cost of the energy of the pump and an IDLER photon is also produced along.

In this approach, two input light beams, pump (ω_P) and along with the signal beam (ω_s) from the OPG stage are incident onto the non-linear crystal (NLC). As a consequence, the pump beam (ω_P) is weakened while the signal beam (ω_S) is simultaneously amplified.

Additionally, in this operation, a new beam with frequency ω_I is generated as well, which is also known as an idler $\omega_I = \omega_P - \omega_s$.

C. White Light Continuum (WLC) Generation

It primarily relies on the optical Kerr effect, also known as the self-focusing effect, which has already been mentioned in relation to being an efficient mode-locking approach.[101] The phenomenon of WLC production, which is frequently exploited in time-resolved spectroscopic research, is caused by the same dependency of refractive index on light intensity. The fact that the phase of the electric field depends on the refractive index (nonlinear) **(Eq.2.12)** provides the physical basis for this phenomena; wave vector k is proportional to the refractive index. This has the effect of causing a wave travelling through such a medium to exhibit phase shift or modulation based on the strength of its own electric field. Given that frequency is the time derivative of phase, phase modulation is identical to frequency modulation. Therefore a wave propagating through any medium with non-zero cubic dielectric susceptibility will undergo self-phase modulation. These underlying processes together with a range of other non-linear optical phenomena lead to an expansion of the spectrum of a femtosecond pulse propagating in such a non-linear medium to a white light super continuum. Such spectrum constitute the probe beam for the TA spectrometers and also serve as the seed pulses in Optical Parametric Amplifiers.

2.5.3 Experimental Setup established in our lab

In the present thesis, we have used "OPERA SOLO" from "Light Conversion" for the generation of tuneable wavelengths ranging from 280 nm to 2600 nm. Since it requires the input to be in the range of 770 nm -830 nm and in horizontal polarisation state, this makes it compatible with the Astrella output. Essentially, the module is a two-stage parametric amplifier for WLC. It mostly employs OPA theory to function. It contains a number of smaller subunits that are all packed tightly together into a single assembly. These include optics for beam splitting and pump beam delivery, a crystal for generating WLC, a pre-amplifier (also known as the first amplifier stage), an expander-collimator for changing the beam size, and finally a power amplifier, which acts as the second amplifier stage. The equipment uses computer-controlled rotation and translation stages to quickly and precisely optimise the orientation of certain optics in order to calibrate the output wavelength at the disposal of OPERA SOLO. Figure 2.19 illustrates the overall layout of the OPERA-SOLO parametric amplification section.

Principle of operation:

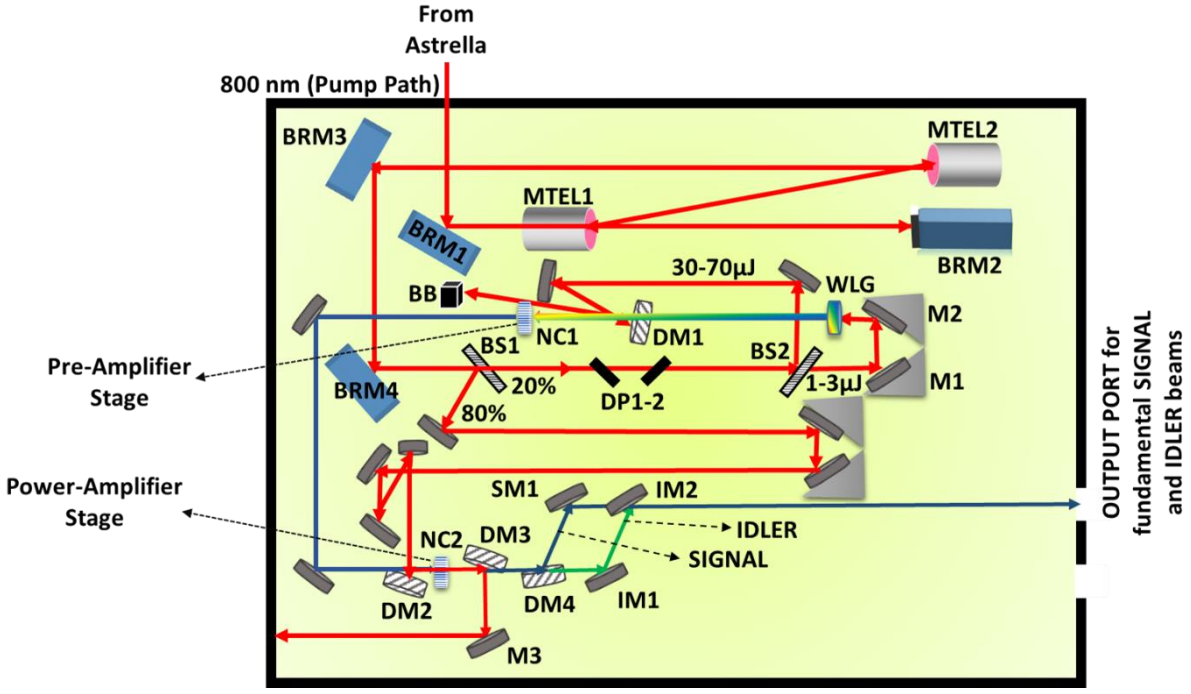

Figure 2.19 Layout of OPERA Solo showing the several steps the incident beam takes to produce the desired frequency at the output port. **(BRM** – Beam Routing Mirror, **MTEL** – Optical Mirror Telescope, **BS** – Beam Splitter, **DM** – Dichroic Mirror, **NC1 & NC2** – Non-linear Crystals (adjustable angles for achieving perfect phase matching condition-software controlled), **BB** – Beam Blocker, **DP** – Brewster Plate (result in adjustable delay- software controlled), **IM** – Idler Mirror (placed in position only if IDLER or its second harmonic/sum frequency has to extracted at the output)).

After passing via the lens telescope and beam routing mirrors, which work to lower the incident beam's size to the ideal level, the 800 nm output from ASTRELLA first hits the beam splitter BS1.It splits the incident pump beam into two, with the transmitted component receiving the remaining 20% of the energy and the reflected portion carrying 80% of the energy. The transmitted beam then strikes another beam splitter, BS2, which divides it once more into two parts. The fraction of this transmitted light beam which carriers very tiny energy (approximately 1-3 µJ) is incident on a sapphire plate (WLG), resulting in the generation of WLC (seed). This WLC, along with another portion of the transmitted pump beam (30-70 µJ), is then fed into the pre-amplifier crystal (NC1), guaranteeing that both beams overlap non-collinearly inside this crystal. This leads to parametric amplification of incident frequencies at this crystal (SIGNAL and IDLER). The SIGNAL frequency is determined by the frequency of

the WLC that overlaps with the pump beam. By altering the white-light pulse's relative delay to the initial pump pulse (by the use of software controlled Brewster angled plates DP1-2 and the adjustable mirrors M1 and M2 all mounted on a computer controlled delay stage) and tweaking the crystal angle for the best phase matching, the wavelength tuning in the pre-amplifier stage may be accomplished. Furthermore, the beam is made to travel through a non-linear geometry in order to conveniently separate the many frequencies that make up this enhanced SIGNAL beam. Just after NC1 crystal, a beam blocker (BB) is placed to stop the IDLER beam and the residual pump. The beam is then propagated towards the power amplifier (NC2), which is the second amplification step.

This amplifier is powered by the remaining component of the input beam which is reflected by the beam splitter BS1, which is quite a significant portion when compared to that utilised for the WLC generation. In order to achieve a high enough intensity, this beam size is decreased using the lens-mirror telescope. The pump and the SIGNAL beams are then made to overlap on the second non-linear crystal (NC2) which leads to OPA and as a result another collimated SIGNAL and IDLER beams are obtained. These collimated beams are then directed towards DM3 which reflects the pump beam onto M3 that further dumps it into a beam block. Then by using another dichroic mirror DM4 after DM3, signal and idler beams are separated, following which they take different routes and are collected at different output ports of OPERA SOLO. The golden mirrors IM1 and IM2 are detachable, and they are often not positioned in the light path when just the SIGNAL beam has to be gathered at the output. However, these mirrors are installed in their designated locations to direct the IDLER beam to the output port if the IDLER is required at the output of OPERA-SOLO. By modifying the preamplifier wavelength and subsequently optimising the second NLC angle and SIGNAL delay w.r.t the second pump beam, the wavelength tuning in the power-amplifier that is the second amplification stage is accomplished. In order to further broaden the scope of wavelengths that OPERA-SOLO can be tuned to, frequency mixers, including second harmonic generators (for frequency doubling), sum frequency generators for both SIGNAL and IDLER are employed to cover a wide range of wavelengths from UV to NIR (the frequency mixing components however have not been shown here in the layout to avoid complexity). To create the sum-frequency of the SIGNAL or IDLER, pump pulses are combined with the SIGNAL or IDLER pulses (SFS, SFI). Type -1 phase matching BBO crystals are used for SHG and SFG .These mixers are all computer controlled and produce a mixture of frequencies as opposed to a pure output. Following the output from these mixers, the wavelength selectors are used to separate

the required frequency. The monochromatic frequency outputs at the disposal of OPERO-SOLO constitute the pump beam for the TA spectrum.

2.5.3.1 Transient Absorption spectrometer- "Helios Fire"

In this dissertation, we have used "*Helios Fire*" from Ultrafast Systems as the TA spectrometer. The method of data acquisition in this broadband spectrometer is based on the simple pump-probe principle which has already been briefed in a previous section. The setup allows probing the transients over three spectral regions- 350 nm to 750 nm, 450 nm to 800 nm and 800 nm to 1600 nm. The switching between these "Probe" (WLC) ranges is achieved by software-controlled crystal motion, which places the appropriate WLC crystal (Wight Light Generator: WLG) in the path of the low intensity 800 nm light provided by the primary laser. For generation of the probe light in the UV domain, CaF_2 crystal is used, Sapphire is employed for producing the white light probe in visible domain and Yt^{3+}: Garnett is used for the NIR domain. The setup houses two detectors: CMOS sensor and InGaAs sensor for detection in the UV/Vis and NIR region respectively. The standard spectral resolution offered by this module is 1.5 nm for visible domain and 3.5 nm for NIR and the installed delay stage allows data acquisition until 8ns. A chopper is also mounted inside the spectrometer in the pump pulse path, synchronised with the 1kHz output from the main laser to ensure the periodic "PUMP ON" and "PUMP OFF" conditions. The Instrument Response Function (IRF) is typically ~ 100 fs which is basically 1.4 times the laser pulse duration. The typical size of the PUMP beam is 250 µm and that of the probe is 100 µm. Because the pump is bigger than the probe, it guarantees uniform excitation and compensates for any delay-related artefacts that may occur. In order to ensure that there are no dipole-dipole interactions making unnecessary contributions in the acquired data, there are two ways and one of which is setting the polarisation of the pump and the probe beam incident on the sample to magic angle 54.7°. The other way to guarantee that the obtained kinetics are free from any rotational deactivation processes is placing a depolariser prior to the sample stage. The setup can be used for the measurement of both liquid phase and solid phase samples. The data collection as well as the motion of the crystals, translating sample holder (to prevent sample damage) and delay stages is performed by Helios^{TM} software and the data is analysed using Surface Xplorer^{TM} software. To nullify the chirp artefacts, the software provides the chirp correction option.

The complete assembly of the ultrafast setup which we have used for the investigations conducted in this dissertation, beginning from the generation of the ultrafast pulses and data analysis can thus be summarised in the following sketch (Figure 2.20).

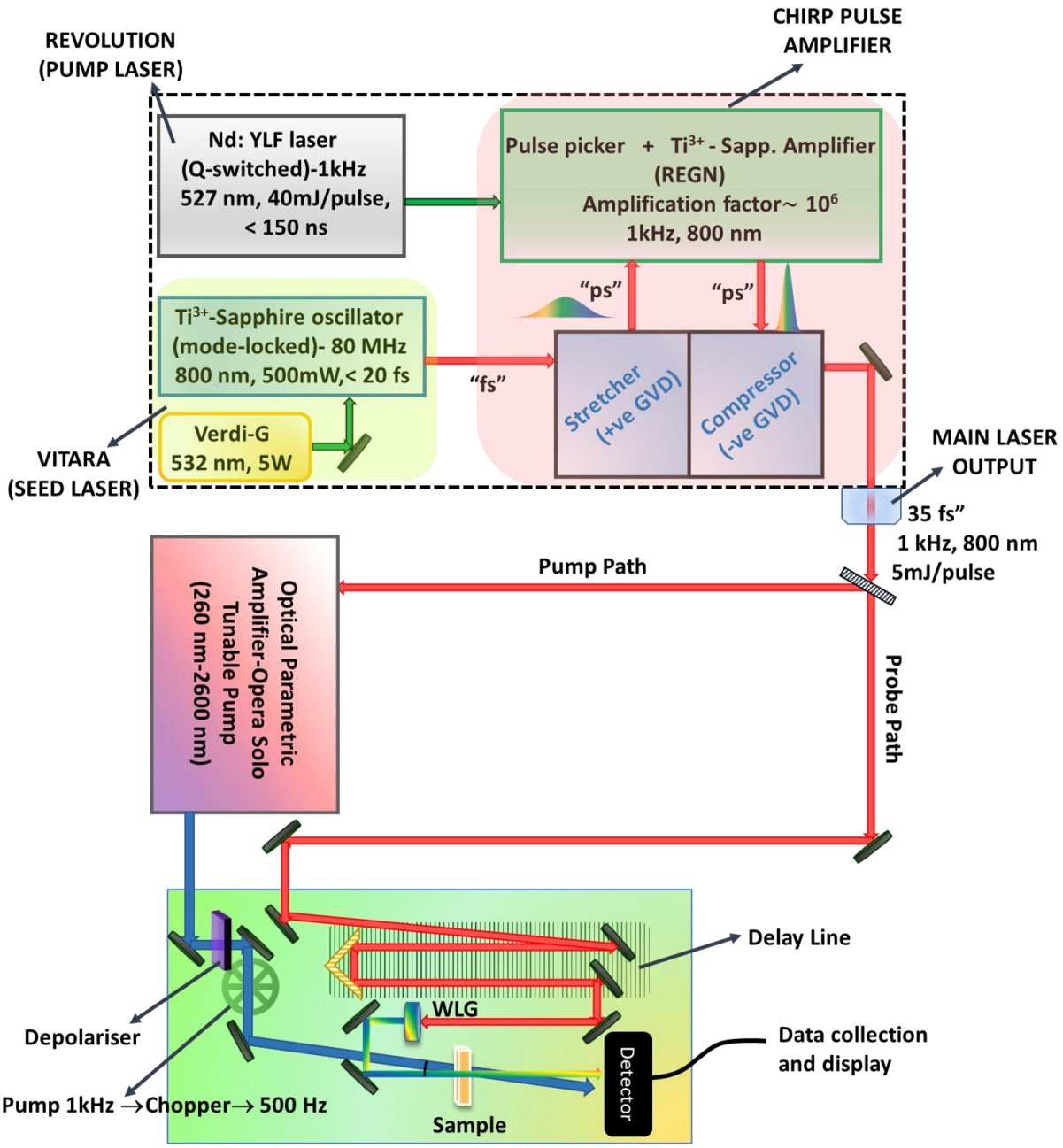

Figure 2.20 The sketch providing a summary of the ultrafast setup that we employed for the research projects included in this dissertation.

2.5.3.2 Surface Xplorer™ software

This labview-based programme fits any kinetic trace S(t) at any specified wavelength using a sum of convoluted exponentials:

$$S(t) = e^{-(\frac{t-t_0}{t_p})^2} * \sum_i A_i\, e^{-\frac{t-t_0}{t_i}} \qquad \textbf{Eq.2.13}$$

$$t_p = \frac{IRF}{2.ln2}, \qquad \textbf{Eq.2.14}$$

Here, IRF is the Instrument Response Function, t_0 is the time zero (that marks the starting point of the signal) and * stands for convolution function. Alongwith the time constants (t_i), the software also delivers the relative amplitudes (A_i) corresponding to each time constant.

Further for conducting the low temperature studies, we mounted the sample inside a closed cycle cryogenic workstation from Cryo industries of America Inc. (4 K- 325 K) assembled together with a Turbo pumping system (TPS- compact) from Agilent Technologies, HC- 4A Zephyr Series Air-Cooled Helium Compressor from Sumitomo cryogenics and a temperature controller from Lakeshore Cryotonics Inc. (Model 335, can measure and control temperatures between 300 mK to 1500 K).

2.5.3.3 Decrypting the spectral signatures observed in the TA data

There are essentially two types of signals encountered in the TA studies based on the sign of the quantity of interest "ΔA" (positive or negative). As already pointed out, this term ΔA basically represents the change in absorption of the probe→ $A_{PUMP\ ON}$ - $A_{PUMP\ OFF}$, and further by combining this with Beer Lambert's law according to which A= log (I_0/I) we can rewrite this term ΔA as:[63]

$$\Delta A = \frac{log I_0^{Probe}(\lambda)}{I^{Probe}(\lambda,\Delta t)}\Big|_{(PUMP\ ON)} - \frac{log I_0^{Probe}(\lambda)}{I^{Probe}(\lambda)}\Big|_{(PUMP\ OFF)} \qquad \textbf{Eq.2.15}$$

$$\therefore \Delta A \text{ becomes } \frac{log\, I^{Probe}(\lambda)\,(PUMP\ OFF)}{I^{Probe}(\lambda,\Delta t)(PUMP\ ON)} \qquad \textbf{Eq.2.16}$$

From the **Eq. 2.16**, it can be deduced that the basic idea is to compare the probe intensity that the detector has collected in the presence (PUMP ON) and absence of the pump beam (PUMP OFF).

For gaining a simplified understanding of these signatures and the possible underlying causes, let us consider a straightforward scenario of a system with its ground state denoted by 'G' and excited states marked as 'A' and 'B' (considered only two excited states to avoid complications) **(Figure 2.21 A)**. At time t < 0, when there is no photo excitation (PUMP OFF condition) and there is only probe incident on this system, all the species reside in the ground state of the system. The fact that this state G is so occupied causes a significant amount of light from the probe to be absorbed, and no light is subsequently delivered to the detector.

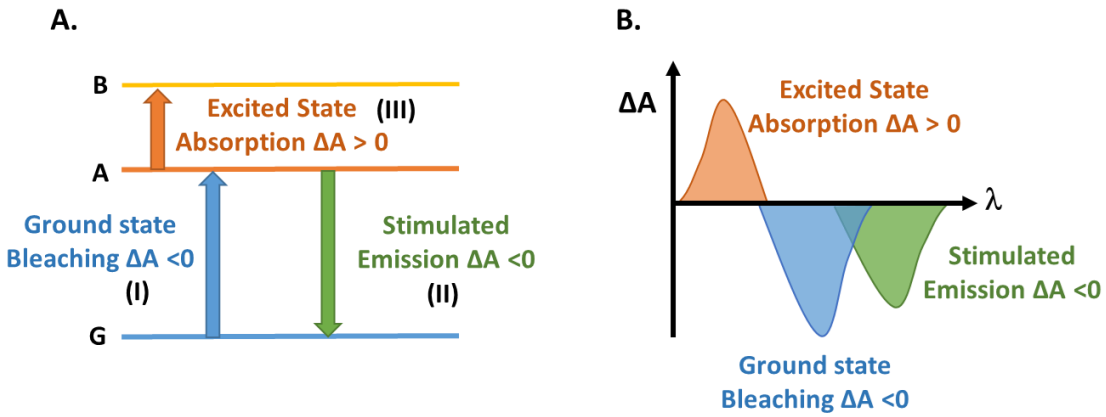

Figure 2.21 (A) Possible origins of the pump probe signals: Ground State Bleaching, Stimulated emission and Excited state Absorption. **(B)** The different ways they are manifested in the TA spectral data.

The time t= 0 marks the instance when the pump is incident on the sample. This results in the excitation of these ground state species into the excited states and depletion of the state G. At t>0, since the ground state G is significantly depleted there is not much absorption of the probe light, resulting in transmission of a huge intensity of the probe onto the detector. The resulting ΔA feature from this type of process is negative **(Figure 2.21 B)** because in this situation log $I^{Probe}(\lambda)$ (PUMP OFF) < $I^{Probe}(\lambda)$ (PUMP ON) and is often called "Ground state bleach" (GSB) (shown as I in **Figure 2.12 A**). Besides this bleaching process, there is another possibility which also results in negative ΔA, i.e. "stimulated emission (SE)" (shown as II in **Figure 2.21 B**).In this process, a photon constituting the incident probe pulse induces stimulated emission from the excited state A to G. The resulting photon, mildly Stoke shifted is emitted in the same direction as the incident probe photon, resulting in increment in the transmitted probe intensity. Since SE results in an increased incidence of probe light intensity on the detector, therefore it also results in a negative ΔA signature **(Figure 2.21 B)**.

However the process of "Excited State Absorption" (ESA) (depicted as III) rather leads to a positive ΔA. This process involves the absorption of the probe leading to transitions from lower excited states (say A, where there is population build-up) to higher excited states (say B). Since the probe is absorbed in this process, so the transmitted probe intensity will be relatively lower than otherwise and hence $I^{Probe}(\lambda)$ (PUMP OFF) > $I^{Probe}(\lambda)$ (PUMP ON), leading to positive ΔA **(Figure 2.21 B)**.

2.5 Terahertz (THz) time-domain spectroscopy

As suggested by the name itself, this spectroscopic method uses frequencies, ranging from a few thousand GigaHertz (10^9) to several THz (10^{12}) commonly referred to as the THz radiation to examine the photo-physical aspects of a system. When considering THz radiation's position in the electromagnetic spectrum (EM) based on energy, it may be found somewhere between the microwave and far-infrared region (Figure 2.22). The energy equivalent of one THz photon is roughly 4 meV and if stated in terms of wavenumber units, it is equivalent to 33.33 cm^{-1}. The energy carried by THz photons is thus very less relative to the energies between any two adjacent electronic energy states of a material. These magnitudes rather are comparable to and fall in the range of low frequency vibrational resonances and rotational transition energies which are unique to any given system and can therefore provide the spectroscopic fingerprint in THz domain. Thus this makes THz spectroscopy particularly well suited for these investigations, which cannot be generally examined by TA domain studies, which are limited to providing insights into the electronic state dynamics.

This method primarily depends on the interaction of the charge carriers present in the sample under investigation with the periodically oscillating THz field. Depending on the strength of the incident field, this interaction builds up an internal polarisation in the sample, and the subsequent dielectric response aids in the characterisation.

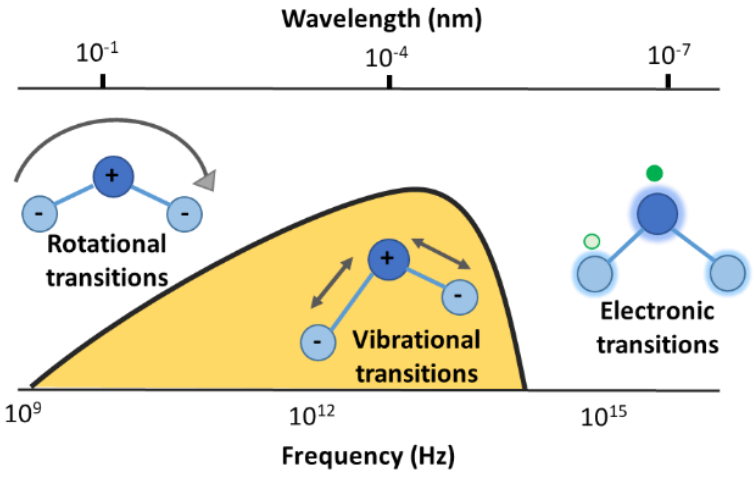

Figure 2.22 The region of the EM spectrum where the THz radiation lies and the frequencies corresponding to the rotational, vibrational and electronic transitions.

Furthermore, the average carrier scattering rates encountered in most of the semiconductor materials are of the order of 10^{11} to 10^{12} s^{-1} which are comparable to THz frequencies, therefore THz spectroscopy allows for the estimation of carrier scattering rates and mobilities. Besides this, because THz radiation is a contactless mode of measurement, it offers a better model and the estimated photo conductivities are both more precise and repeatable than those obtained using the traditional Hall effect or four probe techniques.[102] The other noteworthy advantage of THz spectroscopy is that it detects the transient electric field rather than merely its intensity. These transient fields allow for the direct determination of the amplitude and phase of each spectrum component following Fourier transformation, which can then be utilised to establish the real refractive index (n) and absorption coefficient of the sample (imaginary refractive index (k)). In this way, the sample's complex-valued permittivity may be established without having to resort to a Kramers- Kronig analysis**.**[103]

Terahertz-based spectroscopic investigations are generally divided into three categories: (i) THz Time Domain Spectroscopy (TDS), (ii) Time Resolved THz Spectroscopy (TRTS), and (iii) THz Emission Spectroscopy.[104] While TDS and TRTS measurements seek to determine the static and evolving properties of the sample of interest, respectively, TES is essentially a TDS setup with the sample acting as the THz emitter. In the present dissertation we have employed TRTS to understand the time dependent mobility response of our system under different energy excitations.

Principle of operation: There are numerous techniques that have been employed till date for the detection and the generation of THz radiation. However amongst all the established methods, electro-optic methods are the most often deployed ones. While electro-optic rectification, which is fundamentally the inverse Pockels cell effect, forms the basis of THz generation, electro-optic sampling serves as the core principle of detection. Electro-optic sampling is in principle nothing but the Pockels effect which has been explained before. The entire operation of a typical TDS setup is based on the use of two light beams obtained from the fundamental laser using a beam splitter installed at the entry of the THz spectrometer: the GATE pulse, which sets the polarisation for the electro-optic detection, and the THz beam, which interacts with the sample and disturbs this set polarisation. This change in polarisation causes a net current to flow across the detector, which is measured and then decrypted for further analysis. Thus in other words, by combining the THz radiation field together with the gate pulse in EO1, the temporal trace of the THz amplitude is obtained from the differential signal response collected at the balanced detector pair. TRTS is principally a more advanced

form of TDS in which the samples are photoexcited by an optical or NIR pump and the time-resolved THz spectrum is acquired using THz probe pulses at various time delays.

2.6.1 Experimental setup in our lab

We have used Newport built Terahertz Time-domain Spectrometer (THz-TDS) for conducting the investigations reported *in this thesis*. In this setup, two- color, laser-induced air plasma formation mechanism serves as the basis for THz generation. This THz generation strategy typically uses either the asymmetric transient current model or the four wave mixing method. Our system generates the transient current model in which the oscillating SHG produces an alternating current at the point where it focuses together with the fundamental. This results in stripping off the electrons from the atoms, resulting in strong plasma. The installed system allows data acquisition over the standard detection range (0.25 – 3 THz, best resolution – 1.25GHz), however by upgrading the system the detection range can be extended to 4 THz (best resolution – 0.23 GHz). The maximum Optical pump- THz probe delay range is 4.3 ns (minimum step size – 1 fs) which can be elongated further in the upgraded versions to 8.3 ns (minimum step size - 0.13 fs). Maximum delay range for the THz gate pulse is 0.8 ns (can be upgraded to 4.3 ns) and the minimum step size is 0.25 fs. The system requires a minimum input energy threshold of 1mJ for THz generation and 0.5 μJ for optimal electro-optic detection.

For operating as a TDS setup, the spectrometer requires only one input beam (p-polarised), the one directly incoming from the Astrella system (centered at 800 nm, 1mJ). The Newport TDS unit used in this thesis is provided in **Figure 2.23**.

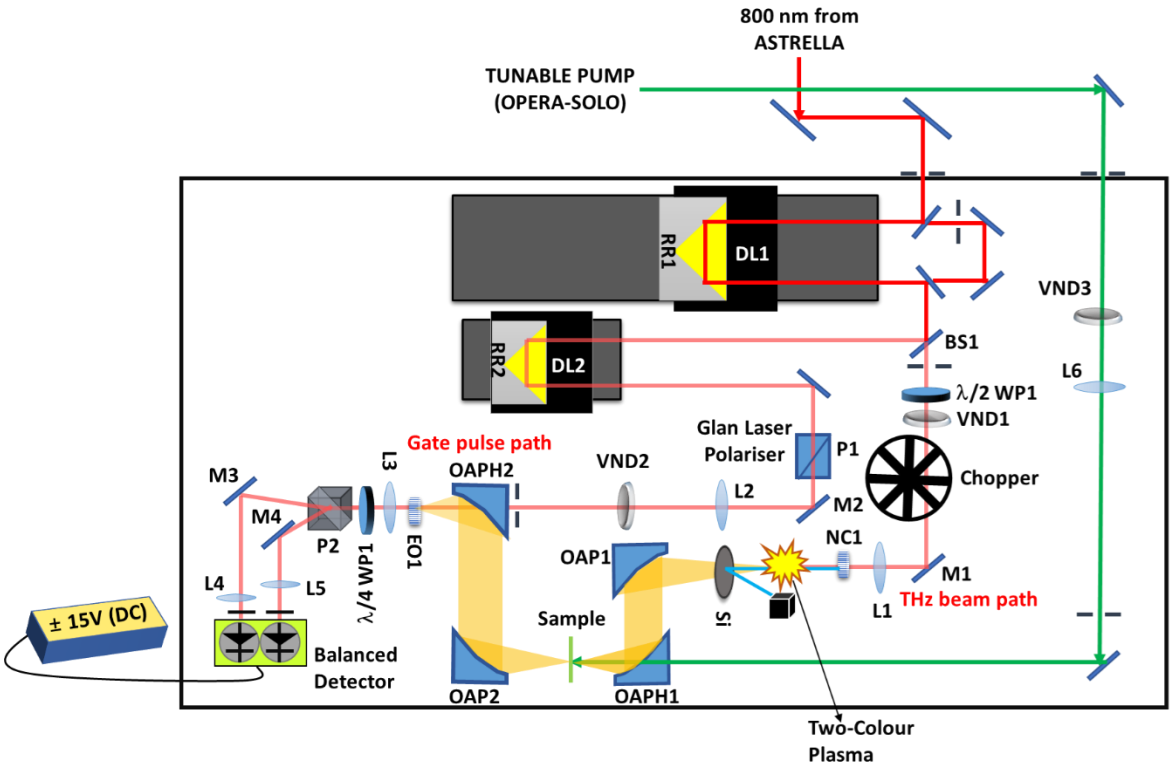

Figure 2.23 Simple layout of the Newport built Terahertz Time Domain spectrometer used in the present dissertation.

This incoming beam is then split into two fractions by deploying a beam splitter (BS1), set at 45° to the incident beam, positioned near the entrance of the spectrometer. The transmitted beam carriers a major fraction of the total energy (~99%) and the reflected portion carries less than even 1% of the total power. Due to the fact that the transmitted beam is used for THz generation while the reflected beam is required for the electro-optic method, the incident energy is divided in this proportion. The transmitted beam is then directed towards a λ/2 WP (WP1). The WP1 rotates the polarisation of the incident beam by 180° and following WP1, a variable neutral density filter (VND1) is placed in the beam path to attenuate the beam intensity. The beam then passes through the optical chopper (synchronised with the laser output frequency) and is then directed towards mirror M1. After falling on the mirror, using lens L1, the light is then focused onto the NLC NC1 (Type-1 BBO , cut at 29.2 °, thickness- 0.2 mm) owing to which there is SHG (400 nm) of the fundamental beam (800 nm). The fundamental along with the second harmonic are focused jointly in air to generate two color laser air plasma, giving off frequencies in the range 0.2 -3 THz. There are however some visible frequencies including the second harmonic generated signal (400 nm) and also the fundamental (800 nm) present along with the THz frequencies. In order to filter out and dump all undesirable optical

frequencies and allow only the THz radiation to be transmitted further, a high resistivity float zone silicon (Si) wafer of sufficient thickness is placed in the beam's path. The THz beam is then focused and collimated onto the sample mounted at the sample holder position by the off-axis parabolic mirror "OAP1" and off-axis parabolic mirror with a hole "OAPH1". The beam is once more gathered and collimated by mirrors "OAP2 and OAPH2" after it has passed through the sample. Next, the beam is focused onto the "EO1" NLC crystal by the parabolic mirror OPAH2. ZnTe serves as the NLC medium in the Newport system, though GaAs and GaP are the other crystals that are typically used if higher detection bandwidths are required.

For serving as the THz gate pulse for electro-optic sampling, the reflected beam is delayed by being directed onto the retro-reflector RR2 mounted on the delay line DL2. Following this, the beam is then transmitted through the Glan calcite Laser Polariser P1, which establishes the beam's initial polarisation for detection. The light beam at the disposal of P1 is then incident on mirror M2, which then travels all way through lens L2, VND2,the centre of OAPH2 (parabolic mirror with a hole at its central axis) and finally hits the EO1 crystal. After that, the lens L3 collimates and focuses this gate light with the concurrently present THz radiation. The polarisation state of the incoming light is then converted from linear to circular by $\lambda/4$ WP2, and the Wollaston prism P2 separates the constituent perpendicular polarisation components. An assembly of mirrors (M3, M4) and lens (L4, L5) then direct each polarisation component towards the balanced detector pair (New Focus^{TM} Nirvana). In absence of THz radiation, the detectors are fairly in balanced state and the differential signal acquired is roughly zero. If this is not the case, WP2 should be rotated until a null response is obtained. However, when there is THz radiation passing through a sample and incident on ZnTe <110> crystal (EO1), then under the influence of this THz field, there is birefringence induced in the crystal. As a consequence, the initially set polarisation of the gate pulse (in the absence of the THz radiation) is disturbed in proportion to the incident THz field and there is a non-zero signal resultant on the detector pair.

By incorporating an additional tuneable pump beam provided by OPERA SOLO for photoexcitation of the samples, the same setup is used for TRTS or also referred as optical pump THz probe (OPTP) spectroscopy. After passing through the necessary optics set up for ideal focusing (L6) and controlling the pump intensity attenuation (VND3), this pump beam, which is collinear with the THz beam, is directed onto the sample through the OAPH1. To guarantee uniform excitation of the sample, it is ensured that the pump beam diameter is greater than the THz beam diameter.

2.6.2 Data collection and analysis

The output file generated by the THz spectrometer's Graphic User Interface (GUI) software is in ASCII CSV format, which may be imported into any appropriate programme for further analysis. The pump-induced TRTS scans can be collected using either frequency averaged or frequency-resolved experiments. The frequency resolved TDS measurements require the delay DL1 (optical-pump THz probe delay- t_p) to be kept constant and only the delay DL2 (THz gate delay-t) to be changed. However in TRTS measurements or frequency averaged experiments, the pump-probe delay DL1 is translated along its length at specific set time steps, while the delay stage DL2 is fixed in position of the THz spectrum maxima. The former set of experiments yield the pump induced changes in the THz waveform $\Delta E\ (t,t_p)$ at a fixed OPTP delay (t_p) but the later category of experiments involve tracking the pump induced changes in the THz field transmission ($\Delta E\ (\ t_{max}, t_p)$) at different pump-probe delays (t_p).

Since we aim to find the peak THz mobility in our NCs film, so we have employed the later strategy of TRTS with variable pump-probe delay.

It is imperative to first determine the peak photoconductivity in order to define the transient peak mobilities because these two quantities are actually related.

By applying the following equation to the peak transients $-\Delta E\ (t_p)/E_0\ (t_p)$ obtained from the TRTS scans, the peak conductivities ($\Delta\sigma$) can be easily calculated.[105]

$$\Delta\sigma\ (t_p) = \frac{d\ \varepsilon_0\ (n_a + n_b)}{c} * \left(\frac{-\Delta E(t_p)}{E_0(t_p)}\right) \qquad \textbf{Eq.2.17}$$

Here d is the sample thickness, n_a and n_b are the refractive index of the sample and the substrate respectively, ε_0 is the permittivity of free space, c is the speed of light, ΔE is the pump induced change in the THz field transmission and E_0 is the THz field transmitted through unexcited samples.

Following the extraction of peak conductivity, the effective mobility ($\varphi\mu$) of the carriers can also be estimated using the relation

$$\varphi\mu = \frac{\Delta\sigma}{eN_0} \qquad \textbf{Eq.2.18}$$

Here N_0 is the total carrier density and φ is the photon to free carrier conversion ratio which is an unknown parameter, so what we measure is actually the effective mobility rather than the absolute one.

2.7 References

(1) Pan, J.; Shang, Y.; Yin, J.; De Bastiani, M.; Peng, W.; Dursun, I.; Sinatra, L.; El-Zohry, A. M.; Hedhili, M. N.; Emwas, A.H.; et al. Bidentate Ligand-Passivated $CsPbI_3$

Perovskite Nanocrystals for Stable Near-Unity Photoluminescence Quantum Yield and Efficient Red Light-Emitting Diodes. *J Am Chem Soc* **2018**, *140* (2), 562–565.

(2) Liu, F.; Zhang, Y.; Ding, C.; Kobayashi, S.; Izuishi, T.; Nakazawa, N.; Toyoda, T.; Ohta, T.; Hayase, S.; Minemoto, T.; et al. Highly Luminescent Phase-Stable $CsPbI_3$ Perovskite Quantum Dots Achieving Near 100% Absolute Photoluminescence Quantum Yield. *ACS Nano* **2017**, *11* (10), 10373–10383.

(3) Polavarapu, L.; Nickel, B.; Feldmann, J.; Urban, A. S. Advances in Quantum-Confined Perovskite Nanocrystals for Optoelectronics. *Adv Energy Mater* **2017**, *7* (16), 1700267.

(4) Hintermayr, V. A.; Richter, A. F.; Ehrat, F.; Döblinger, M.; Vanderlinden, W.; Sichert, J. A.; Tong, Y.; Polavarapu, L.; Feldmann, J.; Urban, A. S. Tuning the Optical Properties of Perovskite Nanoplatelets through Composition and Thickness by Ligand-Assisted Exfoliation. *Adv Mater* **2016**, *28* (43), 9478–9485.

(5) Protesescu, L.; Yakunin, S.; Nazarenko, O.; Dirin, D. N.; Kovalenko, M. V. Low-Cost Synthesis of Highly Luminescent Colloidal Lead Halide Perovskite Nanocrystals by Wet Ball Milling. *ACS Appl Nano Mater* **2018**, *1* (3), 1300–1308.

(6) Wang, N.; Liu, W.; Zhang, Q. Perovskite-Based Nanocrystals: Synthesis and Applications beyond Solar Cells. *Small Methods* **2018**, *2* (6), 1700380.

(7) de Weerd, C.; Gregorkiewicz, T.; Gomez, L. All-Inorganic Perovskite Nanocrystals: Microscopy Insights in Structure and Optical Properties. *Adv Opt Mater* **2018**, *6* (16), 1800289.

(8) Murray, C. B.; Norris, D. J.; Bawendi, M. G. Synthesis and Characterization of Nearly Monodisperse CdE (E = Sulfur, Selenium, Tellurium) Semiconductor Nanocrystallites. *J Am Chem Soc* **1993**, *115* (19), 8706–8715.

(9) Murray, C. B.; Kagan, C. R.; Bawendi, M. G. Synthesis and Characterization of Monodisperse Nanocrystals and Close-Packed Nanocrystal Assemblies. *Annu Rev Mater Sci* **2000**, *30* (1), 545–610.

(10) LaMer, V. K.; Dinegar, R. H. Theory, Production and Mechanism of Formation of Monodispersed Hydrosols. *J Am Chem Soc* **1950**, *72* (11), 4847–4854.

(11) Peng, X.; Wickham, J.; Alivisatos, A. P. Kinetics of II-VI and III-V Colloidal Semiconductor Nanocrystal Growth: "Focusing" of Size Distributions. *J Am Chem Soc* **1998**, *120* (21), 5343–5344.

(12) Carey, G. H.; Abdelhady, A. L.; Ning, Z.; Thon, S. M.; Bakr, O. M.; Sargent, E. H. Colloidal Quantum Dot Solar Cells. *Chem Rev* **2015**, *115* (23), 12732–12763.

(13) Schmidt, L. C.; Pertegás, A.; González-Carrero, S.; Malinkiewicz, O.; Agouram, S.;

Mínguez Espallargas, G.; Bolink, H. J.; Galian, R. E.; Pérez-Prieto, J. Nontemplate Synthesis of $CH_3NH_3PbBr_3$ Perovskite Nanoparticles. *J Am Chem Soc* **2014**, *136* (3), 850–853.

(14) Protesescu, L.; Yakunin, S.; Bodnarchuk, M. I.; Krieg, F.; Caputo, R.; Hendon, C. H.; Yang, R. X.; Walsh, A.; Kovalenko, M. V. Nanocrystals of Cesium Lead Halide Perovskites ($CsPbX_3$, X = Cl, Br, and I): Novel Optoelectronic Materials Showing Bright Emission with Wide Color Gamut. *Nano Lett* **2015**, *15* (6), 3692–3696.

(15) Shekhirev, M.; Goza, J.; Teeter, J. D.; Lipatov, A.; Sinitskii, A. Synthesis of Cesium Lead Halide Perovskite Quantum Dots. *J Chem Educ* **2017**, *94* (8), 1150–1156.

(16) Jellicoe, T. C.; Richter, J. M.; Glass, H. F. J.; Tabachnyk, M.; Brady, R.; Dutton, S. E.; Rao, A.; Friend, R. H.; Credgington, D.; Greenham, N. C.; et al. Synthesis and Optical Properties of Lead-Free Cesium Tin Halide Perovskite Nanocrystals. *J Am Chem Soc* **2016**, *138* (9), 2941–2944.

(17) Handayani, Y. S.; Wulandari, P.; Hidayat, R. Controlled Synthesis of Lead-Free Perovskite Cs_2SnI_6 as Hole Transport Layer in Dye Sensitized Solar Cells. *J Phys Conf Ser* **2018**, *1080*, 12003.

(18) Protesescu, L.; Yakunin, S.; Bodnarchuk, M. I.; Krieg, F.; Caputo, R.; Hendon, C. H.; Yang, R. X.; Walsh, A.; Kovalenko, M. V. Nanocrystals of Cesium Lead Halide Perovskites ($CsPbX_3$, X = Cl, Br, and I): Novel Optoelectronic Materials Showing Bright Emission with Wide Color Gamut. *Nano Lett* **2015**, *15* (6), 3692–3696.

(19) Jia, C.; Li, H.; Meng, X.; Li, H. $CsPbX_3/Cs_4PbX_6$ Core/Shell Perovskite Nanocrystals. *Chem Commun* **2018**, *54* (49), 6300–6303.

(20) Hu, L.; Wang, W.; Liu, H.; Peng, J.; Cao, H.; Shao, G.; Xia, Z.; Ma, W.; Tang, J. PbS Colloidal Quantum Dots as an Effective Hole Transporter for Planar Heterojunction Perovskite Solar Cells. *J Mater Chem A* **2015**, *3* (2), 515–518.

(21) Woolfson, M. M. The Scattering of X-Rays. In *An Introduction to X-ray Crystallography* (2nd Ed.). Cambridge University Press: Cambridge, **2010**; pp 32–49.

(22) Woolfson, M. M. Diffraction from a Crystal. In *An Introduction to X-ray Crystallography*. (2nd Ed.). Cambridge University Press: Cambridge, **2010**; pp 50–75.

(23) Lee, M. X-Ray Diffraction for Materials Research: From Fundamentals to Applications (1st ed.). Apple Academic Press and CRC Press,New York, **2016**.

(24) Birkholz, M. Principles of X-Ray Diffraction. In *Thin Film Analysis by X-Ray Scattering*; Wiley-VCH Verlag GmbH & Co. KGaA, **2005**; pp 1–40.

(25) Seeck, O. H.; Murphy, B. M. X-Ray Diffraction : Modern Experimental Techniques.

Jenny Stanford Publishing, New York, **2015**.

(26) Bunaciu, A. A.; gabriela Udriştioiu, E.; Aboul-Enein, H. Y. X-Ray Diffraction: Instrumentation and Applications. *Crit Rev Anal Chem* **2015**, *45* (4), 289–299.

(27) Ladd, M. F. C.; Palmer, R. A. Structure Determination by X-Ray Crystallography (1st ed.). Springer New York, NY, **1977**.

(28) Shvyd'ko, Y. High-Resolution X-Ray Monochromators BT - X-Ray Optics: High-Energy-Resolution Applications. Springer Berlin Heidelberg: Berlin, Heidelberg, **2004**; pp 215–286.

(29) Luo, Z. *A Practical Guide to Transmission Electron Microscopy : Fundamentals / Zhiping Luo.*, First edit.; Materials characterization and analysis collection. Momentum Press: New York, [New York], **2016**.

(30) Shindo, D.; Oikawa, T. Basic Principles of Analytical Electron Microscopy BT - Analytical Electron Microscopy for Materials Science. Springer Japan: Tokyo, **2002**; pp 1–11.

(31) Pennycook, S. J. Imaging in the STEM BT- Transmission Electron Microscopy: Diffraction, Imaging, and Spectrometry; Carter, C. B., Williams, D. B., Eds.; Springer International Publishing: Cham, **2016**; pp 283–342.

(32) Egerton, R. F. The Transmission Electron Microscope BT - Physical Principles of Electron Microscopy: An Introduction to TEM, SEM, and AEM. Springer US: Boston, MA, **2005**; pp 57–92.

(33) Shindo, D.; Oikawa, T. Constitution and Basic Operation of Analytical Electron Microscopes BT - Analytical Electron Microscopy for Materials Science. Springer Japan: Tokyo, **2002**; pp 13–41.

(34) Kruit, P. Electron Sources BT - Transmission Electron Microscopy: Diffraction, Imaging, and Spectrometry; Carter, C. B., Williams, D. B., Eds.; Springer International Publishing: Cham, **2016**; pp 1–15.

(35) Dima, C.; Assadpour, E.; Dima, S.; Jafari, S. M. 15 - Characterization and Analysis of Nanomaterials in Foods. Academic Press, **2020**; *Handbook of Food Nanotechnology*, 577-653. pp 577–653.

(36) Owen, A. E. Fundamentals of Ultraviolet-Visible Spectroscopy. Hewlett Packard **1996**.

(37) Ball, D. W. Modern Spectroscopy, 4th Ed. J. Michael Hollas. New York: John Wiley & Sons, Inc., **2004**. *Clin Chem* **2004**, *50* (12), 2469–2470.

(38) Albani, J.R. Absorption Spectroscopy Theory. In *Principles and Applications of Fluorescence Spectroscopy*; **2007**; pp 1–12.

(39) Patterson, J. D.; Bailey, B. C. Optical Properties of Solids BT - Solid-State Physics: Introduction to the Theory; Patterson, J. D., Bailey, B. C., Eds.; Springer International Publishing: Cham, **2018**; pp 649–704.

(40) Picollo, M.; Aceto, M.; Vitorino, T. UV-Vis Spectroscopy. **2019**, *4* (4).

(41) Mäntele, W.; Deniz, E. UV-VIS Absorption Spectroscopy: Lambert-Beer Reloaded. *Spectrochimica acta. Part A, Molecular and biomolecular spectroscopy*. England February **2017**, pp 965–968.

(42) Albani, J.R. Fluorescence Spectroscopy Principles. In *Principles and Applications of Fluorescence Spectroscopy*; **2007**; pp 88–114.

(43) Lakowicz, J. R. Introduction to Fluorescence BT - Principles of Fluorescence Spectroscopy; Ed.; Springer US: Boston, MA, **2006**; pp 1–26.

(44) Hirvonen, L. M.; Suhling, K. Fast Timing Techniques in FLIM Applications. *Front Phys* **2020**, *8*.

(45) Phillips, D.; Drake, R. C.; O'Connor, D. V; Christensen, R. L. Time Correlated Single-Photon Counting (Tcspc) Using Laser Excitation. *Instrum Sci Technol* **1985**, *14* (3–4), 267–292.

(46) Bramwell, F. B. Creation and Detection of the Excited State. Volume 3 (Ware, William R., Ed.). *J Chem Educ* **1976**, *53* (5), A276.

(47) Bachrach, R. Z. A Photon Counting Apparatus for Kinetic and Spectral Measurements. *Rev Sci Instrum* **1972**, *43* (5), 734–737.

(48) Liu, X.; Lin, D.; Becker, W.; Niu, J.; Yu, B.; Liu, L.; Qu, J. Fast Fluorescence Lifetime Imaging Techniques: A Review on Challenge and Development. *J Innov Opt Health Sci* **2019**, *12* (11), 1930003.

(49) Bollinger, L. M.; Thomas, G. E. Measurement of the Time Dependence of Scintillation Intensity by a Delayed-Coincidence Method. *Rev Sci Instrum* **1961**, *32* (9), 1044–1050.

(50) Bastiaens, P. I. H.; Squire, A. Fluorescence Lifetime Imaging Microscopy: Spatial Resolution of Biochemical Processes in the Cell. *Trends Cell Biol* **1999**, *9* (2), 48–52.

(51) Building Blocks of Advanced TCSPC Devices BT - Advanced Time-Correlated Single Photon Counting Techniques; Becker, W., Castleman, A. W., Toennies, J. P., Zinth, W., Eds.; Springer Berlin Heidelberg: Berlin, Heidelberg, **2005**; pp 47–60.

(52) Overview of Photon Counting Techniques BT- Advanced Time-Correlated Single Photon Counting Techniques; Becker, W., Castleman, A. W., Toennies, J. P., Zinth, W., Eds.; Springer Berlin Heidelberg: Berlin, Heidelberg, **2005**; pp 11–25.

(53) Shah, J. Cooling of Hot Carriers BT- Ultrafast Spectroscopy of Semiconductors and

Semiconductor Nanostructures; Shah, J., Ed.; Springer Berlin Heidelberg: Berlin, Heidelberg, **1999**; pp 161–192.

(54) Shah, J. Introduction BT- Ultrafast Spectroscopy of Semiconductors and Semiconductor Nanostructures; Shah, J., Ed.; Springer Berlin Heidelberg: Berlin, Heidelberg, 1999; pp 1–26.

(55) Diels, J. C.; Rudolph, W. 3 - Light-Matter Interaction; Diels, J.C., Rudolph, W. B. T.U. L. P. P. (Second E., Eds.); Academic Press: Burlington, 2006; pp 143–219.

(56) Mitchell, A. C. G.; Zemansky, M. W. Resonance Radiation and Excited Atoms. *Am J Phys* **1972**, *40* (8), 1187.

(57) Silfvast, W. T. *Laser Fundamentals / William T. Silfvast.*, 2nd ed.; Cambridge University Press: Cambridge ; **2004**.

(58) Diels, J.C.; Rudolph, W. 11 - Examples of Ultrafast Processes in Matter. (Second E., Eds.;) Academic Press: Burlington, **2006**; pp 531–555.

(59) Svelto, O.; Denardo, G. (Gallieno); De Silvestri, S.; International Symposium on Ultrafast Processes in Spectroscopy (9th : 1995 : Trieste, I. *Ultrafast Processes in Spectroscopy / Edited by O. Svelto, S. De Silvestri, and G. Denardo.*, 1st ed. 19.);New York : Plenum Press: New York, **1996**.

(60) Diels, J.C.; Rudolph, W. 10 - Measurement Techniques of Femtosecond Spectroscopy; (Second E., Eds.;) Academic Press: Burlington, **2006**; pp 491–530.

(61) Abramczyk, H. 8 - Selected Methods of Time-Resolved Laser Spectroscopy BT- Introduction to Laser Spectroscopy . Elsevier Science: Amsterdam, **2005**; pp 175–217.

(62) Weiner A. Ultrafast Time-Resolved Spectroscopy. In *Ultrafast Optics*; **2009**; pp 422–506.

(63) Berera, R.; van Grondelle, R.; Kennis, J. T. M. Ultrafast Transient Absorption Spectroscopy: Principles and Application to Photosynthetic Systems. *Photosynth Res* **2009**, *101* (2–3), 105–118.

(64) Malard, L. M.; Fai Mak, K.; Castro Neto, A. H.; Peres, N. M. R.; Heinz, T. F. Observation of Intra- and Inter-Band Transitions in the Transient Optical Response of Graphene. *New J Phys* **2013**, *15* (1), 15009.

(65) Klimov, V. I.; McBranch, D. W. Femtosecond High-Sensitivity, Chirp-Free Transient Absorption Spectroscopy Using Kilohertz Lasers. *Opt Lett* **1998**, *23* (4), 277–279.

(66) Fork, R. L.; Greene, B. I.; Shank, C. V. Generation of Optical Pulses Shorter than 0.1 Psec by Colliding Pulse Mode Locking. *Appl Phys Lett* **1981**, *38* (9), 671–672.

(67) Diels, J.C.; Rudolph, W. 5 - Ultrashort Sources I: Fundamentals; (Second E., Eds.);

Academic Press: Burlington, 2006; pp 277–339.

(68) Diels, J.C.; Rudolph, W. 6 - Ultrashort Sources II: Examples; (Second E., Eds.); Academic Press: Burlington, **2006**; pp 341–394.

(69) Monmayrant, A.; Weber, S.; Chatel, B. PhD TUTORIAL: A Newcomer's Guide to Ultrashort Pulse Shaping and Characterization. *J Phys B At Mol Phys* **2010**, *43*, 103001.

(70) Abramczyk, H. 3 - Generation of Ultrashort Laser Pulses; Abramczyk, H. B. T.-I. to L. S., Ed.; Elsevier Science: Amsterdam, **2005**; pp 31–58.

(71) Wang, X.; Ren, X.; Peng, J.; Shen, X.; Huang, K.; Yan, M.; Zeng, H. On the Q-Switching Bunch Dynamics in the Build-up of Stretched-Pulse Mode-Locking. *Opt Express* **2019**, *27* (3), 2747–2753.

(72) Kafka, J. D.; Watts, M. L.; Pieterse, J.W. J. Picosecond and Femtosecond Pulse Generation in a Regeneratively Mode-Locked Ti:Sapphire Laser. *IEEE J Quantum Electron* **1992**, *28* (10), 2151–2162.

(73) Corney, A. Atomic and Laser Spectroscopy; **1977**.

(74) Moulton, P. F. Spectroscopic and Laser Characteristics of Ti:Al_2O_3. *J Opt Soc Am B* **1986**, *3* (1), 125–133.

(75) Wagner, W. G.; Lengyel, B. A. Evolution of the Giant Pulse in a Laser. *J Appl Phys* **1963**, *34* (7), 2040–2046.

(76) Koechner, W.; Bass, M. Q-Switching BT - Solid-State Lasers: A Graduate Text; Koechner, W., Bass, M., Eds.; Springer New York: New York, NY, 2003; pp 279–307.

(77) DeMaria, A. J.; Stetser, D. A.; Heynau, H. SELF MODE-LOCKING OF LASERS WITH SATURABLE ABSORBERS. *Appl Phys Lett* **1966**, *8* (7), 174–176.

(78) Mittal, S.; Arvind, K.; A.S., L.; S.S., P. Design and Development of Pockels Cell Driver for Q Switch LASER in Space Applications. *IETE J Res* **2017**, *63* (5), 694–699.

(79) Demtröder, W. Lasers as Spectroscopic Light Sources BT - Laser Spectroscopy: Vol. 1 Basic Principles. Springer Berlin Heidelberg: Berlin, Heidelberg, **2008**; pp 235–396.

(80) Demtröder, W. Absorption and Emission of Light BT - Laser Spectroscopy: Vol. 1 Basic Principles. Springer Berlin Heidelberg: Berlin, Heidelberg, **2008**; pp 5–60.

(81) Weiner A. Principles of Mode-Locking. In *Ultrafast Optics*; **2009**; pp 32–84.

(82) Ducasse, A.; Rullière, C.; Couillaud, B. Methods for the Generation of Ultrashort Laser Pulses: Mode-Locking BT - Femtosecond Laser Pulses: Principles and Experiments; Rullière, C., Ed.; Springer New York: New York, NY, **2005**; pp 57–87.

(83) Fermann, M. E.; Galvanauskas, A. D.; Sucha, G. D. D. Ultrafast Lasers : Technology and Applications; **2002**.

(84) Brabec, T.; Spielmann, C.; Curley, P. F.; Krausz, F. Kerr Lens Mode Locking. *Opt Lett* **1992**, *17* (18), 1292–1294.

(85) Nurhuda, M.; Suda, A.; Midorikawa, K. Generalization of the Kerr Effect for High Intensity, Ultrashort Laser Pulses. *New J Phys* **2008**, *10* (5), 53006.

(86) Paufler, P. Introduction to Nonlinear Optics. By Geoffrey New. Pp. Xv+257. Cambridge: University Press, 2011. *J Appl Crystallography* **2012**, *45* (3), 613.

(87) Negus, D. K.; Spinelli, L.; Goldblatt, N.; Feugnet, G. Sub-100 Femtosecond Pulse Generation by Kerr Lens Mode-Locking in Ti: Al_2O_3. In *Advanced Solid State Lasers*; Dube L., G. and C., Ed.; OSA Proceedings Series; Optica Publishing Group: Hilton Head, South Carolina, **1991**; Vol. 10, p SPL7.

(88) Maine, P.; Strickland, D.; Bado, P.; Pessot, M.; Mourou, G. Generation of Ultrahigh Peak Power Pulses by Chirped Pulse Amplification. *IEEE J Quantum Electron* **1988**, *24* (2), 398–403.

(89) Lai, M.; Lai, S. T.; Swinger, C. Single-Grating Laser Pulse Stretcher and Compressor. *Appl Opt* **1994**, *33* (30), 6985–6987.

(90) Treacy, E. Optical Pulse Compression with Diffraction Gratings. *IEEE J Quantum Electron* **1969**, *5* (9), 454–458.

(91) Abramczyk, H. 6 - Pulse Amplification BT- Introduction to Laser Spectroscopy. Elsevier Science: Amsterdam, **2005**; pp 147–160.

(92) Silfvast, W. T. LASER AMPLIFIERS. In *Laser Fundamentals*; 2nd Ed.; Cambridge University Press: Cambridge, **2004**; pp 223–224.

(93) Silfvast, W. T. Conditions for producing a laser – population inversions, gain, and gain saturation. In *Laser Fundamentals*; 2nd Ed.; Cambridge University Press: Cambridge, **2004**; pp 225–254.

(94) Strickland, D.; Mourou, G. Compression of Amplified Chirped Optical Pulses. *Opt Commun* **1985**, *56* (3), 219–221.

(95) Ashcroft, C. M.; Cole, J. M. 5 - "Molecular engineering of organic and organometallic second-order nonlinear optical materials." *Handbook of Organic Materials for Electronic and Photonic Devices (Second Edition)*; Woodhead Publishing, (**2019**); pp. 139-176.

(96) Solgi, S.; Tafreshi, M. J.; Ghamsari, M. S. Nonlinear Optical Crystals for Second Harmonic Generation. *Crystallography Reports* **2019**, *64* (7), 1138–1149.

(97) Chen, S.; Li, K. F.; Li, G.; Cheah, K. W.; Zhang, S. Gigantic Electric-Field-Induced Second Harmonic Generation from an Organic Conjugated Polymer Enhanced by a

Band-Edge Effect. *Light Sci Appl* **2019**, *8* (1), 17.

(98) Zhang, J. Y.; Huang, J. Y.; Shen, Y. R.; Chen, C. Optical Parametric Generation and Amplification in Barium Borate and Lithium Triborate Crystals. *J Opt Soc Am B* **1993**, *10* (9), 1758–1764.

(99) Tzankov, P.; Buchvarov, I.; Fiebig, T. Broadband Optical Parametric Amplification in the near UV–VIS. *Opt Commun* **2002**, *203* (1), 107–113.

(100) Cerullo, G.; De Silvestri, S.; Manzoni, C. Optical Parametric Amplifiers- Encyclopedia of Modern Optics II, Volume 2. Elsevier: Oxford, **2018**; pp 290–301.

(101) Brodeur, A.; Chin, S. L. Ultrafast White-Light Continuum Generation and Self-Focusing in Transparent Condensed Media. *J Opt Soc Am B* **1999**, *16* (4), 637–650.

(102) Zhuldybina, M.; Ropagnol, X.; Trudeau, C.; Bolduc, M.; Zednik, R. J.; Blanchard, F. Contactless In Situ Electrical Characterization Method of Printed Electronic Devices with Terahertz Spectroscopy. *Sensors* **2019**, *19*(3), 444.

(103) Goyal, R.;Tiwari, A. Terahertz Conductivity of Nanoscale Materials and Systems; In B. You, & J. Lu (Eds.), IntechOpen: Rijeka, **2022**; p Ch. 10.

(104) Dexheimer, S. L. Terahertz Spectroscopy : Principles and Applications; **2007**.

(105) Yettapu, G. R.; Talukdar, D.; Sarkar, S.; Swarnkar, A.; Nag, A.; Ghosh, P.; Mandal, P. Terahertz Conductivity within Colloidal $CsPbBr_3$ Perovskite Nanocrystals: Remarkably High Carrier Mobilities and Large Diffusion Lengths. *Nano Lett* **2016**, *16* (8), 4838–4848.

Chapter 3

Polaron Mediated Slow Carrier Cooling in Type-1 3D/0D $CsPbBr_3$@Cs_4PbBr_6 Core-Shell Perovskite System

Rapid hot carrier cooling is the key loss channel overriding all the possible energy loss pathways that limit the achievable solar conversion efficiency. Thus, delayed hot carrier cooling in the cell absorber layer can make hot carrier extraction a less cumbersome task, assisting in the realization of hot carrier solar cells. There have been plentitude of reports concerning the slow carrier cooling in perovskite materials, which has eventually triggered interest in the radical understanding of the native photophysics driving the device design. Here in this chapter, a further dramatic dip in the cooling rate has been discerned upon growing Cs_4PbBr_6 shell over $CsPbBr_3$ core NCs in contrast to the bare $CsPbBr_3$ core NCs. Using Transient Absorption spectroscopy, we have investigated the disparity in the hot carrier thermalization pathways in the $CsPbBr_3$ and $CsPbBr_3$@Cs_4PbBr_6 core-shell NCs under same laser fluence, which can be validated as a corollary of polaron formation in the later NCs.

3.1 Motivation and Background

All inorganic lead halide perovskite materials ($CsPbX_3$ NCs, where X=Cl, Br, I) have been the center of intense research activity for the scientific community in the past few years pertaining to their diverse unique traits such as captivating counterintuitive high PL quantum yield[1], fine emission line-width[2], extended carrier lifetimes, highly mobile charge carriers[3], versatile energy band gap[4], high extinction coefficient[5] and defect tolerance[6] (exceptionally low defect density~ $10^{10}cm^{-3}$). Furthermore, the defect states are positioned within the bands rather than the mid-gap sites.[7] This is in sharp contrast to that observed for the prototypical III-V, II-VI semiconductor QDs where the intrinsic defect states occupying the mid-gap sites ensue inevitable fall in the PLQY.[8] These novel properties of the perovskite materials and ease of production, drive them to offer prospective high performance and low cost optoelectronic devices.[9–11] Deploying all the unique combination of the luminescence properties, these exotic materials have already showcased themselves as remarkably highly efficient QLEDs, with external quantum efficiency ~10.5% achieved till date.[12] The power conversion efficiency (PCE) of the solar cells utilizing these materials has presently achieved a value of ~31.25%.[13] It is anticipated that the so far attained PCE may undeniably usher to higher numbers in the coming years. In this way, these perovskite NCs may find an opportunity of replacing the potential conventional solar materials. But to great disappointment, after attaining the record PV efficiency, the efficiency numbers have not shown any satisfactorily progressive trend lately. To an added advantage, recently there have been growing literature reports intriguing about the retarded hot carrier relaxation rates in lead halide perovskites (LHPs- $CsPbX_3$ NCs) which is a major factor in which the other competent classic solar cell absorber materials lag behind (first such report for $CsPbBr_3$ in 2013 by Xing et al.). [14–16]

In the quest of surpassing the preset ultimate thermodynamical limit on solar cell efficiency (Shockley Queisser Limit~33% under 1 Sun illumination), [14,16] the excessive energy carried by the hot carriers upon above bandgap excitation needs to be harvested and in this way the energy losses can be minimised.Consequently in this way, a commendable efficiency number (~66% as per the thermodynamical calculations) can be achieved. A possible and unique approach for eliminating the inevitable energy losses is the extraction of the carriers whilst they are still hot, before they dissipate their energy through the innumerable possible loss pathways to equilibrate to the lattice temperature.[17] A hurdle in this process is the rate of cooling of charge carriers, which typically occurs on a time scale of few hundreds of femtoseconds, making the hot carrier extraction quite tedious task. Thus, hot carrier cooling

stands as a foremost aspect that is decisive for determining the application of the LHPs for photovoltaic and optoelectronic devices. This deceleration of the carrier cooling rate can be considered as a consequence of enormous attributable reasons. It can be either the large polaron formation[17, 18] or hot phonon bottleneck [19–21] or even the Auger heating[22] causing the retardation of this process. Thus, a deeper understanding of the charge carrier relaxation dynamics can prove advantageous towards revealing the prominent key factor for this sluggish cooling of the hot carriers. These essential findings can prove extremely strategic for better technological progresses.

In this chapter, in a process to further slowdown the hot carrier cooling rate in the already well established $CsPbBr_3$ system, we have grown a 0D larger band gap perovskite (Cs_4PbBr_6) over the 3D lower band gap perovskite ($CsPbBr_3$) which not only provides a protective envelope over the easily degradable $CsPbBr_3$ but also results in complementarily drastically reduced cooling rate. In particular,Cs_4PbBr_6 has been chosen as it is the ideal contender due to perfect lattice matching, suitable band offsets (Type-1 band alignment)[23] and soft crystalline character.We have employed transient absorption spectroscopy to elucidate the charge carrier cooling dynamics under two different initial carrier energy excitations and also attempted to give a native time domain picture of large polaron formation in the $CsPbBr_3$@Cs_4PbBr_6 core-shell material which is largely responsible for the difference in the resulting photophysical properties exhibited. Ultrafast spectroscopy suits best to describe such processes as they occur on a time scale of sub-picosecond. Such a requisite evaluation may serve as a competent means of improving the presently employed optoelectronic devices. Best to our knowledge, such study has not been undertaken before and the fundamental charge carrier dynamical response in these 3D-0D core-shell materials has been left unexplored.

3.2 Results and discussion

3.2.1 Steady state optical, crystallographic & morphological studies

Most important aspect of the present study is to understand the origin and mechanism ruling the charge carrier cooling, thus accounting for the varied cooling rates in $CsPbBr_3$ and $CsPbBr_3$@Cs_4PbBr_6 core-shell NC systems using the time resolved spectroscopic measurements. The colloidal NCs namely $CsPbBr_3$, Cs_4PbBr_6 and $CsPbBr_3$@Cs_4PbBr_6 core-shell systems with mean edge length of 14 nm, 23 nm and 18 nm respectively, well-illustrated by the acquired High Resolution Transmission Electron Microscopy images (HR-TEM) **(Figure 3.1 A)** have been synthesized following a previously reported synthesis methodology with minor modifications[23] (synthesis details have been briefed in Chapter 2). Since the average

edge parameter for $CsPbBr_3$ NCs is 14 nm, which is much outsized (almost double) in contrast to the Bohr diameter (~7 nm) of the Warnier Mott excitons,[24] the spatial confinement is quite weak. X-Ray Diffraction (XRD) patterns of newly synthesized $CsPbBr_3$, Cs_4PbBr_6 and $CsPbBr_3$@Cs_4PbBr_6 NCs are depicted in **figure 3.1 B**. The XRD peaks are well defined and are in good agreement with the reference data set. The XRD studies reveal that in the case of $CsPbBr_3$@Cs_4PbBr_6 core-shell NCs system, the orthorhombic phase of the $CsPbBr_3$ core is maintained, indicating that the 3D structure of $CsPbBr_3$ is retained even after the growth of the shell. Moreover, additional new strong peaks are noticed at 2θ = 12.9°, 22.2° and 39.2° corresponding to (110), (300) and (324) confirming the formation of Cs_4PbBr_6 shell over 3D $CsPbBr_3$ core **(Figure 3.1 B)**.

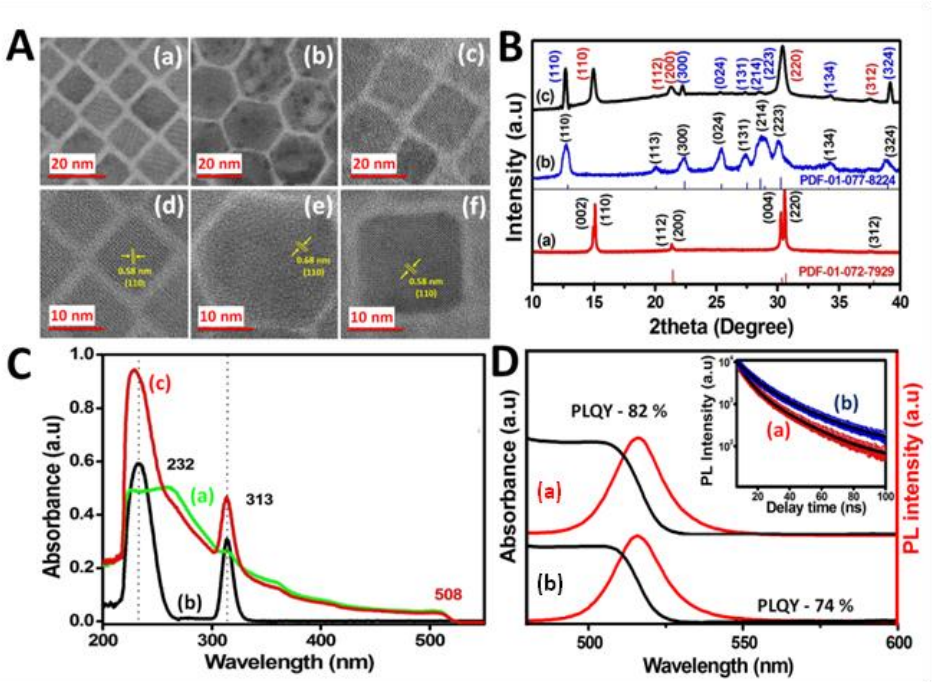

Figure 3.1 (A) High Resolution TEM images of (a, d) $CsPbBr_3$, (b, e) Cs_4PbBr_6 and (c, f) $CsPbBr_3$@ Cs_4PbBr_6 core-shell NCs. **(B)** Powder XRD patterns of the deposited films of (a) $CsPbBr_3$, (b) Cs_4PbBr_6 and (c) $CsPbBr_3$@ Cs_4PbBr_6 core-shell NCs. **(C)** Steady state optical absorption spectra of (a) $CsPbBr_3$, (b) Cs_4PbBr_6 and (c) $CsPbBr_3$@ Cs_4PbBr_6 core-shell NCs. **(D)** Typical UV-vis absorption (black line) and the corresponding steady state PL emission spectra (red line) for the same concentration of NCs depicting a Stokes' shift (Δ_S) of ~30 meV (inset: Corresponding Time-resolved PL decay curves of (a) $CsPbBr_3$@ Cs_4PbBr_6 NCs (τ_{av}=8 ns) and (b) $CsPbBr_3$ (τ_{av}=12 ns).

The optical absorption data of the as-synthesized $CsPbBr_3$ and $CsPbBr_3$@Cs_4PbBr_6 NCs share a common feature *viz.* a sharp ascent in the spectral curve at~ 514 nm **(Figure 3.1 C)**

marking the onset of absorption corresponding to the 1st excitonic transition in both $CsPbBr_3$ and $CsPbBr_3@Cs_4PbBr_6$ NC systems. This similar absorption feature arises because of the octahedral structure, which is common to both the 3D and 0D perovskite counterparts. This almost featureless absorption profile of the band edge in $CsPbBr_3$ NCs can be attributed to the weak confinement.

From the steady state PL studies, there has been observed a sharp emission peak for both the $CsPbBr_3$ and $CsPbBr_3@Cs_4PbBr_6$ NC systems at ~516 nm, which can be attributed to luminescence due to first excitonic state of $CsPbBr_3$ **(Figure 3.1 D)**. It has also been observed that there is an 8 % evident increase in the absolute PLQY (74 % to 82 %) upon coating Cs_4PbBr_6 shell over the $CsPbBr_3$ seed core due to superior surface defects passivation**.**

3.2.2 Time resolved PL measurements

The time resolved PL studies (TCSPC) estimate the average lifetime (τ_{PL}) of the as-synthesized $CsPbBr_3@Cs_4PbBr_6$ core-shell NCs to be 8 ns, which is lower than that of $CsPbBr_3$ NCs (τ_{PL}=12 ns) (see inset of **Figure 3.1 D**). In response to this, here can be two probable reasons accounting for the reduced PL lifetime, *viz.,* core size reduction or enhanced exciton binding energy.[23] The former possibility cannot provide any plausible explanation since it has been found that the PL bandwidth (~18 nm) and the emission peak position (~516 nm) remains unchanged even after the shell coating. The only possibility remaining is the higher exciton binding energy for Cs_4PbBr_6 shell phase (~160 meV)[25] in crude contrast to the much lower values reported for $CsPbBr_3$ phase.[26] This strong overlap of the carrier wave-functions in $CsPbBr_3$ facilitates a quicker recombination of the photo-generated charge carriers. In the $CsPbBr_3@ Cs_4PbBr_6$ core-shell system, the protective shell in addition to providing improved stability to $CsPbBr_3$ core, also grants ample large band offsets which facilitates the excitons to follow carrier dynamics as in Type I core-shell system. This confines the carriers in the core since the band offsets provide a thermodynamically viable pathway for both the electron and hole to effectively transfer from shell to the core.

3.2.3 Ultrafast Transient Absorption measurements

Previous work reported on the synthesis of $CsPbBr_3@Cs_4PbBr_6$ NCs by Jia.et.al.[23] has been prominently limited to the basic optical characterization and study of the PL response of the 3D-0D core shell structures. However in the present investigation, our main endeavor is to monitor the unique and retarded charge cooling dynamics of $CsPbBr_3@Cs_4PbBr_6$ core-shell and compare it with the core $CsPbBr_3$ NCs through broadband femtosecond TA technique.

This two beam, pump-probe technique offers a profound opportunity to make an attempt towards deciphering the photo-generated charge carrier population build up and the subsequent cooling dynamics on an ultrafast timescale. Here, emphasis has been laid on correlating both the linear and non-linear optical properties, the exciton dynamics and polaron formation mediated cooling of the charge carriers. Extreme pump excitation energies (near and far above the band gap) have been opted for embarking upon the studies of both the hot and cold carrier dynamics differently in the above two systems. Above all, the incident pump intensity is kept sufficiently low to suppress the multiple exciton generation in both the systems.

3.2.3.1 Upon near band gap excitation (480 nm)

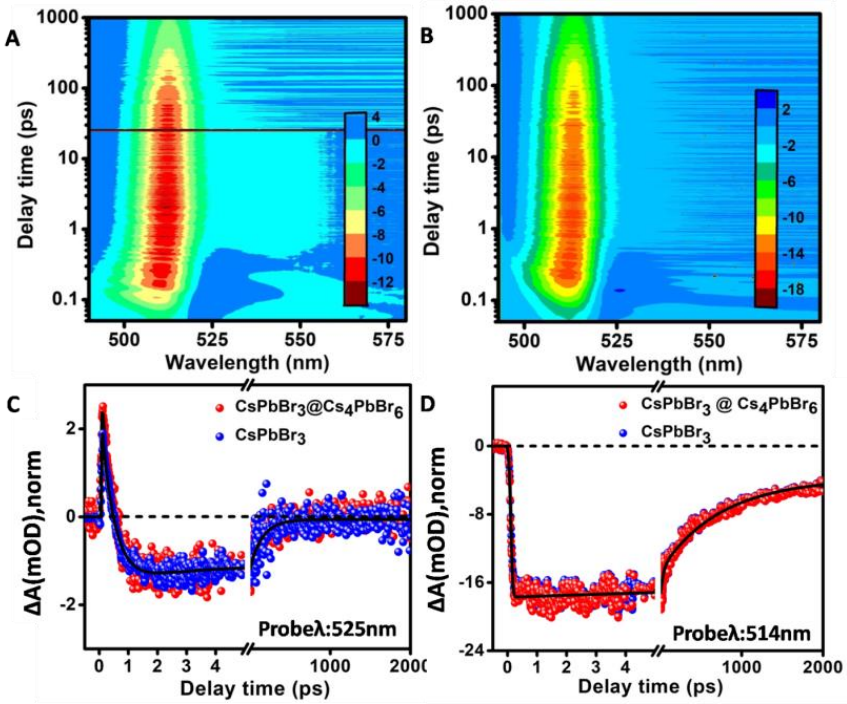

Figure 3.2 (A, B) Representative pseudo colored plots for $CsPbBr_3$ and $CsPbBr_3$@ Cs_4PbBr_6 core-shell NC systems respectively under just above the band gap excitation (λ_{ex} = 480 nm). **(C, D)** Comparative kinetic traces for both the systems probed at probe wavelength λ = 525 nm (positive band) and probe wavelength λ = 514 nm (bleach band) respectively.

A suitably chosen, low energy 480 nm pump excitation was employed to generate quite thermalized charge carriers for the consideration of the near band gap cooling dynamics in both $CsPbBr_3$ and $CsPbBr_3$@Cs_4PbBr_6 core-shell systems. **Figure 3.2 A and 3.2 B** show the comparative representative pseudo color plots for $CsPbBr_3$ and $CsPbBr_3$@Cs_4PbBr_6 core-shell NC systems respectively, for 480 nm excitation. The transient spectra shows up a negative

absorption band that extends over a narrow wavelength range 490-520 nm having a minimum at 514 nm (corresponding to 1S excitonic bleach).

The transient bleach is an absolute consequence of Pauli blocking (interband transitions are governed by Pauli's exculsion principle) due to the decrement in probe beam absorption from the depleted ground state.[27] This ground state bleach has a minor contribution from the stimulated emission which cannot be completely shrugged off therefore, the overall signal is the blend of the two components which merge together to give the strong negative signal. The formation of the photo-induced bleach (~514 nm) for both the systems is almost instantaneous (limited by the instrument response function) and can be ascribed to the excitons created near the band edge **(Figure 3.2 A and 3.2 B)**.

Moreover for such a low energy excitation, it is impractical to generate excitons in the large band gap shell (Cs_4PbBr_6). This is at par with the fact that the charge carriers are generated only in the core and there is no contribution from the shell towards the population of the charge carriers at the band edges of the confined core. In addition, excitation close to the band edge results in the localization of the charge carriers and hence, the spectral bandwidth of the bleach is quite narrow. This is quite apparent from the TA data obtained that depicts almost analogous trend for both the $CsPbBr_3$ and $CsPbBr_3@Cs_4PbBr_6$ systems. Complementary to this negative TA feature, two positive absorption bands on either side of the bleach valley are also discernible. The appearance of the typical asymmetric derivative like feature around the first excitonic absorption peak of $CsPbBr_3$ in the ultrafast studies during the early probe delay times ($\Delta t \sim 0.3$ ps) can be solely attributed to Stark effect induced due to the Coulombic correlation between the excitons generated by the pump and the probe pulse respectively due to the perfect match with the second derivative of the optical absorption spectrum data. This sort of interaction causes a redshift in the excitonic peak which is seen as the prominent bleach and positive signal around the longer wavelength region **(Figure 3.3 A and 3.3 B)**.This is completely in line with the previously reported works.[28,29] In order to ascertain the occurrence of this biexciton induced Stark effect, the continuum states contribution can be de-convoluted from that of the excitonic absorption.[30] The deconvolution affirms the prevalence of bi-exciton induced Stark effect during the early probe delay times, which comes from the coupling of the hot exciton formed in the continuum band energy states, just after photoexcitation, with the band edge exciton (that corresponds to the excitonic peak deconvoluted from the steady state absorption spectra). The resultant TA spectra is a sum total of the signal due to the bleach (-ve signal) centered about the excitonic peak (band edge exciton, E_g=2.41eV) and induced

absorption (+ve signal) holding the contribution from the continuum states, centered at $E_g + \Delta_{XX}$ (Δ_{XX}, being the biexciton binding energy). This drives the energy band gap to renormalise itself as a function of time.[31]

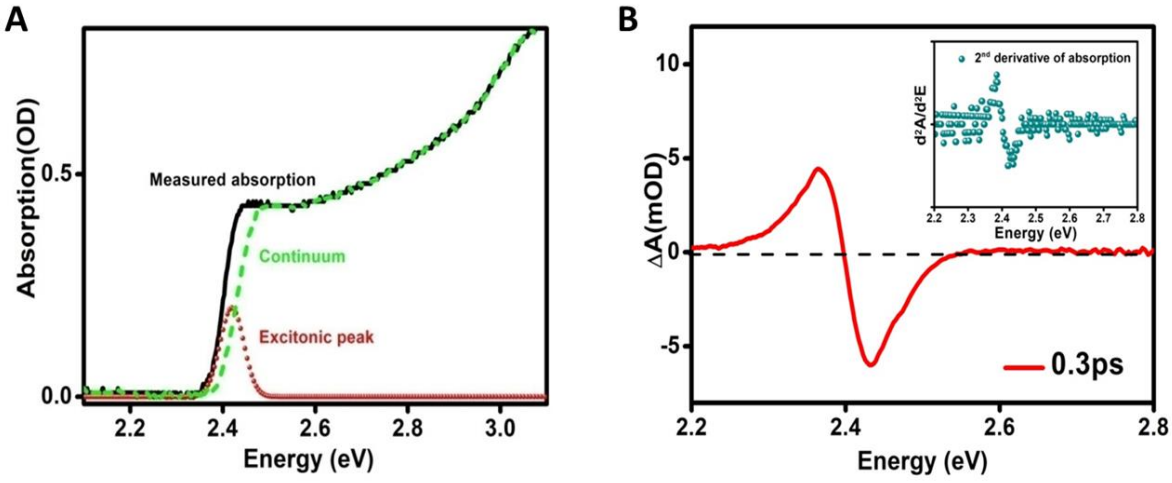

Figure 3.3 (A) De-convoluted absorption spectra of $CsPbBr_3$ NCs showing the separated excitonic contribution from the continuum states contribution. **(B)** Early time (0.3 ps) TA spectra of $CsPbBr_3$ NC matches with the second derivative of steady state absorption for $CsPbBr_3$ (Inset) which clearly represents the biexciton induced Stark effect in the TA spectra.

The other small positive absorption band towards the higher energy regime of the bleach in **figure 3.2 A** and **3.2 B** can be attributed to the photo-induced excited state absorption. Soon after the completion of intra-band cooling as the charges populate the band edges, state filling induced bleach dominates the spectra and the carrier induced stark effect vanishes. The formation of bi-exciton in the $CsPbBr_3$@Cs_4PbBr_6 core-shell NC system is found to be more facilitated as compared to the bare $CsPbBr_3$ NCs. The transient kinetics trace of $CsPbBr_3$ NC and $CsPbBr_3$@Cs_4PbBr_6 core-shell at 525 nm have been plotted after normalizing the bleach intensity at 514 nm. **Figure 3.2 C and 3.2 D** indicate the comparison kinetics for both core and core-shell samples at 525 nm and 514 nm respectively.

In both the systems, in case of near band gap excitation, bleach growth is pulse width limited. Although in our earlier studies bi-exponential growth of <100 fs and 600 fs while exciting the $CsPbBr_3$ samples at 400 nm was observed, where the hot charge carriers were generated.[32] However, in the present investigation near bandgap excitation (480 nm) charge carriers are pretty much thermalized **(Table 3.1)**.

Table 3.1 Kinetics fitting parameters for $CsPbBr_3$ and $CsPbBr_3@Cs_4PbBr_6$ core-shell systems dispersed in n-hexane after exciting the samples at 480 nm.

System	Probe λ (nm)	τ_{growth}	τ_1	τ_2	τ_3	τ_4
$CsPbBr_3$	514	τ_{g1}=<100 fs (100%)	15 ps (-21.8%)	280 ps (-52.1%)	>1 ns (-26.1%)	
	525	τ_{g1}=<100 fs (62%)	0.43 ps (-100%)	1.5 ps (4.8%)	76 ps (30%)	400 ps (3.2%)
$CsPbBr_3$@ Cs_4PbBr_6	514	τ_{g1}=<100 fs (100%)	15.1ps (-22.3%)	290 ps (-49.5%)	>1ns (-28.2%)	
	525	τ_{g1}=<100 fs (63%)	0.45 ps (-100%)	1.46 ps (8.5%)	97 ps (28.5%)	

3.2.3.2 Far above band gap excitation (300 nm)

Exciting with pump excitation energy (4.1 eV) much higher than the energy band gap provides a profound opportunity to explicate the complex hot carrier cooling dynamics in both $CsPbBr_3$ and $CsPbBr_3@Cs_4PbBr_6$ core-shell systems. **Figure 3.4 A and 3.4 B** represent the two dimensional color contour picture of the spectral TA response of the NC systems.

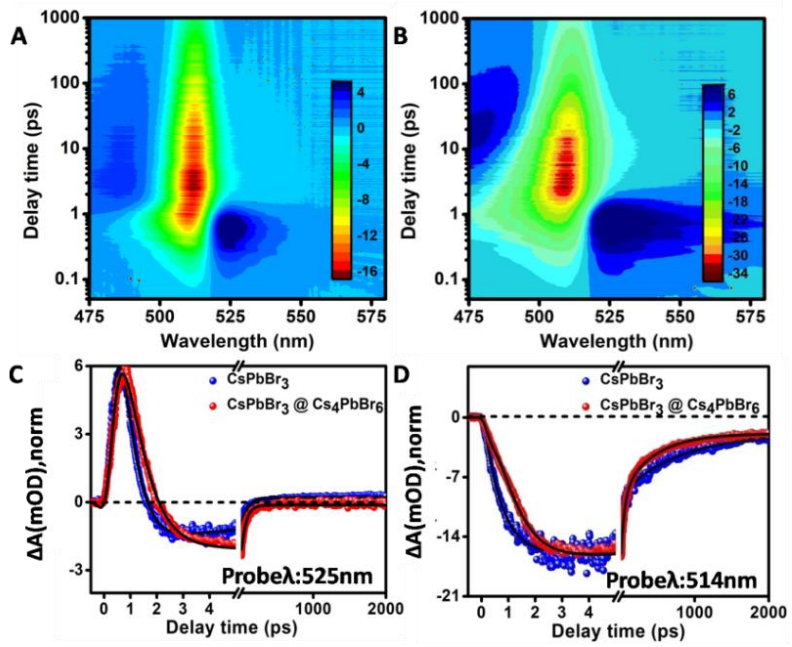

Figure 3.4 (A, B) Representative pseudo color plots depicting the extremely slow hot carrier cooling for $CsPbBr_3$ and $CsPbBr_3@Cs_4PbBr_6$ core-shell NC systems respectively under far above band gap energy excitation (λ_{ex} = 300 nm, ~ 4.1 eV). **(C, D)** Comparative kinetic traces for probe wavelength λ = 525 nm (positive band) and probe wavelength λ = 514 nm (bleach band) respectively.

The prominent broad photoinduced bleach (~514 nm) expands initially over a large range of wavelengths, then narrows down to a symmetric one, undergoes a red shift and grows as the charge carriers thermalize in instances of long probe delays. The shift in the bleach minimum over time suggests the involvement of continuum states which can be deconvoluted from the excitonic absorption,[28] shown in **figure 3.3 A and 3.3 B** (treatment shown only for $CsPbBr_3$ NCs). The bleach broadening is obvious due to the time taken to achieve quasi thermal distribution of the charge carriers in accordance with the difference between the carrier temperature (T_C) and the lattice temperature (T_L) (under dark condition). But there is a marked difference in the broadness of absorption linewidth (FWHM), which is much more diverse in case of $CsPbBr_3@Cs_4PbBr_6$ core- shell system ($\Delta\lambda \sim 60$ nm) as compared to the $CsPbBr_3$ system ($\Delta\lambda \sim 45$ nm), quite differentiable from the TA contour plot. This might be due to the pronounced delocalization of the charge carriers in the respective bands of both the core and shell since 4.1 eV excitation (300 nm) has the ample potential to excite the shell in addition to the instantaneous formation of excitons in the core. The resultant charge carriers generated immediately upon photoexcitation are more in number for both the systems in contrast to that observed in case of near band gap excitation. In comparison to the excitation of the NCs into the lower excitonic state, the TA spectral shape bears comparatively higher contribution from the PA signal during the initial time delays. The schematic diagram depicted in **figure 3.5 A** supports the explanation to the possible pathways viable among the hot charge carriers (both electron and hole) in the core and the shell that accounts as one of the reason for the observed difference in carrier cooling rates.

The apparent energy band gap shift ΔE_g^{BM} **(Figure 3.5 B)** produced as an immediate consequence of Burstein-Moss effect can be narrated quantitatively in terms of the following equation:[33]

$$\Delta E_g^{BM} = \frac{\hbar^2}{2m_{eh}^*}(3\pi^2 n)^{2/3} \qquad \textbf{Eq.3.1}$$

where, m_{eh}^* is the reduced effective exciton mass, ħ is the Planck constant (reduced), n is the charge carrier density. The injected charge carrier density ($n_{inj} \sim 10^{23}/cm^3$) is much more than the critical number required for the onset of the Burstein-Moss effect ($n_c \sim 10^{16}/cm^3$). The resultant energy band gap is the additive of the essential energy band gap and the shifted one. This equation gives a rigid evidence depicting the rough linear dependence of the band-gap shift on number of charge carriers. Thus, for the case of core-shell structure upon far band edge excitation, more number of charge carriers are confined into the core owing to the resultant

Type-1 band edge alignment henceforth, resulting in an overall enhanced spectral shift (BGR) during the early time delays.

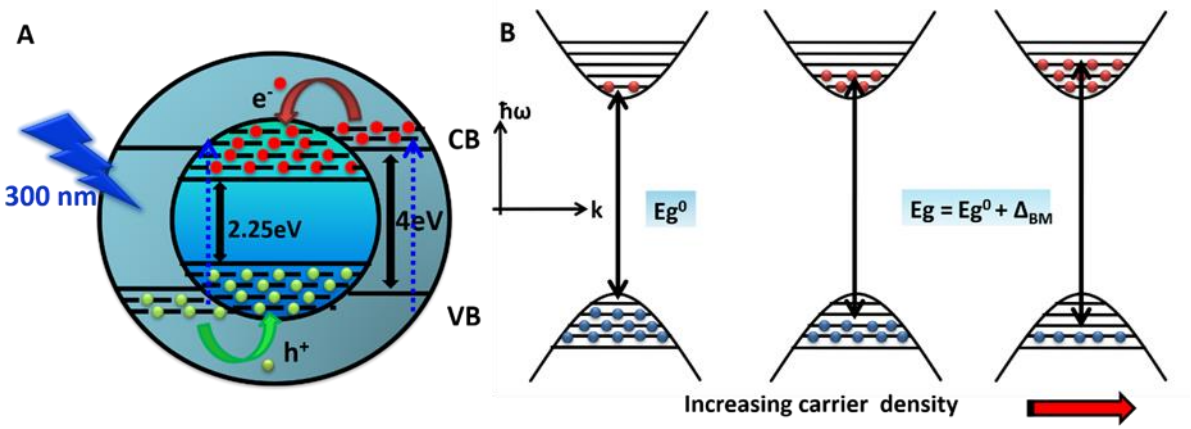

Figure 3.5. (A) The band energy alignment in $CsPbBr_3@Cs_4PbBr_6$ NCs showing the various probable processes can undergo on above band gap excitation. **(B)** Schematic representation of Burstein-Moss effect depicting the wideness of the energy band gap with different charge carrier density. (blue spheres represent the valence band electrons which upon photoexcitation move to the conduction band (red spheres) leaving behind the holes (vacant sites)).

Although, the effective electron and hole masses are nearly similar in these NCs, it has already been demonstrated that the TA signal withholds a major contribution from the electrons (67.2 %), rather than the holes because of the higher degeneracy in the valence band than the conduction band.[34] The bleach amplitude (ΔA) increases nonlinearly with the initial charge density which elucidates the much intense bleach for the core-shell system in contrast to $CsPbBr_3$, due to the increased number of charge carriers in the core for the core-shell system.[33] Also with the aid of the previous reports, it may not be wrong to assume that the oscillator strength in core-shell system is enhanced in comparison to the pure $CsPbBr_3$ system which can also add up to the highly intense bleach.[35]

Figure 3.4 C and 3.4 D indicate the comparison kinetics for both core and core-shell samples at 525 nm and 514 nm respectively and the corresponding kinetic traces are fitted multi-exponentially with the fitting constants mentioned in **(Table 3.2)**. Interestingly, unlike 480 nm excitation (pulse-width limited bleach growth), bleach at 514 nm can be fitted bi-exponentially with time constants, τ_{g1}= 0.12 ps (80 %) and τ_{g2}=0.7 ps (20 %) for $CsPbBr_3$ while for the core-shell system, the best fit can be done with time constants τ_{g1}=0.14 ps (46.8 %), τ_{g2}=0.35 ps (18.5 %), τ_{g3}= 1 ps (34.7 %). Near band gap excitation (480 nm), the carrier (electron) cooling is pulse width limited as the electrons are excited just above the band edge of $CsPbBr_3$ in both the cases. However, at 300 nm excitation both electrons and holes are

generated at high energy excitonic states and they take longer time to populate the band edge states, as a result bi-exponential growth with 120 fs and 700 fs time constants has been observed.

Most interestingly with the same 300 nm excitation bleach growth kinetics for the $CsPbBr_3$@Cs_4PbBr_6 core-shell found to be fitted with tri-exponential time constants 0.14 ps, 0.35 ps, and 1 ps, clearly suggesting slow carrier cooling in core-shell as compared to core $CsPbBr_3$. For core-shell NCs photo-excited generated hot charge carriers by 300 nm can be de-localized in the CB and VB of both $CsPbBr_3$ core and Cs_4PbBr_6 shell, so both the electrons and holes are de-coupled in core-shell structure as compared to pure core, which finally concentrate into the core taking extra time. As a result, carrier cooling time in core-shell NCs found to be much slower in core.

Table 3.2 Kinetics fitting parameters for $CsPbBr_3$ and $CsPbBr_3$@Cs_4PbBr_6 core-shell systems dispersed in n-hexane after exciting the samples at 300 nm.

System	Probe λ (nm)	τ_{growth}	τ_1	τ_2	τ_3	τ_4
$CsPbBr_3$	514	$\tau_{g1}=0.12$ ps (80 %), $\tau_{g2}=0.7$ ps (20%)	4.2 ps (-21%)	22 ps (-43%)	160 ps (-15%)	>1ns (-21%)
	525	$\tau_{g1}=0.12$ ps (80%)	0.52 ps (-100%)	28 ps (13%)	>1ns (7%)	
$CsPbBr_3$@ Cs_4PbBr_6	514	$\tau_{g1}=$ 0.14 ps (46.8%), $\tau_{g2}=0.35$ ps (18.5%), $\tau_{g3}=1$ ps (34.7%)	5 ps (-20%)	30 ps (-41%)	140 ps (-17%)	>1ns (-22%)
	525	$\tau_{g1}=0.14$ ps (79%)	0.58 ps (-100%)	13ps (11.5%)	90 ps (9.5%)	

3.2.3.3 *Hot carrier cooling dynamics*

Earlier, HC cooling dynamics in II-VI semiconductor core-shell has been demonstrated in various systems, where slow cooling was observed due to de-coupling of electron and hole in the core-shell structure.[36] However so far, there has not been any detailed discussion of hot carrier cooling kinetics in core-shell system involving $CsPbBr_3$ materials. So addressing the reason responsible for the observation of such extended cooling rate in $CsPbBr_3$@Cs_4PbBr_6

core shell is of great scientific interest. It is well known that the hot phonon bottleneck effect can take place in case of high excitation intensities which can retard the carrier cooling process. However in the present investigation, this possibility cannot be the governing factor for the slow carrier cooling here since the excitation intensity is not adequate enough for causing hot phonon bottleneck[22] (pump fluence ~20 uJ/cm^2). Another possible reason for this can be the presence of defect state in the core-shell structure, which can also be categorically ruled out since the Stokes' shift observed in the PL studies is negligible. Subsequently, the formation of the large polarons in the $CsPbBr_3@Cs_4PbBr_6$ core-shell NCs (discussed further in the later part of the chapter) may be held responsible for the deceleration in the cooling rate due to the prevalent strong FrÖhlich interactions.[37] In addition to this, enhanced delocalization of the charge carriers over the core as well as the shell also adds to increased cooling time in $CsPbBr_3@Cs_4PbBr_6$ core-shell NCs while exciting at higher energy excitation (300 nm). The difference in the carrier temperatures (above band gap excitation, in a way giving excessive energies to the carriers) monitored as a function of different probe time delays can assist in defining the difference in the carrier-cooling mechanisms in the above two systems under observation. The overall cooling process, which is basically a manifestation of numerous contributions is very complicated. This process includes the carrier-carrier (dephasing occurs in very short fs timescale which falls beyond femtosecond laser resolution), carrier-phonon, phonon-phonon scatterings.[38] But it is reported in the literature that particularly at early delay times (few hundreds of femtoseconds), it is the carrier-phonon coupling plays a major role towards the polaron formation.[17]

In order to ascertain that a quasi-equilibrium state (corresponding to quasi temperature T_C) has been attained by the redistribution of the kinetic energy among the hot charge carriers via carrier thermalization, the carrier recombination dynamics has been studied only after 400 fs delay. The similarity in the electron and hole mass ($m_h \sim m_e$) makes it quite convenient for us to consider the extracted temperature as the electron temperature.[33]

Since, the major interest of this chapter has been the study of the charge carrier cooling, thereafter the detailed study of the factors detrimental for deciding the charge carrier cooling rate is mandatory. Fundamentally, the high energy regime in the TA bleach gives a measure of the carrier temperature which is an outcome of the carrier scatterings. For the two systems under study, due to difference in bleach broadening as an immediate consequence of different number of charge carriers, this high energy bleach region required for the MB fitting for T_C extraction is different.

The hot carrier temperature T_e **(Figure 3.6)** can be estimated from the Maxwell-Boltzmann (MB) fitting of the high energy tail of the normalized TA data (since the Fermi Dirac distribution can be approximated to MB type of distribution for energies far above the Fermi energy), which can be quantitatively represented as,[33]

$$\Delta T(\hbar\omega) = -T_0\,(\hbar\omega)\exp\left(-\frac{\hbar\omega}{k_B T_e}\right) \qquad \textbf{Eq.3.2}$$

Here, ΔA stands for the bleach amplitude at a particular probe wavelength, k_B is the Boltzmann constant. For 300 nm excitation, the temporal evolution in the carrier temperature (T_e) in the conditions of same fluence is illustrated for both the systems in **figure 3.6**. It is found that as an immediate effect of the stronger carrier-phonon coupling in $CsPbBr_3$@Cs_4PbBr_6 core-shell system, the initial carrier temperature (T_e) for this system (1600 K) is more noticeable as compared to $CsPbBr_3$ NCs (460 K). Additionally, because of pretty larger number of charge carriers, the accumulation of the charge carriers over the lattice results in larger build-up of longitudinal optical (LO) phonons in case of $CsPbBr_3$@Cs_4PbBr_6 core-shell system, which is responsible for inelastic carrier-phonon interactions (Polar FrÖhlich interactions dominate these scatterings in polar crystals).

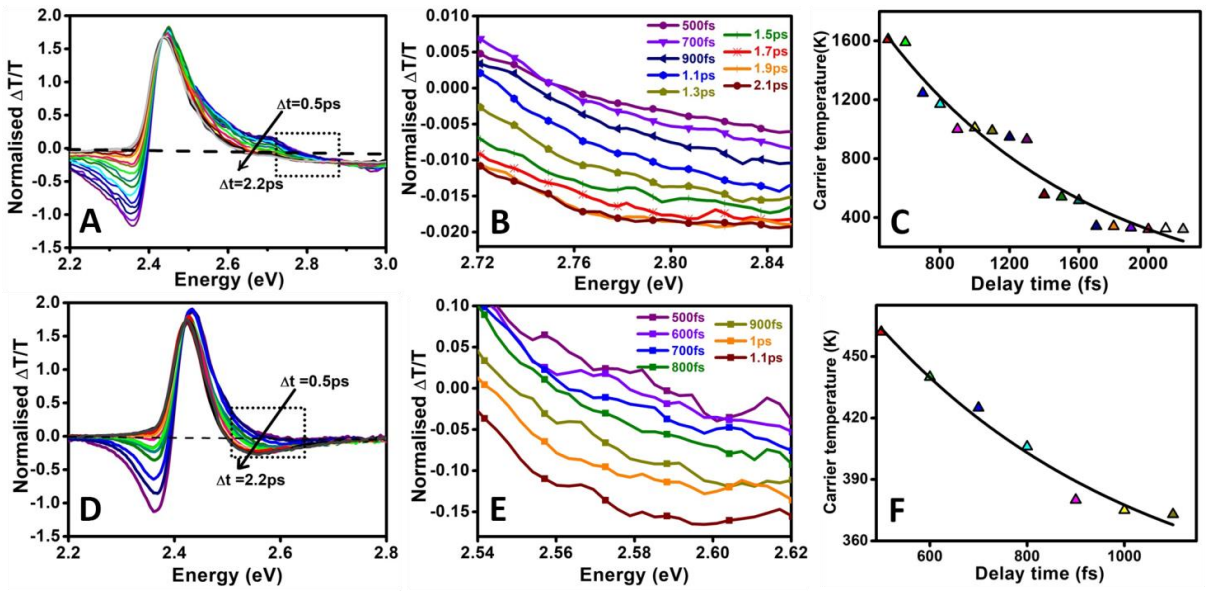

Figure 3.6 (A), (D) Normalised TA spectra under non-resonant pump excitation (300 nm) for varying probe delays (from 0.5 to 2.2 ps), the dashed boxes drawn show the high energy tail region over which Maxwell Boltzmann fitting has been done for $CsPbBr_3$@Cs_4PbBr_6 core-shell, $CsPbBr_3$ NCs respectively. **(B), (E)** show the magnified high energy tail region which have been fitted using Maxwell Boltzmann fitting to extract the T_e values. **(C), (F)** The corresponding temporal evolution of the carrier temperature T_e.

The LO phonons further decay to build-up a sea of acoustic phonons which interact with the carriers and affect their mobility.[38] Under the same energy used for excitation (300 nm), the $CsPbBr_3$@Cs_4PbBr_6 core-shell NCs show much longer hot carrier cooling time as compared to the $CsPbBr_3$ NCs**,** to achieve the lattice temperature. Higher energy pump excitation results inconsequently initial higher T_e for the charge carriers and hence the cooling times are comparatively longer for 300 nm pump excitation as compared to the 480 nm.

3.2.3.4 *Polaron formation*

The electronic as well as the optical properties,[39] exhibited by both the systems under study differ drastically. The pronounced disparity in the energy dispersion relations followed by the carriers in the two phases, viz. $CsPbBr_3$ and Cs_4PbBr_6 decoupled $[PbBr_6]^{4-}$ octahedral in Cs_4PbBr_6 in contrast to the corner shared octahedral network in $CsPbBr_3$ can be held responsible for such differences.[40] As an immediate consequence of this, the charge carrier wave-functions localization differ largely for the $CsPbBr_3$ and Cs_4PbBr_6 phases.[41] It has been found in the literature from the DFT studies[37] conducted for $CsPbBr_3$, with electron-hole interactions taken into consideration, that the excitonic wave-functions are delocalised over the lattice ion sites. Such a delocalisation can be explained as an outcome of small exciton binding energy. In contrast to this, for the higly polar Cs_4PbBr_6 phase shell, as a consequence of higher exciton binding energy (160 meV), the electron-hole interactions are much enhanced, as a result of which ,strong confinement has been observed in this material. This strong confinement results in the localisation of excitons over the octahedral unit $[PbBr_6]^{4-}$ Furthermore, due to the presence of an additional charge in Cs_4PbBr_6 shell lattice (highly polar), carrier-phonon couplings are more pronounced in core-shell as compared to $CsPbBr_3$.[42] The outcome of the localization (due to stronger confinement, as a consequence of higher binding energy) of this extra charge over a very small volume is the local lattice site disturbances (phonon emissions) resulting in the formation of FrÖhlich polarons in these 0D perovskite NCs.[43] With the theoretical support from the hybrid-DFT calculations, it has been claimed previously that there are some polaronic features observable in Cs_4PbBr_6 which are missing in $CsPbBr_3$ phase. It has been observed theoretically employing the single unit model that for Cs_4PbBr_6, a positive absorption band appearing towards the extreme low energy side of the bleach can be attributed to the polaron absorption.[37]

The dispersive band features of $CsPbBr_3$ are such that they hinder the localization of charge carriers, so the carriers remain free.[41] Even after the excitons are formed spontaneous

to photoexcitation, the excitons can dissociate in no time to yield free charge carriers, thus annihilating any chance for polaron formation. This is not the case with the 0D Cs_4PbBr_6 shell phase, where the excitons do not easily dissociate due to large exciton binding energy. Here, charge carrier are quite prone to trapping due to stronger quantum confinement and near non-dispersive transport.[44,45] Due to this, the original crystal lattice is spontaneously deformed and the carrier-longitudinal optical phonon coupling (which lasts for ~1 ps) leads to the formation of large polarons. These LO phonons give off their energy as acoustic phonons (over few ps).[46,47] This leads to the observation of large polarons in core-shell systems, manifested as a broad positive feature towards the lower energy region of the observed bleach, which scarcely last only for 3 ps since the longitudinal phonons decay in this time scale.

The observed time scale of polaron formation goes well with the previous reported lifetimes of the polarons observed in the similar spectral spread.[39] There is no such significant positive band observed for the $CsPbBr_3$ NCs across the spectral range beyond 560 nm. The difference can be clearly seen from the early time transient kinetics probed at 550 nm **(Figure 3.7)**.

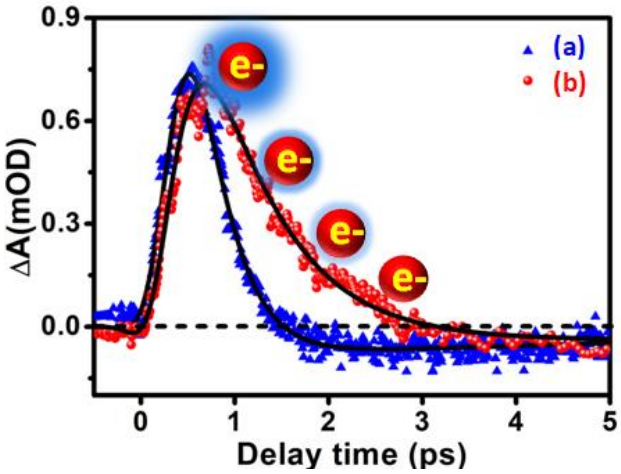

Figure 3.7 Normalized photo induced absorption kinetics of the (a) $CsPbBr_3$ and (b) $CsPbBr_3$@Cs_4PbBr_6 core-shell NCs probed at 550 nm during early time scale (the black solid lines gives the best fit eligible for the corresponding kinetic traces)**.** The electron covered by the phonon cloud implicates the polaron formation followed by the polaron decay in correspondence to the approximate time scale for the events.

As an immediate consequence of the dressing of the charge carriers by the LO phonons, forming the large polarons in the Cs_4PbBr_6 shell, the charge carriers localization over the lattice sites results in reduced mobility of the charge carriers and increased effective mass of the charge carriers. The large carrier-phonon interactions (FrÖhlich) hinder the easy movement of

the carriers. Undoubtedly, the increase in the effective mass of the charge carrier is not much, but it is adequate enough to compensate for the reduction in the charge carrier-LO phonon scattering and account for the decreased mobility, thus increasing the overall time taken by the hot carriers to cool down.[48]

For $CsPbBr_3$, the kinetics follow the trend as followed by biexciton induced effect. The competition between the two opposing processes i.e., initial hot carrier cooling and polaron formation decide the ultimate fate of the charge carriers. For the CsPbBr3@Cs_4PbBr_6 system, since the carriers take longer time to cool down to the band edges, so the interaction of these carriers with the LO phonons is magnified and hence, the polaron formation process triumphs. The high value of exciton binding energy as well as the extreme ionic character of the 0D perovskite favors the polaron formation because of extremely high exciton-phonon coupling. The 3D counterparts do not allow the accumulation of longitudinal phonons, consequently there is no strong exciton-phonon coupling possible in these materials.

3.3 Summary

In summary in this chapter, we have attempted to further decelerate the cooling rate of the charge carriers in the $CsPbBr_3$ system by facilitating the system to undergo Type-1 decay as a consequence of coating a high band gap material, Cs_4PbBr_6, providing the desired band offsets. Here, ultrafast spectroscopy has played a vital role to unwind the complicated underlying photo-physics ruling the unique carrier dynamics just after photoexcitation. There are clear evidences of polaron formation in the femtosecond TA data of the core-shell system which is much suppressed in case of $CsPbBr_3$. This knowledge can be steered to drive towards the achievement of higher V_{oc}, which is a commanding factor detrimental for the efficiency of the solar cell. It can be anticipated that the detailed insights into the hot carrier cooling mechanism and the subsequent retarded carrier cooling discussion provided in this work can assist in the manifestation of these core-shell systems as absorbing layer in real time stable photovoltaic devices. Also, such systems may be looked upon as the ideal candidates for the realization of hot carrier extraction based applications.

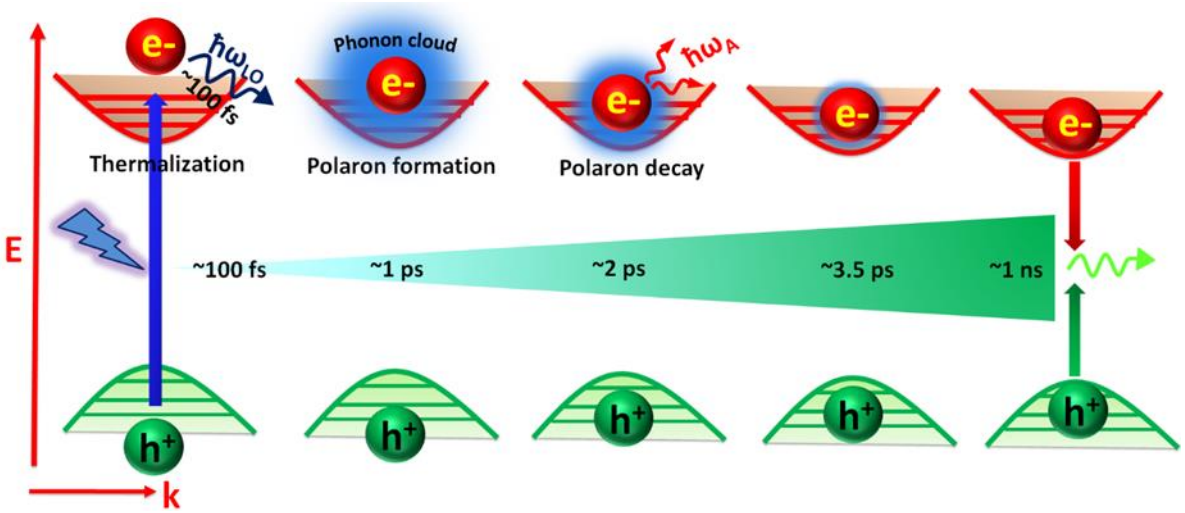

"Polaron formation and decay dynamics followed by the charge carriers in $CsPbBr_3$@ Cs_4PbBr_6 core-shell NCs"

3.4 References

(1) Protesescu, L.; Yakunin, S.; Bodnarchuk, M. I.; Krieg, F.; Caputo, R.; Hendon, C. H.; Yang, R. X.; Walsh, A.; Kovalenko, M. V. Nanocrystals of Cesium Lead Halide Perovskites ($CsPbX_3$, X = Cl, Br, and I): Novel Optoelectronic Materials Showing Bright Emission with Wide Color Gamut. *Nano Lett* **2015**, *15* (6), 3692–3696.

(2) Zhang, X.; Lin, H.; Huang, H.; Reckmeier, C.; Zhang, Y.; Choy, W. C. H.; Rogach, A. L. Enhancing the Brightness of Cesium Lead Halide Perovskite Nanocrystal Based Green Light-Emitting Devices through the Interface Engineering with Perfluorinated Ionomer. *Nano Lett* **2016**, *16* (2), 1415–1420.

(3) Yettapu, G. R.; Talukdar, D.; Sarkar, S.; Swarnkar, A.; Nag, A.; Ghosh, P.; Mandal, P. Terahertz Conductivity within Colloidal $CsPbBr_3$ Perovskite Nanocrystals: Remarkably High Carrier Mobilities and Large Diffusion Lengths. *Nano Lett* **2016**, *16* (8), 4838–4848.

(4) Akkerman, Q. A.; D'Innocenzo, V.; Accornero, S.; Scarpellini, A.; Petrozza, A.; Prato, M.; Manna, L. Tuning the Optical Properties of Cesium Lead Halide Perovskite Nanocrystals by Anion Exchange Reactions. *J Am Chem Soc* **2015**, *137* (32), 10276–10281.

(5) Maes, J.; Balcaen, L.; Drijvers, E.; Zhao, Q.; De Roo, J.; Vantomme, A.; Vanhaecke, F.; Geiregat, P.; Hens, Z. Light Absorption Coefficient of $CsPbBr_3$ Perovskite Nanocrystals. *J Phys Chem Lett* **2018**, *9* (11), 3093–3097.

(6) Kang, J.; Wang, L.W. High Defect Tolerance in Lead Halide Perovskite $CsPbBr_3$. *J Phys*

Chem Lett **2017**, *8* (2), 489–493.

(7) Manser, J. S.; Christians, J. A.; Kamat, P. V. Intriguing Optoelectronic Properties of Metal Halide Perovskites. *Chem Rev* **2016**, *116* (21), 12956–13008.

(8) Swarnkar, A.; Chulliyil, R.; Ravi, V. K.; Irfanullah, M.; Chowdhury, A.; Nag, A. Colloidal $CsPbBr_3$ Perovskite Nanocrystals: Luminescence beyond Traditional Quantum Dots. *Angew Chemie Int Ed* **2015**, *54* (51), 15424–15428.

(9) Huang, C.Y.; Wu, C.C.; Wu, C.L.; Lin, C.W. $CsPbBr_3$ Perovskite Powder, a Robust and Mass-Producible Single-Source Precursor: Synthesis, Characterization, and Optoelectronic Applications. *ACS Omega* **2019**, *4* (5), 8081–8086.

(10) Xin, B.; Pak, Y.; Mitra, S.; Almalawi, D.; Alwadai, N.; Zhang, Y.; Roqan, I. S. Self-Patterned $CsPbBr_3$ Nanocrystals for High-Performance Optoelectronics. *ACS Appl Mater Interfaces* **2019**, *11* (5), 5223–5231.

(11) Fu, Y.; Zhu, H.; Chen, J.; Hautzinger, M. P.; Zhu, X.Y.; Jin, S. Metal Halide Perovskite Nanostructures for Optoelectronic Applications and the Study of Physical Properties. *Nat Rev Mater* **2019**, *4* (3), 169–188.

(12) Wang, H.; Zhang, X.; Wu, Q.; Cao, F.; Yang, D.; Shang, Y.; Ning, Z.; Zhang, W.; Zheng, W.; Yan, Y.; et al. Trifluoroacetate Induced Small-Grained $CsPbBr_3$ Perovskite Films Result in Efficient and Stable Light-Emitting Devices. *Nat Commun* **2019**, *10* (1), 665.

(13) Liu, H.; Xiang, L.; Gao, P.; Wang, D.; Yang, J.; Chen, X.; Li, S.; Shi, Y.; Gao, F.; Zhang, Y. Improvement Strategies for Stability and Efficiency of Perovskite Solar Cells. *Nanomaterials*. 2022.

(14) Price, M. B.; Butkus, J.; Jellicoe, T. C.; Sadhanala, A.; Briane, A.; Halpert, J. E.; Broch, K.; Hodgkiss, J. M.; Friend, R. H.; Deschler, F. Hot-Carrier Cooling and Photoinduced Refractive Index Changes in Organic–Inorganic Lead Halide Perovskites. *Nat Commun* **2015**, *6*, 8420.

(15) Shen, Q.; Ripolles, T. S.; Even, J.; Ogomi, Y.; Nishinaka, K.; Izuishi, T.; Nakazawa, N.; Zhang, Y.; Ding, C.; Liu, F.; et al. Slow Hot Carrier Cooling in Cesium Lead Iodide Perovskites. *Appl Phys Lett* **2017**, *111* (15), 153903.

(16) Xing, G.; Mathews, N.; Sun, S.; Lim, S. S.; Lam, Y. M.; Grätzel, M.; Mhaisalkar, S.; Sum, T. C. Long-Range Balanced Electron- and Hole-Transport Lengths in Organic-Inorganic $CH_3NH_3PbI_3$. *Science* **2013**, *342* (6156), 344 LP – 347.

(17) Fu, J.; Xu, Q.; Han, G.; Wu, B.; Huan, C. H. A.; Leek, M. L.; Sum, T. C. Hot Carrier Cooling Mechanisms in Halide Perovskites. *Nat Commun* **2017**, *8* (1), 1300.

(18) Joshi, P. P.; Maehrlein, S. F.; Zhu, X. Dynamic Screening and Slow Cooling of Hot Carriers in Lead Halide Perovskites. *Adv Mater* **2019**, *0* (0), 1803054.

(19) Heitz, R.; Born, H.; Guffarth, F.; Stier, O.; Schliwa, A.; Hoffmann, A.; Bimberg, D. Existence of a Phonon Bottleneck for Excitons in Quantum Dots. *Phys Rev B* **2001**, *64* (24), 241305.

(20) Li, X.Q.; Nakayama, H.; Arakawa, Y. Phonon Bottleneck in Quantum Dots: Role of Lifetime of the Confined Optical Phonons. *Phys Rev B* **1999**, *59* (7), 5069–5073.

(21) Yang, Y.; Ostrowski, D. P.; France, R. M.; Zhu, K.; van de Lagemaat, J.; Luther, J. M.; Beard, M. C. Observation of a Hot-Phonon Bottleneck in Lead-Iodide Perovskites. *Nat Photonics* **2015**, *10*, 53.

(22) Chen, J.; Messing, M. E.; Zheng, K.; Pullerits, T. Cation-Dependent Hot Carrier Cooling in Halide Perovskite Nanocrystals. *J Am Chem Soc* **2019**, *141* (8), 3532–3540.

(23) Jia, C.; Li, H.; Meng, X.; Li, H. $CsPbX_3/Cs_4PbX_6$ Core/Shell Perovskite Nanocrystals. *Chem Commun* **2018**, *54* (49), 6300–6303.

(24) Wei, K.; Zheng, X.; Cheng, X.; Shen, C.; Jiang, T. Observation of Ultrafast Exciton–Exciton Annihilation in $CsPbBr_3$ Quantum Dots. *Adv Opt Mater* **2016**, *4* (12), 1993–1997.

(25) De Bastiani, M.; Dursun, I.; Zhang, Y.; Alshankiti, B. A.; Miao, X.-H.; Yin, J.; Yengel, E.; Alarousu, E.; Turedi, B.; Almutlaq, J. M.; et al. Inside Perovskites: Quantum Luminescence from Bulk Cs_4PbBr_6 Single Crystals. *Chem Mater* **2017**, *29* (17), 7108–7113.

(26) Li, X.; Wu, Y.; Zhang, S.; Cai, B.; Gu, Y.; Song, J.; Zeng, H. Quantum Dots: $CsPbX_3$ Quantum Dots for Lighting and Displays: Room-Temperature Synthesis, Photoluminescence Superiorities, Underlying Origins and White Light-Emitting Diodes. *Adv Funct Mater* **2016**, *26* (15), 2584.

(27) Oum, K.; Lenzer, T.; Scholz, M.; Jung, D. Y.; Sul, O.; Cho, B. J.; Lange, J.; Müller, A. Observation of Ultrafast Carrier Dynamics and Phonon Relaxation of Graphene from the Deep-Ultraviolet to the Visible Region. *J Phys Chem C* **2014**, *118* (12), 6454–6461.

(28) Aneesh, J.; Swarnkar, A.; Kumar Ravi, V.; Sharma, R.; Nag, A.; Adarsh, K. V. Ultrafast Exciton Dynamics in Colloidal $CsPbBr_3$ Perovskite Nanocrystals: Biexciton Effect and Auger Recombination. *J Phys Chem C* **2017**, *121* (8), 4734–4739.

(29) Li, B.; Huang, H.; Zhang, G.; Yang, C.; Guo, W.; Chen, R.; Qin, C.; Gao, Y.; Biju, V. P.; Rogach, A. L.; et al. Excitons and Biexciton Dynamics in Single $CsPbBr_3$ Perovskite Quantum Dots. *J Phys Chem Lett* **2018**, *9* (24), 6934–6940.

(30) Wang, D.; Dignam, M. M.; Hawton, M. Phase Space Filling Effects on Exciton Dynamics. In *Conference on Lasers and Electro-Optics/Quantum Electronics and Laser Science and Photonic Applications Systems Technologies*; Technical Digest (CD); Optical Society of America: Baltimore, Maryland, 2005; p JThE119.

(31) Yumoto, G.; Tahara, H.; Kawawaki, T.; Saruyama, M.; Sato, R.; Teranishi, T.; Kanemitsu, Y. Hot Biexciton Effect on Optical Gain in $CsPbI_3$ Perovskite Nanocrystals. *J Phys Chem Lett* **2018**, *9* (9), 2222–2228.

(32) Dana, J.; Maity, P.; Jana, B.; Maiti, S.; Ghosh, H. N. Concurrent Ultrafast Electron- and Hole-Transfer Dynamics in $CsPbBr_3$ Perovskite and Quantum Dots. *ACS Omega* **2018**, *3* (3), 2706–2714.

(33) Manser, J. S.; Kamat, P. V. Band Filling with Free Charge Carriers in Organometal Halide Perovskites. *Nat Photonics* **2014**, *8*, 737.

(34) Wu, K.; Liang, G.; Shang, Q.; Ren, Y.; Kong, D.; Lian, T. Ultrafast Interfacial Electron and Hole Transfer from $CsPbBr_3$ Perovskite Quantum Dots. *J Am Chem Soc* **2015**, *137* (40), 12792–12795.

(35) Xu, J.; Huang, W.; Li, P.; Onken, D. R.; Dun, C.; Guo, Y.; Ucer, K. B.; Lu, C.; Wang, H.; Geyer, S. M.; et al. Imbedded Nanocrystals of $CsPbBr_3$ in Cs_4PbBr_6: Kinetics, Enhanced Oscillator Strength, and Application in Light-Emitting Diodes. *Adv Mater* **2017**, *29* (43), 1703703.

(36) Maiti, S.; Debnath, T.; Maity, P.; Ghosh, H. N. Lattice-Strain-Induced Slow Electron Cooling Due to Quasi-Type-II Behavior in Type-I CdTe/ZnS Nanocrystals. *J Phys Chem C* **2015**, *119* (15), 8410–8416.

(37) Yin, J.; Maity, P.; De Bastiani, M.; Dursun, I.; Bakr, O. M.; Brédas, J. L.; Mohammed, O. F. Molecular Behavior of Zero-Dimensional Perovskites. *Sci Adv* **2017**, *3* (12), 2–10.

(38) Li, M.; Bhaumik, S.; Goh, T. W.; Kumar, M. S.; Yantara, N.; Grätzel, M.; Mhaisalkar, S.; Mathews, N.; Sum, T. C. Slow Cooling and Highly Efficient Extraction of Hot Carriers in Colloidal Perovskite Nanocrystals. *Nat Commun* **2017**, *8* (May), 3–12.

(39) Cha, J.-H.; Han, J. H.; Yin, W.; Park, C.; Park, Y.; Ahn, T. K.; Cho, J. H.; Jung, D.-Y. Photoresponse of $CsPbBr_3$ and Cs_4PbBr_6 Perovskite Single Crystals. *J Phys Chem Lett* **2017**, *8* (3), 565–570.

(40) Almutlaq, J.; Yin, J.; Mohammed, O. F.; Bakr, O. M. The Benefit and Challenges of Zero-Dimensional Perovskites. *J Phys Chem Lett* **2018**, *9* (14), 4131–4138.

(41) Kang, B.; Biswas, K. Exploring Polaronic, Excitonic Structures and Luminescence in $Cs_4PbBr_6/CsPbBr_3$. *J Phys Chem Lett* **2018**, *9* (4), 830–836.

(42) Chen, Y.; Yi, H. T.; Wu, X.; Haroldson, R.; Gartstein, Y. N.; Rodionov, Y. I.; Tikhonov, K. S.; Zakhidov, A.; Zhu, X.Y.; Podzorov, V. Extended Carrier Lifetimes and Diffusion in Hybrid Perovskites Revealed by Hall Effect and Photoconductivity Measurements. *Nat Commun* **2016**, *7*, 12253.

(43) Yin, J.; Li, H.; Cortecchia, D.; Soci, C.; Brédas, J.-L. Excitonic and Polaronic Properties of 2D Hybrid Organic–Inorganic Perovskites. *ACS Energy Lett* **2017**, *2* (2), 417–423.

(44) Steinleitner, P.; Merkl, P.; Nagler, P.; Mornhinweg, J.; Schüller, C.; Korn, T.; Chernikov, A.; Huber, R. Direct Observation of Ultrafast Exciton Formation in a Monolayer of WSe_2. *Nano Lett* **2017**, *17* (3), 1455–1460.

(45) Xiao, Z.; Meng, W.; Wang, J.; Mitzi, D. B.; Yan, Y. Searching for Promising New Perovskite-Based Photovoltaic Absorbers: The Importance of Electronic Dimensionality. *Mater Horizons* **2017**, *4* (2), 206–216.

(46) The Principal Quasi-Particles in Material Physics. In *Solid-State Physics for Electronics*; 2009; pp 335–383.

(47) Yang, J.; Wen, X.; Xia, H.; Sheng, R.; Ma, Q.; Kim, J.; Tapping, P.; Harada, T.; Kee, T. W.; Huang, F.; et al. Acoustic-Optical Phonon up-Conversion and Hot-Phonon Bottleneck in Lead-Halide Perovskites. *Nat Commun* **2017**, *8*, 14120.

(48) Bretschneider, S. A.; Ivanov, I.; Wang, H. I.; Miyata, K.; Zhu, X.; Bonn, M. Quantifying Polaron Formation and Charge Carrier Cooling in Lead-Iodide Perovskites. *Adv Mater* **2018**, *30* (29), 1–8.

Chapter 4

Temperature Dependent Interplay of Polaron formation and Hot Carrier Cooling Dynamics in $CsPbBr_3$ Nanocrystals: Role of Carrier-Phonon Coupling Strength

Photovoltaic devices lodged with $CsPbBr_3$ nanocrystals as the working layer are generally subjected to wide variant of extreme temperatures whilst under operation. Thus, the underlying photo-physics which is undeniably a temperature dependent entity demands intricate understanding. Here in this finding, with the assistance of temperature dependent transient absorption spectroscopy, an endeavour has been made to disentangle the detrimental conflict between polaron formation and hot carrier relaxation for $CsPbBr_3$ nanocrystals system. Carrier relaxation pathways are seen to diverge drastically upon varying the lattice temperature from 300 K to 5 K. Acquired results indicate the involvement of polaron for retarded carrier cooling dynamics observed at 300 K whereas its absence at lower temperatures (< 200 K) provides the ground for relatively quicker cooling. Additionally, despite the expected participation from the polaron due to onset of strong carrier-longitudinal optical phonon coupling at 200 K, reason for its non-indulgence in the cooling dynamics at 200 K has been unfolded.

4.1 Motivation and Background

Ever since the revolutionary breakthrough made by the solid state perovskite solar cell discovery in 2012,[1,2] the all inorganic lead halide perovskites (LHPs) ($CsPbX_3$, X=Br, Cl or I) have enjoyed overwhelming attention from the scientific forefront. Thereafter, the subsequent years have witnessed an unprecedented, progression in figures, indicative of number of concerned reports. The counterintuitively high photoluminescence (PL),[3,4] extended carrier diffusion length,[5] remarkably low trap concentration and unusually positioned trap states are merely a few of the highlighted assets that rank these materials above the conventional exemplary photovoltaic and optically relevant materials.[6,7] As an addendum to these miscellaneous attributes, their exceptionally relaxed carrier cooling has lately been the subject matter of plenitude of literature reports after Xing *et al.* published the earliest work in this regard in 2013 w.r.t. $CH_3NH_3PbI_3$.[5]Anticipation further suggests that the approach towards utilisation of this decelerated cooling for HC extraction can be strategically steered for crafting HC based devices, driving further intrigue into probing these materials.

Hot phonon bottleneck and Auger heating have been the long-standing answers for this sluggish relaxation.[8-10] However, at comparatively lower carrier densities, plentiful reports have outlined FrÖhlich polaron formation as the chief ground that adversely affects the effective carrier masses and thereby the cooling rate.[11,12] Amongst all widely discussed perovskites, the engaging native photo-physics in the else well-studied $CsPbBr_3$ NCs has so far been a missing clause that hinders the exploitation of such advantageous cooling rate.[13-15] This carrier relaxation is primarily driven by the coupling of the carriers with the available phonon modes. However, energetically diverse phonon modes manifest themselves in distinct manners at different temperatures, thus altering the effective carrier-phonon coupling strength.[16] This varied correlation of carriers with different phonon modes is a pivotal factor not merely for polaron formation but also in driving rapid cooling of the HCs.[17,18] Hence, temperature variant investigations into such processes offer new ventures which otherwise remain obscure at room temperature.[19] The insights delivered by similar preceding work in relevance to $CsPbBr_3$ conducted by Miyata *et al.*, claim polaron formation to be incompetent *w.r.t* HC cooling, with the studies restricted simply to room temperature.[20] Evan *et al.* further investigated this conflict of disparate mechanisms with added temperature dependent perspective, demonstrating both the processes to be fairly temperature dependent. Likewise, results from these investigations held agreement with inferences drawn by Miyata *et al.* despite the finding that the polaron formation rate fastens upon raising the temperature.[21]

With only few reports emphasising on deciphering such temperature dependent interplay in $CsPbBr_3$ NCs, the complicated picture of evolution of polaron and HC cooling with carrier-phonon coupling has so far missed an insightful surveillance. The present finding, relying on temperature dependent TA measurements of $CsPbBr_3$ NCs attempts to address the specific relevant process dominating the dynamics at different lattice temperatures. Drastic variation in carrier relaxation mechanisms is identified upon varying the lattice temperature from 300 K to 5 K. At 300 K, the observed retarded cooling reflects the anticipated indulgence of polaron abstaining HCs to follow rapid cooling dynamics, which clearly indicates polaron formation process dominating over HC cooling at such temperatures. Contrarily, HC cooling is entrusted as the only prevailing process at cryogenic temperatures owing to the inability to form polarons. Further, it is seen that nearby the onset of strengthened carrier- LO phonon coupling, the competition becomes more engaging. It is believed that this featured discussion concerning polaron formation influencing the charge carrier cooling rate can prove strategically advantageous towards technological evolution.

4.2 Results and discussion

4.2.1 Sample preparation

To begin with, $CsPbBr_3$ NCs were prepared following hot-injection synthesis method as already discussed in Chapter 2. All the investigations executed in this present chapter have been undertaken using uniform film of the prepared sample. In order to prepare the required film, colloidal $CsPbBr_3$ solution was spin coated over the glass substrate (1cm x 1cm) at rate of 1000 rpm for 30s, followed by 2000 rpm for 10s.To ensure a uniform deposition of the multiple layers of $CsPbBr_3$, this entire process was repeated thrice and the sample was left to dry in vacuum oven at room temperature for approximately 10min in the period between two successive depositions.

4.2.2 Steady state optical absorption & crystallographic studies

The optical absorption data acquired for the representative $CsPbBr_3$ deposited film bears a sharp onset at the energetic position of 2.48 eV due to absorption from 1S exciton **(Figure 4.1 A)**. The peak positions in the X-ray diffraction pattern **(Figure 4.1 B)** certainly confirm that the NCs crystallize in the orthorhombic phase $CsPbBr_3$ (*Pnma* space group; 'a'~ 8.18 Å, 'b'~ 8.22 Å and 'c' ~ 11.72 Å, d-spacing 0.24 nm).The obtained data is at par with the standard reference data file(PDF-01-072-7929), clearly establishing the formation of $CsPbBr_3$.

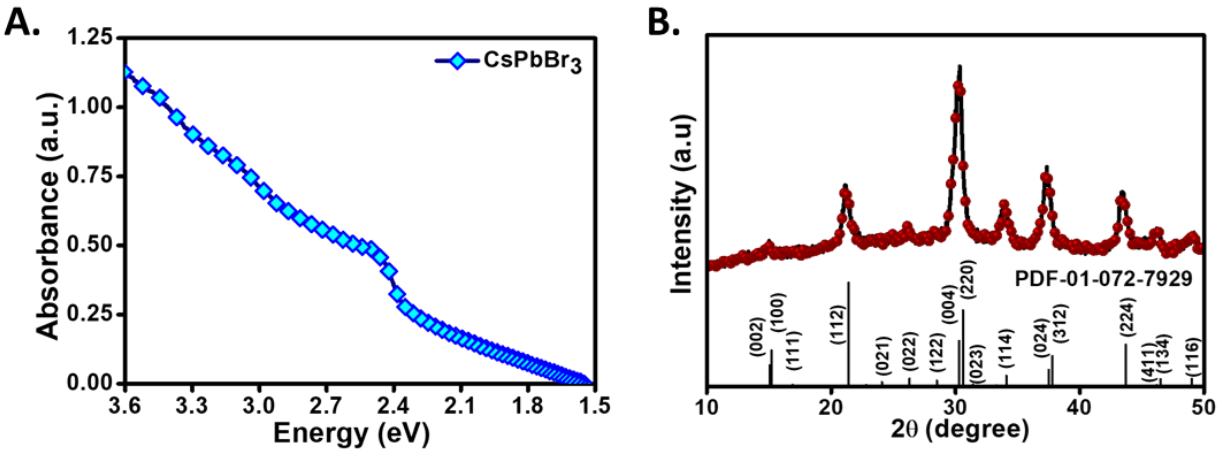

Figure 4.1 (A) Absorption spectrum of the $CsPbBr_3$ NCs deposited over the glass substrate via spin-coating. **(B)** Powder X-Ray Diffraction pattern for the as deposited $CsPbBr_3$ film.

4.2.3 Temperature dependent Photoluminescence studies

As previously stated, the foremost aspect of the present investigation is to unfold the critical role of the temperature dependent carrier-phonon coupling strength in laying the foundation of the varied HC cooling rates observed for different lattice temperatures. So, to get a preliminary impression of the temperature dependence of carrier-phonon coupling strength, we employed photoluminescence as an initial characterisation. The excitation energy (3.54 eV) employed for PL investigation was same as that for TA studies.

The PL spectral width **(Figure 4.2A)** when examined close to 300 K and that at utterly low temperature (5 K) reveals a striking contrast. We attribute this to the involvement of energetically diverse modes which appends to overall PL broadness **(Figure 4.2A)**. Extension of PL spectrum towards higher energies (regime 2), evidently indicates the involvement of higher energy phonon modes. However, when the lattice is almost frozen at extremely low temperature (kT<< 16meV), the lattice vibration is inadequate enough to accommodate any high frequency *viz*. the LO mode (Raman analysis proposes LO phonon energies of an order close to 16 meV[22] or 19 meV[6] for $CsPbBr_3$) thus limiting the PL line width. Further, the almost monotonous trend of line width **(Figure 4.2 B)** showcased for low temperatures (Regime1-acoustic phonon exciton coupling) affirms the abundance of only the low energy *i.e.* acoustic phonons (<10 meV) in equivalence with the equation mentioned in earlier literature records,[19]

$$\Gamma = \Gamma_0 + \Gamma_{AC}T + \frac{\Gamma_{LO}}{e^{(\hbar\omega - kT)}} \qquad \textbf{Eq.4.1}$$

where, Γ_0 stands for the inevitable inhomogeneous widening, Γ_{AC} and Γ_{LO} imply the broadening arising as a response to the coupling of excitons to acoustic and LO phonons correspondingly.

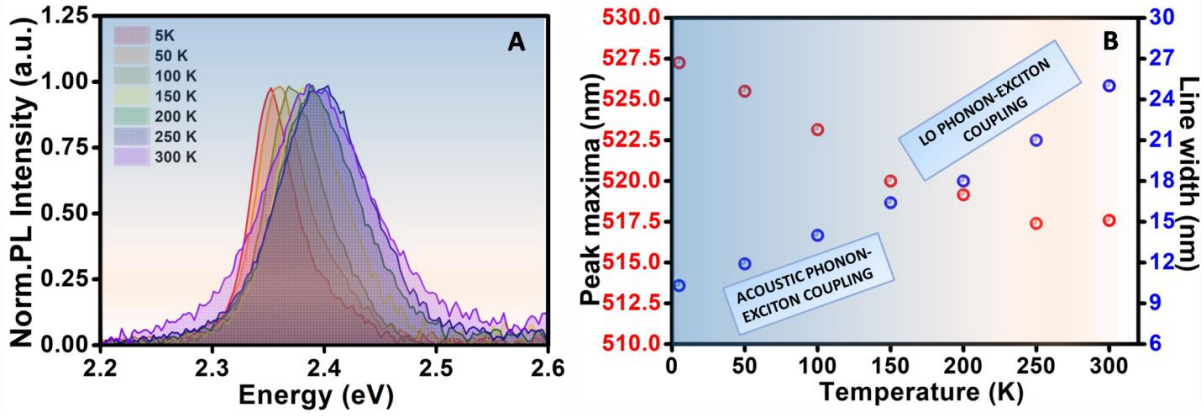

Figure 4.2 (A) Normalised temperature dependent PL plots for $CsPbBr_3$ NC film. (**B)** The quantitative shift in the peak maxima and the altered PL linewidth tracked as a function of temperature, representing the two sections of the probed temperature region over which the different couplings dominate distinctly (Regime 1 (5 K-200 K), Regime 2 (200 K-300 K)).

As temperature is raised, for the period of transition from 150 K (12 meV) to 200 K (16 meV), we however encountered a discontinuity in the otherwise monotonous trend of line width. Such discontinuity has also been observed in the previous reports concerned with the temperature dependent PL study in $CsPbBr_3$ system, where two different slopes have been encountered in the temperature dependency of line width in the region around the inflection point.[23] This can be justified as that for high lattice temperatures, when the equivalent thermal energy k_BT exceeds $\hbar\omega_{LO}$, the LO phonons (augments carrier-LO phonon interaction) become plentifully abundant, assuring an impactful FrÖhlich interaction.[16,24] An added intriguing aspect is the PL spectral shape. It bears contribution from the bound exciton feature at low temperatures **(Figure 4.3)**.

The temperature dependent PL spectra were extracted from the differential absorption data itself at a time scale much prior to the spectral overlap of the pump and the probe beams. An advantage provided by these low temperature PL studies is that the interference from the thermal complexities can be readily subdued. Also, these studies provide a profound opportunity to watchfully separate the contributions stemming from the acoustic and the optical phonons. The disproportionate non-Lorentzian PL spectra examined at 5 K is the sum of two overlying Gaussian peaks, one with its centre lying at 2.35 eV originating from the bound exciton and the other centered at 2.43 eV which originates from free exciton **(Figure 4.3)**.

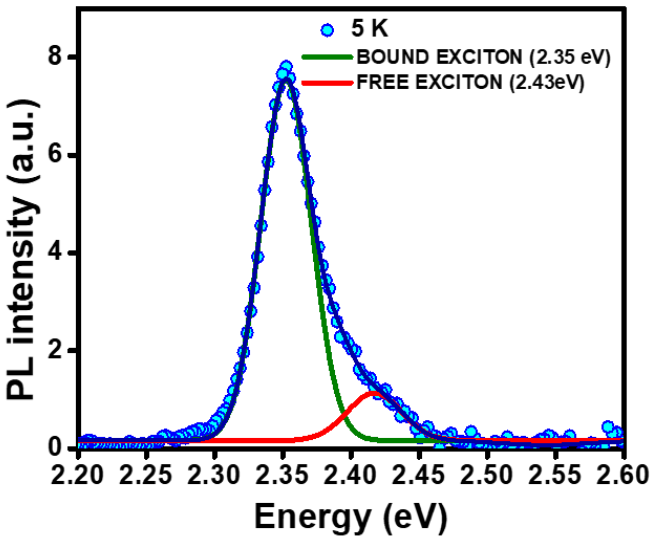

Figure 4.3 The deconvoluted non- Lorentzian PL spectrum (5 K) presenting the contribution from the two Gaussian peaks coming up from the bound exciton and the free exciton.

With the assistance of the reported literature, the assignment of the low energy peak to bound exciton can be duly claimed.[29] Notably, the amplitude of the deconvoluted peak at the site of bound exciton is manifold in comparison to that for the free exciton. As the temperature increases, the deconvolution becomes a challenging task since the bound exciton and the free exciton can no more be spectrally resolved and the quantification of the factual aspects becomes inaccessible.

4.2.4 Temperature dependent TA measurements

Due to its commendable sensitivity (Instrument Response Function (IRF) ~ 35 fs), the femtosecond (fs) TA pump-probe strategy serves as a model analytical tool to accomplish the endeavour of mapping the processes photo-generated carriers indulge in ultrafast time scale. Thus, for further informative addition to the PL studies we performed rigorous analysis of TA data to extract simultaneous information of both radiative as well as non- radiative events in the temporal and spectral domain. A highly non-resonant fs pump corresponding to an energy of 3.54 eV was employed to optically excite the NC ensemble.

Such energy choice was made to warrant a truly hot phonon population and involve large density of microscopic states. **Figure 4.4 (A-E)** is a clear typical representative of the comparative TA spectra of the deposited $CsPbBr_3$ NCs, enveloping a vast range of temperatures (5 K-300 K). Three prominent traits are markedly evident in common in all spectral responses. The key attribute *viz.* the ground state bleach (GSB) centred at 500 nm (2.48 eV, 300 K) arising

as a corollary of Pauli blocking[25] of the 1S excitonic transition and concurrently, two positive characteristics are prominently noticeable on either side.[26]

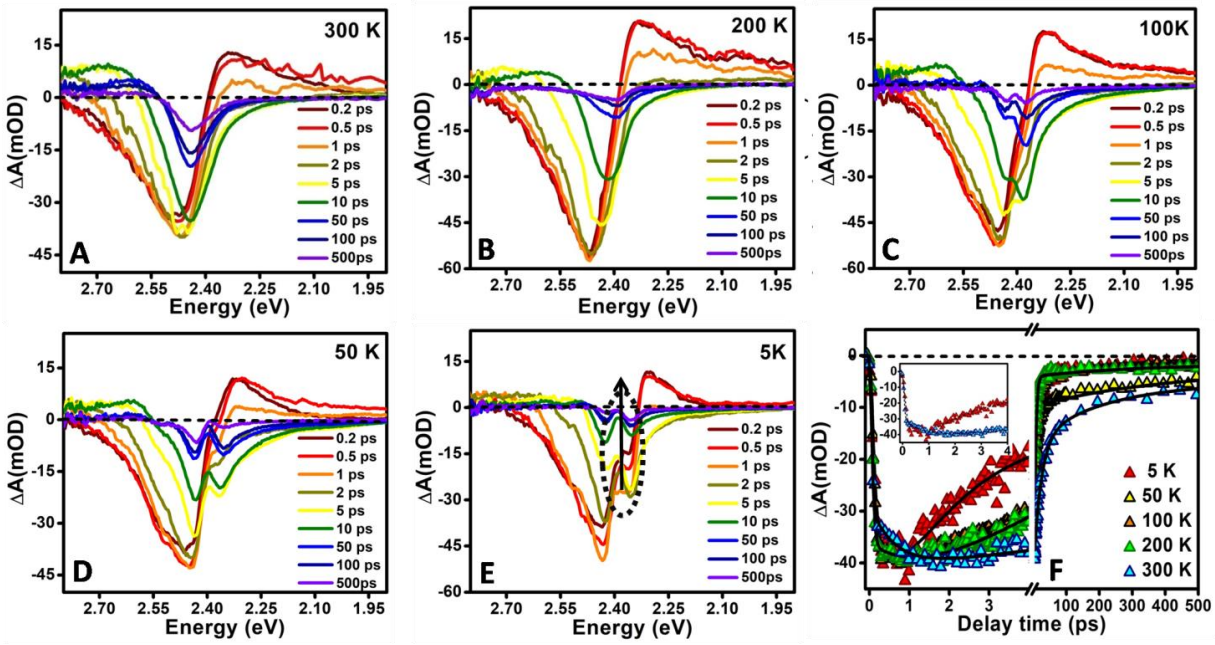

Figure 4.4 (A)- (E) The TA spectra spanning a wide range of temperatures, from 300 K to 5 K under 3.54 eV pump excitation. A supplementary low energy feature, which is completely missing around 300 K markedly emerges at cryogenic temperatures. (F) The normalized TA dynamical responses illustrated by probing the kinetics at the position of the free excitonic bleach.

For the one towards the higher energy side, the anticipated photo-induced absorption of the charge carriers from the excited states can be held responsible.[26] Towards the lower energy, the asymmetric derivative sort of feature, asserts itself as a positive signal initially for the early time probe delays, which is later entirely replaced by the negative bleach (~ 1.5 ps, 300 K). This is a prototypical signature of the probe induced biexcitonic Stark effect as claimed in various reported literature works before (discussion in later sections).[14,27] For lower temperatures, in addition to the pronounced bleach, one more isolated resonance is pragmatic on the lower energy side that we ascribe to defect bound emission[28] due to its temporal intactness (5 K). The bound exciton in turn holds its contribution from the shallow trap states stemming from the Br^- vacancies.[29] TA spectroscopy is expected to yield a bleach like negative signal for stimulated emission arising from the transitions involving shallow trap states. [30]

4.2.4.1 Influence of temperature on carrier relaxation and polaron formation

The interactive response of the charge carriers with the energetically assorted phonon modes is one key aspect influencing the carrier cooling rates. Also, following the TA spectra **(Figure 4.4 (A-E))**, we can indisputably assert that the basic entity that stimulates the optical response here, *i.e.* the "exciton" behaves in an altogether diverse manner at cryogenic and room temperatures. Accordingly, the thermalization mechanisms undertaken by HC for dispelling the excessive energy are completely diverse. Upon closely scrutinizing the bleach minima kinetics **(Figure 4.4 F)**, we notice a speedy carrier cooling for temperatures ≤ 200 K, whilst upon striding towards higher temperatures (> 200 K), we find the carriers indulging in comparatively relaxed cooling. Moreover, for the temperatures amid 5 K and 200 K, we find the bleach growth kinetics to altogether follow modestly similar trend as expected from the lack of strong carrier-LO phonon coupling in this temperature range. However, the preliminary cooling (upto ~ 0.28 ps) pursued by the HCs is almost analogous even for the two extreme scenarios, *viz.* 5 K and 300 K whereas the trend manifested in the later growth dynamics (> 0.28 ps) differs quite extensively. **Table 4.1** contains the time constants.

Table 4.1 Kinetic Fitting parameters for the probe monitored at the bleach position for $CsPbBr_3$ NCs deposited over a glass substrate under a pump excitation of 3.54 eV (The values in the brackets in the table indicate the respective weightages for the time constants mentioned)

Lattice Temp. (K)	τ_{G1}	τ_{G2}	τ_1	τ_2	τ_3	τ_4
300	<100fs (80%)	0.6ps (20%)	4.4ps (-37.5%)	32.5ps (-35%)	189ps (-15%)	>1ns (-12.5%)
200	<100fs (89.8%)	0.21ps (10.2%)	2.5ps (-51%)	11ps (-34%)	>1ns (-15%)	
100	<100fs (97.2%)	0.18ps (2.8%)	2.5ps (-46%)	27ps (-42%)	>1ns (-12%)	
50	<100fs (98%)	0.16ps (2%)	2.4ps (-49%)	80ps (-42%)	>1ns (-9%)	
5	<100fs (98%)	0.12ps (2%)	2ps (-74%)	75ps (-26%)		

Additional factor playing role at temperatures ≥ 200 K (16 meV) is the strong carrier-phonon interaction (regime 2, PL) which induces the host lattice to adapt itself and distort in the vicinity of the photo-generated carrier density. [16,29] This triggers a swift, momentary build-

up of non-equilibrium hot LO phonon cloud. Such an accumulation of hot LO-phonons is naturally evident from the carrier temperature T_C calculations which we have presented in later sections. Thus, for temperatures ≥ 200 K, an energetically favourable eigenstate *i.e.* large polaron is expected to come into picture. The presently employed incident energy flux of 50 μJ cm^{-2} corresponds to an equivalent charge carrier density of order 10^{18} cm^{-3} (see SI for thorough calculations). This order lies close to the critical threshold that separates the low fluence regime from the high one. Hence, the vital role played by the hot phonon-bottleneck cannot be completely ignored.[18,31] So, we regard the overall cooling process to be an outcome of both the hot phonon bottleneck effect and involvement of large polaron at a later time. Also, as it has been already mentioned for case of low temperatures (< 200 K), there are negligible polarization induced lattice fluctuations likely to support the abundance of the LO phonons, hence eliminating the probability of polaron formation at such temperatures and thus, compelling the HC to undergo the conventional relaxation mechanisms. Thus, since hot phonon bottleneck remains a common factor for the entire span of the investigated temperatures, in this crude evaluation of the cooling dynamics we foresee the polaron formation as the utter reason for the sluggish charge carrier relaxation observed for temperatures > 200 K. Whereas the incapability to support polaron for temperatures falling in the regime 1, provides the basis for the observed rapid cooling. The other possibility *i.e.* the up-conversion of the available acoustic phonons into longitudinal optical phonons is also very inefficient in Cs based systems, thus it subsides any possibility of polaron formation due to the upconverted acoustic phonons at low temperatures.[32] However, determining the exact polaron size is a cumbersome task, yet a rough estimate can be drawn with the assistance of the FrÖhlich model.[33] For present carrier density, an overlap of the polaron states in space is quite realistic since the polaron radius (~34 Å) is much larger in extent than the lattice parameter (5.87 Å) .

***Polaron size estimation*.** Polaron size is directly related to the amount of the injected charge carriers. Therefore, its estimation requires the calculation of injected carrier density. The overall number of injected photo charge carriers N can be approximated using the formula[33]

$$N = \frac{(A(E)X\ I)}{t\ X\ E} \qquad \textbf{Eq.4.2}$$

Where, A(E) implies the absorption intensity (Optical density) monitored at the pump excitation energy (E), I is the incident laser energy flux and t is the thickness of the deposited sample. Here, Incident laser pump power = 25 μW. Equivalent energy flux I, corresponding to a pump beam diameter of 250 μm= 50 μJcm^{-2}. Thickness (t) of the as-deposited film

estimated using cross sectional FESEM studies **(Figure 4.5)** = 600nm. $A(E)$ monitored at the pump excitation energy (E) 3.54 eV =1.04.Thus, the number of injected charge carriers (N) can be estimated to be close to 1.48 x 10^{18} cm^{-3}.Employing the calculated N and utilising the relation between the injected charge carriers (N) and the FrÖhlich Polaron radius[4] (r_F) (N = $(2(2r_F)^3)^{-1}$, the Polaron radius is calculated as 34.7 Å. This value is roughly 6 times larger than the $CsPbBr_3$ lattice parameter (5.47 Å), implying that the span of the polaron is extended to about 6 unit cells of the lattice.

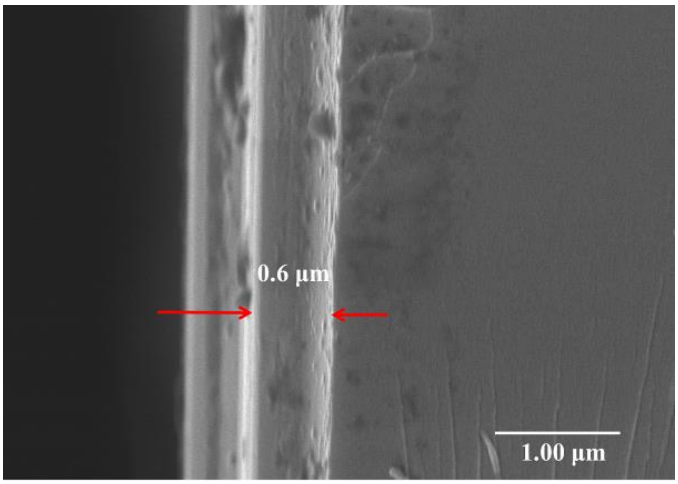

Figure 4.5 Field Emission Scanning Electron Microscopy (FE-SEM) images of the as-deposited $CsPbBr_3$ NCs over the glass substrate, showing the uniformity of the thickness of the deposited film.

Henceforth, we can regard this resultant polaron overlapping to be an added probable reason for the observable deceleration in the charge carrier cooling rate. Tracking the extended time scale kinetics (onset of bleach recovery), a significantly noticeable lower recombination rate is apparent at temperatures where LO phonon abundance becomes appreciable (300 K). We can address this slowed cooling and recombination dynamics to the lower diffusive coefficient due to the non-parabolic diffusive dispersion exhibited by these polaronic carriers.[34] However, the quick bleach recovery observed at temperatures ≤ 50 K, can be a clear implication of involvement from bound exciton and absence of polaron.

To explain the interplay of the decisive processes we focused our assessment to the regime 2 **(Figure 4.1 B)** alone which lands up with the observation that the later slope in the cooling rate further slows down as the temperature transits from 200 K to 300 K **(Figure 4.4 F)**. This can be primarily proffered as that the polaron concentration at 300 K is much abundant in disparity to that expected at 200 K, paving the way towards greater overlap of available

phonon modes. It can be described in accordance with the temperature dependent polaron density relation, $n = (2/h^3)(2\pi MkT)^{3/2} e^{(\zeta - H_0)/kT}$ where, M stands for the band mass, ζ is the chemical potential of the charge carriers in the crystal system.[34] We explicate this observation further with the aid of another vital factor that is the local temperature gradient that germinates between the carrier and the lattice ($\Delta = T_c - T_L$) post photoexcitation. The difference Δ is decisive for both the polaron cloud build-up rate as well as the LO phonon emission probability. Thus, the feeble difference discerned in the early carrier cooling (faster in 300 K than 200 K) originates from dominance of the phonon emission process whereas the later difference in the cooling rate comes from the involvement of the polaron. However if there would not have been any active participation from the large polaron at higher temperatures, then the cooling rate would have else taken up the conventional trend followed by the carriers *i.e.* slower cooling at lower temperatures. [35] This is the situation when the polaron formation is not practical, since the formation is entirely dependent on the dielectric constant of the material that itself is decisive towards the screening of the Coloumb mediated carrier-phonon interactions.[36] In such instances, the only probable process is the LO phonon mediated cooling with not much phonon accumulation possible to form polarons in spite of the carrier-LO phonon coupling being strong, since the lattice is incapable of supporting polaron.

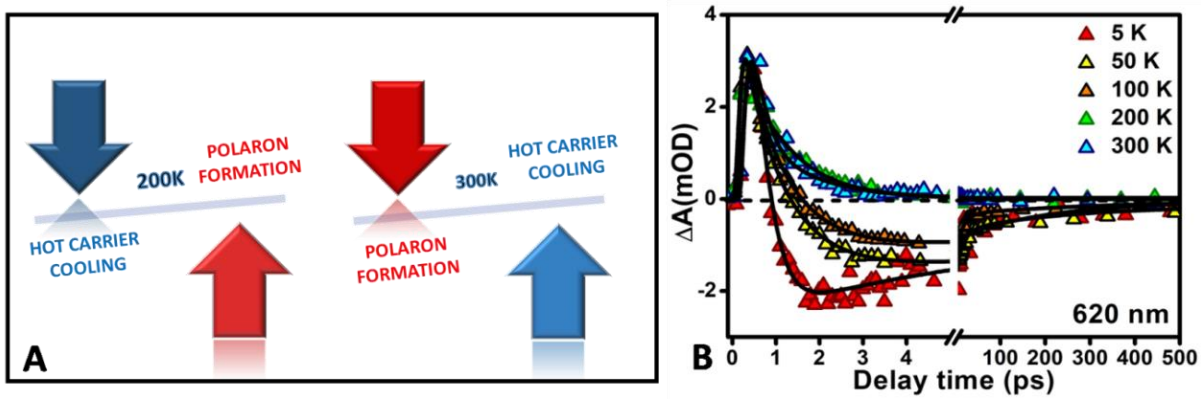

Figure 4.6. (A) Schematic representation of two competitive processes namely, polaron formation and hot carrier cooling, deciding the eventual governing relaxation mechanism *w.r.t* different temperatures, **(B)** The low energy positive signal maxima (620 nm, 2.0 eV) for the entire range of investigated temperatures (normalised).

However interestingly, it is not the robust exciton-LO phonon coupling alone that authenticates the polaron formation. Another decisive aspect we require to consider for the whole process of carrier relaxation is the ultimate possibility in the close conflict between polaron formation and carrier cooling.[18] Besides, it should be noted that the same LO phonons involved in the process

of polaron formation, are also accountable for the relaxation of the hot charge carriers. For sufficiently low carrier density, cooling tends to be sufficiently fast enough to eliminate any chance of polaron formation. On the contrary at typically moderate densities, due to phonon modes sharing, the polaron formation rate is fast enough to give a meaningful competition to the carrier cooling.[18] At such carrier densities as also in our case, we expect polaron formation to take place quite prior to HC cooling which appends to the relaxation bottleneck. Also, this anticipation goes well with our observation. Moreover, it is known from the previous literature reports that the polaron buildup rate increases with enhancement of temperature.[21] The immediate consequence is that we expect a possibility of faster polaron formation at higher temperature. Thus, the pace at which the polaron builds for 300 K is presumed to be marginally faster when compared to 200 K. Consequently for 300 K, we designate polaron mediated cooling to be the sole dominating process, resulting in the slow relaxation, whereas for 200 K, initial HC cooling wins over the delayed polaron formation leading to relatively quick carrier relaxation **(Figure 4.6 A)**. One such finding has been encountered in the recent literature reports which bears signature of the temperature dependent trend in the carrier cooling dynamics noticed in our study, but it provides no concerned discussion.[37] Moreover, the previous studies have been limited down to 80 K or 165 K incapable of reaching the point where the lattice is absolutely frozen assuring the complete polaron absence.[21, 29, 37]

To ascertain the polaron formation, we monitored the TA dynamical response at the position of positive signal (~ 2 eV). A clear polaron formation is observed for 300 K (formation time ~ 0.55 ps), since the signal lasts for merely 3 ps, that is the prototypical time scale for involved LO phonons decay **(Figure 4.6 B)**.[38] Interestingly, this signal behaviour is drastically distinct from that obscured at other temperatures which follow clear biexciton dynamics **(Figure 4.7 F)**. This implies that polaron involvement takes place only above 200 K. The inference of the polaron formation can also be drawn from the previous findings[26] which state polaron formation time in $CsPbBr_3$ to be ~0.69 ps for 300 K,[21] which is in close match with what we obtained in our finding (~550 fs).

To emphasize our claim a little further we have carried out a comparative analysis of T_c. In this pursuit, the estimation of the carrier temperature T_c has been made by fitting the high energy tail of the normalised TA bleach data **(Figure 4.7 A and 4.7 C)**, modelling it using the well-established modified Maxwell Boltzmann (MB) approximation (Fermi-Dirac statistics can be approximated as MB when $E > E_F$.[39,40,41] . Convincingly, the fitting region has been slightly varied for the different temperatures under consideration since there is enormous alteration in the conduction band minima and valence band maxima with temperature. An

interesting point here is that after the attainment of quasi-equilibrium state (carrier- carrier scattering), the initial T_C for 300 K **(Figure 4.7 B)** situation is nearly thrice of that observed for 5 K scenario **(Figure 4.7 D)**.

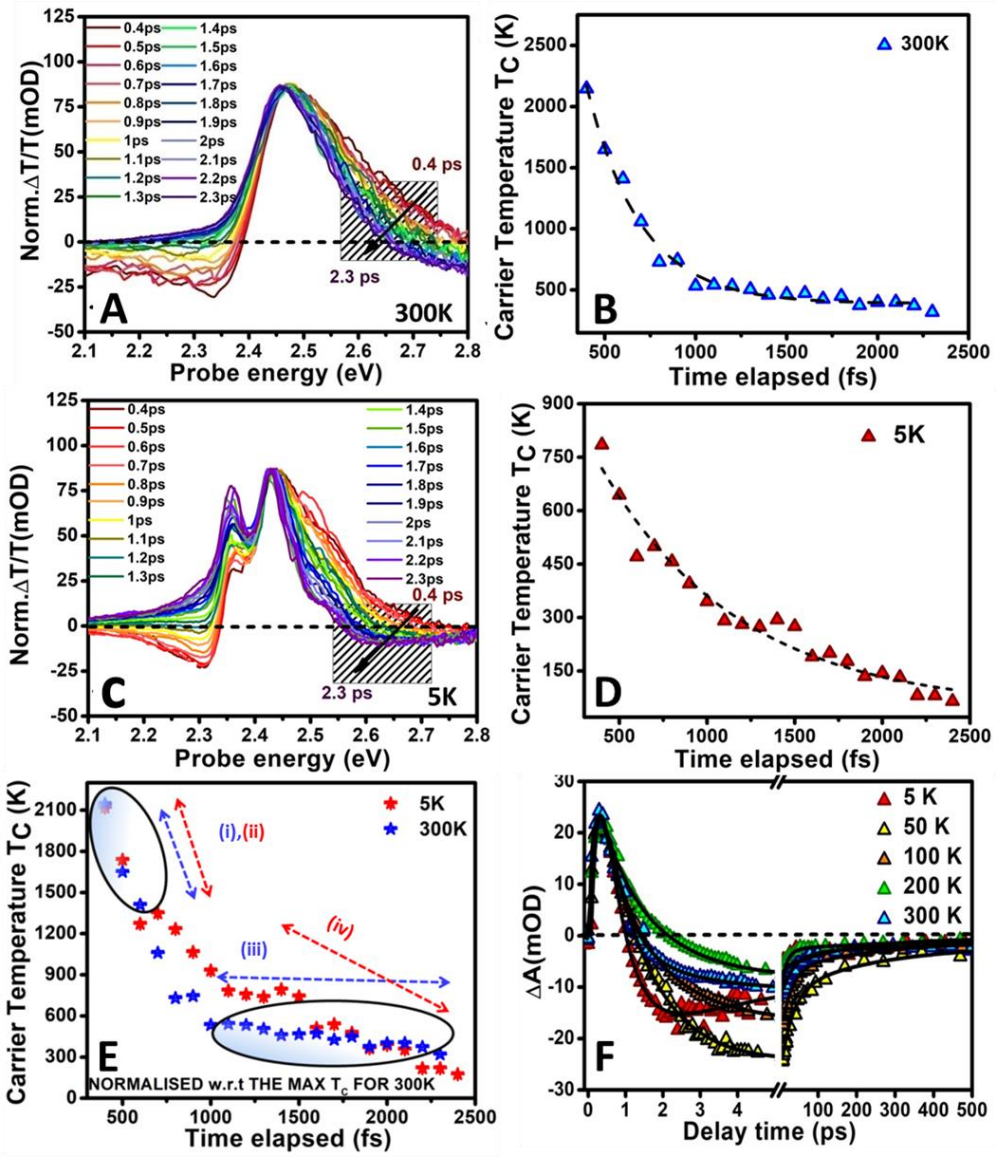

Figure 4.7 (A), (C) Characteristic TA spectra traces normalized at the position of maximum amplitude of bleach for 300 K, 5 K plotted for the early probe delay time scales (0.4 ps to 2.3 ps), the marked region (dashed boxes drawn) signify the high energy section opted for carrying on the Maxwell-Boltzmann fitting to pull out the carrier temperature values (T_c). **(B), (D)** plots represent the temporal progression of T_c for extreme ends of the investigated temperatures 300 K, 5 K. **(E)** Relative plots for T_c normalized at 0.4 ps, illustrating the difference in the various relaxation trails embarked upon by the HC. **(F)** Relative biexcitonic dynamics (~2.34 eV), showing the distinction in the formation and decay dynamics as a function of temperature (Normalised).

This is a clear inference that after identical delay in time, LO phonon concentration is much more pronounced around 300 K, enhancing the probability of polaron formation. For early periods of probe delays, the cooling rate for 300 K is quite hasty having its origin from the large Δ (which increases the LO phonon emission probability **(Figure 4.7 B))**. While for 5 K, as an outcome of LO phonon scarcity, the charge carriers opt for acoustic mode mediated decay as a payoff for the less significant Δ, so marginally slows initial cooling **(Figure 4.7 D)**. The slope encountered by the HC for lattice subjected to 5 K, remains mostly the same, designating the whole process to only one type of relaxation mode (**Figure 4.7 E** marked as (ii), (iv)). Nevertheless, a marked variation in the slope for 300 K T_C analysis (**Figure 4.7 E** marked as (i), (iii)) is discerned as the delay progresses in contrast to that observed for 5 K, clearly suggesting the involvement of some additional mode. This later slope segment (**Figure 4.7 E** (iii)) which appears quite flat due to absence of sufficient thermal gradient can be ascribed to have its origin from the phonon diffusive process as a consequence of polaronic states overlap resulting in heating of other neighbouring polaronic states.

4.2.4.2 Temperature dependent biexciton dynamics

The kinetics at the position of the biexciton (~2.34 eV) **(Figure 4.7F)** shows that the formation time(< 100fs) seems to be barely different for the entire range of temperatures considered, quite comparable to the initial carrier cooling trend monitored at the bleach position. Nevertheless, a distinct trend in the decay dynamics is noticed unpredictably around 300 K in the otherwise monotonically progressive trend displayed in the decay constant. In accordance with the conventional concept, the biexciton decay is expected to decelerate with increasing temperature due to reduced Auger recombination, owing to the screening of the charge carriers.[42] Interestingly, this discrepancy is exactly found in the same temperature range *i.e.* in the region above 200 K where there is an abrupt alteration expected in the strength of carrier-LO phonon coupling.

It is noticed that the although the biexciton decays following a similar fashion up to a delay of 0.55 ps for all the temperatures, be it 5 K or 300 K yet a variance in the decay dynamics is found for higher magnitudes of probe delay (beyond 0.55 ps). Since the fairly accurate time for polaron formation estimates to 550 fs for 300 K so the instant the polaron formation is complete (~0.55 ps), the decay of the longitudinal optical phonons steps in **(Table 4.2)**. The rapid increment in the strength of the charge-phonon interaction which is decisive for the decay channel followed by the biexciton (dissociates via dephasing mediated by the charge-phonon coupling) can be considered as the root for the observed anomaly.[43]

Table 4.2 Kinetic Fitting parameters for the probe monitored at the biexciton position (2.34eV).

LATTICE TEMP. (K)	τ_{G1}	τ_1	τ_2	τ_3	τ_4	τ_5
300	<100fs (69.5%)	0.42ps (-65%)	2.2ps (-35%)	23ps (19%)	122ps (8.5%)	>1ns (3%)
200	<100fs (72.4%)	0.6ps (-71.4%)	1.8ps (-28.6%)	25ps (16.6%)	120ps (8%)	>1ns (3%)
100	<100fs (59.7%)	0.48ps (-79%)	1.53ps (-21%)	24ps (28.3%)	125ps (7.5%)	>1ns (4.5%)
50	<100fs (50%)	0.37ps (-56%)	1.5ps (-44%)	17ps (29%)	71ps (15%)	>1ns (6%)
5	<100fs (60.5%)	0.31ps (-60%)	0.5ps (-40%)	4.75ps (23.6%)	84.5ps (13.1%)	>1ns (2.8%)

4.3 Summary

In a wider perspective, in this chapter with the aid of TA spectroscopy we have attempted to reveal the temperature dependence of the native processes involved in the HC cooling in $CsPbBr_3$ NCs. It simply reveals the indulgence of polaron at temperatures ~ 300 K as the sole factor responsible for the retarded HC cooling in striking contrast to the rapid cooling undertaken by the carriers at temperatures as low as 5 K incapable of supporting polaron formation in $CsPbBr_3$ NCs. At 200K, where the carrier-LO phonon coupling strength exhibits a sudden increment, despite expected polaron involvement it is seen that the quick HC cooling subsides away the polaron formation. It is also observed that the temperature dependent alterations in the carrier relaxation rate are more evident in this region of transition as expected. Such prior knowledge of the characteristic response of the HCs under different temperature conditions can be steered to manoeuvre the device performance to the fullest.

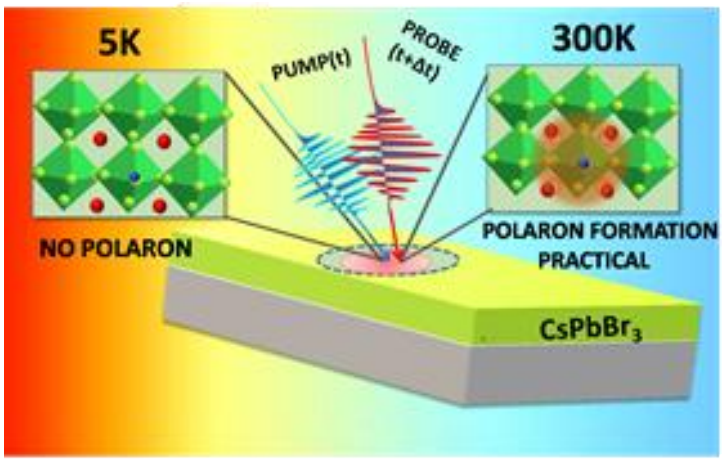

"Graphic representation of the main findings that can be gathered from the current project- at cryogenic temperatures close to 5 K, it is not realistic to form polarons in $CsPbBr_3$ lattice, while there is emergence of polaron as the lattice temperature is brought close to 300 K"

4.4 References

(1) Kojima, A.; Teshima, K.; Shirai, Y.; Miyasaka, T. Organometal Halide Perovskites as Visible-Light Sensitizers for Photovoltaic Cells. *J. Am. Chem. Soc.* **2009**, *131* (*17*), 6050–6051.

(2) Chung, I.; Lee, B.; He, J.; Chang, R. P. H.; Kanatzidis, M. G. All-Solid-State Dye-Sensitized Solar Cells with High Efficiency. *Nature* **2012**, *485* (*7399*), 486–489.

(3) Protesescu, L.; Yakunin, S.; Bodnarchuk, M. I.; Krieg, F.; Caputo, R.; Hendon, C. H.; Yang, R. X.; Walsh, A.; Kovalenko, M. V. Nanocrystals of Cesium Lead Halide Perovskites ($CsPbX_3$, X = Cl, Br, and I): Novel Optoelectronic Materials Showing Bright Emission with Wide Color Gamut. *Nano Lett.* **2015**, *15* (*6*), 3692–3696.

(4) Yettapu, G. R.; Talukdar, D.; Sarkar, S.; Swarnkar, A.; Nag, A.; Ghosh, P.; Mandal, P. Terahertz Conductivity within Colloidal $CsPbBr_3$ Perovskite Nanocrystals: Remarkably High Carrier Mobilities and Large Diffusion Lengths. *Nano Lett.* **2016**, *16* (*8*), 4838–4848.

(5) Xing, G.; Mathews, N.; Sun, S.; Lim, S. S.; Lam, Y. M.; Grätzel, M.; Mhaisalkar, S.; Sum, T. C. Long-Range Balanced Electron- and Hole-Transport Lengths in Organic-Inorganic $CH_3NH_3PbI_3$. *Science* **2013**, *342* (*6156*), 344–347.

(6) Li, X.; Wu, Y.; Zhang, S.; Cai, B.; Gu, Y.; Song, J.; Zeng, H. Quantum Dots: $CsPbX_3$ Quantum Dots for Lighting and Displays: Room-Temperature Synthesis, Photoluminescence Superiorities, Underlying Origins and White Light-Emitting Diodes *Adv. Funct. Mater.* **2016**, *26* (*15*), 2584.

(7) Song, J.; Li, J.; Li, X.; Xu, L.; Dong, Y.; Zeng, H. Quantum Dot Light-Emitting Diodes Based on Inorganic Perovskite Cesium Lead Halides ($CsPbX_3$). *Adv. Mater.* **2015**, *27* (*44*), 7162–7167.

(8) Heitz, R.; Born, H.; Guffarth, F.; Stier, O.; Schliwa, A.; Hoffmann, A.; Bimberg, D. Existence of a Phonon Bottleneck for Excitons in Quantum Dots. *Phys. Rev. B* **2001**, *64* (*24*), 241305.

(9) Li, X.Q.; Nakayama, H.; Arakawa, Y. Phonon Bottleneck in Quantum Dots: Role of Lifetime of the Confined Optical Phonons. *Phys. Rev. B* **1999**, *59* (*7*), 5069–5073.

(10) Chen, J.; Messing, M. E.; Zheng, K.; Pullerits, T. Cation-Dependent Hot Carrier Cooling in Halide Perovskite Nanocrystals.*J. Am. Chem. Soc.* **2019**, *141* (*8*), 3532–3540.

(11) Fu, J.; Xu, Q.; Han, G.; Wu, B.; Huan, C. H. A.; Leek, M. L.; Sum, T. C. Hot Carrier Cooling Mechanisms in Halide Perovskites. *Nat. Commun.* **2017**, *8* (*1*), 1300.

(12) Shen, Q.; Ripolles, T. S.; Even, J.; Ogomi, Y.; Nishinaka, K.; Izuishi, T.; Nakazawa, N.; Zhang, Y.; Ding, C.; Liu, F.; et al. Slow Hot Carrier Cooling in Cesium Lead Iodide Perovskites. *Appl. Phys. Lett.* **2017**, *111* (*15*), 153903.

(13) Li, B.; Huang, H.; Zhang, G.; Yang, C.; Guo, W.; Chen, R.; Qin, C.; Gao, Y.; Biju, V. P.; Rogach, A. L.; et al. Excitons and Biexciton Dynamics in Single $CsPbBr_3$ Perovskite Quantum Dots. *J. Phys. Chem. Lett.* **2018**, *9* (*24*), 6934–6940.

(14) Aneesh, J.; Swarnkar, A.; Kumar Ravi, V.; Sharma, R.; Nag, A.; Adarsh, K. V. Ultrafast Exciton Dynamics in Colloidal $CsPbBr_3$ Perovskite Nanocrystals: Biexciton Effect and Auger Recombination. *J. Phys. Chem. C* **2017**, *121* (*8*), 4734–4739.

(15) Cinquanta, E.; Meggiolaro, D.; Motti, S. G.; Gandini, M.; Alcocer, M. J. P.; Akkerman, Q. A.; Vozzi, C.; Manna, L.; De Angelis, F.; Petrozza, A.; et al. Ultrafast THz Probe of Photoinduced Polarons in Lead-Halide Perovskites. *Phys. Rev. Lett.* **2019**, *122* (*16*), 166601.

(16) Iaru, C. M.; Geuchies, J. J.; Koenraad, P. M.; Vanmaekelbergh, D.; Silov, A. Y. Strong Carrier-Phonon Coupling in Lead Halide Perovskite Nanocrystals. *ACS Nano* **2017**, *11* (11), 11024–11030.

(17) Bretschneider, S. A.; Ivanov, I.; Wang, H. I.; Miyata, K.; Zhu, X.; Bonn, M. Quantifying Polaron Formation and Charge Carrier Cooling in Lead-Iodide Perovskites. *Adv. Mater.* **2018**, *30* (29), 1707312.

(18) Burgos-Caminal, A.; Moreno-Naranjo, J. M.; Willauer, A. R.; Paraecattil, A.A.; Ajdarzadeh, A.; Moser, J.E. Hot Carrier Mobility Dynamics Unravel Competing Sub-Ps Cooling Processes in Lead Halide Perovskites. **2019**, arXiv:1909.04589v1 [cond-mat.mtrl-sci]

(19) Sadhukhan, P.; Pradhan, A.; Mukherjee, S.; Sengupta, P.; Roy, A.; Bhunia, S.; Das, S. Low Temperature Excitonic Spectroscopy Study of Mechano-Synthesized Hybrid Perovskite. *Appl. Phys. Lett.* **2019**, *114,131102*.

(20) Miyata, K.; Meggiolaro, D.; Trinh, M. T.; Joshi, P. P.; Mosconi, E.; Jones, S. C.; De Angelis, F.; Zhu, X.Y. Large Polarons in Lead Halide Perovskites. *Sci. Adv.* **2017**, *3* (8), e1701217.

(21) Evans, T. J. S.; Miyata, K.; Joshi, P. P.; Maehrlein, S.; Liu, F.; Zhu, X. Y. Competition between Hot-Electron Cooling and Large Polaron Screening in $CsPbBr_3$ Perovskite Single Crystals. *J. Phys. Chem. C* **2018**, *122* (*25*), 13724–13730.

(22) Stoumpos, C. C.; Malliakas, C. D.; Peters, J. A.; Liu, Z.; Sebastian, M.; Im, J.; Chasapis, T. C.; Wibowo, A. C.; Chung, D. Y.; Freeman, A. J.; et al. Crystal Growth of the Perovskite Semiconductor $CsPbBr_3$: A New Material for High-Energy Radiation Detection. *Cryst. Growth Des.* **2013**, *13* (7), 2722–2727.

(23) Du, W.; Zhang, S.; Wu, Z.; Shang, Q.; Mi, Y.; Chen, J.; Qin, C.; Qiu, X.; Zhang, Q.; Liu, X. Unveiling Lasing Mechanism in $CsPbBr_3$ Microsphere Cavities. *Nanoscale* **2019**, *11* (7), 3145–3153.

(24) Ramade, J.; Andriambariarijaona, L. M.; Steinmetz, V.; Goubet, N.; Legrand, L.; Barisien, T.; Bernardot, F.; Testelin, C.; Lhuillier, E.; Bramati, A.; et al. Exciton-Phonon Coupling in a $CsPbBr_3$ Single Nanocrystal. Appl. Phys. Lett. **112**, 072104 (2018).

(25) Richter, J.M.; Branchi, F.; Valduga de Almeida Camargo; Zhao,B.; Friend, H.R.; Cerullo,G.; Deschler, F. Ultrafast carrier thermalization in lead iodide perovskite probed with two-dimensional electronic spectroscopy. *Nat. Commun.* **2017,**8**,** 376.

(26) Kaur, G.; Justice Babu, K.; Ghorai, N.; Goswami, T.; Maiti, S.; Ghosh, H. N. Polaron-Mediated Slow Carrier Cooling in a Type-1 3D/0D $CsPbBr_3$@Cs_4PbBr_6 Core–Shell Perovskite System. *J. Phys. Chem. Lett.* **2019**, *10* (18), 5302–5311.

(27) Maity, P.; Dana, J.; Ghosh, H. N. Multiple Charge Transfer Dynamics in Colloidal $CsPbBr_3$ Perovskite Quantum Dots Sensitized Molecular Adsorbate. *J. Phys. Chem. C* **2016**, *120* (32), 18348–18354.

(28) Diroll, B. T.; Zhou, H.; Schaller, R. D. Low-Temperature Absorption, Photoluminescence, and Lifetime of $CsPbX_3$ (X = Cl, Br, I) Nanocrystals. *Adv. Funct. Mater*. **2018**, *28* (30), 1–7.

(29) Lee, S. M.; Moon, C. J.; Lim, H.; Lee, Y.; Choi, M. Y.; Bang, J. Temperature-Dependent Photoluminescence of Cesium Lead Halide Perovskite Quantum Dots: Splitting of the Photoluminescence Peaks of $CsPbBr_3$ and $CsPb(Br/I)_3$ Quantum Dots at Low Temperature. *J. Phys. Chem. C* **2017**, *121* (46), 26054–26062.

(30) Ruan, Q.; Miao, T.; Wang, H.; Tang, J. Insight on Shallow Trap States-Introduced Photocathodic Performance in n-Type Polymer Photocatalysts. *J Am Chem Soc* **2020**, *142* (6), 2795–2802.

(31) Manser, J. S.; Kamat, P. V. Band Filling with Free Charge Carriers in Organometal Halide Perovskites. *Nat. Photonics* **2014**, *8*, 737-743.

(32) Yang, J.; Wen, X.; Xia, H.; Sheng, R.; Ma, Q.; Kim, J.; Tapping, P.; Harada, T.; Kee, T. W.; Huang, F.; et al. Acoustic-Optical Phonon up-Conversion and Hot-Phonon Bottleneck in Lead-Halide Perovskites. *Nat Commun* **2017**, *8*, 14120.

(33) Frost, J. M.; Whalley, L. D.; Walsh, A. Slow Cooling of Hot Polarons in Halide Perovskite Solar Cells. *ACS Energy Lett.* **2017**, *2* (12), 2647–2652.

(34) Landau, L. D.; Pekar, S. I. The Effective Mass of the Polaron. Collection of Papers. L.D. Landau **1965**, *423* (5), 478–483.

(35) Diroll, B. T. Temperature-Dependent Intraband Relaxation of Hybrid Perovskites. *J*

Phys Chem Lett **2019**, *10* (18), 5623–5628.

(36) Hintermayr, V. A.; Polavarapu, L.; Urban, A. S.; Feldmann, J. Accelerated Carrier Relaxation through Reduced Coulomb Screening in Two-Dimensional Halide Perovskite Nanoplatelets. *ACS Nano* **2018**, *12*, 10151–10158.

(37) Li, Y.; Lai, R.; Luo, X.; Liu, X.; Ding, T.; Lu, X.; Wu, K. On the Absence of a Phonon Bottleneck in Strongly Confined $CsPbBr_3$ Perovskite Nanocrystals. *Chem. Sci.* **2019**, *10* (*23*), 5983–5989.

(38) Li, M.; Fu, J.; Xu, Q.; Sum, T. C. Slow Hot-Carrier Cooling in Halide Perovskites: Prospects for Hot-Carrier Solar Cells. *Adv. Mater.* **2019**, *31* (*47*), 1802486.

(39) Price, M.; Butkus, J.; Jellicoe, T.; Sadhanala, A.; Briane, A.; Halpert, E. J.; Broch, K.; Hodgkiss, M. J.; Friend, H. R.; Deschler, F. Hot-Carrier Cooling and Photoinduced Refractive Index Changes in Organic–Inorganic Lead Halide Perovskites. *Nat. Commun.* **2015**, ***6,*** 8420.

(40) Maity, P.; Yin, J.; Cheng, B.; He, J.-H.; Bakr, O. M.; Mohammed, O. F. Layer-Dependent Coherent Acoustic Phonons in Two-Dimensional Ruddlesden–Popper Perovskite Crystals. *J Phys Chem Lett* **2019**, *10* (17), 5259–5264.

(41) Dursun, I.; Maity, P.; Yin, J.; Turedi, B.; Zhumekenov, A. A.; Lee, K. J.; Mohammed, O. F.; Bakr, O. M. Why Are Hot Holes Easier to Extract than Hot Electrons from Methylammonium Lead Iodide Perovskite? *Adv Energy Mater* **2019**, *9* (22), 1900084.

(42) Kholmicheva, N.; Budkina, D. S.; Cassidy, J.; Porotnikov, D.; Harankahage, D.; Boddy, A.; Galindo, M.; Khon, D.; Tarnovsky, A. N.; Zamkov, M. Sustained Biexciton Populations in Nanoshell Quantum Dots. *ACS Photonics* **2019**, *6 (4),* 1041–1050.

(43) Prezhdo, O. V. Multiple Excitons and the Electron-Phonon Bottleneck in Semiconductor Quantum Dots: An Ab Initio Perspective. *Chem. Phys. Lett.* **2008**, *460* (1–3), 1–9.

Chapter 5

Unravelling the Underlying Hot Carrier Transfer and Relaxation Pathways in Type -1 $CsPbBr_3$–PbS System

The scientific community around the globe has developed a great deal of interest in hetero-junction devices based on the conjunction of perovskite and other semiconducting materials due to the extensive range of properties demonstrated by them. Among the various probable combinations, the $CsPbBr_3$ and PbS hetero-structure system by now has proved itself as a strong contender for usage in phototransistor applications. This hetero-system has already demonstrated its dominance over the individual constituting systems in terms of superior photo-responsivity and broader response-width. However, it lacks an in-depth investigation of the fundamental dynamics which can elucidate the ground for such efficient behaviour. For this purpose, here we have used femtosecond broadband TA spectroscopy employing energetically distinct pump excitations (300 nm, 480 nm, 620 nm) to elaborately understand the essential interplay between the native carrier relaxation and carrier transfer mechanisms in this interesting $CsPbBr_3$/PbS Type -1 architecture. Such a careful choice of different pump excitations has been made to obtain the photogenerated carriers in differently densed energy states of $CsPbBr_3$ and PbS. Consequentially, it was observed that the HC transfer process tends to be bidirectional (from $CsPbBr_3$ to PbS and vice versa) when the photogeneration takes place in the hot states (300 nm).On the contrary it was however found that for the instance of close to band edge excitation w.r.t. $CsPbBr_3$ band edge (480 nm), the transfer of carriers occurs merely in one direction, i.e. from $CsPbBr_3$ to PbS states. This detailed investigation thus provides an opportunity to understand the competition between two processes whose interplay is strongly dependent on the initial energy of the carriers and the density of states in which the carriers are initially excited.

5.1 Motivation and Background

All inorganic perovskites have so far established themselves as the most potential photovoltaic materials due to the impressive candidature showcased by them.[1-2] However, apart from $CsPbI_3$ which serves the utmost prospect of exploiting the low energy regime of the spectral range (near-infrared), the usage of other all-inorganic members in photovoltaic devices is still limited because of the intermediate energy band gaps offered by these contenders.[3] But that doesn't conclude the list of hindrances that avert the practical applicability of the all-inorganic perovskites.[4,5] There is further major dilemma that holds back the deployment of $CsPbI_3$- " its poor stability".[6,7] One way of banishing such obstacles is using other all-inorganic perovskites in conjunction with low band gap materials.

There can be innumerable permutations of such combinations possible, however among all the diverse range of possibilities, as of now the combination of $CsPbBr_3$ and PbS has proved itself to be quite promising, principally for phototransistor applications.[8] The main advantage of employing such a composite constituted by an intermediate band gap material ($CsPbBr_3$, bulk band gap ~2.25 eV)[9] along with a low energy band gap material (PbS, bulk band gap ~0.41 eV)[10], where the entire dominion of the spectral range (ultraviolet to infrared) can be availed advantageously. The foremost reason for the selection of $CsPbBr_3$ among the available all-inorganic perovskites is its intermediate band gap (though greater than $CsPbI_3$) which permits to cover wider range of optical spectrum.[11] Likewise, the ground for choosing PbS as the low energy candidate is due to its easily tuneable band gap[12], high absorption coefficient[13], good infrared sensitivity[14]and high air stability.[15,16] Such hetero-structures in turn provide a profound opportunity of harnessing the indispensible characteristics of both the individual constituents which are overlooked otherwise. Briefly, sensitizing $CsPbBr_3$ with PbS introduces both high carrier mobility in the system (carrier mobility is really high in $CsPbBr_3$[17] as compared to PbS) and broadband response which is not practical if only the individual systems are deployed. Yu *et. al* has already demonstrated the responsivity for $CsPbBr_3$-PbS hybrid system to be immensely high (4.5×10^5 AW^{-1}), approximately three order of magnitude higher than the individual system. [8,18] The enhanced hybrid device responsivity obtained can be in a way directly attributed to its Type-I band alignment as suggested by the previous literature reports.[19] The redox levels for this composite under investigation are apt for an unhindered transfer of both the carriers *i.e.* holes and electrons from $CsPbBr_3$ towards PbS, enhancing the number of available carriers in PbS. Therefore, understanding the native photo-physics of such a fascinating architecture is essentially crucial for improving the performance

of the devices based on these materials. It is a widely established notion that hot carrier transfer process competes strongly with hot carrier (HC) cooling. Increment of excitation energy is expected to yield higher HC transfer efficiency since in such scenario, ultrafast transfer process triumphs over carrier cooling.[20,21] This can be explained in terms of availability of different density of states at different pump excitation energies.[22] The strong interplay of HC cooling and transfer in such an intriguing composite system like $CsPbBr_3$– PbS is a real deal of interest, which at this point lacks detailed understanding.

In the present chapter, we have therefore made a venture to identify such underneath lying competition of carrier cooling and carrier transfer in $CsPbBr_3$– PbS hybrid composite with the aid of femtosecond differential absorption spectroscopy. The explanation reported in the recent work conducted by Zhang *et al* relies absolutely on the concept of energy transfer.[19] However here in this present chapter, we find HC transfer accountable for the observed kinetic behaviour. Further, we find noticeable enhancement of HC transfer efficiency from $CsPbBr_3$ to PbS with increment of excitation energy. For the case of high energy excitation, HC transfer is observed to be bidirectional (from $CsPbBr_3$ to PbS and vice versa) while on the other hand upon lowering the pump energy, the hot carrier transfer tends to proceed in one direction alone *i.e.* only from $CsPbBr_3$ to PbS. Stating in brief, this chapter can provide assistance in gaining an extensive understanding over the various possibilities of charge transfer feasible in $CsPbBr_3$– PbS composite which can be attained by merely playing with the incident excitation energies.

5.2 Results and Discussion

5.2.1 Preliminary crystallographic and morphological studies

The individual systems under study, *viz.* $CsPbBr_3$ and PbS NCs were synthesized following standard synthesis protocol with trivial modifications as described earlier in the experimental section chapter. Subsequent to synthesis, $CsPbBr_3$ and PbS NCs were mixed and left for over-night stirring to obtain the composite system ($CsPbBr_3$-PbS).To advance further and to authenticate the formation of the nanocrystals, X-Ray Diffraction (XRD) and High Resolution Transmission Electron Microscopy (HR-TEM) studies were undertaken. The diffraction peaks in the acquired XRD data are seen to show perfect concurrence with the desired peaks as per the JCPDS data files for $CsPbBr_3$ and PbS respectively. The XRD pattern of as-deposited $CsPbBr_3$ NCs **(Figure 5.1 A)** shows definite peaks at 2θ = 15.1, 15.2, 21.4, 30.3, 30.6˚ corresponding to (002), (110), (112), (004), (220) plane respectively. This is in well agreement

with JCPDS data set for $CsPbBr_3$ (JCPDS 54-752) and matches with the orthorhombic lattice structure for $CsPbBr_3$. Similarly, the XRD pattern for PbS NCs shows distinguished peaks at 2θ = 26, 30, 43, 51, 53.5, 62.5, 69, 71, 79˚corresponding to (111), (200), (220), (311), (222), (400), (331), (420), (422) planes and the positions are in well agreement with JCPDS data set for PbS (JCPDS 65-346) **(Figure 5.1 B)**. The diffraction pattern indicates that the PbS QDs exist in cubic phase.

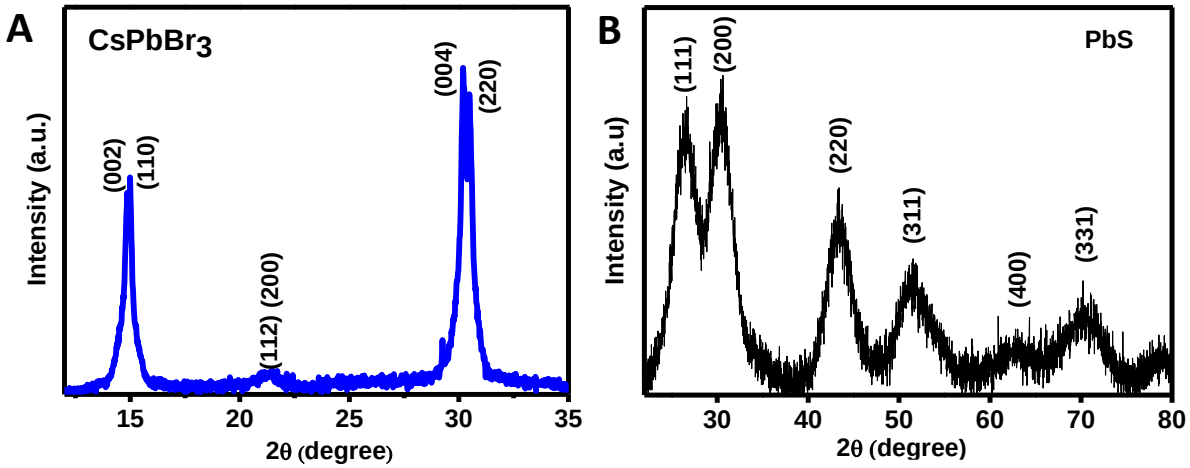

Figure 5.1 Powder XRD data for **(A)** $CsPbBr_3$ NCs and **(B)** PbS QDs deposited on glass film.

The as-prepared $CsPbBr_3$ and PbS NCs display an average approximate edge diameter of 13 ± 0.3 nm and 3.5 ± 0.2 nm respectively in the representative High Resolution Transmission Electron Microscopy (HR-TEM) images **(Figure 5.2 A,B and 5.2 C,D,E respectively)**. This clearly suggests that the synthesised $CsPbBr_3$NCs exhibit weak confinement since the corresponding particle size is much outsized in comparison to the exciton Bohr radius of $CsPbBr_3$ (~ 7 nm).[23] Further, the images suggest the average d-spacing for $CsPbBr_3$to be around 0.58 nm. .On the contrary, the synthesised PbS NCs are anticipated to illustrate absolute strong confinement because their particle size (~ 3.5 nm) **(Figure 5.2 E)** is significantly small in contrast to PbS effective exciton Bohr radius (~18 nm).[24] The suggestive mean d-spacing for PbS comes close to 0.303 nm as seen in the HRTEM **(Figure 5.2 E)**.

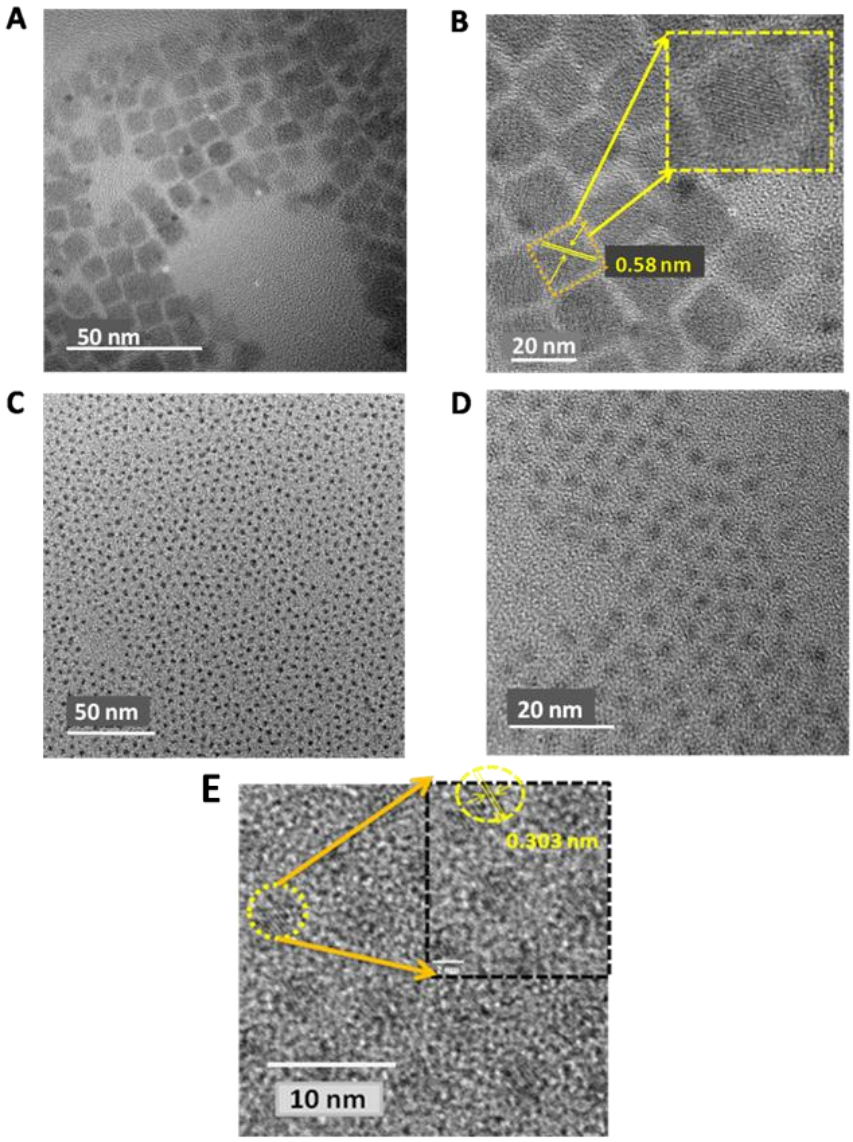

Figure 5.2 High Resolution Transmission Electron Microscopy (HR-TEM) images of **(A,B)** $CsPbBr_3$ NCs and **(C,D,E)** PbS QDs dispersed in Toluene.

5.2.2 Steady state optical studies- Absorption and PL

The optical signatures corresponding to the band edge excitonic transitions of the two constituents separately and in the mixture (for $CsPbBr_3$ NCs peaked around 496 nm and for PbS QDs centered around 955 nm) are evidently apparent in the steady state optical absorption plots **(Figure 5.3 A)**. Interestingly, formation of composite is observed to induce significant red shift at the excitonic absorption of PbS QDs (*955 nm to 990 nm*) with relatively a trivial alteration discernible at $CsPbBr_3$ excitonic absorption position. This key shift in the absorption feature at the near infrared energy region can straightforwardly be related to the partial fusion of the QDs which can occur at high concentrations.[25] It can be explained as a direct outcome of the reduction in the pre-existing confinement that shrinks the band gap and the energy

spacing between the consecutive states, which in turn sets this red shift. Such shifts have been observed by Sargent *et al.* in their studies conducted for "dot-in-perovskite" hybrid colloidal QDs and the underlying reason for the same has been elucidated by them in their investigation.[25] However, the nearly intact photoluminescence (PL) spectra monitored for $CsPbBr_3$ NCs (red shift around 2nm) clearly indicates that the emissive characteristics of the perovskite NCs remain more or less identical even subsequent to the addition of PbS QDs **(Figure 5.3 B)**. This further certifies that unlike PbS, $CsPbBr_3$ band gap is not significantly changed.

With the assistance of the previously asserted reports relevant in accord to the present studies, the conduction band (CB) and valence band (VB) positions for $CsPbBr_3$ NCs can be roughly estimated to be -3.35 eV and -5.85 eV respectively.[26] Similarly, taking reference from the documented literature for similar sized PbS QDs (~3.5 nm) the band levels can be approximated as -3.7 eV and -4.99 eV (CB and VB respectively) **(Figure 5.3 F)**.[27] However, in the instance of the colloidal mixture, as an effect of the modulation of the PbS energy band gap (due to partial fusion of QDs) as suggested by the steady state optical absorption spectra (PbS absorption maxima peak is shifted to 990 nm), the band levels may tend to modulate trivially (-3.77 eV and -5.02 eV).[27] This type of energy band alignment distinctly indicates Type -1 arrangement for the resulting hetero-structure allowing the unhindered, thermodynamically viable transfer of the carriers, *i.e.* both electrons and holes from higher band gap material towards lower band gap, here from $CsPbBr_3$ to PbS. Such transfer pathway is clearly implicated by the decrement in the PL intensity observed at the emission position of $CsPbBr_3$ in the composite system for both far band gap (300 nm) and close band gap excitations (480 nm) made w.r.t. $CsPbBr_3$ **(Figure 5.3 B and 5.3 C)**.

Further upon monitoring the emission intensity in NIR domain, we found the PL intensity at the position of PbS emission increased in the composite sample when the samples were excited with 300 nm light. This indicates that although there are bidirectional transfer pathways feasible under such high energy excitation, the the hot carriers undergo preferential transfer from $CsPbBr_3$ to PbS states **(Figure 5.3 D)**. On similar lines, the increment in the PL intensity in the composite sample for the instance of 480 nm excitation also justifies the transfer of carriers from $CsPbBr_3$ to PbS states **(Figure 5.3 E)**. However, we observed that the magnitude of increment is much lesser for 480 nm that can be attributed to the trapping of some of the carriers in the interfacial defect states while transferring as also justified by the bleach intensities in the transient absorption measurements.

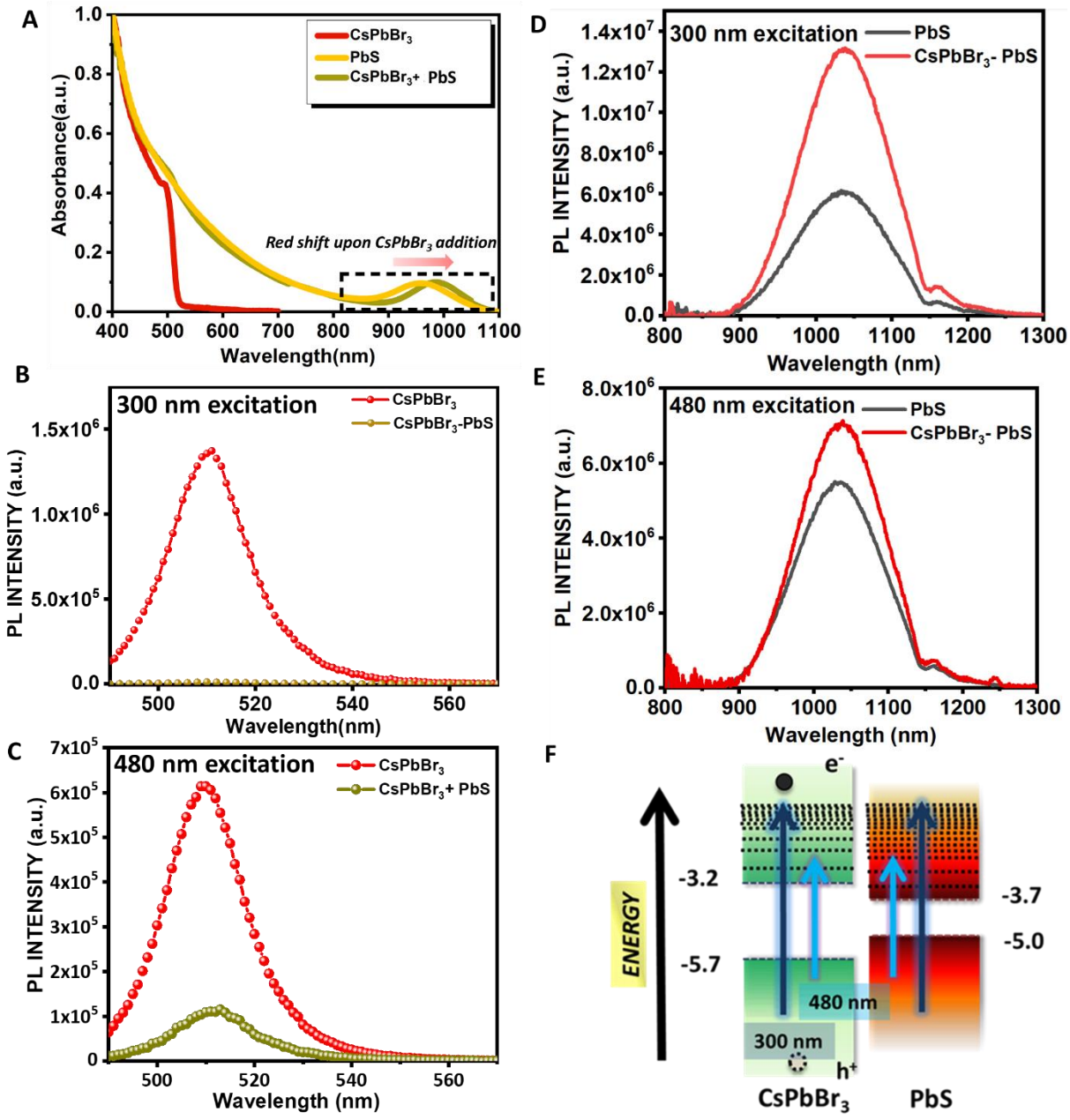

Figure 5.3 (A) Steady state optical absorption spectra for the pure $CsPbBr_3$ NCs, PbS QDs and their resultant composite colloidal mixture ($CsPbBr_3$ + PbS); The corresponding PL data illustrates the quenching of PL intensity in the composite system monitored at the emission position of $CsPbBr_3$. **(B)** in the case of far band gap excitation (w.r.t $CsPbBr_3$)- 300 nm and **(C)** for near band gap excitation- 480 nm). **(D)** Simultaneous increment in the PL intensity probed in the NIR region at the position of PbS emission peak potraying a transfer of charge carriers from $CsPbBr_3$ towards PbS states under 300 nm excitation and **(E)** 480 nm excitation. **(F)** Schematic illustration depicting the difference in the density of electronic states encountered in the composite system when excited using different excitation wavelengths.

5.2.3 Femtosecond Transient Absorption studies

For venturing the diversity in the carrier relaxation and carrier transfer rates with alteration in the excitation energies, pump energy dependent ultrafast TA studies were undertaken to embark upon the variation in the different transfer strategies taken up by hot and cold charge carriers. For accomplishing this task, a thoughtful selection of pump excitation energies corresponding to a range of wavelengths- 300 nm, 480 nm, 620 nm was made and in this process a set of assorted observations can be realized **(Figure 5.3 F)**. In brief, the entire purpose is thus to excite the carriers in distinctly dense energy states, which are encountered upon exciting the samples with energetically diverse pumps. The main difference that stems in due to the fact that the employment of extremely high energy pump (300 nm) warrants charge carriers to be photogenerated in the closely densed states of both $CsPbBr_3$ and PbS, while for near band gap excitation (480 nm) the charge carriers introduced into the heterosystem initially land in the discrete states of $CsPbBr_3$ and closely spaced energy states of PbS. Finally to verify that the change in the kinetic branches from the underlying transfer and delocalisation mechanism, where PbS QDs were excited using 620 nm pump excitation. Above all, for the sake of affirming similar experimental conditions, the incident laser flux was kept similar ($\sim 50 \mu J/cm^{-2}$) for each of the systems under study for different excitation wavelengths like 300 nm, 480 nm and 620 nm.

5.2.3.1 300 nm excitation

The choice of 300 nm laser excitation has been made with a prime motive that subsequent to photoexcitation, the photogenerated charge carriers in both $CsPbBr_3$ and PbS initially occupy highly dense energy states. To disentangle the ultrafast carrier dynamics which includes both carrier cooling and carrier transfer, a comparative analysis of the kinetics was carried out by probing the $CsPbBr_3$ NCs system in the visible regime, PbS QDs in the NIR regime and finally $CsPbBr_3$-PbS NC composite in both visible regime and NIR regime as shown in **Figure 5.4 (A-D).** A noticeable negative valley feature *i.e.* absorption bleach for $CsPbBr_3$ NCs corresponding to the 1S transition extended over a wide range (460 nm – 550 nm, centered at 504 nm) is seen in the visible range of differential absorption data **(Figure 5.4 A)**. The bleach signal for $CsPbBr_3$ NCs is sensitive to both electron and hole population due to approximately similar effective mass of hole and electron.[28]

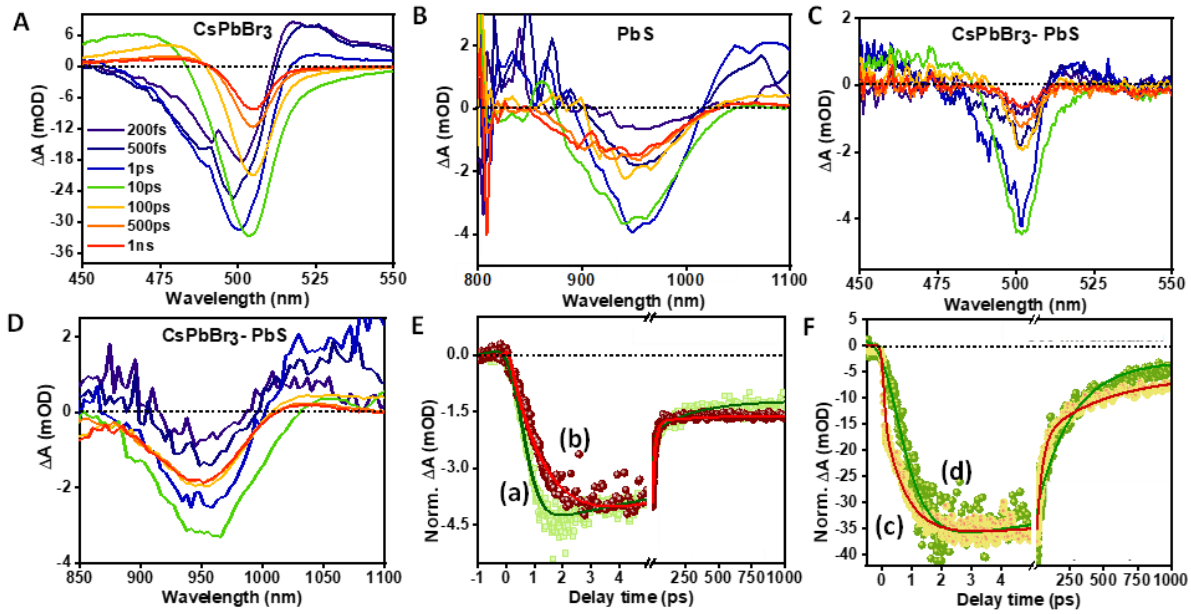

Figure 5.4 Representative Transient Absorption spectra for (**A)** $CsPbBr_3$ NCs in the visible regime; (**B)** PbS QDs in NIR regime; (**C)** $CsPbBr_3$-PbS NC composite in visible; and (**D)** $CsPbBr_3$-PbS NC composite in the NIR regime; (**E)** Normalised bleach kinetics for PbS NCs ((a), probe wavelength = 955 nm) and $CsPbBr_3$-PbS NC composite ((b), probe wavelength = 962 nm); (**F)** Normalised bleach kinetics for $CsPbBr_3$- NCs (c) and $CsPbBr_3$-PbS NC composite (d) probed at visible bleach maxima (504 nm). The data presented here are for the samples after exciting at 300 nm.

In a similar manner, conventional bleach pertaining to the state filling due to $1S_h - 1S_e$ transition (centered around 955 nm) is clearly noticeable in the representative transient absorption (TA) spectra for the bare PbS QDs when the system is probed in the NIR region **(Figure 5.4 B)**.[29] The physical attributes for both the bleaches straightforwardly relate to the first excitonic absorption prominently observed in the linear optical absorption spectra. Similar to the case of $CsPbBr_3$, the effective mass of both holes and electrons is quite similar in case of PbS ($m_e^* = m_h^* = 0.085$),[30] so the contribution of both holes and electrons to the 1S bleach of PbS is quite equal. Even in the composite system, the PbS bleach still divulges itself as a strong negative feature **(Figure 5.4 D)**.An analogous effect is noticeable in the visible probe range at the position of $CsPbBr_3$ NC bleach, but the reduction here is much more pronounced **(Figure 5.4 C).** Similar effect is also observed in $CsPbBr_3$ bleach broadness where $CsPbBr_3$ bleach width is seen to be drastically reduced in the $CsPbBr_3$-PbS composite system, which is a clear hint of sharp reduction in the carriers in $CsPbBr_3$ system since bleach width is directly proportional to the number of charge carriers.[31]

Further, monitoring the kinetics at the NIR bleach minima for both the samples *viz.*, PbS QDs and $CsPbBr_3$-PbS composite, we find the bleach growth dynamics to be decelerated in the composite situation which undeniably suggests that there is an additional pathway that impedes the otherwise prevalent simple process of carrier cooling **(Figure 5.4 E)**. Thereby, the NIR bleach growth kinetics for the composite is seen to be best fitted using longer time constants: 0.35 ps (42%), 1.2 ps (58%) while for the pure PbS QDs, the kinetics fits best merely with 0.25 ps (68%), 0.46 ps (32%) **(Table 5.1)**.This additional lag is a consequence of the hot carriers; *i.e.* both holes and electrons making their way from $CsPbBr_3$ energy states to PbS which later on pursue the conventional relaxation pathways. An interesting, add-on here at this point surfaced when a watchful analysis of the comparative kinetics of the systems was made in the visible domain. In the visible probe, 1S excitonic transition of $CsPbBr_3$ NCs reveals itself as a photoinduced negative bleach feature centered around 504 nm in both the pure NC sample and in the colloidal mixture. Yet again in the visible region, the bleach growth kinetics were observed to be delayed in the case of the composite sample than pure $CsPbBbr_3$ NCs. **(Figure 5.4 F)** (For $CsPbBr_3$: the growth components are 0.13 ps (78%), 0.68 ps (22%); for composite: 0.2 ps (75%), 0.85 ps (25%)) **(Table 5.1)**.

Table 5.1: Kinetic fitting parameters for the probe monitored at the bleach position (probe wavelength (WL) mentioned in bracket) for pure $CsPbBr_3$, pure PbS and $CsPbBr_3$ – PbS composite NCs under a pump excitation of 300 nm.

SYSTEM (probe WL)	τ_{G1} (ps)	τ_{G2} (ps)	τ_1 (ps)	τ_2	τ_3
$CsPbBr_3$ (504 nm)	0.13 ± 0.01 (78%)	0.68 ± 0.03 (22%)	30.2 ± 2 (-55%)	250 ± 15 ps (-25%)	>1ns (-20%)
PbS (955 nm)	0.25 ± 0.01 (68%)	0.46 ± 0.02 (32%)	1.36 ± 0.2 (-9.5%)	29 ± 2 ps (-47.6%)	>1ns (-42.9%)
$CsPbBr_3$- PbS (504 nm)	0.2 ± 0.02 (75%)	0.85 ± 0.01 (25%)	125 ± 7 (-72.2%)	>1ns (-27.8%)	
$CsPbBr_3$- PbS (962 nm)	0.35 ± 0.03 (42%)	1.2 ± 0.01 (58%)	22 ± 1.5 (-57.5%)	>1 ns (-42.5%)	

Hot carrier transfer and delocalisation of the carriers from PbS towards $CsPbBr_3$ states can be held liable for such delayed dynamics. The comparative dynamics in the ultrafast femtosecond studies for 300 nm thus are strongly indicative of the readily viable, bi-directional transfer of charge carriers from $CsPbBr_3$ towards PbS and vice-versa. Wang et.al however explained this observation to be entirely an outcome of efficient energy transfer from $CsPbBr_3$

to PbS.[8] But here in our studies, we found this observation to be an effect of underlying carrier transfer processes on the grounds of the conclusions drawn in addition to the other probable channel of energy transfer which cannot be entirely neglected.

Furthermore, close scrutiny of the bleach intensities reveals that such composite design under 300 nm excitation permits two way charge transfer still there seems to be more inclination for carrier transfer from $CsPbBr_3$ towards PbS. Upon maintaining similar optical density of the samples for the steady state measurements at 300 nm, it is anticipated that the individual systems namely $CsPbBr_3$ and PbS constituting the composite should absorb roughly equal quantity of light when excited with 300 nm laser light. In line with this, for $CsPbBr_3$ – PbS system the bleach intensity for $CsPbBr_3$ is expected to be half but it is observed that it is reduced to much larger extent that suggests hot carrier transfer from $CsPbBr_3$ to PbS. Similarly, the PbS intensity is anticipated to be half for the composite sample in contrast to pure PbS QDs however it is found to be enhanced. This can be explained as a straight consequence of rapid hot carrier transfer from $CsPbBr_3$ towards PbS, due to which there is a huge decline seen in $CsPbBr_3$ bleach intensity. However, as discussed in the previous section the delayed kinetics of the composite system probed at the NIR bleach is clearly indicative that the HC transfer also takes place from PbS to $CsPbBr_3$ energy states. Thus, the PbS bleach intensity also presents a complicated reciprocation of the two counter transfer processes. Instead of exhibiting an equal enhancement in PbS intensity (relative to the decrease in $CsPbBr_3$ bleach intensity), the increase is much lesser which implies that carrier transfer from $CsPbBr_3$is much more pronounced. Nevertheless, also owing to the dominance of the carrier transfer process from $CsPbBr_3$ to PbS due to its thermodynamic viability, out of the either possible directions of transfer, it is primarily expected that $CsPbBr_3$ to PbS transfer should be more dominating. This claim is further strengthened by the NIR PL investigations where a drastic increment in the PL intensity of PbS emission in the composite sample is noticeable in contrast to what is observed in PbS QDs **(Figure 5.3 D,E)**. Hence the overall picture seems to be quite multifaceted and complex. Another aspect is the interfacial defects that can also serve as obstructions in the else unhindered process of transfer, acting as traps for the free carriers, thereby preventing the carriers to reach the band edge of the individual constituents following the process of transfer.[19] This can also play a role in affecting the bleach intensities as some of the carriers may get themselves trapped on the way during the transfer process. In brief, a convincing remark on the carrier transfer possibilities can be inferred from the deceleration of the carrier cooling rate noticeable in both the situations but drawing further quantitative conclusions from the current studies is a seemingly difficult task because of the involved complexity.

This observation can be understood in terms of the strong conflict that prevails when a carrier has two available pathways of dissipating its excess of energy- conventional relaxation and carrier transfer. Conventionally in the instance of direct excitation into the high energy manifold states of a semiconductor quantum dot, the process of carrier cooling is expected to be facilitated rather than the other possible channel available *i.e.* charge transfer. But there is another foremost important decisive aspect that has an ultimate say towards the observed kinetics. It is also the density of available energy states of the carrier acceptor that keeps a check over the feasibility of carrier transfer.[20,21] In the circumstance of very high energy excitation like 300 nm, the density of states accessible for either constituents of the hetero-structure is roughly similar (representative illustration provided in Scheme 1). This makes bi-directional transfer practical since there are enough and similar density of states in both $CsPbBr_3$ and PbS available to receive the carriers which elucidates the observed kinetics.

Apart from the sturdy bleach feature, two positive characteristics on either side of the bleach valley were clearly noticeable in all the samples under study. The one lying towards the high energy side of the bleach signal can straightforwardly be attributed to photoinduced absorption (PIA) of the charge carriers into higher excited states and the one on the lower energy side can be considered a result of biexciton formation. The detailed discussion in the present investigation has been limited mainly to bleach alone. However, we find that in the composite system, the biexciton amplitude for $CsPbBr_3$ is drastically diminished which can be directly related to the preferential transfer of the hot carriers from $CsPbBr_3$ to PbS.

5.2.3.2 480 nm excitation

To probe the difference in the transfer mechanism undertaken by relatively cold carriers (the notation of "hot" and "cold" carriers is in context of the energy of the carriers in $CsPbBr_3$), we have excited the charge carriers near the band edge (relative to $CsPbBr_3$) in all the three systems and compared the dynamics of the composite samples with the pure NC samples. Here again, similar negative bleach signatures were observed in the spectral responses for the systems under study **(Figure 5.5 A-D)**. Astonishingly, exciting the samples with 480 nm (2.58 eV), much lower energy as compared to 300 nm (4.13eV) yielded set of different yet interesting kinetics. Upon reducing the excitation energy by an amount of 1.6eV, a drastic variation in the carrier cooling and transfer pathways has been observed.

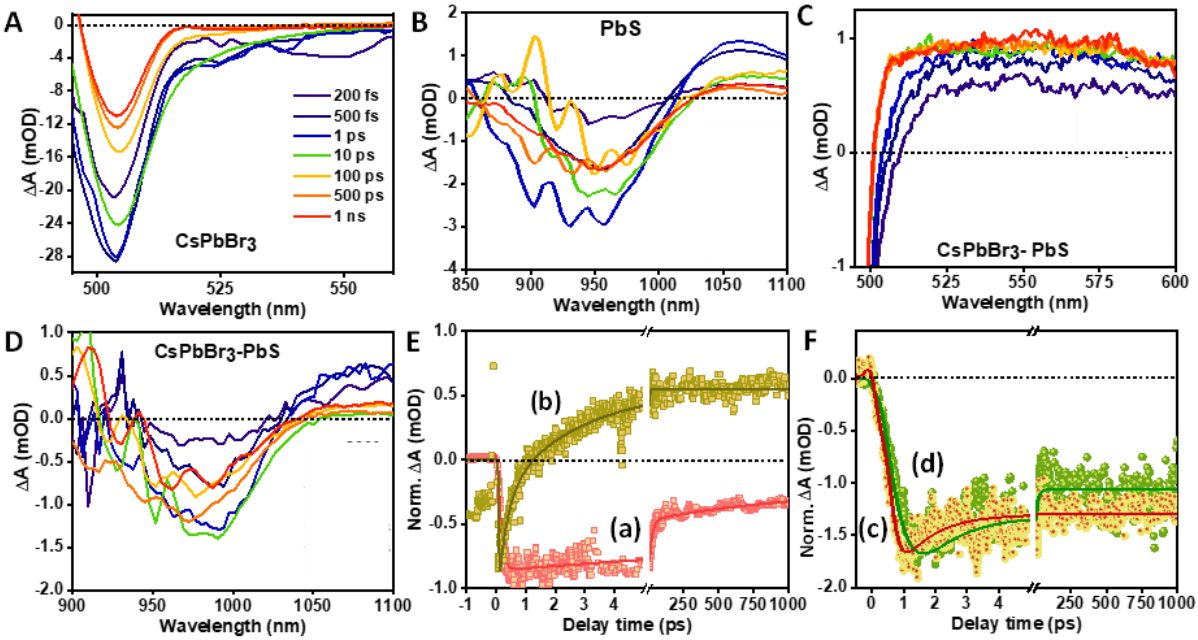

Figure 5.5 TA spectra for (**A)** $CsPbBr_3$NCs in the visible regime; (**B)** PbS QDs in NIR region; (**C)** $CsPbBr_3$–PbS composite in NIR region; (**D)** $CsPbBr_3$–PbS composite in NIR region; (**E)** Normalised bleach kinetics at 503 nm for (a) pure $CsPbBr_3$ NCs and (b) $CsPbBr_3$–PbS composite; (**F)** Normalised bleach kinetics at 955 nm/976 nm for (c) pure $CsPbBr_3$ NCs and (d) $CsPbBr_3$–PbS composite; after exciting the samples at 480 nm.

Contrary to our anticipation, it was observed that upon exciting the composite mixture with an energy equivalent of 480 nm, we observed an instantaneous growth and recovery of negative bleach signature arising from the excitonic absorption of $CsPbBr_3$ which is otherwise an obvious prolonged feature expected in the pure $CsPbBr_3$ NCs sample under such excitation **(Figure 5.5 E)**. The negative bleach signal in no time replaced by a broad positive signal throughout the visible region of the probe spectrum. This positive signal can be attributed to the PIA undergone by the hot carriers in the process of carrier transfer which can occur either from the interfacial defect states or from the excited states. Further the excitonic position of $CsPbBr_3$ provides a hint that in the instance of close to band edge excitation, the transfer of charge carriers towards PbS states tends to be an utterly fast process. This is further consolidated by the comparatively shorter time scale observed upon fitting the bleach growth as well as early recovery kinetics for the composite system. Growth kinetics of the transient bleach for both the samples is IRF limited but the difference is clearly seen in the bleach recovery kinetics. For $CsPbBr_3$–PbS composite system the first recovery component is found to be 0.5 ps, while for $CsPbBr_3$ NCs it is found to be 6.25 ps **(Figure 5.5 E)** (**Table 5.2**). The faster carrier cooling and bleach recovery kinetics at 503 nm for $CsPbBr_3$–PbS composite

clearly suggest ultrafast hot carrier transfer from $CsPbBr_3$ to PbS in the composite. It is interesting to observe bi-directional carrier transfer pathway accessible in the case of 300 nm excitation, however in the instance of 480 nm, only one way channel of carrier transfer ($CsPbBr_3$ to PbS) remains more preferable as suggested by the monitored kinetics (no retardation is observed for the dynamics monitored at the bleach of $CsPbBr_3$).Conclusively, in case of near band gap excitation it seems that transfer mechanism significantly dictates over other feasible channel of carrier cooling. This observation is further strengthened by monitoring the sequential kinetics at the site of the PbS bleach **(Figure 5.5 F)**. The bleach growth kinetics for the $CsPbBr_3$-PbS bleach monitored at the position of the NIR bleach fits best with an additional and also a relatively longer time component (0.15 ps (60%), 0.32 ps (40%)) than that for PbS QDs (0.25 ps (100%)) (**Table 5.2**).

Table 5.2 Kinetic fitting parameters for the probe monitored at the bleach position (probe wavelength (WL) mentioned in bracket) for pure $CsPbBr_3$, pure PbS and $CsPbBr_3$ – PbS composite NCs under a pump excitation of 480 nm.

SYSTEM (probe WL)	τ_{G1}	τ_{G2}	τ_1	τ_2	τ_3
$CsPbBr_3$ (503 nm)	<100 fs (100%)	-	6.25 ± 0.3ps (-26.4%)	96± 3 ps (-28.2%)	>1 ns (-45.4%)
PbS (955 nm)	0.25 ± 0.01ps (100%)		0.9 ± 0.03ps (-23.5%)	>1ns (-76.5%)	
$CsPbBr_3$-PbS (503 nm)	<100 fs (100%)	-	0.5± 0.06 ps (-70.5%)	2.26± 0.04 ps (-25.9%)	>1 ns (-3.6%)
$CsPbBr_3$-PbS (976 nm)	0.15± 0.03ps (60%)	0.32 ± 0.04ps (40%)	1.23± 0.02 ps (-20%)	>1ns (-80 %)	

The slow bleach growth trend noticed for the composite sample clearly implies that there is transfer of carriers from $CsPbBr_3$ states towards PbS band edge which adds an additional lag into the otherwise time observed for carrier cooling. Increment in the PbS bleach intensity is however not seen in the composite sample which may be the consequence of trapping of the carriers in the interfacial defects. It should be noted that unlike the case of 300 nm where delocalization remains largely feasible, 480 nm excitation doesn't facilitate delocalization. It is because when the excitation is made using 480 nm laser light, the charge carriers are excited

in strongly confined states of $CsPbBr_3$ but for PbS the states are comparatively less sparse. As a consequence of this, the delocalization of the carriers wavefunctions across the two constituents is difficult leaving carrier transfer as the most practical pathway. PL measurements conducted by investigating the emission in the NIR region also go in accordance with these derived conclusions where a relative increment in the PL emission is clearly observed in the composite sample.

5.2.3.3 620 nm excitation

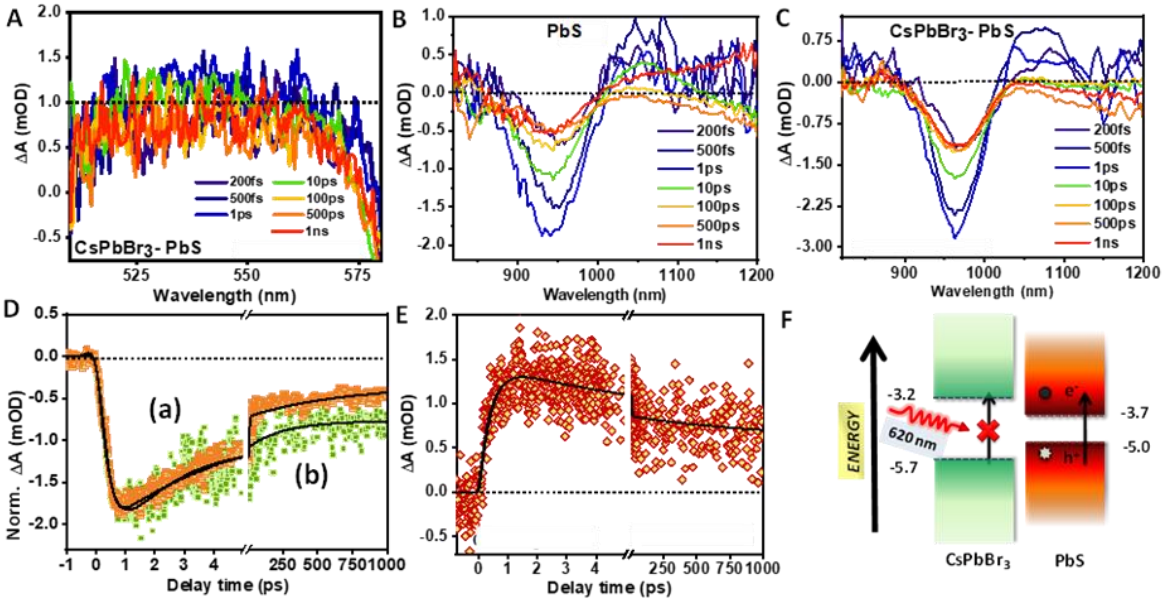

Figure 5.6 Representative Transient Absorption (TA) spectral maps under 620 nm excitation for (**A).** $CsPbBr_3$-PbS NCs in the visible probe region. (**B)** PbS QDs in the NIR regime; (**C)** $CsPbBr_3$-PbS NC composite in the NIR regime. (**D)** Comparative normalized TA kinetics at NIR bleach position for (a) PbS QDs probing at 945 nm; and (b) $CsPbBr_3$-PbS NC composite probing at 960 nm); (**E)** TA kinetics for $CsPbBr_3$-PbS NC composite at 540 nm. **(F)** Schematic illustration of the processes taking place when the $CsPbBr_3$-PbS composite sample is excited at 620 nm.

Finally, a very low energy excitation is selected with a consideration to ensure that the corresponding employed pump excitation energy (2eV) is inadequate for generating charge carriers in the $CsPbBr_3$ structure (Energy band gap (E_g) > 2eV). Thereby, system of pure $CsPbBr_3$ NCs fails to yield any TA data (visible as well as NIR region), while in the process of probing the $CsPbBr_3$-PbS composite system in the visible region of the electromagnetic spectrum, a broad positive signal prevails throughout that can be related to the expected photoinduced absorption (PIA) from the carriers photo-generated in the PbS domain **(Figure**

5.6 A). However in the NIR probe region, the typical bleach corresponding to PbS is clearly observable in both the pure PbS and $CsPbBr_3$-PbS composite systems **(Figure 5.6 B, C)**.The TA spectral response for the early time domain for both PbS and $CsPbBr_3$-PbS composite systems hold close resemblance in the NIR probe range. Upon investigating the dynamics at the bleach position of PbS, the relative carrier cooling kinetics obtained upon normalising the data for both pure PbS and $CsPbBr_3$-PbS composite is found to be quite similar which can be fitted with roughly the same fitting time constants (0.22ps) **(Figure 5.6 D) (Table 5.3)**.The kinetics for the PIA observed in the visible region for the composite system is provided in **Figure 5.6 E**.The simplistic mechanism illustrating the underneath dynamics prevailing the picture under 620 nm excitation is presented in **Figure 5.6 F**.

Table 5.3: Kinetic fitting parameters for the probe monitored at the bleach position (probe wavelength (WL) mentioned in bracket) for pure PbS and $CsPbBr_3$ – PbS composite NCs under a pump excitation of 620 nm.

SYSTEM (probe WL)	τ_{G1}	τ_1	τ_2	τ_3
PbS (960 nm)	0.22 ± 0.02 ps (100%)	3 ± 0.05ps (-20%)	>1ns (- 80%)	
$CsPbBr_3$- PbS (540 nm)	0.3 ± 0.02 ps (100%)	5 ± 0.75ps (-34.6%)	>1 ns (-65.4%)	
$CsPbBr_3$- PbS (945 nm)	0.22 ± 0.01 ps (100%)	4.6± 0.6 ps (-61%)	101 ± 6 ps (-10.5%)	>1 ns (-28.5%)

5.3 Summary

In summary, here in this investigation an endeavour has been made to comprehensively understand the $CsPbBr_3$-PbS colloidal hetero-structure which is a widely known system for fabrication of highly sensitive photodetectors. The work has been designed to explore underlying hot carrier relaxation and transfer strategies with in the $CsPbBr_3$-PbS hetero-structure. For this intent, we have vigilantly chosen a set of different excitation energies which have helped us in gaining an in-depth insight of this system while comparing the individual constituents of the overall system namely, $CsPbBr_3$ and PbS NCs simultaneously. Upon comparing the bleach growth kinetics, we found the transfer of the hot carriers in this Type -1 hetero-structure to be bidirectional since the bleach growth dynamics are noticed to be quite decelerated in contrast to those monitored for the pure NCs while exciting at high energy

photon (300 nm). However, there was a drastic variation observed when the composite was excited close to the band edge. The probe dynamics in such instance of near band gap excitation (480 nm), however suggested that unlike the hot carriers, the cold carriers on the other hand tend to opt for only one way transfer of carriers, *i.e.* from $CsPbBr_3$ to PbS energy states. Such a detailed knowledge of carrier relaxation and transfer mechanisms can prove utterly advantageous for the design and further improvement in the performance of any sort of photo electronic devices employing $CsPbBr_3$-PbS colloidal hetero-structure.

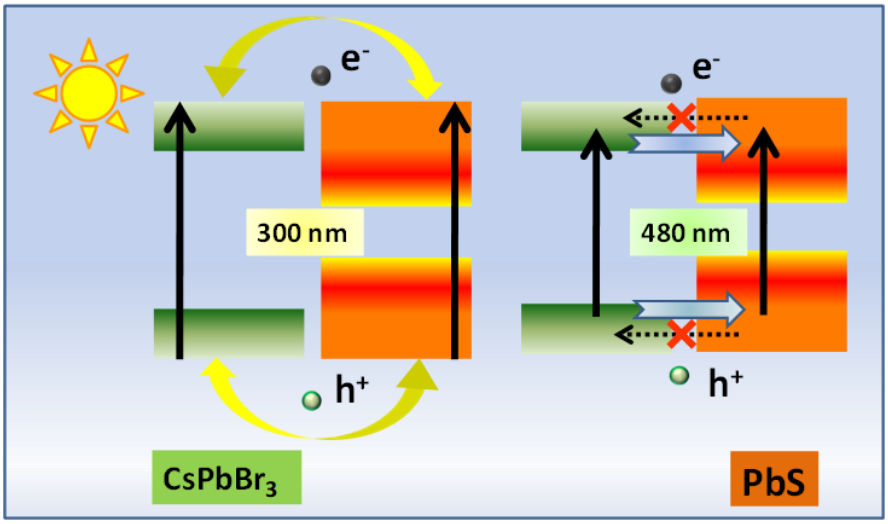

"In this study conducted for $CsPbBr_3$–PbS hybrid system, the deductions suggest that under high energy excitation, the charge carrier transfer is bidirectional; however, upon resonant stimulation, it is revealed to be unidirectional"

5.4 References

(1) König, D.; Casalenuovo, K.; Takeda, Y.; Conibeer, G.; Guillemoles, J. F.; Patterson, R.; Huang, L. M.; Green, M. A. Hot Carrier Solar Cells: Principles, Materials and Design. *Phys E Low-dimensional Syst Nanostructures* **2010**, *42* (10), 2862–2866.

(2) Kaur, G.; Ghosh, H. N. Hot Carrier Relaxation in $CsPbBr_3$-Based Perovskites: A Polaron Perspective. *J Phys Chem Lett* **2020**, *11* (20), 8765–8776. h

(3) Maiti, S.; Ferro, S.; Poonia, D.; Ehrler, B.; Kinge, S.; Siebbeles, L. D. A. Efficient Carrier Multiplication in Low Band Gap Mixed Sn/Pb Halide Perovskites. *J Phys Chem Lett* **2020**, *11* (15), 6146–6149.

(4) Dutta, A.; Pradhan, N. Phase-Stable Red-Emitting $CsPbI_3$ Nanocrystals: Successes and Challenges. *ACS Energy Lett* **2019**, *4* (3), 709–719.

(5) Pan, J.; Shang, Y.; Yin, J.; De Bastiani, M.; Peng, W.; Dursun, I.; Sinatra, L.; El-Zohry, A. M.; Hedhili, M. N.; Emwas, A.-H.; et al. Bidentate Ligand-Passivated $CsPbI_3$ Perovskite

Nanocrystals for Stable Near-Unity Photoluminescence Quantum Yield and Efficient Red Light-Emitting Diodes. *J Am Chem Soc* **2018**, *140* (2), 562–565.

(6) Shpatz Dayan, A.; Cohen, B.-E.; Aharon, S.; Tenailleau, C.; Wierzbowska, M.; Etgar, L. Enhancing Stability and Photostability of $CsPbI_3$ by Reducing Its Dimensionality. *Chem Mater* **2018**, *30* (21), 8017–8024.

(7) Liu, D.; Zha, W.; Guo, Y.; Sa, R. Insight into the Improved Phase Stability of $CsPbI_3$ from First-Principles Calculations. *ACS Omega* **2020**, *5* (1), 893–896.

(8) Yu, Y.; Zhang, Y.; Song, X.; Zhang, H.; Cao, M.; Che, Y.; Dai, H.; Yang, J.; Zhang, H.; Yao, J. High Performances for Solution-Pocessed 0D–0D Heterojunction Phototransistors. *Adv Opt Mater* **2017**, *5* (24), 1700565.

(9) Kang, J.; Wang, L.W. High Defect Tolerance in Lead Halide Perovskite $CsPbBr_3$. *J Phys Chem Lett* **2017**, *8* (2), 489–493.

(10) Kang, I.; Wise, F. W. Electronic Structure and Optical Properties of PbS and PbSe Quantum Dots. *J Opt Soc Am B* **1997**, *14* (7), 1632–1646.

(11) Baranowski, M.; Plochocka, P.; Su, R.; Legrand, L.; Barisien, T.; Bernardot, F.; Xiong, Q.; Testelin, C.; Chamarro, M. Exciton Binding Energy and Effective Mass of $CsPbCl_3$: A Magneto-Optical Study. *Photon Res* **2020**, *8* (10), A50--A55.

(12) Garcia-Gutierrez, D. F.; Hernandez-Casillas, L. P.; Cappellari, M. V.; Fungo, F.; Martínez-Guerra, E.; García-Gutiérrez, D. I. Influence of the Capping Ligand on the Band Gap and Electronic Levels of PbS Nanoparticles through Surface Atomistic Arrangement Determination. *ACS Omega* **2018**, *3* (1), 393–405.

(13) Hines, M. A.; Scholes, G. D. Colloidal PbS Nanocrystals with Size-Tunable Near-Infrared Emission: Observation of Post-Synthesis Self-Narrowing of the Particle Size Distribution. *Adv Mater* **2003**, *15* (21), 1844–1849.

(14) Kamat, P. V. Quantum Dot Solar Cells. Semiconductor Nanocrystals as Light Harvesters. *J Phys Chem C* **2008**, *112* (48), 18737–18753.

(15) Wang, Y.; Yang, X.; Xiao, G.; Zhou, B.; Liu, B.; Zou, G.; Zou, B. Shape-Controlled Synthesis of PbS Nanostructures from −20 to 240 °C: The Competitive Process between Growth Kinetics and Thermodynamics. *CrystEngComm* **2013**, *15* (27), 5496–5505.

(16) Mastria, R.; Rizzo, A.; Giansante, C.; Ballarini, D.; Dominici, L.; Inganäs, O.; Gigli, G. Role of Polymer in Hybrid Polymer/PbS Quantum Dot Solar Cells. *J Phys Chem C* **2015**, *119* (27), 14972–14979.

(17) Cha, J.H.; Han, J. H.; Yin, W.; Park, C.; Park, Y.; Ahn, T. K.; Cho, J. H.; Jung, D.-Y. Photoresponse of $CsPbBr_3$ and Cs_4PbBr_6 Perovskite Single Crystals. *J Phys Chem Lett* **2017**,

8 (3), 565–570.

(18) Song, J.; Xu, L.; Li, J.; Xue, J.; Dong, Y.; Li, X.; Zeng, H. Monolayer and Few-Layer All-Inorganic Perovskites as a New Family of Two-Dimensional Semiconductors for Printable Optoelectronic Devices. *Adv Mater* **2016**, *28* (24), 4861–4869.

(19) Zhang, X.; Wu, X.; Liu, X.; Chen, G.; Wang, Y.; Bao, J.; Xu, X.; Liu, X.; Zhang, Q.; Yu, K.; et al. Heterostructural $CsPbX_3$-PbS (X = Cl, Br, I) Quantum Dots with Tunable Vis–NIR Dual Emission. *J Am Chem Soc* **2020**, *142* (9), 4464–4471.

(20) Li, M.; Bhaumik, S.; Goh, T. W.; Kumar, M. S.; Yantara, N.; Grätzel, M.; Mhaisalkar, S.; Mathews, N.; Sum, T. C. Slow Cooling and Highly Efficient Extraction of Hot Carriers in Colloidal Perovskite Nanocrystals. *Nat Commun* **2017**, *8* (1), 14350.

(21) Grimaldi, G.; Crisp, R. W.; ten Brinck, S.; Zapata, F.; van Ouwendorp, M.; Renaud, N.; Kirkwood, N.; Evers, W. H.; Kinge, S.; Infante, I.; et al. Hot-Electron Transfer in Quantum-Dot Heterojunction Films. *Nat Commun* **2018**, *9* (1), 2310.

(22) Kambhampati, P. Hot Exciton Relaxation Dynamics in Semiconductor Quantum Dots: Radiationless Transitions on the Nanoscale. *J Phys Chem C* **2011**, *115* (45), 22089–22109.

(23) Wei, K.; Zheng, X.; Cheng, X.; Shen, C.; Jiang, T. Observation of Ultrafast Exciton–Exciton Annihilation in $CsPbBr_3$ Quantum Dots. *Adv Opt Mater* **2016**, *4* (12), 1993–1997.

(24) Fu, X.; Pan, Y.; Wang, X.; Lombardi, J. R. Quantum Confinement Effects on Charge-Transfer between PbS Quantum Dots and 4-Mercaptopyridine. *J Chem Phys* **2011**, *134* (2), 24707.

(25) Ning, Z.; Gong, X.; Comin, R.; Walters, G.; Fan, F.; Voznyy, O.; Yassitepe, E.; Buin, A.; Hoogland, S.; Sargent, E. H. Quantum-Dot-in-Perovskite Solids. *Nature* **2015**, *523* (7560), 324–328.

(26) Ma, X.-J.; Wang, Z.Q.; Xiong, Z.-Y.; Zhang, Y.; Yu, F.-X.; Chen, P.; Xiong, Z.-H.; Gao, C.-H. 30-Fold Efficiency Enhancement Achieved in the Perovskite Light-Emitting Diodes. *RSC Adv* **2017**, *7* (80), 50571–50577.

(27) Jasieniak, J.; Califano, M.; Watkins, S. E. Size-Dependent Valence and Conduction Band-Edge Energies of Semiconductor Nanocrystals. *ACS Nano* **2011**, *5* (7), 5888–5902.

(28) Kaur, G.; Justice Babu, K.; Ghorai, N.; Goswami, T.; Maiti, S.; Ghosh, H. N. Polaron-Mediated Slow Carrier Cooling in a Type-1 3D/0D $CsPbBr_3$@Cs_4PbBr_6 Core–Shell Perovskite System. *J Phys Chem Lett* **2019**, *10* (18), 5302–5311.

(29) Gesuele, F.; Sfeir, M. Y.; Koh, W. K.; Murray, C. B.; Heinz, T. F.; Wong, C. W. Ultrafast Supercontinuum Spectroscopy of Carrier Multiplication and Biexcitonic Effects in Excited States of PbS Quantum Dots. *Nano Lett* **2012**, *12* (6), 2658–2664.

(30) Okuhata, T.; Kobayashi, Y.; Nonoguchi, Y.; Kawai, T.; Tamai, N. Ultrafast Carrier Transfer and Hot Carrier Dynamics in PbS–Au Hybrid Nanostructures. *J Phys Chem C* **2015**, *119* (4), 2113–2120.

(31) Manser, J. S.; Kamat, P. V. Band Filling with Free Charge Carriers in Organometal Halide Perovskites. *Nat Photonics* **2014**, *8*, 737.

(32) Kaur, G.; Babu, K. J.; Ghosh, H. N. Temperature-Dependent Interplay of Polaron Formation and Hot Carrier Cooling Dynamics in $CsPbBr_3$ Nanocrystals: Role of Carrier–Phonon Coupling Strength. *J Phys Chem Lett* **2020**, 6206–6213.

(33) Maity, P.; Dana, J.; Ghosh, H. N. Multiple Charge Transfer Dynamics in Colloidal CsPbBr3 Perovskite Quantum Dots Sensitized Molecular Adsorbate. *J Phys Chem C* **2016**, *120* (32), 18348–18354.

(34) Shukla, A.; Kaur, G.; Babu, K. J.; Ghorai, N.; Goswami, T.; Kaur, A.; Ghosh, H. N. Effect of Confinement on the Exciton and Biexciton Dynamics in Perovskite 2D-Nanosheets and 3D-Nanocrystals. *J Phys Chem Lett* **2020**, 6344–6352.

Chapter 6

Mapping the Real-Time Vibrational Infrastructure of Cs_2SnI_6 Nanocrystals through Coherent Phonon dynamics

Isolated polyhedra constituting the framework of Cs_2SnI_6 renders surplus degrees of dynamic freedom making it an abode of inherent anharmonicity. The ensuing properties of the integrated devices are thus inevitably governed by the underlying lattice vibrational dynamics. Here with the aid of femtosecond transient absorption (TA) spectroscopy, we have made an attempt to capture a real-time picture of the vibrational modes prevalent in the Cs_2SnI_6 system and allocate the origin of the thus far unidentified modes. Further, we have also inspected the generation mechanism of the fully symmetric coherent phonon mode "A_{1g}" which is manifested as strong oscillations in the time domain data for Cs_2SnI_6 and also the other low symmetry modes observable in the frequency domain in the unified framework of displacive excitation and impulsive scattering. As another major accomplishment, we pinpointed the position of the theoretically predicted yet never experimentally observed silent modes which usually are left undetected in the conventional frequency domain spectroscopic techniques. Strong support has been lent from the phase analysis of excitation pump and intensity-dependent TA measurements. Subsequent to accounting all the modes, the anharmonicity of the phonon modes, a straightforward consequence of phonon-phonon coupling has been addressed. Furthermore, we executed temperature-dependent investigations which together with the pump dependent studies provide insights into the extent of carrier-phonon coupling. All this critical information regarding the phonon modes can lend assistance in improving the performance of the devices based on Cs_2SnI_6.

6.1 Motivation and Background

The last decade has been a witness to the impressive performance of the Lead based perovskites in multiple research domains. But despite this, the hazard stemming from lead toxicity limits their commercialisation in the real world. Among all possible environmental friendly substitutes, tin (Sn^{2+}) based perovskites have been recognized as the best alternatives mainly due to size proximity of Sn^{2+} with Pb^{2+}.[1-3] However owing to the facile oxidation of Sn^{2+} to its higher oxidation state Sn^{4+}, $CsSnX_3$ compounds are utterly unstable. Rather, their vacancy ordered derivatives, Cs_2SnX_6 exhibit better stability and persistent performance over long durations of time.[4] Specifically Cs_2SnI_6, a member of this family of emerging vacancy ordered Lead-free double perovskites (DP) is one such contender that has deep-rooted its thorough suitability for various applications. It has emerged as a potential light-absorbing layer in PV devices because of its optimal energy bandgap and high absorption coefficient. PCE exceeding 10% has already been reported for Cs_2SnI_6 based solar cells.[5-9] Indeed, it has also illustrated exotic candidature as a hole transporting layer.[10-12] Aside from the potent candidature displayed for solar cell applications, thermo-electrics is another such classified field where Cs_2SnI_6 by virtue of its low thermal conductivity (k) has witnessed commendable success.[13,14] Such low magnitudes of "k" have often been linked to vibrational chaos stemming from anharmonicity in the lattice dynamics. [15-19] Even more, recent literature has attributed the photoconversion efficiencies of PV devices with lattice anharmonicity.[20-22]

Contrasting these defect ordered Cs_2SnI_6 architectures with their counterparts exhibiting ideal corner shared octahedral network reveals that the isolated $[SnI_6]^{4-}$ polyhedra in the former allow greater degrees of freedom for free motion.[23,24] This dynamic motion originating primarily from the coupling of Cs^+ displacements and octahedral tilting results in divergence from pure harmonic approximation, setting in intense anharmonic vibrations.[25] Moreover, both the optical and electronic traits of the charge carriers which eventually rely on how the mobile charge carriers couple to the low energy phonon modes and which are fundamental for device performance germinate from such dynamics.[25,26] Thus for further significant technological advancements deploying this Sn^{4+} based all inorganic perovskites, it is utmost important to have extensively fundamental inspection concerning the phonon vibrational modes and the subsequent carrier phonon scattering pathways.[27,28] However till date not only the vibrational phonon features in the ground state configuration of this tin based all inorganic DP system lack comprehensive exploration but also the correlation of the underlying phonon modes and electronic transitions is scarcely investigated.

Here in this investigation, we have employed femtosecond TA measurements with an intent to provide a unified picture of the phonon vibration modes and for identification of carrier-phonon coupling feasible in Cs_2SnI_6. Though such information on the subject of phonon spectra can be very well extracted from Raman and IR spectroscopy yet, gaining insights on the phonon modes in the low frequency regime and carrier-phonon coupling from such techniques is quite challenging.[29,30] The time domain measurements on the other hand present the full vibrational manifold supported by a lattice which extends even beyond the resolution of conventional techniques.[31-37] Another aspect where the conventional spectroscopies are inadequate is where the study demands the investigation of silent modes since Raman and IR silent modes cannot be detected by such techniques.[38]

TA measurements executed on Cs_2SnI_6 in the present endeavour deliver some very intriguing and new information. Results obtained clearly reveal the definite location of the so far unaddressed Raman active phonon modes for Cs_2SnI_6. The existence of these modes was previously only theoretically predicted but was never experimentally observed until now. The underlying generation mechanism of the coherent phonons is also investigated which is pivotal to understand the origin of the phonon modes. Another major accomplishment of this finding is the successful determination of the position of the silent modes which otherwise are undetectable in the conventional Frequency domain techniques. Most importantly as far as we are aware, such modes have never been identified before by employing TA measurements. Following this, we have also attempted capturing the anharmonicity in the Cs_2SnI_6 lattice, the subsequent phonon-phonon couplings and also obtained a qualitative idea of the carrier-phonon coupling by undertaking pump dependent measurements. Further, we have also conducted temperature dependent investigations to consolidate the conclusions drawn from the pump dependent TA studies regarding the carrier-phonon coupling strength. Besides this, the temperature dependent results suggest the dephasing rate to be unusually consistent over the entire range of investigated temperatures. This indicates the dephasing process of the coherent phonons in Cs_2SnI_6 to be mediated by coupling to the charge carriers or defects rather than through acoustic phonons. Best to our knowledge, this is the earliest study which has investigated such detailed aspects of the phonon framework (notably the low frequency and silent modes) and the carrier-phonon/phonon-phonon coupling mechanisms prevalent in Cs_2SnI_6. It is thus proposed that our results can be pivotal in making insightful predictions on the device performance and therefore can be reckoned beforehand while designing the devices based on Cs_2SnI_6 towards utmost efficiency.

6.2 Results and discussion

6.2.1 Primary characterisation of Cs_2SnI_6 DP NCs

The typical NC system under study has been synthesised employing the prototypical hot injection synthesis methodology in accordance with previously reported literature findings.[39] The details of the same have been included in the "Synthesis section" provided in Chapter 2. Subsequently, crystallographic and morphological investigations were undertaken to affirm the properties of the synthesized materials.

6.2.1.1 Crystallographic studies (X-Ray Diffraction (XRD)) and Morphological investigations (Transmission Electron Microscopy (TEM))

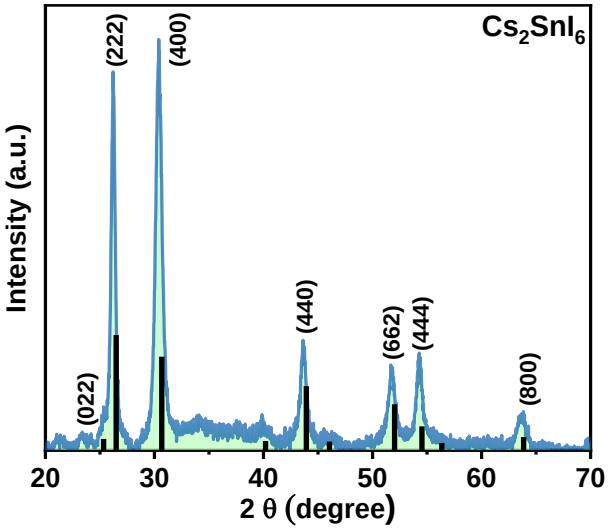

Figure 6.1 XRD pattern for the synthesised Cs_2SnI_6 NCs spin-coated over glass substrate (the black lines represent the standard XRD pattern of Fm-3m Cs_2SnI_6.

XRD has been performed for the determination of the crystal structure of the prepared NCs. The diffractogram displayed in **Figure 6.1** shows the XRD peaks indexed with the diffraction planes for Cs_2SnI_6. The crystallographic data further infers that the NCs adopt cubic phase with Fm-3m space group crystal symmetry having an edge parameter of 11.65Å and holds fair agreement with the standard pattern (PDF#51-0466).

HR-TEM image depicts d-spacing of 0.29 nm corresponding to the (004) plane and an interplanar spacing of 0.37 nm that corresponds to the (222) plane (**Figure 6.2**).

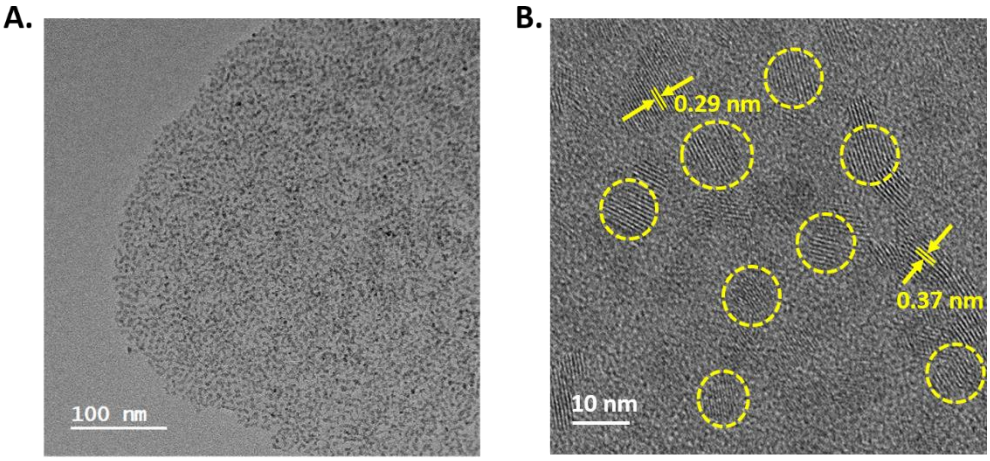

Figure 6.2 (A) Large area TEM image of the synthesised pristine Cs_2SnI_6 NCs **(B)** High Resolution (HR)-TEM image.

6.2.1.2 Steady State optical studies

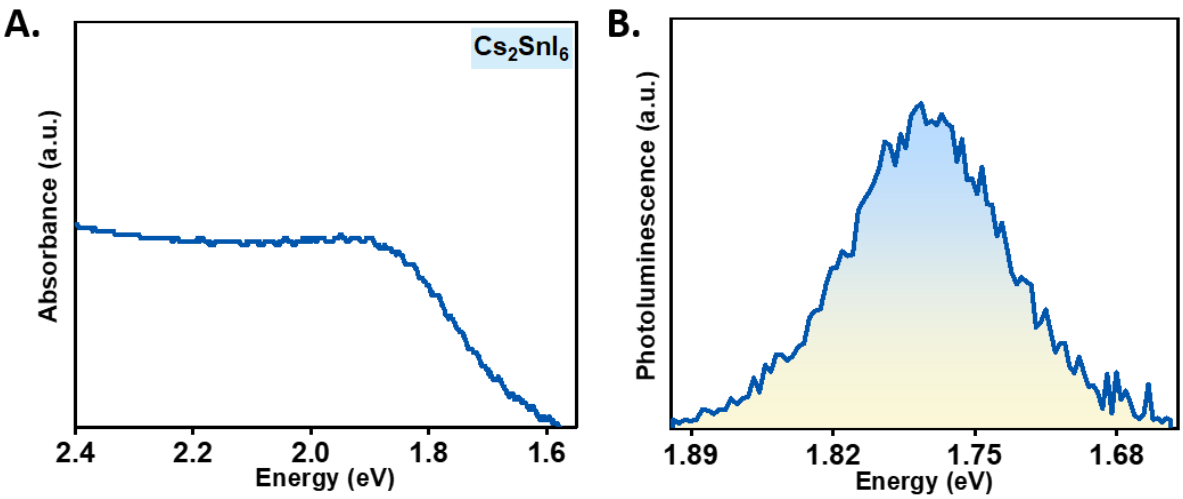

Figure 6.3 (A) Steady state optical absorption spectra for Cs_2SnI_6 NCs and **(B)** the corresponding photoluminescence (PL) spectra. (Excitation energy= 2eV).

The optical absorption spectra for the as-synthesized Cs_2SnI_6 NCs illustrates band edge excitonic peak around 1.87 eV and the corresponding PL emission spectrum for NCs is obtained at 1.78 eV (Full Width at Half Maxima (FWHM) ~110meV) **(Figure 6.3)**.

6.2.2 Vibrational information from resonant TA dynamics

To commence the investigation of the vibrational dynamics in these DP NCs, we initially chose to photo-excite the NCs across the band gap. For this purpose, ultrashort 2eV pump pulses were

chosen and the subsequently incurred TA changes were monitored simultaneously as a function of time delay (the experimental technique is illustrated through a schematic in **Figure 6.4 A**). **Figure 6.4 B** depicts the 2D coloured contour map obtained as a consequence of photo-excitation.

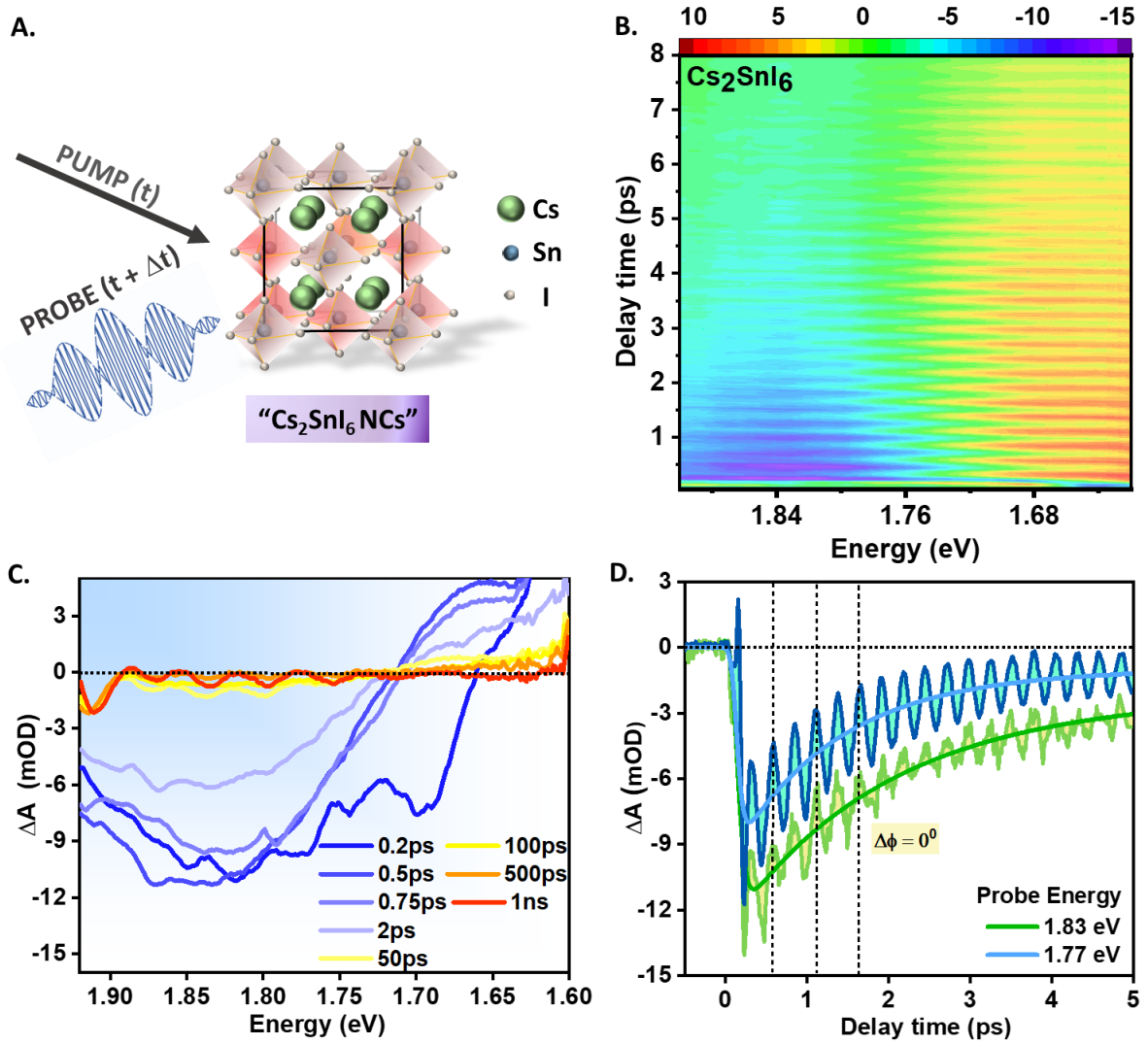

Figure 6.4 (**A)** Schematic representation of the pump-probe technique employed for data acquisition, (**B)** Pseudo-colour 2D contour representation for the TA response recorded upon photo-excitation of Cs_2SnI_6 NCs (pump energy = 2 eV), (**C)** The corresponding TA spectral traces for selected delay times, (**D)** Resultant kinetics monitored at specific probe energies (1.77 eV, 1.83 eV) illustrating the periodic modulations due to coherent phonon generation superimposed over the carrier dynamics. The oscillations perceived in the TA data at two different probe energies are in phase ($\Delta\varphi = 0^0$) indicating that the oscillations are an outcome of amplitude modulation.

Interestingly, along with the anticipated differential absorption signal *i.e.* the ground state bleach (GSB) **(Figure 6.4 C)** complementary to the 1st excitonic peak for Cs_2SnI_6 **(Figure 6.3 A)**, there are periodic oscillations noticeable in the time domain superimposed on the otherwise exponentially decaying kinetics for these iodide DP NCs **(Figure 6.4 C, D)**.

There are two well-known ways in which the coherent nuclear motion can affect the linear absorption spectrum: frequency modulation and amplitude modulation. The distinction between them can be realized by monitoring the phase shift between the oscillatory time domain data at different probe energies.[40-43] In both the scenarios, the transient data monitored at any particular probe energy presents oscillatory features. However, the phase difference recorded for the oscillations at two different probe energies would show different behaviour depending on the mechanism responsible for the modulations. Here in this finding we found that the oscillations in the t-domain are all aligned in the same phase ($\Delta\varphi = 0^0$) for two different probe energies as seen in **Figure 6.4 D**. Therefore, the oscillations observed are a consequence of the nuclear wavepackets setting in dynamic amplitude modulations in the linear absorption spectrum. Such modulations in amplitude take place as a consequence of the oscillating transition moment via non-Condon effects. On the contrary, if the phase difference between the oscillatory t-domain data would have been non-zero at different probe regions, then it could have been frequency modulation which takes place due to the coherent phonons altering the level structure.[40-43]

These recurrent oscillations manifested in the TA data are apparent with a consistent period of "0.26 ps" **(Figure 6.5 A)**. It can thus be stated that there is one explicit characteristic category of phonon mode which is being emitted coherently and which presides over the other viable phonon modes conforming to the observed temporal behaviour.

To account for the origin of this oscillatory feature and to unveil the information concerning the underlying vibrational degrees of freedom, we processed the residual oscillatory signal **(Figure 6.5 A)** (obtained after deducting the TA dynamics from the corresponding fit) using Fast Fourier Transform (FFT) function **(Figure 6.5 B)**. In general, for any ordered double perovskite ($A_2BB'X_6$) system with $Fm\bar{3}m$ space group crystallographic symmetry, factor group theory analysis predicts following zone centered (Γ) optical normal modes of vibration depictable by the irreducible representation;[44,45]

$$A_{1g} + E_g + 2F_{2g} + F_{1g} + 3F_{1u} + F_{2u} \ldots\ldots\ldots\ldots \quad \textbf{Eq. 6.1}$$

Amongst these enlisted modes, four of them are Raman allowed active normal modes - (A_{1g}, E_g, two F_{2g}), three are known to be IR active - (all the F_{1u} modes) whereas the rest two are silent ones, i.e. are forbidden in Raman as well as IR (F_{1g}, F_{2u}).[46] In line with the

expectation, the Raman spectroscopic measurements conducted in previously reported works, both theoretical and experimental have procured three primary order branches in Cs_2SnI_6 system peaked at: 78 (δ (F_{2g})), 92 (ν (E_g)) and 126 (ν (A_{1g})) cm^{-1}.[47] Majority of the peaks apparent in the FFT power spectrum **(Figure 6.5 B)** lend fair agreement either with the fundamental vibration modes (either Raman or IR active) as stated by the theoretical and experimental findings conducted before or if not then with the corresponding overtones or combination modes as discussed later.[46] Most importantly, the frequency domain analysis suggests that the observed wave packets in the TA data can be attributed to be an effect of coherent generation of the Raman active Sn-I stretching vibration mode (A_{1g}) (121 cm^{-1} → 3.63 THz → 0.27 ps). This suggests that at such excitation conditions (near band gap and low intensity (100μW)) it is the fully symmetric "breathing mode" A_{1g} mode (pictorial representation provided in **Figure 6.5 B**) that presides over the other modes and couples most effectively with the photogenerated charge carriers. The spectral position of the other F_{2g} mode, *i.e.* the Raman mode representing the vibrations of Cs^+ ions in $[SnI_6]^{4-}$ octahedra and the two presumed silent modes (F_{1g}, F_{2u}) however is yet undetermined.[48] Although the existence of these silent modes has been theoretically figured yet no experimental investigation till date has been able to locate the position of these modes.

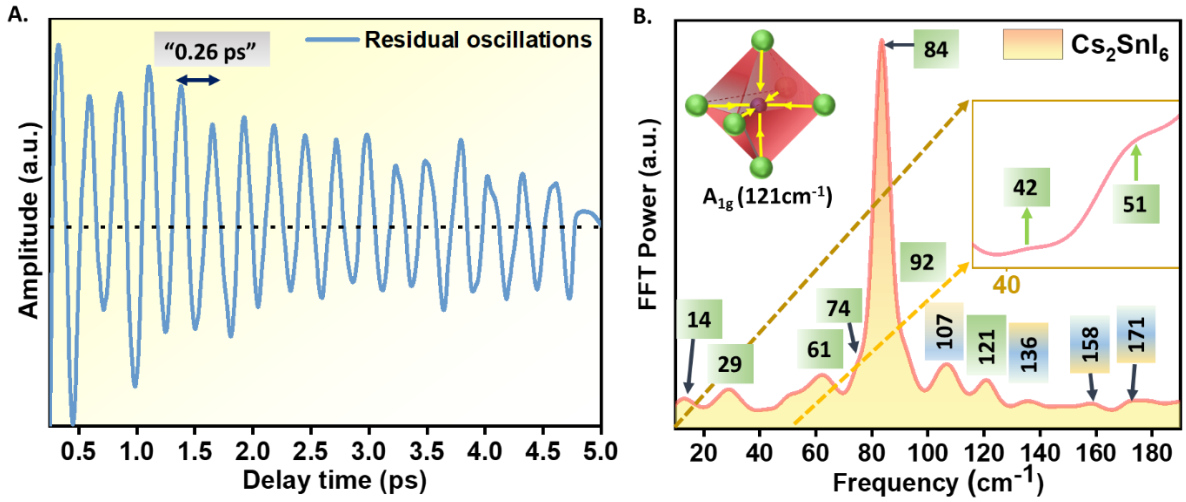

Figure 6.5 **(A)** Extracted residual oscillations with a typical time period of "0.26 ps" after subtracting the exponential decay behaviour from the TA trace**, (B)** Power spectrum obtained after Fast Fourier transforming these residual oscillations revealing the distinct phonon modes feasible in Cs_2SnI_6.

Three unidentified peaks at 14 cm^{-1}, 29 cm^{-1} and 61 cm^{-1} are distinctly noticeable in the low frequency region of the FFT power spectrum **(Figure 6.5 B)**. Amid these, the

unaddressed peak at 61 cm^{-1} can be categorically ruled out from the possibility of being the other ν^L (F_{2g}) Raman active lattice mode, leaving behind the former two peaks as the potential candidates. The ground for this assignment follows from the fact that the equivalent lattice mode ν^L (F_{2g}) observed for Cs_2SnCl_6 is positioned at 51 cm^{-1}, therefore the normal Raman mode stemming from the same origin for Cs_2SnI_6 is supposed to lie at a wavenumber much lower than 51 cm^{-1}.[46] This interpretation is a straightforward effect of the bond strength of Cs vibrations which is weaker in Iodide system than the former one, thus lowering the vibrational frequency (ν) of Cs-I bond. Apart from the bond strength, the oscillator mass ($\boldsymbol{\mu}$) of the Iodide system contrasted to the Chloride analogue is much enhanced which can be considered as the other factor accountable for expected lower ν value ($\nu \propto \sqrt{(\boldsymbol{k}/\boldsymbol{\mu})}$, k is the force constant that determines the bond strength).[46] Having said that, this still leaves us in an unsettled state since either one of the two modes – the one at 14 cm^{-1} or at 29 cm^{-1} can be the other F_{2g} Raman active phonon mode. To further resolve this conflict for identifying the exact position of F_{2g} mode, we made a comparative analysis for this particular mode for Cs_2SnI_6 with its lighter Chloride analogue:

6.2.2.1 Estimation of the Raman active F_{2g} mode

Considering a molecular vibration to be in close analogy to a spring-mass system, Hooke's law has always been looked upon as a perfect approximation for quantifying the vibrational frequencies (ν). This frequency is a strong function of the bond parameters for the constituting system as

$$\nu = \frac{\sqrt{k/\mu}}{2\pi} \quad \ldots\ldots\ldots\ldots\ldots \quad \textbf{Eq. 6.2}$$

Here, k implies the force constant which is a measure of the bond strength (bond enthalpy); μ stands for the reduced mass of the atoms involved in the corresponding vibration.

Following this, we made an attempt to locate the unidentified F_{2g} mode, i.e. the fourth Raman active mode by making a comparative investigation with the corresponding known mode for the Chloride counterpart (reported at 51 cm^{-1}).

$$\nu_{Sn\text{-}I} = c\sqrt{k_{(Sn-I)}/\mu_{(Sn-I)}} \quad \ldots\ldots\ldots\ldots \quad \textbf{Eq. 6.3}$$

The reported value of $k_{(Sn\text{-}I)}$ is 234 kJ/mol and the reduced mass μ for Tin-Iodide system can be calculated by employing the molecular masses of Tin (~119 u) and Iodine (127 u) as:

$$\mu_{Sn-I} = \frac{M_{Sn} \cdot M_I}{M_{Sn}+M_I} = 61.4 \text{ u} \quad \ldots\ldots\ldots\ldots \quad \textbf{Eq. 6.4}$$

On similar grounds, the vibrational frequency for Sn-Cl ($k_{(Sn\text{-}Cl)}$ is 406 kJ/mol, μ_{Sn-Cl}= 27.04 u) can be quoted down as

$$\nu_{Sn\text{-}Cl} = c\sqrt{k_{(Sn-Cl)}/\mu_{(Sn-Cl)}} \quad \ldots\ldots\ldots\ldots \quad \textbf{Eq. 6.5}$$

Substituting the respective values of k and μ back in **Eqs**. **6.3 and 6.5** lead to

$$\nu_{Sn\text{-}I} = 1.95c \quad \text{and} \quad \nu_{Sn\text{-}Cl} = 3.87c$$

Upon contrasting these equations, it is expected that the frequency of the mode in the iodide system should be roughly twofold (~1.95) than the Chloride equivalent. Since the phonon mode in discussion for the Chloride system is known to lie around 51 cm^{-1}, therefore it can proposed that the analogous phonon mode F_{2g} in Iodide NCs should be positioned somewhere around 26 cm^{-1}. Our findings obtained thereupon suggest that most likely, the mode at 29 cm^{-1} is the other Raman active lattice mode which is theoretically predicted yet unspecified in literature so far.

Further, we proceeded towards allocating the origin of the other two unassigned modes mentioned above. For this purpose, it seems justifiable to compare the phonon modes viable for Cs_2SnI_6 and Cs_2TeI_6 because of their iso-structural networks. With this strategical approach, we referred to the phonon mode database supplied for Cs_2TeI_6 system by Vảzquez-Fernảndez and co-workers in their recent work employing exhaustive DFT-phonopy calculations.[49] With same line of reasoning as that employed for calculation of Raman active F_{2g} mode, we estimated the approximate position of the inactive F_{1g} mode.

6.2.2.2 Estimation of the Raman and IR inactive F_{1g} mode

For Cs_2TeI_6 system, this particular mode has been reported to lie around 12.95 cm^{-1}.

The frequency of Te-I mode vibration can be given in the same manner as before

$$\nu_{Te\text{-}I} = c\sqrt{k_{(Te-I)}/\mu_{(Te-I)}} \quad \ldots\ldots\ldots\ldots\ldots \quad \textbf{Eq. 6.5}$$

$k_{(Te\text{-}I)}$ is known to be 193 kJ/mol and the reduced mass μ for Tellurium-Iodide system can be calculated as 63.7 u.

Upon substituting these in **eq.(6.5)**, the equation simplifies to $\nu_{Te\text{-}I} = 1.73c$. Therefore, a comparison of the frequenices of tin-iodide and tellurium-iodide based system directs us towards considering that the frequency of parallel phonon mode in the tin system would be 1.13 times of the value in tellurium equivalent. This predicts that the peak emerging at 14.63 cm^{-1} is the silent F_{1g} mode. Relying on the DFT calculated F_{1g} silent mode located at 12.95 cm^{-1} for Cs_2TeI_6 for deducing the equivalent mode in the tin based system, yields 14.6 cm^{-1} as the probable position Thus, by drawing an analogy between these two systems we can propose that the peak emerging at 14 cm^{-1} **(Figure 6.5 B)** is one of the two expected silent modes of vibration, in particular the F_{1g} one which is otherwise forbidden in both Raman and IR

investigations. Nevertheless realising the origin of undesignated mode peaked at 61 cm^{-1} is a laborious task and has been presented in detail in later sections.

6.2.3 Coherent phonon generation mechanisms in Cs_2SnI_6 NCs

Two widely known approaches have been employed so far to understand the coherent generation of phonon modes namely "Impulsive Stimulated Raman Scattering (ISRS)" and "Displacive Excitation of Coherent Phonons (DECP)".[50,51] The former mechanism, ISRS chiefly results in vibrational coherences in the ground state (G.S.) and is found to be relevant exclusively in situation of below band gap excitation. While when the employed pump energy is in resonance or near resonance with the electronic transitions (above or close to band gap excitation), the displacive strategy yields relevant conclusions.[52] But unlike ISRS, DECP mediated generation prompts coherent oscillations in the electronically excited state (E.S.) **(Figure 6.6 A, B)**. Indeed, there are also some instances when the generation mechanism is neither purely impulsive nor displacive as already reported for the case of Bismuth and Antimony.[52-54]

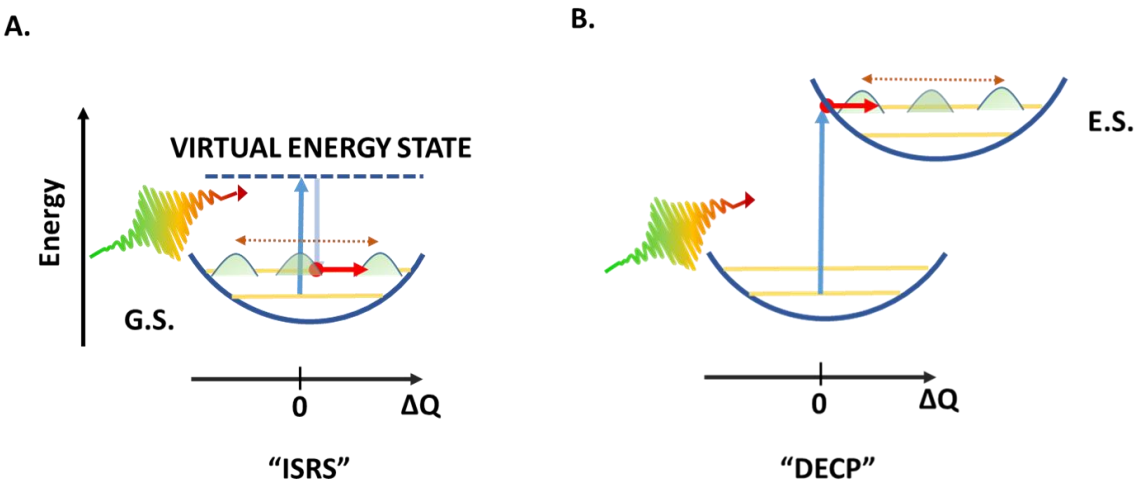

Figure 6.6 (A) Schematic illustration of ISRS mechanism displaying the induction of coherent lattice motions in the ground electronic state. Such translational motions in turn trigger vibrational wavepackets with their maxima around the equilibrium position and are thus manifested as oscillations in the vicinity of the normal mode coordinate. **(B)** For DECP strategy, the G.S wavepacket as a consequence of photoexcitation is initially projected into higher excited electronic state, where later this wavepacket begins to oscillate around a point different from the equilibrium position.

Here for Cs_2SnI_6, we also made a similar observation and found evidences for the existence of both mechanisms of coherent phonon generation; 1) The FFT power spectrum

reveals all possible modes of symmetry consistent with the reported Raman scattering data. Yet the oscillatory behaviour reflected in the time domain kinetic traces only portrays the vibrations with a characteristic period relatable to A_{1g} mode. Such observation of merely the fully symmetric A_{1g} Raman-active mode in the time domain out of all the other different lower symmetry modes spectacular in the frequency domain (with equally comparable intensities) is the characteristic of DECP mechanism.[51] 2) Intensity dependent studies also support this presumption. These studies present proportional increment of the oscillation amplitude with increasing photo-generated carrier density (plots presented in the **Figure 6.7**).

Linearly proportional trend is expected for the situations where DECP activated mechanism takes a leading role.[52,53,55] 3) Also, if the coherent phonon generation purely followed the ISRS approach, then the mode which reveals itself most exclusively in the time domain data would have been the most intense in the frequency domain data as well. But it is observed for instance in the case of 2eV excitation that in the time domain data, A_{1g} (121 cm^{-1}) reveals more strongly while in the frequency domain data F_{1u} (84 cm^{-1}) is the most prominent one and thus are not equivalent. Thereby it seems appropriate to embrace both DECP and ISRS approach of coherent phonon generation together for understanding the vibrational dynamics encountered here. In other words, the generation mechanism here is neither purely displacive nor purely impulsive.

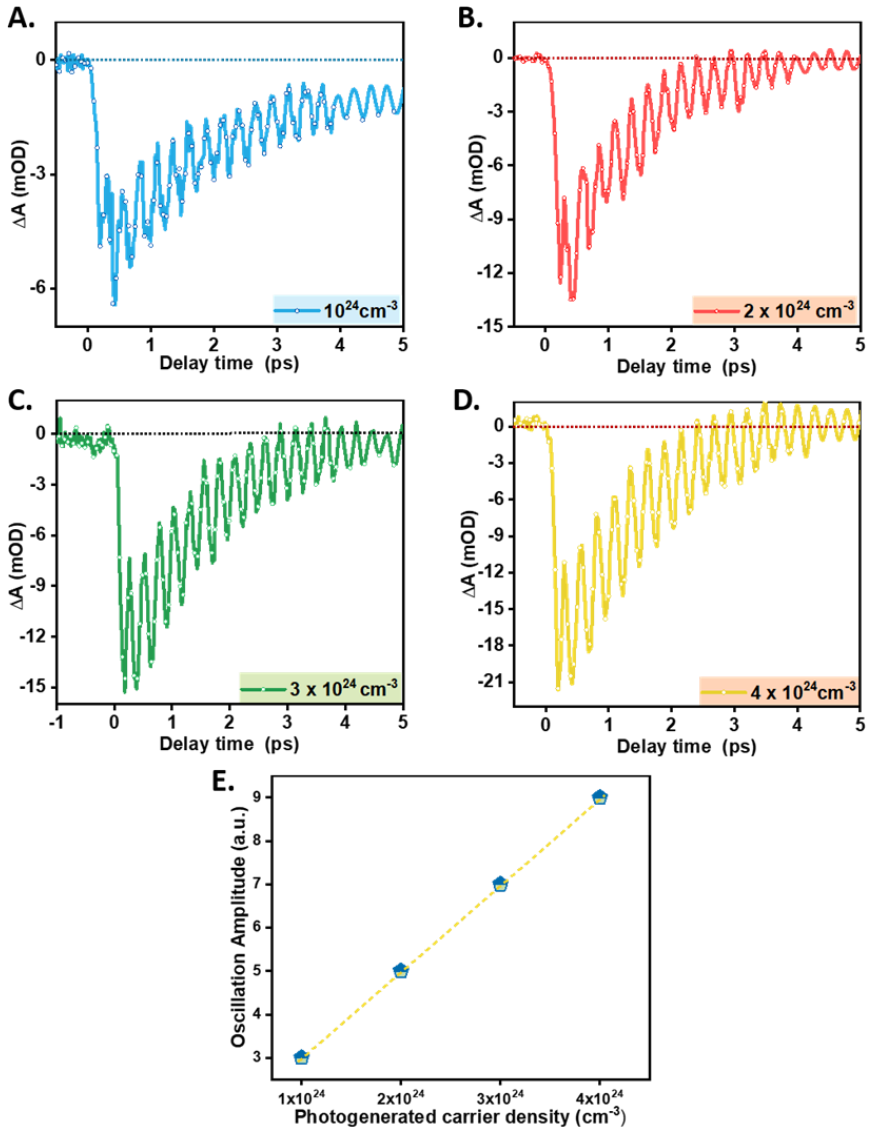

Figure 6.7 (A-D) TA kinetic traces for Cs_2SnI_6 NCs obtained while irradiating the samples with different photogenerated charge carrier densities (2 eV pump) at the position of excitonic bleach and **(E).** Intensity dependent plots depicting the linear increment of the coherent phonon amplitude with increasing photogenerated charge carrier density.

6.2.4 Origin of the 61cm^{-1} mode

It is important to emphasize here that the vibrations observed for Cs_2SnI_6 are more prominent in the excited state as compared to the G.S. This is justified by stronger periodic modulations noticeable in the excited state absorption (ESA) than in the GSB region (**Figure 6.4 B**). On that account, there stands a fair possibility that the mode positioned at 61 cm^{-1} may be an excited state DECP vibrational mode generated by the displacement of the excited state potential energy surface. But also at the same time there is comparable chance that this peak can be the other expected mode F_{2u} dormant in both Raman and IR studies. The remaining possibility of

it being a combination mode (14+51) can be straightforwardly ruled out since a combination mode cannot be stronger than the constituent parent modes. In order to distinguish between the ground state and the excited state modes, mainly two approaches have been followed before: pulse chirp measurements a relative phase analysis. [56-58] We have adopted the later approach to further substantiate this discrepancy. FFT power spectra were plotted **(Figure 6.8 A)** under varied pump excitations and relative phase analysis was conducted for the different modes probing at different regions of the spectral response **(Figure 6.8 B-D)**. This relies on a simple ground; if the concerned mode, namely the mode at 61 cm^{-1} is a consequence of wavepacket oscillations in the excited states then, the oscillations at the position of PIA and that at the bleach would be absolutely out of phase. In other words, the phase difference between the oscillations at these two different probe positions in such case would be roughly 180^0.[57,58] However, this expectation is not met as clearly inferred in the acquired data. The relative phase difference perceived at GSB and PIA for 67 cm^{-1} mode and that for all the other majorly observed modes are moderately same (ranging between 0°-70°) **(Figure 6.8 B-D).** This advocates that 67cm^{-1} (or 61 cm^{-1}) is not an excited state mode as per our two probable anticipated strategies leaving only one possibility wide open of it being the "silent F_{2u}" mode. In addition to providing the phase information, excitation pump energy dependent studies can prove advantageous for the precise consignment of the modes to their relevant origin based on the strength of the different phonon modes. Moreover, these investigations can also aid in drawing remarks on the carrier-phonon coupling. The pump dependent data acquired here directly suggests that the coherent phonons with different symmetries manifest themselves in distinct manners merely depending upon colour of the excitation pump. For instance, for 2eV excitation it can be observed that out of all the available phonon modes, the mode at 84 cm^{-1} (F_{1u}) is the one that projects most strongly. While for 4eV pump it is the mode at 78 cm^{-1} (F_{2g}) which is the most dominant one (deconvoluted plot provided in S6). For the case of further lower pump energy excitation of 1.63 eV, 67 cm^{-1} is seen as the most intense mode. Indeed as per the phase analysis, the mode that is most out of phase among the other vibrational modes is seen most intensely **(Figure 6.8A)**. Likewise all the observed modes are seen to manifest themselves in varied ways, certain new modes emerge whereas few modes disappear upon changing the excitation energies. However amongst all the prevalent modes, mode at "67 cm^{-1} (61cm^{-1})" is the one that demonstrates an exclusively fascinating behaviour.

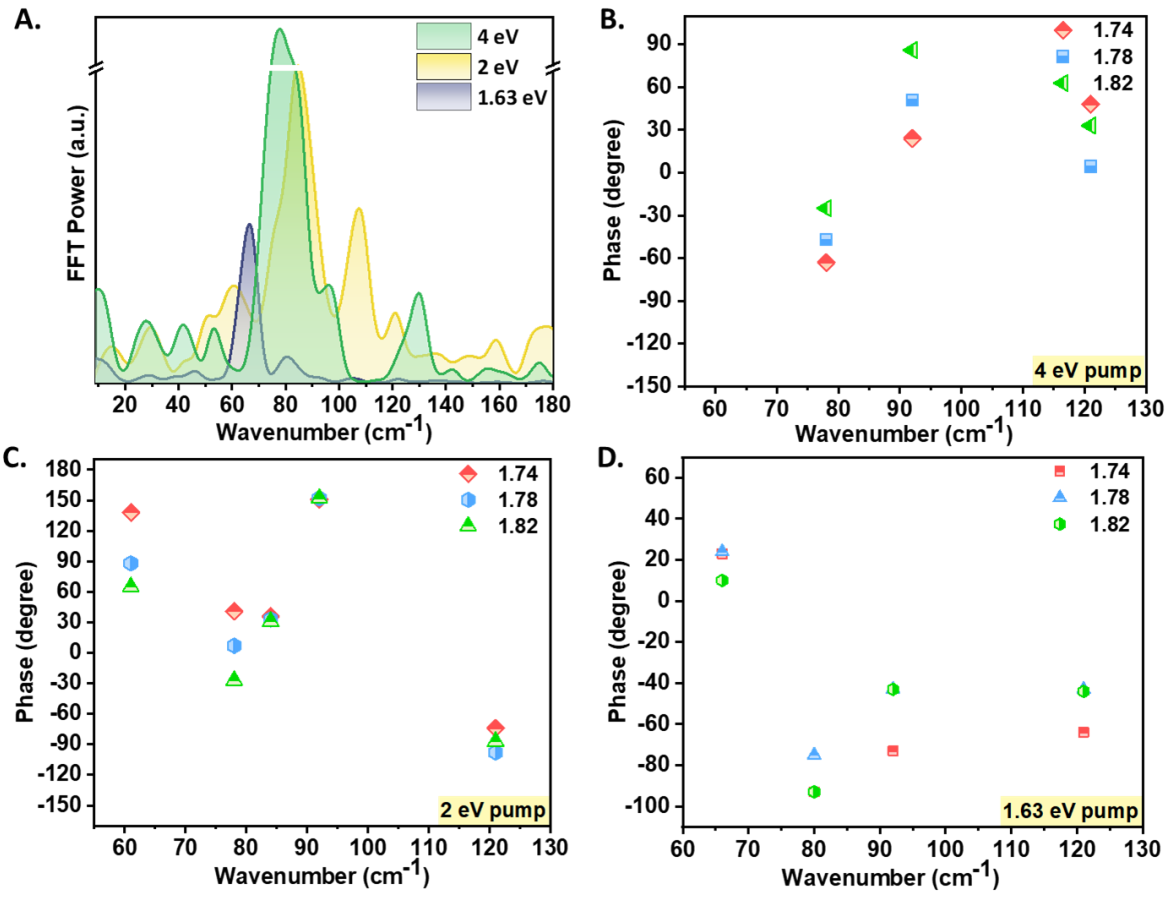

Figure 6.8 (A) FFT Power spectra generated upon Fourier transforming the residual oscillations for three different pump excitations. **(B-D)** Phase angle analysis for the different modes under these different excitation conditions (monitored at three distinct probe energies: 1.74 eV, 1.78 eV, 1.82 eV).

For the wide span of pump excitations employed, this unaddressed mode sustains throughout but with different weights. This phonon mode, most strongly manifested at 1.63 eV pump is still clearly intact in the FFT plot, for 2eV excitation though its amplitude is significantly compromised. However when the photoexcitation is made into very high energy electronic states *i.e.* 4eV there is no such mode distinguishable. Our data proposes that not only this mode presents itself more substantially as we further lower the excitation pump energy (1.63eV) but also displays a huge lateral redshift (appears at 67 cm^{-1}). This strong pump dependency of the different phonon modes can be attributed to the variable coupling between the electronic and lattice states.

Another important thing worth mentioning here is that the photo-excitation of the samples with 1.63eV pump implies non-resonant excitation (below band gap excitation). Interestingly, even below band gap excitation with 1.63eV pump yields an excitonic 1S bleach

similar to that noticeable for near resonant excitation discussed above (pump = 2eV) despite the fact that the incident photon energy is insufficient to excite the charge carriers above the bandgap of Cs_2SnI_6. But it should be noted that the bleach appears only when high intensity 1.63eV pump pulses (1mW) were employed which endorses that its observation is a direct outcome of Two Photon Absorption (TPA). This sets in the tendency of Hyper-Raman scattering (HRS) operative in the system whose essence lies in simultaneous scattering of two incident photons, similar to TPA which is mediated by virtual energy states. This scattering mechanism is not much distinct from the conventional Raman scattering (incident photon-ω_i, scattered photon- $\omega_i \pm \omega_{phonon}$) with the only difference that instead of only one incident photon, two photons are involved (incident photon-$2\omega_i$, scattered photon- $2\omega_i \pm \omega_{phonon}$).[59,60] Therefore it is quite likely that the additional phonon mode discernible most intensely in the FFT spectrum (67 cm^{-1}) for 1.63eV excitation is a consequence of Hyper Raman scattering which engages two photons, resembling the TPA process. Such category of modes generally remain silent, are neither Raman active nor IR active owing to symmetry restrictions but are observable in HRS (selection rules for HRS are different from Raman and IR spectroscopy).[61] We therefore propose this unaddressed mode at 67 cm^{-1} (61cm^{-1}) most plausibly as the F_{2u} mode along with the F_{1g} mode positioned at 14 cm^{-1} which is itself a silent mode.

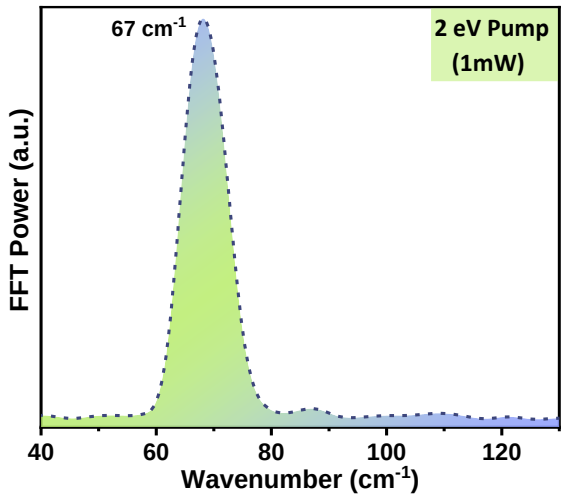

Figure 6.9 Power spectrum obtained as a consequence of fast fourier transforming the oscillatory TA data acquired using extremely intense 2eV pump pulses (Laser power :1mW) displaying the mode at 67cm^{-1} (silent mode) to stand out of all the other modes.

Indeed executing high intensity measurements upon irradiating the samples with same pump energy as before, for which the presence of the mode is discerned but with not much significant strength can further consolidate this proof of concept linking the genesis of the mode.[62] Upon incidenting very high intensity 2eV pump pulses (1mW) on the samples, the

peak corresponding to the mode at 67 cm^{-1} is found to outstand the others on similar lines as for 1.63eV pump (**Figure 6.9**). This verifies that this mode is most strongly generated under intense laser powers fortifying our claim of the mode at 67cm^{-1} to be HRS generated (more detailed discussion has been briefed in Supporting Note 10.2) Previously employing HRS, Zein *et al.* successfully observed the silent F_{2u} mode for $PbMg_{1/3}Nb_{2/3}O_3$, a perovskite sharing the same $Fm\bar{3}m$ symmetry as that of Cs_2SnI_6.[60]

6.2.5 Inherent anharmonicity in the lattice and the combination modes

Lattice anharmonicity has been previously known to allow the observation of otherwise silent modes in perovskites like $SrTiO_3$.[63] The appearance of silent modes "F_{2u}, F_{1g}" here in our finding therefore can be associated with the inherent anharmonicity in Cs_2SnI_6 lattice. Earlier the First principle lattice dynamics calculations put through by *Yu et al.* professed Lyddane Sachs-Teller type LO-TO splitting in Cs_2SnI_6 owing to the Transverse Optical (TO) phonon energy being smaller than that of Longitudinal Optical (LO) phonon.[27] Likewise, another theoretical investigation conducted by Falaras and group suggests the three IR active vibration modes for Cs_2SnI_6 lattice liable to LO-TO phonon splitting at k= 0 (Γ).[46] This anticipated splitting is straightforwardly speculated for the F_{1u} IR active modes in our acquired data. The vibrations marked as "G" and "H" for instance are δ (F_{1u}) IR active triply degenerate I-Sn-I asymmetric bending modes. However the degeneracy is lifted up as an effect of TO-LO phonon splitting and breaking of lattice periodicity. Similar conclusions stand true for the other F_{1u} modes: "C-D" and "K-L" modes. The experimental findings obtained in our present investigation thereby suggest anharmonicity prevalent in the Sn-I cage in accordance with earlier reports which have predicted anharmonicity in this system.[14] The vibrational feature at 108 cm^{-1}, a combination mode corresponding to the parent lattice modes at 29 cm^{-1} and 84 cm^{-1} is a confirmation of this fact. Shriver *et al.* has previously ascribed the mode peaking at 138 cm^{-1} for Cs_2SnI_6 to either an overtone or combination of lattice modes.[48] The attributes of all the peaks have been stated in **Table 6.1**.Our finding herein is suggestive that this mode at 138 cm^{-1} like few others as tabulated is an outcome of lattice anharmonicity which results in phonon-phonon coupling and is a combination mode with its parent modes lying at 51cm^{-1} (D) and 86 cm^{-1} (H).

Further the very high frequency vibrational modes noticeable here like 149 cm^{-1}, 171 cm^{-1} which differ from the fundamental resonances are also the outcome of anharmonicity and are not liberational modes. For example, the mode located at 149 cm^{-1} (2F) can be considered as the overtone of 76 cm^{-1} (F) mode. This is because liberational modes in $Fm\bar{3}m$ lattices are

Table 6.1 Assigning the origin to the various observed modes (2 eV pump excitation, (Intensity-100 µW))

Wavenumber(cm^{-1})	Mode Type	Denotion
14	Lattice Raman (ν^L (F_{2g}))- *this work*	"A"
29	F_{1g}(Raman and IR silent) - *this work*	"B"
42	Lattice-Infrared (ν^L (F_{1u})) - TO [46]	"C"
51	Lattice-Infrared (ν^L (F_{1u})) - LO [46]	"D"
61	F_{2u} (Raman and IR silent) - *this work*	"E"
76	I-Sn-I asymmetric bending -Raman (δ (F_{2g})) [46]	"F"
84	I-Sn-I asymmetric bending -Infrared(δ (F_{1u})) –TO [46]	"G"
86	I-Sn-I asymmetric bending -Infrared(δ (F_{1u})) –LO [46]	"H"
91	Sn-I asymmetric stretch- Raman (ν (E_g)) [46]	"I"
108	Combination mode- *this work*	"B+G"
121	Sn-I symmetric stretch -Raman (ν (A_{1g})) [46]	"J"
138	Combination mode- *this work*	"D+H"
149	Overtone- *this work*	"2F"
159	Sn-I Asymmetric stretch –IR (ν (F_{1u})) - TO [46]	"K"
171	Combination mode- *this work*	"G+H"
176	Sn-I Asymmetric stretch –IR (ν (F_{1u})) - LO [46]	"L"

generally dormant unlike as observed for the other lattice systems.[32] The appearance of such second harmonics has been previously linked with strong carrier-phonon coupling prevalent in the lattice.[64] On similar grounds, previously reported findings observed overtones corresponding to the Raman-active modes in Cs_2SnI_6. This is straightforwardly suggestive of the existence of strong carrier-phonon coupling in this material.

6.2.6 Temperature dependent investigations

Along with the room temperature studies which furnished a comprehensive picture of phonon modes in Cs_2SnI_6, we also executed low temperature investigations to get a better perception. Moreover it is a well versed fact that the lateral shift in the bleach position as a function of lattice temperature (T_L) is a decisive factor in estimating the extent of carrier-phonon coupling prevalent in any system.[65,66] In the same context, the spectral responses obtained upon descending the T_L to cryogenic extent (down to 5 K) do not display any other noteworthy differences apart from the significant lateral shift (50 meV) reflected in the bleach minima position (**Figure 6.10 A-C**). Such blue shifting of the bleach imparts widening of optical band gap at low T_L which can be interpreted as an effect of strong carrier- phonon coupling overriding the thermal expansion contribution in Cs_2SnI_6. This intense coupling can be justified as a consequence of small effective mass of the carriers in this material.[67] Nevertheless, this is

contrary to the other perovskite systems where there is band gap narrowing seen at low temperatures due to the thermal expansion effect dominating the picture. Thus the low temperature data obtained further provides a validation to the strong carrier-phonon coupling prevalent in Cs_2SnI_6 as already pointed out in the pump dependent inspections.

As it can be observed from **Figure 6.10 D, E**, there is no noticeable narrowing down of the phonon mode linewidth at low temperatures and also the dephasing rate remains almost unaffected even when the lattice temperature is lowered down to 5 K. This is again contrary to what is conventionally observed. Generally, a linear trend is observed between the dephasing rate and lattice temperature, at low temperature the dephasing is observed to slow down. The linear dependence of both the quantities as a function of lattice temperature is usually a strong evidence that decoherence is mediated by coupling to acoustic phonons.[68] Nevertheless there are some reports where the dephasing rate has been observed to be independent of the lattice temperature.[69] In such scenarios, it has been concluded that the dephasing process of the phonons is rather dominated by the coupling to charge carriers or defects.

Here in our finding, since the dephasing rate is identical throughout the range of investigated temperatures therefore we propose that the decoherence process in Cs_2SnI_6 may be mediated by coupling to charge carriers or defects or even the longitudinal optical phonons rather than through acoustic phonons. That can also be the reason held accountable for the unaltered phonon linewidth with temperature.

Also, there is no phonon softening observed in the residual vibrations drawn from the TA data for Cs_2SnI_6 NCs upon subjecting its lattice to a wide range of temperatures (300K-5K). The results obtained are contrary with respect to the theoretically predicted phase transition at 44 K and 137 K (Figure 5D).[14] If there would have been any transition into lower symmetry phase, there should have been higher number of Raman modes observable (nine, suggested by the irreducible representation from group theory analysis).[70] But the number of modes remain the same and there is no emergence of new modes even at lower temperatures indicating that the crystals retain their highest possible symmetry i.e. average cubic symmetry **(Figure 6.10 E)**. This immediate finding reconciles well with the temperature dependent Raman investigations executed very recently by Belessiotis *et al.* where no impression of restructuring or phase transformation is noticeable in the acquired data.[14] Our study indeed disproves any kind of phase transition to occur along the range of investigated temperatures.

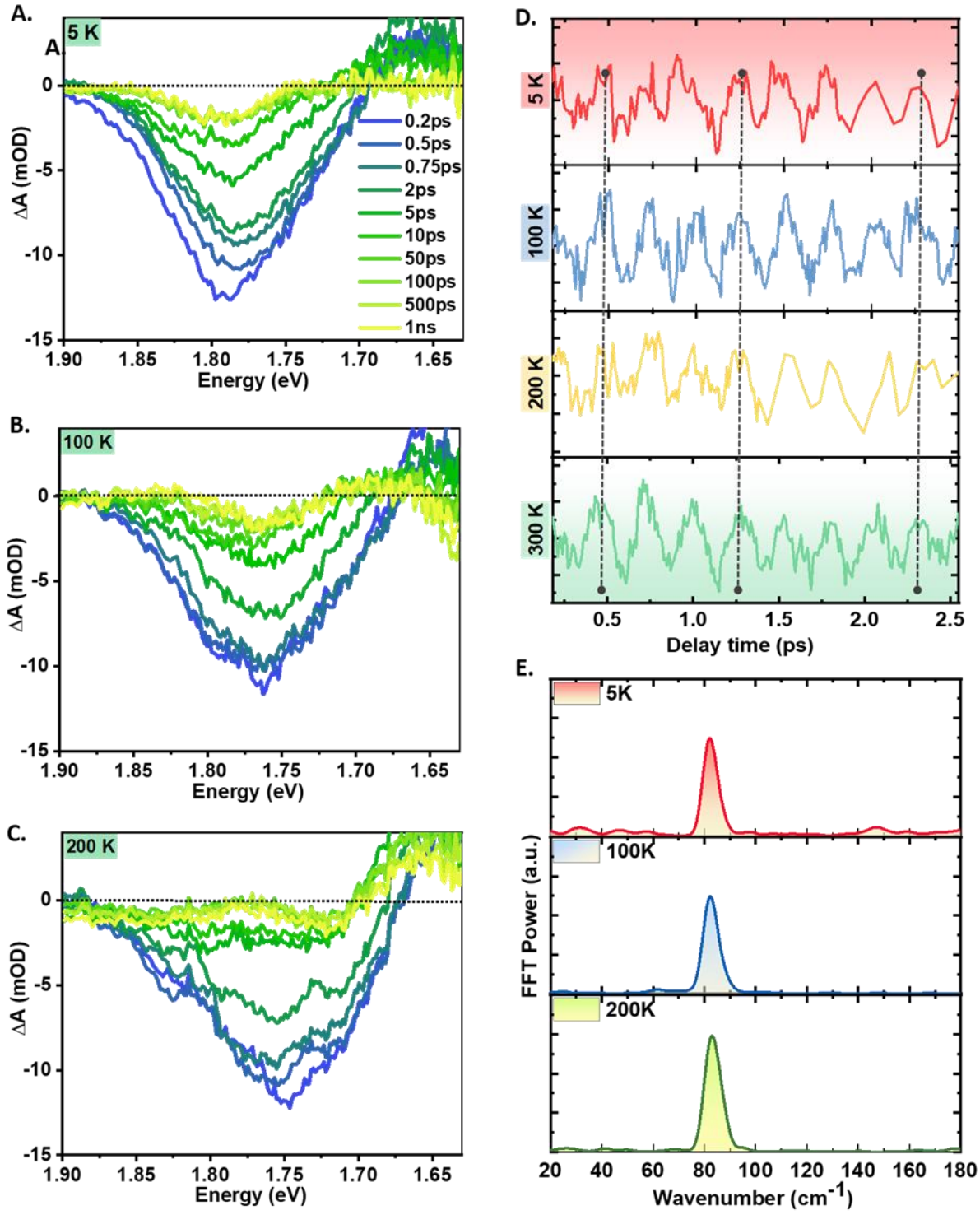

Figure 6.10 (A-C) Transient spectral plots for Cs_2SnI_6 acquired upon cooling the lattice down to cryogenic temperatures (5 K – 200 K) for 2eV pump excitation, **(D)** Corresponding residual oscillations demonstrating no phonon softening over the investigated temperature range. **(E)** FFT power spectra plotted for cryogenic temperatures, displaying no possible structural distortion as a function of lattice temperature.

6.3 Summary

Summarising this entire chapter, here in this work we have successfully investigated the phonon modes stemming from the lattice vibrations in Cs_2SnI_6 with the assistance of TA spectroscopy. We have laid specific emphasis on addressing those less explored modes in particular, which are otherwise missed in the routinely employed frequency domain techniques. Furthermore, we have accounted for the origin of residual oscillations discerned in the TA data relying on the modes obtained in the FFT power spectrum and consequently identified A_{1g} (fully symmetric Raman active Sn-I stretching vibration mode) as the liable mode. Another significant inference earned from this investigation is the unveiling of the silent modes which usually escape both Raman and IR studies, through phase analysis of the pump dependent studies and intensity dependent TA data. Most fascinating accomplishment amongst all is the observation of these modes which have never been stated before in TA studies. Our analysis however is not limited to merely assigning the origin of the modes but also determining their generation mechanism. Emergence of combination modes in the FFT spectrum, as an outcome of phonon-phonon coupling validates the native anharmonicity in Cs_2SnI_6 lattice. Besides this, extent of carrier-phonon coupling also has been qualitatively realised through pump dependent and low temperature measurements. Such exclusive knowledge reviewing the phonon modes governing the lattice vibrational dynamics can be leveraged advantageously for the technological prospects and must be given considerable attention before sketching the design for the devices based on Cs_2SnI_6.

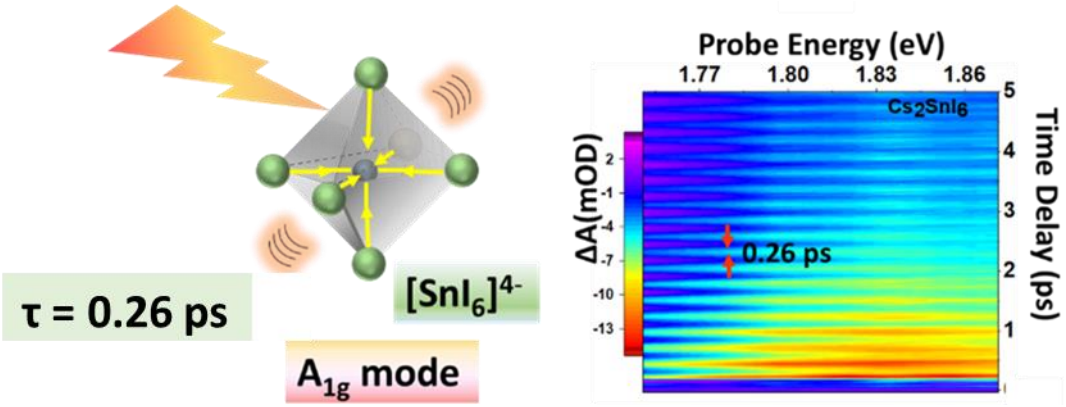

"Periodic modulations observed in the transient absorption response of Cs_2SnI_6 with a consistent time period of 0.26 ps are a result of the fully symmetric breathing mode of $[SnI_6]^{4-}$ (A_{1g})"

6.4 References

(1) Jeon, I.; Kim, K.; Jokar, E.; Park, M.; Lee, H.-W.; Diau, E. W. Environmentally

Compatible Lead-Free Perovskite Solar Cells and Their Potential as Light Harvesters in Energy Storage Systems. *Nanomaterials* ***2021***, *11, 2066.*

(2) Kour, R.; Arya, S.; Verma, S.; Gupta, J.; Bandhoria, P.; Bharti, V.; Datt, R.; Gupta, V. Potential Substitutes for Replacement of Lead in Perovskite Solar Cells: A Review. *Glob Challenges* **2019**, *3* (11), 1900050.

(3) Jiang, X.; Zang, Z.; Zhou, Y.; Li, H.; Wei, Q.; Ning, Z. Tin Halide Perovskite Solar Cells: An Emerging Thin-Film Photovoltaic Technology. *Accounts Mater Res* **2021**, *2* (4), 210–219.

(4) Cao, J.; Yan, F. Recent Progress in Tin-Based Perovskite Solar Cells. *Energy Environ Sci* **2021**, *14* (3), 1286–1325.

(5) Ullah, S.; Wang, J.; Yang, P.; Liu, L.; khan, J.; Yang, S.-E.; Xia, T.; Guo, H.; Chen, Y. Lead-Free Cs_2SnI_6 Perovskites for Optoelectronic Applications: Recent Developments and Perspectives. *Sol RRL* **2021**, *5* (5), 2000830.

(6) Maughan, A. E.; Ganose, A. M.; Bordelon, M. M.; Miller, E. M.; Scanlon, D. O.; Neilson, J. R. Defect Tolerance to Intolerance in the Vacancy-Ordered Double Perovskite Semiconductors Cs_2SnI_6 and Cs_2TeI_6. *J Am Chem Soc* **2016**, *138* (27), 8453–8464.

(7) Lee, B.; Ezhumalai, Y.; Lee, W.; Chen, M.-C.; Yeh, C.-Y.; Marks, T. J.; Chang, R. P. H. Cs_2SnI_6-Encapsulated Multidye-Sensitized All-Solid-State Solar Cells. *ACS Appl Mater Interfaces* **2019**, *11* (24), 21424–21434.

(8) Qiu, X.; Jiang, Y.; Zhang, H.; Qiu, Z.; Yuan, S.; Wang, P.; Cao, B. Lead-Free Mesoscopic Cs_2SnI_6 Perovskite Solar Cells Using Different Nanostructured ZnO Nanorods as Electron Transport Layers. *Phys status solidi – Rapid Res Lett* **2016**, *10* (8), 587–591.

(9) Qiu, X.; Cao, B.; Yuan, S.; Chen, X.; Qiu, Z.; Jiang, Y.; Ye, Q.; Wang, H.; Zeng, H.; Liu, J.; et al. From Unstable $CsSnI_3$ to Air-Stable Cs_2SnI_6: A Lead-Free Perovskite Solar Cell Light Absorber with Bandgap of 1.48eV and High Absorption Coefficient. *Sol Energy Mater Sol Cells* **2017**, *159*, 227–234.

(10) Peedikakkandy, L.; Naduvath, J.; Mallick, S.; Bhargava, P. Lead Free, Air Stable Perovskite Derivative Cs_2SnI_6 as HTM in DSSCs Employing TiO_2 Nanotubes as Photoanode. *Mater Res Bull* **2018**, *108*, 113–119.

(11) Lee, B.; Stoumpos, C. C.; Zhou, N.; Hao, F.; Malliakas, C.; Yeh, C.-Y.; Marks, T. J.;

Kanatzidis, M. G.; Chang, R. P. H. Air-Stable Molecular Semiconducting Iodosalts for Solar Cell Applications: Cs_2SnI_6 as a Hole Conductor. *J Am Chem Soc* **2014**, *136* (43), 15379–15385.

(12) Handayani, Y. S.; Wulandari, P.; Hidayat, R. Controlled Synthesis of Lead-Free Perovskite Cs_2SnI_6 as Hole Transport Layer in Dye Sensitized Solar Cells. *J Phys Conf Ser* **2018**, *1080*, 12003.

(13) Xie, H.; Hao, S.; Bao, J.; Slade, T. J.; Snyder, G. J.; Wolverton, C.; Kanatzidis, M. G. All-Inorganic Halide Perovskites as Potential Thermoelectric Materials: Dynamic Cation off-Centering Induces Ultralow Thermal Conductivity. *J Am Chem Soc* **2020**, *142* (20), 9553–9563.

(14) Belessiotis, G. V; Arfanis, M.; Kaltzoglou, A.; Likodimos, V.; Raptis, Y. S.; Falaras, P.; Kontos, A. G. Temperature Effects on the Vibrational Properties of the Cs_2SnX_6 'Defect' Perovskites (X = I, Br, Cl). *Mater Chem Phys* **2021**, *267*, 124679.

(15) Zhao, L.-D.; Lo, S.-H.; Zhang, Y.; Sun, H.; Tan, G.; Uher, C.; Wolverton, C.; Dravid, V. P.; Kanatzidis, M. G. Ultralow Thermal Conductivity and High Thermoelectric Figure of Merit in SnSe Crystals. *Nature* **2014**, *508* (7496), 373–377.

(16) Lim, Y. S.; Park, K.-H.; Tak, J. Y.; Lee, S.; Seo, W.-S.; Park, C.-H.; Kim, T. H.; Park, P.; Kim, I. H.; Yang, J. Colligative Thermoelectric Transport Properties in N-Type Filled $CoSb_3$ Determined by Guest Electrons in a Host Lattice. *J Appl Phys* **2016**, *119* (11), 115104.

(17) Zhou, F.; Nielson, W.; Xia, Y.; Ozoliņš, V. Lattice Anharmonicity and Thermal Conductivity from Compressive Sensing of First-Principles Calculations. *Phys Rev Lett* **2014**, *113* (18), 185501.

(18) Dangić, Đ.; Hellman, O.; Fahy, S.; Savić, I. The Origin of the Lattice Thermal Conductivity Enhancement at the Ferroelectric Phase Transition in GeTe. *npj Comput Mater* **2021**, *7* (1), 57.

(19) Shi, X.; Yang, J.; Salvador, J. R.; Chi, M.; Cho, J. Y.; Wang, H.; Bai, S.; Yang, J.; Zhang, W.; Chen, L. Multiple-Filled Skutterudites: High Thermoelectric Figure of Merit through Separately Optimizing Electrical and Thermal Transports. *J Am Chem Soc* **2011**, *133* (20), 7837–7846.

(20) M., L. M.; Joël, T.; Tsutomu, M.; N., M. T.; J., S. H. Efficient Hybrid Solar Cells Based on Meso-Superstructured Organometal Halide Perovskites. *Science 80* **2012**, *338* (6107), 643–

647.

(21) Stranks, S. D.; Snaith, H. J. Metal-Halide Perovskites for Photovoltaic and Light-Emitting Devices. *Nat Nanotechnol* **2015**, *10* (5), 391–402.

(22) Zhang, P.; Hou, Z.; Jiang, L.; Yang, J.; Saidi, W. A.; Prezhdo, O. V; Li, W. Weak Anharmonicity Rationalizes the Temperature-Driven Acceleration of Nonradiative Dynamics in Cu_2ZnSnS_4 Photoabsorbers. *ACS Appl. Mater. Interfaces* **2021**, *13*, *51*, *61365–61373.*

(23) Karim, M. M. S.; Ganose, A. M.; Pieters, L.; Winnie Leung, W. W.; Wade, J.; Zhang, L.; Scanlon, D. O.; Palgrave, R. G. Anion Distribution, Structural Distortion, and Symmetry-Driven Optical Band Gap Bowing in Mixed Halide Cs_2SnX_6 Vacancy Ordered Double Perovskites. *Chem Mater* **2019**, *31* (22), 9430–9444.

(24) Folgueras, M. C.; Jin, J.; Gao, M.; Quan, L. N.; Steele, J. A.; Srivastava, S.; Ross, M. B.; Zhang, R.; Seeler, F.; Schierle-Arndt, K.; et al. Lattice Dynamics and Optoelectronic Properties of Vacancy-Ordered Double Perovskite Cs_2TeX_6 ($X = Cl^-, Br^-, I^-$) Single Crystals. *J Phys Chem C* **2021**, *125* (45), 25126–25139.

(25) Maughan, A. E.; Paecklar, A. A.; Neilson, J. R. Bond Valences and Anharmonicity in Vacancy-Ordered Double Perovskite Halides. *J Mater Chem C* **2018**, *6* (44), 12095–12104.

(26) Dugdale, J. S.; MacDonald, D. K. C. Lattice Thermal Conductivity. *Phys Rev* **1955**, *98* (6), 1751–1752.

(27) Jong, U.G.; Yu, C.-J.; Kye, Y.-H.; Choe, S.-H.; Kim, J.-S.; Choe, Y.-G. Anharmonic Phonons and Phase Transitions in the Vacancy-Ordered Double Perovskite Cs_2SnX_6 from First-Principles Predictions. *Phys Rev B* **2019**, *99* (18), 184105.

(28) Ni, L.; Huynh, U.; Cheminal, A.; Thomas, T. H.; Shivanna, R.; Hinrichsen, T. F.; Ahmad, S.; Sadhanala, A.; Rao, A. Real-Time Observation of Exciton–Phonon Coupling Dynamics in Self-Assembled Hybrid Perovskite Quantum Wells. *ACS Nano* **2017**, *11* (11), 10834–10843.

(29) Castro Neto, A. H.; Guinea, F. Electron-Phonon Coupling and Raman Spectroscopy in Graphene. *Phys Rev B* **2007**, *75* (4), 45404.

(30) Ferrante, C.; Virga, A.; Benfatto, L.; Martinati, M.; De Fazio, D.; Sassi, U.; Fasolato, C.; Ott, A. K.; Postorino, P.; Yoon, D.; et al. Raman Spectroscopy of Graphene under Ultrafast Laser Excitation. *Nat Commun* **2018**, *9* (1), 308.

(31) Kambhampati, P. Learning about the Structural Dynamics of Semiconductor Perovskites from Electron Solvation Dynamics. *J Phys Chem C* **2021**, *125* (43), 23571–23586.

(32) Debnath, T.; Sarker, D.; Huang, H.; Han, Z.K.; Dey, A.; Polavarapu, L.; Levchenko, S. V; Feldmann, J. Coherent Vibrational Dynamics Reveals Lattice Anharmonicity in Organic–Inorganic Halide Perovskite Nanocrystals. *Nat Commun* **2021**, *12* (1), 2629.

(33) Brivio, F.; Frost, J. M.; Skelton, J. M.; Jackson, A. J.; Weber, O. J.; Weller, M. T.; Goñi, A. R.; Leguy, A. M. A.; Barnes, P. R. F.; Walsh, A. Lattice Dynamics and Vibrational Spectra of the Orthorhombic, Tetragonal, and Cubic Phases of Methylammonium Lead Iodide. *Phys Rev B* **2015**, *92* (14), 144308.

(34) Jeong, T. Y.; Jin, B. M.; Rhim, S. H.; Debbichi, L.; Park, J.; Jang, Y. D.; Lee, H. R.; Chae, D.-H.; Lee, D.; Kim, Y.-H.; et al. Coherent Lattice Vibrations in Mono- and Few-Layer WSe_2. *ACS Nano* **2016**, *10* (5), 5560–5566.

(35) Leguy, A. M. A.; Goñi, A. R.; Frost, J. M.; Skelton, J.; Brivio, F.; Rodríguez-Martínez, X.; Weber, O. J.; Pallipurath, A.; Alonso, M. I.; Campoy-Quiles, M.; et al. Dynamic Disorder, Phonon Lifetimes, and the Assignment of Modes to the Vibrational Spectra of Methylammonium Lead Halide Perovskites. *Phys Chem Chem Phys* **2016**, *18* (39), 27051–27066.

(36) Dhar, L.; Rogers, J. A.; Nelson, K. A. Time-Resolved Vibrational Spectroscopy in the Impulsive Limit. *Chem Rev* **1994**, *94* (1), 157–193.

(37) Trovatello, C.; Miranda, H. P. C.; Molina-Sánchez, A.; Borrego-Varillas, R.; Manzoni, C.; Moretti, L.; Ganzer, L.; Maiuri, M.; Wang, J.; Dumcenco, D.; et al. Strongly Coupled Coherent Phonons in Single-Layer MoS_2. *ACS Nano* **2020**, *14* (5), 5700–5710.

(38) Keiter, R. L. Spectroscopically Silent Fundamental Vibrations. *J Chem Educ* **1983**, *60* (8), 625.

(39) Wang, A.; Yan, X.; Zhang, M.; Sun, S.; Yang, M.; Shen, W.; Pan, X.; Wang, P.; Deng, Z. Controlled Synthesis of Lead-Free and Stable Perovskite Derivative Cs_2SnI_6 Nanocrystals via a Facile Hot-Injection Process. *Chem Mater* **2016**, *28* (22), 8132–8140.

(40) Son, D. H.; Kambhampati, P.; Kee, T. W.; Barbara, P. F. Femtosecond Multicolor Pump−Probe Study of Ultrafast Electron Transfer of $[(NH_3)_5Ru^{III}NCRu^{II}(CN)_5]^-$ in Aqueous Solution. *J Phys Chem A* **2002**, *106* (18), 4591–4597.

(41) Kambhampati, P.; Son, D. H.; Kee, T. W.; Barbara, P. F. Solvent Effects on Vibrational Coherence and Ultrafast Reaction Dynamics in the Multicolor Pump−Probe Spectroscopy of Intervalence Electron Transfer. *J Phys Chem A* **2000**, *104* (46), 10637–10644.

(42) Lynch, M. S.; Slenkamp, K. M.; Khalil, M. Communication: Probing Non-Equilibrium Vibrational Relaxation Pathways of Highly Excited C≡N Stretching Modes Following Ultrafast Back-Electron Transfer. *J Chem Phys* **2012**, *136* (24), 241101.

(43) Anderson, K. E. H.; Sewall, S. L.; Cooney, R. R.; Kambhampati, P. Noise Analysis and Noise Reduction Methods in Kilohertz Pump-Probe Experiments. *Rev Sci Instrum* **2007**, *78* (7), 73101.

(44) Umedov, S. T.; Grigorieva, A. V; Lepnev, L. S.; Knotko, A. V; Nakabayashi, K.; Ohkoshi, S.; Shevelkov, A. V. Indium Doping of Lead-Free Perovskite Cs_2SnI_6. *Front Chem* **2020**, *8*, 564.

(45) Brüesch, P. *Phonons: Theory and Experiments II. Experiments and Interpretation of Experimental Results.*, Springer S.; Springer nature, **1986**.

(46) Kaltzoglou, A.; Antoniadou, M.; Kontos, A. G.; Stoumpos, C. C.; Perganti, D.; Siranidi, E.; Raptis, V.; Trohidou, K.; Psycharis, V.; Kanatzidis, M. G.; et al. Optical-Vibrational Properties of the Cs_2SnX_6 (X = Cl, Br, I) Defect Perovskites and Hole-Transport Efficiency in Dye-Sensitized Solar Cells. *J Phys Chem C* **2016**, *120* (22), 11777–11785.

(47) Torres, D. I.; Freire, J. D.; Katiyar, R. S. Lattice Dynamics of Crystals Having R_2MX_6 Structure. *Phys Rev B* **1997**, *56* (13), 7763–7766.

(48) Wharf, I.; Shriver, D. F. Vibrational Frequencies and Intramolecular Forces in Anionic Tin-Halogen Complexes and Related Species. *Inorg Chem* **1969**, *8* (4), 914–925.

(49) Vázquez-Fernández, I.; Mariotti, S.; Hutter, O. S.; Birkett, M.; Veal, T. D.; Hobson, T. D. C.; Phillips, L. J.; Danos, L.; Nayak, P. K.; Snaith, H. J.; et al. Vacancy-Ordered Double Perovskite Cs_2TeI_6 Thin Films for Optoelectronics. *Chem Mater* **2020**, *32* (15), 6676–6684.

(50) Batignani, G.; Ferrante, C.; Fumero, G.; Scopigno, T. Broadband Impulsive Stimulated Raman Scattering Based on a Chirped Detection. *J Phys Chem Lett* **2019**, *10* (24), 7789–7796.

(51) Zeiger, H. J.; Vidal, J.; Cheng, T. K.; Ippen, E. P.; Dresselhaus, G.; Dresselhaus, M. S. Theory for Displacive Excitation of Coherent Phonons. *Phys Rev B* **1992**, *45* (2), 768–778.

(52) Melnikov, A. A.; Misochko, O. V; Chekalin, S. V. Generation of Coherent Phonons in Bismuth by Ultrashort Laser Pulses in the Visible and NIR: Displacive versus Impulsive Excitation Mechanism. *Phys Lett A* **2011**, *375* (19), 2017–2022.

(53) Ishioka, K.; Kitajima, M.; Misochko, O. V. Coherent A_{1g} and E_g Phonons of Antimony. *J Appl Phys* **2008**, *103* (12), 123505.

(54) Shojaei, I. A.; Pournia, S.; Le, C.; Ortiz, B. R.; Jnawali, G.; Zhang, F.C.; Wilson, S. D.; Jackson, H. E.; Smith, L. M. A Raman Probe of Phonons and Electron–Phonon Interactions in the Weyl Semimetal $NbIrTe_4$. *Sci Rep* **2021**, *11* (1), 8155.

(55) Mishina, T. Novel Theory for Transient Light Matter Interaction. 11 Sep 2016. *Mesoscale Nanoscale Phys*. arXiv:1607.06045v2 [cond-mat.mes-hall] (accessed 2022-05-31)

(56) Mooney, J.; Saari, J. I.; Myers Kelley, A.; Krause, M. M.; Walsh, B. R.; Kambhampati, P. Control of Phonons in Semiconductor Nanocrystals via Femtosecond Pulse Chirp-Influenced Wavepacket Dynamics and Polarization. *J Phys Chem B* **2013**, *117* (49), 15651–15658,

(57) Batignani, G.; Fumero, G.; Srimath Kandada, A. R.; Cerullo, G.; Gandini, M.; Ferrante, C.; Petrozza, A.; Scopigno, T. Probing Femtosecond Lattice Displacement upon Photo-Carrier Generation in Lead Halide Perovskite. *Nat Commun* **2018**, *9* (1), 1971.

(58) Park, M.; Neukirch, A. J.; Reyes-Lillo, S. E.; Lai, M.; Ellis, S. R.; Dietze, D.; Neaton, J. B.; Yang, P.; Tretiak, S.; Mathies, R. A. Excited-State Vibrational Dynamics toward the Polaron in Methylammonium Lead Iodide Perovskite. *Nat Commun* **2018**, *9* (1), 2525.

(59) Kozina, M.; Fechner, M.; Marsik, P.; van Driel, T.; Glownia, J. M.; Bernhard, C.; Radovic, M.; Zhu, D.; Bonetti, S.; Staub, U.; et al. Terahertz-Driven Phonon Upconversion in $SrTiO_3$. *Nat Phys* **2019**, *15* (4), 387–392.

(60) Al-Zein, A.; Hehlen, B.; Rouquette, J.; Hlinka, J. Polarized Hyper-Raman Scattering Study of the Silent F_{2U} Mode in $PbMg_{1/3}Nb_{2/3}O_3$. *Phys Rev B* **2008**, *78* (13), 134113.

(61) Neddersen, J. P.; Mounter, S. A.; Bostick, J. M.; Johnson, C. K. Nonresonant Hyper-Raman and Hyper-Rayleigh Scattering in Benzene and Pyridine. *J Chem Phys* **1989**, *90* (9), 4719–4726.

(62) Vogt, H.; Neumann, G. Observation of Infrared Active and Silent Modes in Cubic Crystals by Hyper-Raman Scattering. *Phys Status Solidi B, Basic Res* **1979**, *92* (1), 57–63.

(63) Denisov, V. N.; Mavrin, B. N.; Podobedov, V. B.; Scott, J. F. Hyper_Raman Spectra and Frequency Dependence of Soft Mode Damping in $SrTiO_3$. *J Raman Spectrosc* **1983**, *14*, 276–283.

(64) Zhang, Q.; Liu, X.; Utama, M. I. B.; Zhang, J.; de la Mata, M.; Arbiol, J.; Lu, Y.; Sum, T. C.; Xiong, Q. Highly Enhanced Exciton Recombination Rate by Strong Electron–Phonon Coupling in Single ZnTe Nanobelt. *Nano Lett* **2012**, *12* (12), 6420–6427.

(65) Yu, C.; Chen, Z.; J. Wang, J.; Pfenninger, W.; Vockic, N.; Kenney, J. T.; Shum, K. Temperature Dependence of the Band Gap of Perovskite Semiconductor Compound $CsSnI_3$. *J Appl Phys* **2011**, *110* (6), 63526.

(66) Kaur, G.; Babu, K. J.; Ghosh, H. N. Temperature-Dependent Interplay of Polaron Formation and Hot Carrier Cooling Dynamics in $CsPbBr_3$ Nanocrystals: Role of Carrier–Phonon Coupling Strength. *J. Phys. Chem. Lett.* **2020***, 11, 6206−6213*.

(67) Dolzhnikov, D. S.; Wang, C.; Xu, Y.; Kanatzidis, M. G.; Weiss, E. A. Ligand-Free, Quantum-Confined Cs_2SnI_6 Perovskite Nanocrystals. *Chem Mater* **2017**, *29* (18), 7901–7907.

(68) Laussy, F. P.; del Valle, E.; Tejedor, C. Luminescence Spectra of Quantum Dots in Microcavities. I. Bosons. *Phys Rev B* **2009**, *79* (23), 235325.

(69) Ishioka, K.; Misochko, O. V. Coherent Lattice Oscillations in Solids and Their Optical Control BT - Progress in Ultrafast Intense Laser Science: Volume V; Yamanouchi, K., Giulietti, A., Ledingham, K., Eds.; Springer Berlin Heidelberg: Berlin, Heidelberg, **2010**; pp 23–46.

(70) Andrews, R; Probing the Local Structure of Perovskites Using Raman Scattering Spectroscopy,The Ohio State University, **2012**.

(71) Kaur, G.; Justice Babu, K.; Ghorai, N.; Goswami, T.; Maiti, S.; Ghosh, H. N. Polaron-Mediated Slow Carrier Cooling in a Type-1 3D/0D $CsPbBr_3$@Cs_4PbBr_6 Core–Shell Perovskite System. *J Phys Chem Lett* **2019**, *10* (18), 5302–5311.

(72) Shukla, A.; Kaur, G.; Babu, K. J.; Ghorai, N.; Goswami, T.; Kaur, A.; Ghosh, H. N. Effect of Confinement on the Exciton and Biexciton Dynamics in Perovskite 2D-Nanosheets and 3D-Nanocrystals. *J. Phys. Chem. Lett.* **2020**, *11, 15, 6344–6352*.

Chapter 7

Ultrafast Glimpses of the Excitation Energy-Dependent Exciton Dynamics and Charge Carrier Mobility in Cs_2SnI_6 Nanocrystals

Out of all the potential substitutes, Tin-based perovskites are anticipated to have the best chance of surpassing the well-established lead-containing counterparts or, at the very least, performing on par with them. Cs_2SnI_6, in particular is one such vacancy ordered variant of this tin family that has demonstrated exceptional performance in a variety of sectors, including PVs. Despite this, even after reaching commendable numbers, lately there has not been any significant increment in the photoconversion efficiency observed for Cs_2SnI_6 based devices. The best way to help realise the full potential of any PV material is by a thorough investigation of its photo-physical properties which are extremely relevant from the standpoint of PV applications. In this present effort, we first carried out theoretical investigations to identify the location of the energetically diverse excitons in the Brillouin zone of Cs_2SnI_6. Then employing TA spectroscopy, we examined the temporal evolution of these excitons where we discovered the decay of the high energy exciton to be unusually slow. Strikingly, we also spotted the generation of high energy excitons even when the incident pump energy is insufficient for their formation. Keeping track of the TA kinetics reveals that such a finding is a consequence of the interwoven generation and decay mechanisms of these high energy excitons with the low energy ones, mediated by IV scattering and phonon absorption processes. Furthermore from the transient mobility investigations conducted using optical pump THz probe spectroscopy, it is established that the hot carriers in Cs_2SnI_6 are highly mobile and also participate in polaron generation. Our findings thereby altogether propose that Cs_2SnI_6 would be a good choice in hot carrier-based solar cell devices which require materials that have both delayed decay of high energy excitons and augmented mobility of hot carriers.

7.1 Motivation and Background

Over the last few years, lead based perovskites ($APbX_3$) have undoubtedly displayed exemplary performance in multiple applications. Unfortunately in spite of this, due to the potential environmental hazard pertaining to the lead content their commercialisation is still very restricted.[1–6] In quest for low–toxicity but equally compelling replacements of lead, researchers have found plentitude of competent substitutes. Among all, tin based perovskites ($ASnX_3$) have grabbed the maximum spotlight majorly due to the close proximity in size of tin (Sn^{2+}) with lead (Pb^{2+}).[7–12] It is further anticipated that the throughput of the devices employing tin based perovskites can even surpass that otherwise achievable with the lead based analogues.[13,14] But pertaining to the easy oxidation of Sn^{2+} to Sn^{4+}, the major concern that bothers their practical applicability is their poor stability. On the contrary in context of prolonged stability, tin based double perovskite structures (A_2SnX_6) which are fundamentally the defect variants and higher oxidation state derivatives of $ASnX_3$, are quite robust.[15]

The iodide member of this family, Cs_2SnI_6, in particular, has intrigued the interest of the research community due to its captivating merits and has shown promising results when put to operation. It has shown remarkable potential as an outstanding absorbing layer material in PV systems, with Photoconversion Efficiency (PCE) attained close to 8% owing to its perfect band gap, near ideal for solar light absorption, and high absorption coefficient.[16,17] Aside from that, it has been used as an excellent hole transportation layer in dye-sensitized solar cells, as an effective functional layer in photodetectors, and even as a promising candidate for photo-electrochemical water splitting.[16–18] All this commendable performance exhibited by Cs_2SnI_6 is closely tied to its photophysical properties. Therefore realisation of the underlying opto-electronic properties is utterly essential because these set a demarcation line for the achievable device efficiency. So far, research concerning Cs_2SnI_6 is chiefly limited to exploring the ways to enhance the device efficiency by working on the device structure but the photophysical aspects of Cs_2SnI_6 are till date unexplored. As a result, the efficiency numbers attained have remained stagnant for long despite the fact that theoretical maximum efficiency achievable for Cs_2SnI_6 is expected to be 20%.[19] The little information known about the charge carrier dynamics in Cs_2SnI_6 is restricted to band edge excitons, but the study of the high energy excitonic states, which are just as significant, has been overlooked so far. The charge carrier dynamics of band edge excitons are frequently entangled with the dynamics of high energy excitons. Therefore, we believe that only detailed research of Cs_2SnI_6's opto-electronic characteristics can assist in unlocking its full potential.

Here in the present finding, using theoretical calculations, we first deduced the electronic structure of Cs_2SnI_6 and identified the likely positions of the different excitonic species in its Brillouin zone. Then we looked at the temporal development of these excitons by carrying out excitation energy dependent TA spectroscopic investigations. Drawing the conclusions from these studies, we then proposed the likely mechanisms of their formation and decay. We also discovered that some excitonic characteristics appeared even when the input photon energy was insufficient to directly photogenerate them, which is rather exciting. Also, the high energy excitons are seen to decay more slowly than the band edge exciton, which is surprising. The findings collectively indicate that the formation and decay of the various energy excitons are interlinked and mediated by intervalley (IV) scattering and phonon absorption processes. Carrier mobility is just as vital as carrier relaxation when it comes to carrier transportation. As a result, we investigated the carrier transport behaviour and compared the typical behaviour of carriers injected in high-energy electronic states to those at the band edge by executing optical pump Terahertz probe measurements. The hot carriers photo-generated in the high energy states of Cs_2SnI_6 enjoy increased mobility than the band edge carriers, according to the mobility plots. The overall results thus indicate that in Cs_2SnI_6, the two conditions for a hot carrier solar cell absorber layer, namely slow decay of high energy exciton and high mobility of the hot carriers, coexist. Hence, it is reasonable to assume that Cs_2SnI_6 has the potential to compete as a hot carrier solar cell material in the future.

Here in the present chapter, using theoretical calculations, we first deduced the electronic structure of Cs_2SnI_6 and identified the likely sites of the different excitonic species in its Brillouin zone. Then we looked at the temporal development of these excitons by carrying out excitation energy dependent TA spectroscopic investigations. Drawing the conclusions from these studies, we then proposed the likely mechanisms of their formation and decay. We also discovered that some excitonic characteristics appeared even when the input photon energy was insufficient to directly photogenerate them, which is rather exciting. Also, the high energy excitons are seen to decay more slowly than the band edge exciton, which is surprising. The findings collectively indicate that the formation and decay of the various energy excitons are interlinked and mediated by IV scattering and phonon absorption processes. Carrier mobility is just as vital as carrier relaxation when it comes to carrier transportation. As a result, we investigated the carrier transport behaviour and compared the typical behaviour of carriers injected in high-energy electronic states to those at the band edge by executing optical pump Terahertz probe measurements. The hot carriers photo-generated in the high energy states of Cs_2SnI_6 enjoy increased mobility than the band edge carriers, according to the mobility plots.

The overall results thus indicate that in Cs_2SnI_6, the two conditions for a hot carrier solar cell absorber layer, namely slow decay of high energy exciton and high mobility of the hot carriers, coexist. Hence, it is reasonable to assume that Cs_2SnI_6 has the potential to compete as a hot carrier solar cell material in the future.

7.2 Results and Discussion

7.2.1 Preliminary morphological and steady state optical studies

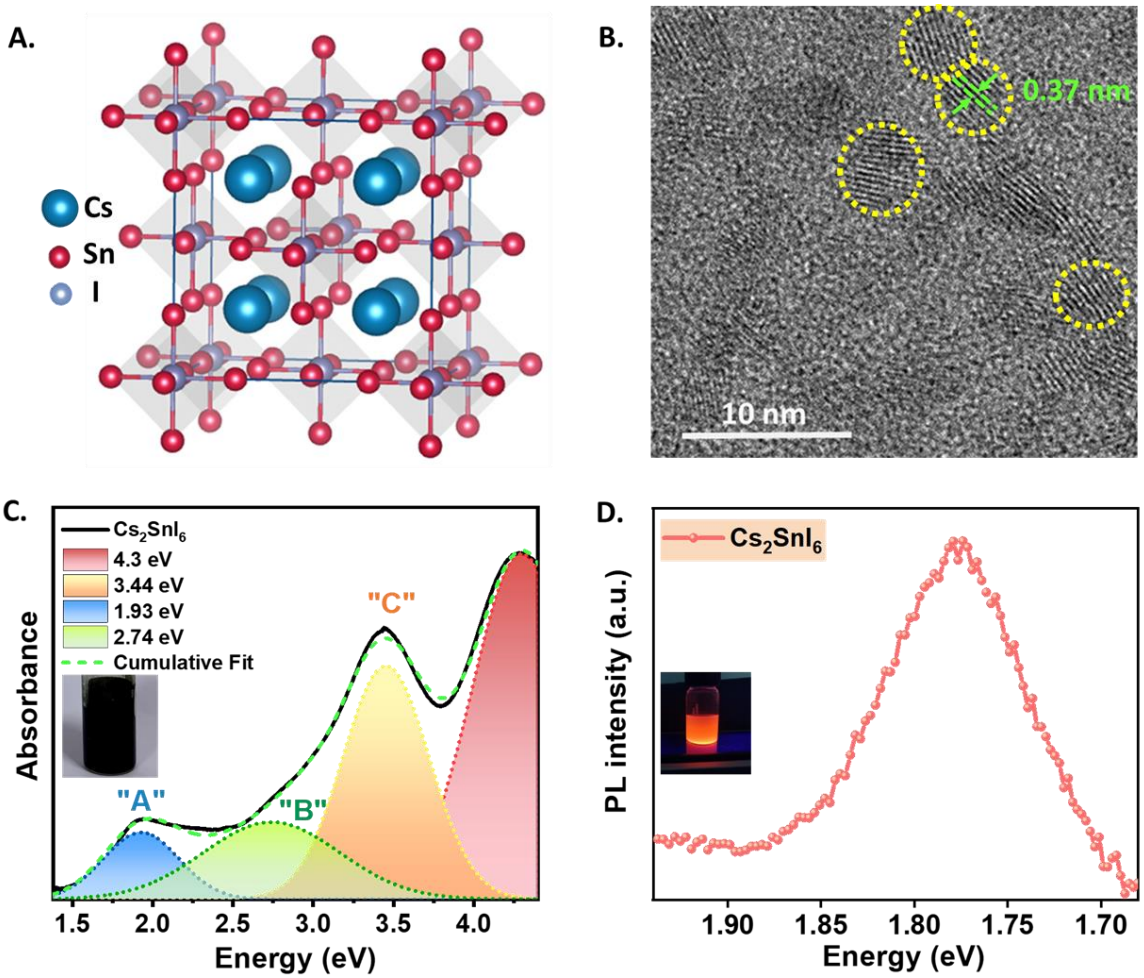

Figure 7.1 (**A)** 3D model for the $Fm\bar{3}m$ crystal structure of Cs_2SnI_6. (**B)** HR-TEM image of the synthesized Cs_2SnI_6 DP NCs; Steady state optical properties. (**C)** Optical absorption spectrum along with the de-convoluted fits (Inset shows the photograph of the prepared sample). (**D)** Corresponding photoluminescence spectrum of the dispersed samples (Inset displays the sample illuminated with UV radiation)

The system under study, namely the Cs_2SnI_6 NCs were synthesised adopting the hot-injection synthesis methodology followed by Wang et.al.[20] Details of the synthesis are supplied in the

experimental methods chapter 2. As depicted in **Figure 7.1 A**, in ideal environment Cs_2SnI_6 is known to crystallise in antiflourite crystal structure with $Fm\bar{3}m$ space group symmetry.[21,22] Each constituent unit cell of Cs_2SnI_6 comprises of four $[SnI_6]^2$ octahedra situated at the corners and face centres while eight Cs^+ cations are located at the tetragonal interstitial sites. The elementary crystallographic and morphological characterisations executed subsequent to synthesis substantiate the successful formation of the NCs. High-Resolution Transmission Electron Microscope (HR-TEM) images **(Figure 7.1 B)** clearly establish the crystallisation of the as-synthesized NCs in cubic ($Fm\bar{3}m$) phase with an inter-planar spacing of 0.37 nm corresponding to 222 plane.

Figure 7.1 C presents the optical absorption spectrum of Cs_2SnI_6 NCs. The recorded trace reveals two notable and distinctly defined peaks at 1.93 eV ("A") and 3.44 eV ("C") along with a less prominent hump-like broad feature at 2.74 eV ("B"). A better picture is disclosed by de-convolution of the spectrum. Labelling of peaks is done following the approach frequently adapted for 2D Transition Metal Di-Chalcogenides (TMDCs).[23] Corresponding PL is peaked at 1.77 eV, indicating a modest Stokes' shift w.r.t. the absorption onset **(Figure 7.1 D)**. Besides being structurally different from $CsSnX_3$ systems, in terms of the optical aspects also, Cs_2SnI_6 exhibits contrasting properties. Unlike the $CsSnX_3$ counterparts, where the first perceptible peak marks the excitonic transition from valence band maxima (VBM) to conduction band minima (CBM), analogous transition in this centrosymmetric crystal structure is known to be optically inactive.[24] This is an outcome of the quantum selection constraint due to the existence of inversion symmetry which renders this transition, dipole forbidden.[24–27] Therefore, the peak labelled as "A" is although a direct band transition but it doesn't stem from VBM to intermediate band minima (IBM) at Γ point in the k space (instead of CBM, it is IBM in this case). Rather, it occurs from another band lying energetically lower than the VBM (Γ) to IBM (Γ). Thereby, this makes the fundamental electronic E_g of Cs_2SnI_6 different from the optically observed band gap (E_A). However, other than peak "A", the origin and character of the other salient features apparent in the absorption spectra is unidentified. Infact, no previous research has attempted to pinpoint the exact position of these excitons in the Brillouin zone of Cs_2SnI_6.

7.2.2 Theoretical findings

In the process of identifying the electronic transitions accountable for the peaks perceived in the steady-state optical response, we first performed Density Functional Theory (DFT) calculations to ascertain the band structure of Cs_2SnI_6. The calculations were undertaken by

Prof. Waghmare and group at Jawaharlal Nehru Centre for Advanced Scientific Research (JNCASR), Bangalore.

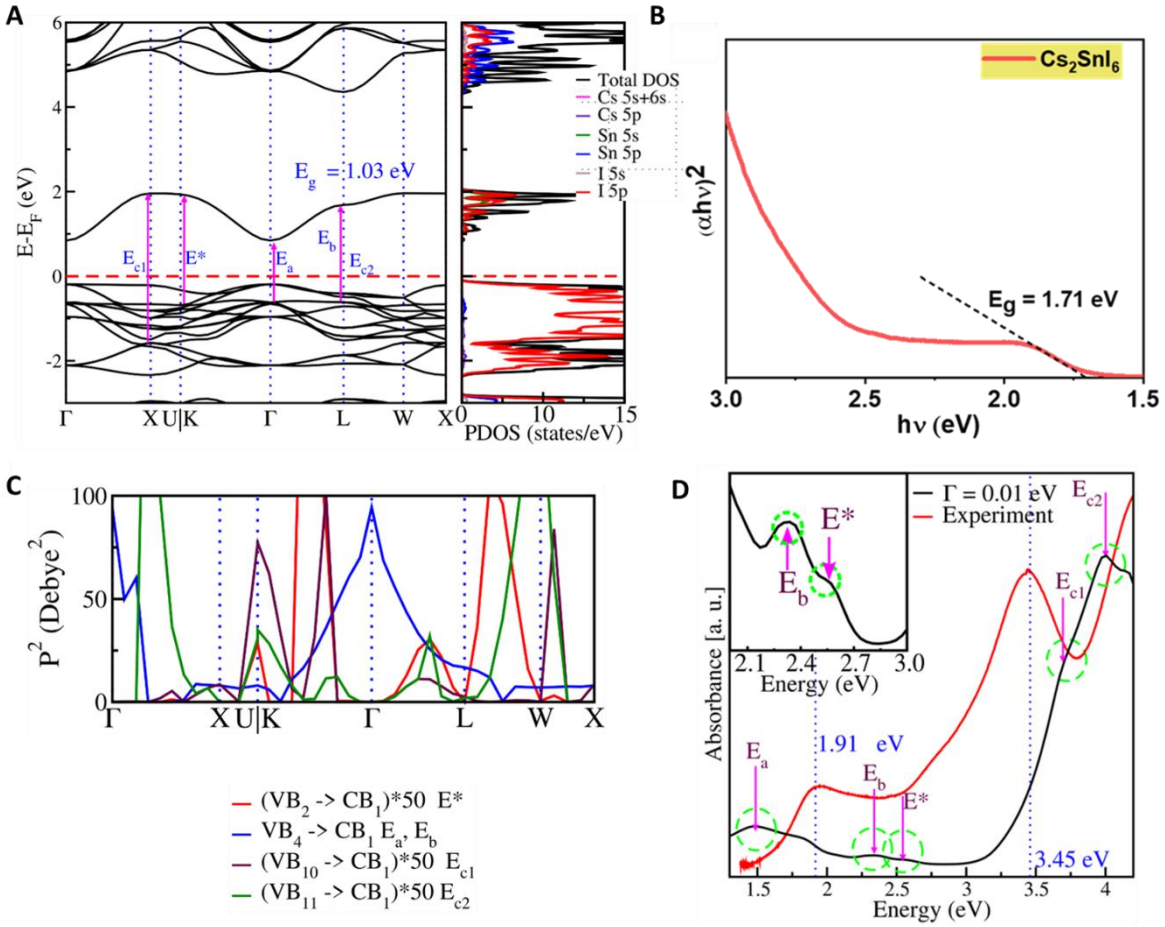

Figure 7.2 (A) Band structure of Cs_2SnI_6 in $Fm\bar{3}m$ phase calculated with hybrid functional HSE06 revealing that Cs_2SnI_6 is a semiconductor with a direct band gap of 1.03 eV at Γ point of the Brillouin zone, **(B)** Tauc plot used for the estimation of the energy band gap (E_g), obtained from steady-state absorption keeping in consideration that Cs_2SnI_6 is a direct band gap material, **(C)** the electronic transition dipole moment (TDM) between the KS states is shown along the high-symmetry path which shows the transition probability of electrons across the high symmetry path in the Brillouin zone; Our estimated optical absorption spectra (with HSE06) are shown in **(D)**, which qualitatively agrees with the experimental one. We have assigned transitions (shown in **(A)** by pink arrows) corresponding to the peaks in absorption spectra, inset is showing expanded transitions in energy range 2.0 eV to 3.0 eV. We find states lying –2 eV deep in VBM also contributing to peaks in the absorption spectra (denoted as E_D).

These *first-principles* calculations are based on quantum mechanical DFT as implemented in VASP (Vienna Ab initio Simulation Package) with interactions between valence electrons and ion cores treated using projector-augmented-wave (PAW) potentials.[28–30] As also mentioned earlier, under ambient conditions, Cs_2SnI_6 exists in cubic $Fm\bar{3}m$ (225) phase with 4 formula units (f. u.) per unit cell. We have used primitive unit cell for calculations which have 1 f. u. per cell to reduce computation cost. Hybrid functional HSE06 yields an energy band gap of 1.03 eV (see **Figure 7.2 A**) which is comparable with experimental value of electronic band gap (1.71 eV) deduced by means of Tauc plot provided in **Figure 7.2 B**.

The number of dipole permitted transitions is constrained by the crystal symmetry and orbital nature of the CB and VB bands. We therefore estimated electronic band-wise transition dipole moment (TDM) along high symmetry paths of the Brillouin zone between Kohn-Sham (KS states) shown in **Figure 7.2 C**. TDM reveals that Cs_2SnI_6 has one single dispersive band as the lowest unoccupied conduction band because of which it shows high electron and hole mobilities.[16] While earlier works have reported absorption spectra from first-principles, no study has shed light on the electronic transitions giving rise to distinct peaks in absorption spectra for Cs_2SnI_6. In this work using TDM, we assigned the origin of these peaks appearing at varied energies (see **Figure 7.2 D**) in the calculated absorption spectra to the respective transitions in the VB and CB states. The peak noticeable at 1.45eV corresponds to 4^{th} VB → 1^{st} CB transition at Γ Point (E_A) (equivalent to the optical band gap), 2.3 eV peak comes from 4^{th} VB → 1^{st} CB transition at L point (E_B), 2.56 eV peak agrees with the 10^{th} VB → 1^{st} CB at U or K point (E^*), the peak at 3.7 eV can be associated with 10^{th} VB to CB transition (E_C) at X point (E_C) and on similar lines the high energy peak at 4 eV corresponds to the 11^{th} VB to 1^{st} CB transition (E_D). Our calculated absorption spectrum with HSE06 functional indeed holds a good qualitative match with the experimental one and is also in excellent agreement with the earlier reported one.[25] But it is well known GW calculation is more appropriate for absorption spectra studies since it considers excitonic effects as well. However due to its high computational cost, we avoided using GW and instead chose the HSE06 functional, which provided reasonable absorption spectrum and electronic structure. Contrasting the theoretical results with the observations made from the steady state optical absorption, it can thus be stated that the peaks lying at 1.93eV, 2.74 eV and 3.44 eV in the absorption spectrum correspond to these E_A, E_B and E_C transitions respectively. Nevertheless, there is an energy discrepancy between the observed peak positions and those derived theoretically, which is a result of the excitonic effects being excluded. Additionally, it should be noted that there is no peak

discernible in the experimental data corresponding to the E* transition. This may be because the corresponding bands at the U or K points lack any singularities.

7.2.3 Positioning of band edge levels from experimental analysis

The theoretical calculations have been performed presuming the system to be pristine, free of any intrinsic defects and vacancies. However there are several reports which demonstrate that Cs_2SnI_6 intrinsically exhibits properties analogous to an intrinsic n-type semiconductor because of the easy formation of V_I (iodine vacancy) and Sn_I (tin interstitial) donors during the synthesis process.[27,31,32] In a very recent experimental finding, Noh and co-workers found the Fermi level in Cs_2SnI_6 lying very close to the IBM edge (only 0.04eV below the IBM).[32] Therefore, it may not be reasonable to make a straightforward remark regarding the occupancy of IB by analysing the position of the Fermi level deduced from theory. But then in order to address the photo-physical processes taking place subsequent to photo-excitation, understanding the whereabouts of these excitons is not sufficient. It is also essential to know that whether the states constituting IB that are involved in the excitonic transition are filled with electrons or are vacant. For this realisation, the knowledge of the positioning of the Fermi level (E_f) *w.r.t.* the IB edge (E_I) is crucial. Therefore we executed Ultraviolet Photoelectron Spectroscopic (UPS) measurements (using XPS/ ESCALAB250Xi, Thermo Fisher Scientific, America) which provided the position of the band edge levels and the Fermi level relative to vacuum. The band level diagram presented in **Figure 7.3 B** demonstrates all the energy levels obtained from the combined Tauc Plot and UPS analysis **(Figure 7.2 B, 7.3 A respectively)**. From the Tauc plot (**Figure 7.2 B)**, the band gap (E_g) is estimated to be 1.71 eV. The binding energy plot yields the secondary cutoff energy edge E_{CutOff} at 17.5 eV **(Figure 7.3 A)** and then in accordance with the equation, E_f = 21.22 eV (He I)-E_{CutOff},[33] the fermi energy level (E_f) is determined close to 3.72 eV. Further to extract the VB edge (E_v), we linearly extrapolated the low energy binding region (E_v - E_f) which yields E_v as 5.82 eV. Thereby the IB edge is found to lie at 4.11 eV (E_v + E_g). It is previously reported that in Cs_2SnI_6, IB is typically spread over a wide energy range of roughly 1.35 eV.[25] Considering this along with the inferences drawn from the UPS analysis conducted in the present work reveals that the Fermi level in Cs_2SnI_6 passes through IB, directly suggesting that Cs_2SnI_6 is a degenerate n-type semiconductor material. Thereby, IB is not an absolutely vacant band. Instead, the states constituting the band lying below E_f in close proximity with the IBM edge are filled with electrons, thus making this band partially filled but only near the edge.

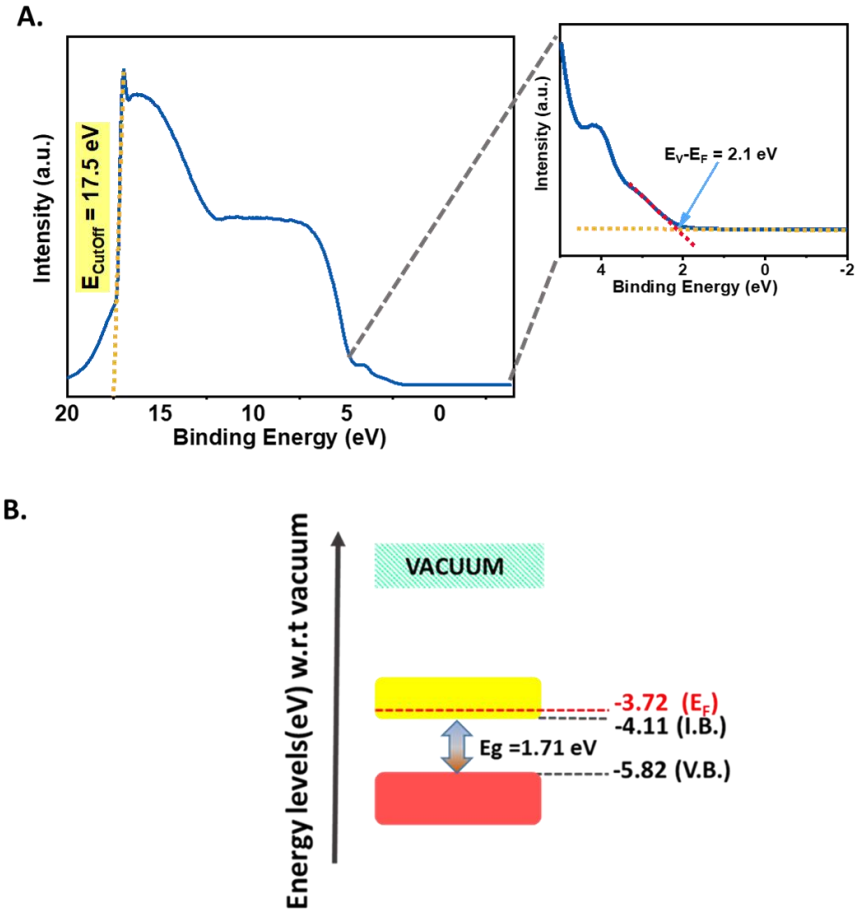

Figure 7.3 (A) UPS plot in the high binding energy regime employed for the estimation of E_f from the secondary cutoff energy. The zoomed region shows the linear extrapolation of the low energy region of the plot yielding "$E_v - E_f$", **(B)** The band level diagram displaying the band levels of Cs_2SnI_6 after summarising the collective results obtained from the UPS investigations and Tauc plot.

7.2.4 Transient absorption deductions

7.2.4.1 Spectral analysis

Bearing in mind the theoretical predictions regarding the location of the excitons in the k-space and taking note of the occupancy of the involved electronic states, we then conducted femtosecond TA measurements for unfolding the subsequent temporal evolution of the three excitons in Cs_2SnI_6. The sample was prepared by spin coating the NCs on a quartz substrate. Here, we deployed excitation pulses varying over a wide span of energy, ranging from 4 eV down to 2eV to excite the NCs ensemble (injected charge carrier density n~ 10^{18} cm^{-3}). Such broad range of pump colors was chosen for the purpose of selectively exciting certain excitons and then monitoring the formation and decay of the other excitons. Interestingly with different

pump energies, significant differences are noticeable in the TA response which assists in understanding these underlying mechanisms. Based on the observations, the entire set of acquired TA response can be categorised into two sub-sections:

(a) When the excitation pump energy is beyond the threshold required for the direct population of the "B" exciton state ($E>E_B$, E_B: Threshold energy required for the formation of B-exciton**).**

To begin with the investigations, the NCs were excited using a very high energy pump (4 eV) that guarantees the direct photoexcitation of all the three excitonic features appearing in **Figure 7.1 C**. The subsequent photoinduced reduction of the ground state absorption which is manifested as photobleaching signals in the TA is monitored using a time delayed white light continuum. Intriguingly, instead of obtaining three negative photoinduced bleach (PIB) signatures owing to the band-filling of the corresponding excitonic transitions, only two bleaches with their minima located at 3.42 and 1.82 eV are distinctly evident in the TA spectral maps **(Figure 7.4 A, Figure 7.5 A)**. These are the ones that correspond to the "C" and "A" exciton as projected in the steady state absorption spectra. Despite providing sufficient surplus energy (ΔE = 1.26 eV), the bleach feature associated with "B" exciton (2.74 eV) fails to come into sight. In place of the anticipated negative bleach, rather a positive signal is observable. Two possibilities can account for such observation. One plausible reason may be that the bleach intensity is relatively very weak in comparison to the positive signal thus causing positive signal to dominate. Such types of strong broad positive feature can arise from the photo-induced absorption (PIA) of probe which carries the excited carriers to further higher-lying electronic states.[34] The other equally possible reason that can be held liable for the absence of an anticipated bleach is the ultrafast transfer of the carriers constituting this bleach to some other electronic states lying elsewise in the k-space.[35] This second possibility appears to be more appropriate in this present case. The bleach due to C-exciton is unusually wide (wider than that for lower energy excitations) and stretched towards the low energy end, indicating a possible its overlap with B-exciton bleach. Because the intensity of this B exciton bleach may be so low due to the transfer process being so fast and efficient, we fail to see the characteristic clearly. This is further validated by the observations made in the later sections.

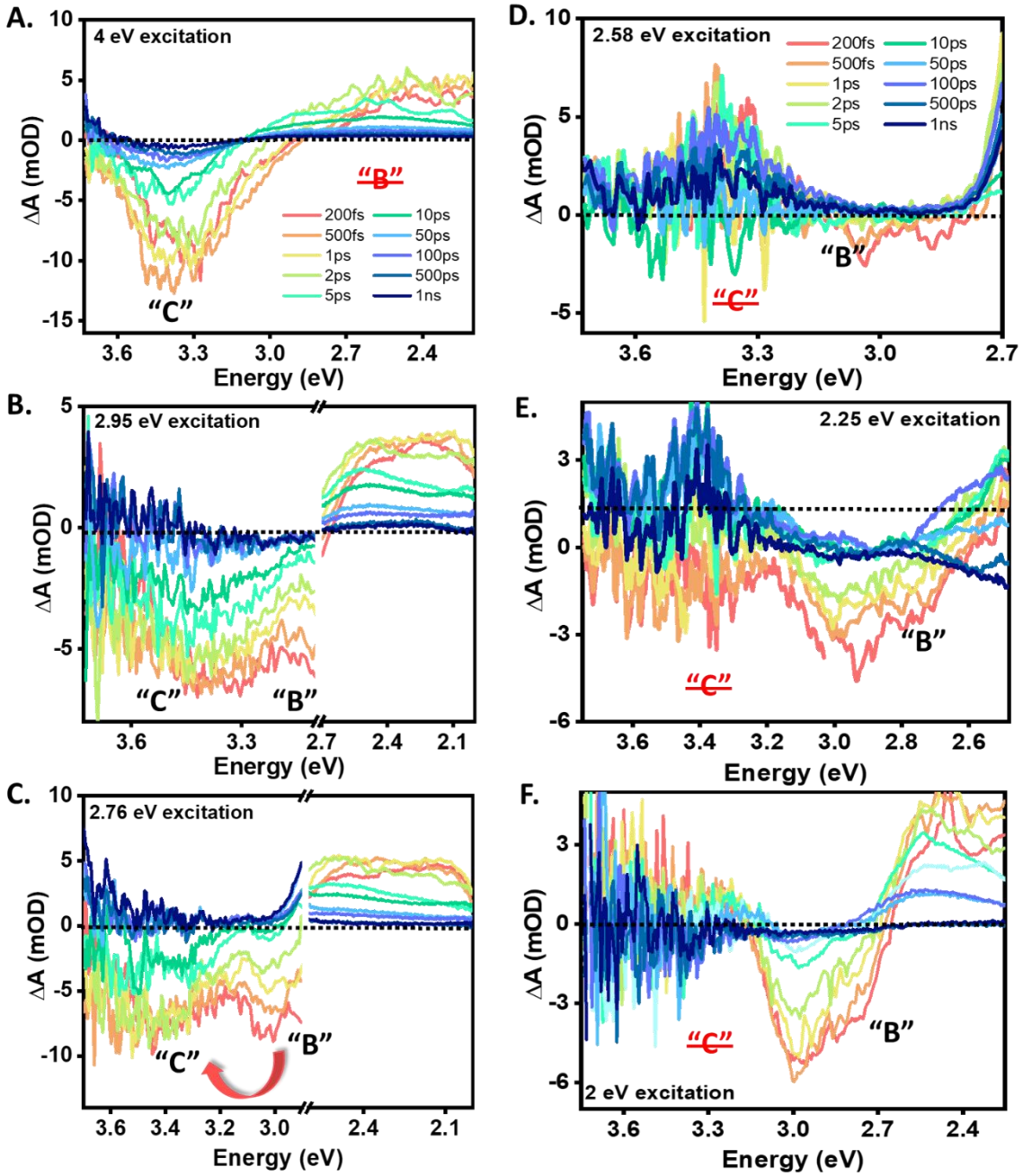

Figure 7.4 TA spectral responses acquired in the UV domain upon exciting the Cs_2SnI_6 NCs with **(A-C)** pump energies adequate to directly populate the exciton "B", **(D-F)** pump energies less than that required for the direct excitation of exciton "B".

Interesting observations reveal when the excitation pump is tuned to further lower excitation energies (2.95 eV and 2.76 eV) **(Figure 7.4 B, C)**, meanwhile ensuring that the exciton "B" is still directly photoexcited. In such cases, all the three bleach features corresponding to those marked in the linear absorption spectrum are clearly observed in the TA spectrum **(Figure 7. 4 B,C and 7.5 B,C)**. This is unusual since the energy provided is

insufficient for the direct photogeneration of "C" exciton. Despite this, "C" exciton is clearly observable in the acquired data.

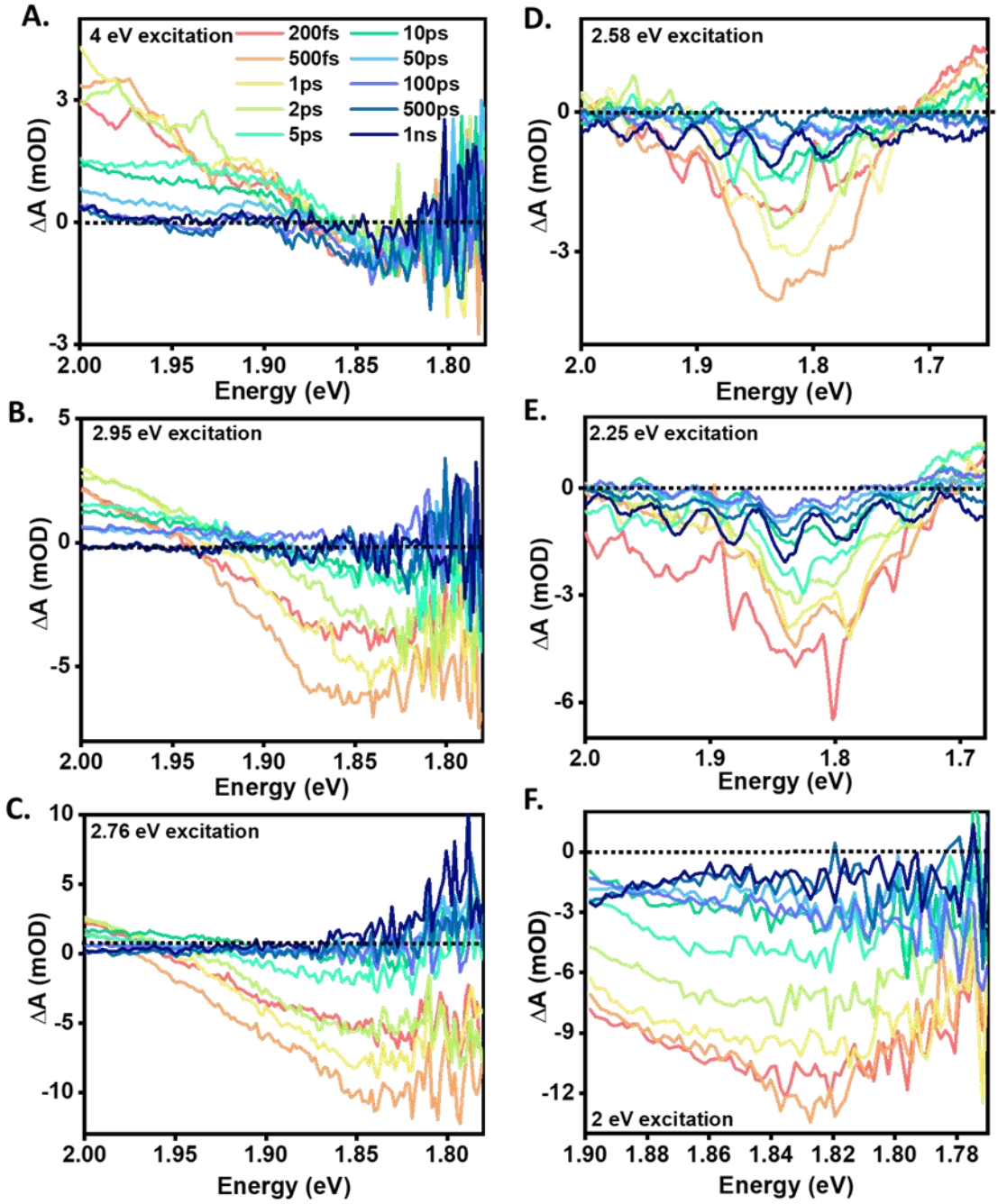

Figure 7.5 TA spectral responses recorded in the visible probe region upon exciting the Cs_2SnI_6 NCs with different pump energies.

(b) When the excitation pump energy is insufficient to directly populate the "B" exciton state ($E<E_B$).

We found that upon further lowering the incident pump energy (2.58 eV, 2.25 eV, 2 eV) *i.e.* when the exciton "B" also cannot be excited directly, and bleach at 3.45 eV that corresponds to "C exciton" fails to show up (Figure 3D-F). But alongwith the appearance of excitonic bleach feature "A" **(Figure 7.5 D,E,F)**, the excitonic "B" bleach is also still intact despite the fact that the incident energy is not ample for its generation.

Summing up the collective conclusions from both sets of TA spectral data ($E > E_B$ and $< E_B$), it can be inferred that there is something unusual related with the exciton "C". The data reflects that only those instances when the excitation energy is adequate enough to directly photo-excite the exciton "B" ($E > E_B$) allow us to observe the "C" exciton. In the contrasting situation $E < E_B$, "C" excitonic feature is not observed in the TA spectra, nevertheless "B" exciton is still distinctly noticeable. This clearly indicates the likelihood of the high energy C-exciton to have its origin from the carriers injected into the electronic states related to "B" exciton. In fact, there is only one sole interpretation for this unexpected appearance of C exciton bleach even under low energy excitations. Such observation is feasible only if there is IV electron transfer taking place from L point (that accommodates B exciton) to fill electronic states at X point in the k-space that constitute the C exciton. The proposed mechanism is depicted through the representation in **Figure 7.6**. The temporal evolution of the bleach intensities corresponding to "C" and "B" exciton in the TA data captured subsequent to shining 2.76 eV pump clearly approve the indulgence of this IV transfer process in the formation of the "C" exciton. It is noticeable that at very early time scales (time delay t_d) ~ 200 fs, the intensities of both the bleaches are quite similar **(Figure 7.4 C)**. However with increasing delays (t_d ~ 1 ps, 2 ps), there is a significant decrement observable in the B exciton bleach intensity. Intriguingly, there is no notable modulation witnessed in the intensity of C exciton bleach at these delay times. Such a rapid dip in the intensity can occur due to relocation of the carrier population between the two high symmetry points in k-space where these excitons are formed. The hot electrons which were earlier blocking the probe absorption at the B exciton edge in the L valley that account for the signal bleaching now undergo IV scattering to reach the X point in the k-space. Ultimately, this leads to buildup of huge population at these k- points which results in the formation of C exciton. Furthermore, it is well stated before in earlier literature studies that this IV transfer mechanism is proportional to incident photon energy. There is an augmentation in the IV transfer efficiency with the increment in the incident photon energy.[36] This may explain the distinct appearance of B exciton at high energy irradiation as pointed out in the preceding segment.

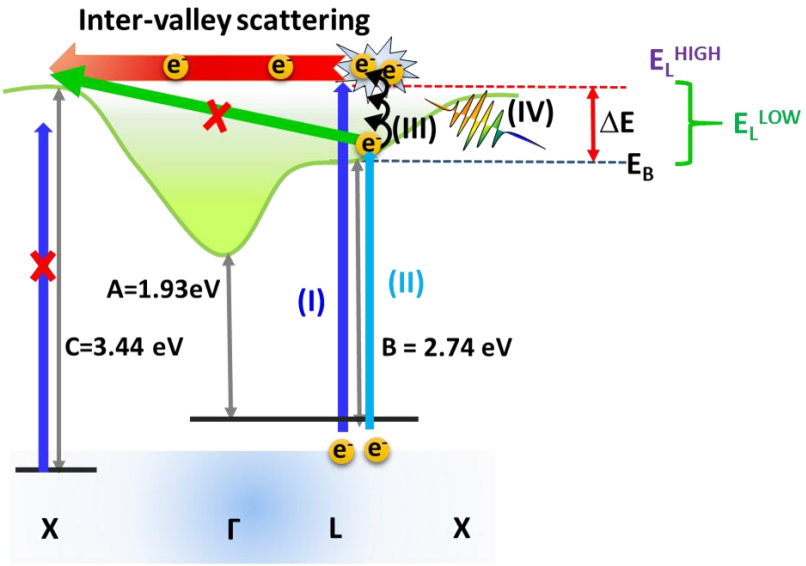

Figure 7.6 Schematic representation illustrating that how the IV scattering process results in the formation of "C" exciton from the charge carriers initially injected into the electronic states lying in the L valley above the threshold excitonic transition "B". These $E > E_B$ excitations can be further sub-categorised into two domains: (I) depicts the excitations with pump energies $E_C > E >> E_B$ (the region denoted by E_L^{High} - high energy electronic states lying at L site situated far from the band edge of B-exciton) (II) the region described as E_L^{Low} refers to relatively low energy electronic states lying at L site close to the B- exciton edge. In the former situation when the charge carriers are injected into sufficiently high energy electronic states (E_L^{High}), the situation is quite simple as IV scattering is practical. However in the later situation, when the photon energy E is just above the threshold required for the formation of B-exciton , *i.e.* E_L^{Low} and the charge carriers are injected into relatively lower energy electronic states, there is an energy offset (ΔE) involved that needs to be surpassed for IV scattering processes to take place. This offset seen by the injected charge carriers can be circumvented in two ways: by absorption of the emitted phonons (III) or by the absorption of the probe (IV).

The model proposed above, no doubt provides a straightforward and simple explanation for the formation mechanism of C exciton but it holds validity only when the photogenerated electrons are initially injected into high lying states at L (E_L^{High}) (for situations similar to as depicted as (l) in Scheme 1). In such situations, the electrons can straightforwardly transport to the states at X point in the Brillouin zone by undergoing IV scattering to enable the formation of C exciton. Nevertheless for the cases of excitation like 2.76 eV pump (in the E_L^{Low} regime), the situation may be a bit complicated. We simply chose 2.76 eV data for sketching the inference in previous section because it is one such pump that allows monitoring all the three

excitonic transitions altogether although IV alone cannot justify its dynamics as well. In instances of E_L^{Low} excitation (II) *i.e.* when the charge carriers are injected into the states just above B-exciton, IV scattering exclusively cannot expedite this process. This is due to the existence of some sort of energy offset that exists between the point where the carriers initially land subsequent to being irradiated by pump beam and the point from where direct transfer between the two valleys (L→ X) takes place steadily. Thereby, indulgence of an additional channel *viz.* Photoinduced absorption (PIA) of the probe or reabsorption of the emitted phonons as a result of which the electrons from the low energy electronic states (E_L^{Low}) can be carried to higher states (E_L^{High}) is demanded in such instances to negotiate this energy gap.

7.2.4.2 Temporal analysis

In order to better understand the critical role of these probe/phonon absorption events and IV scattering processes in the creation of C exciton from B exciton, we studied the pump-dependent transient growth kinetics at the position of both B and C excitons. The bleach rising time for these excitonic characteristics is noticed to change dramatically when the incident pump is tuned to different energies **(Figure 7.7)**. For the case of 4 eV and 2.95 eV pump excitation however, the bleach rise time observed in the transient kinetics profile for C exciton is found to be identical (τ_{gC} ~ 0.35 ps) **(Figure 7.7A)**. The case of 4eV pump excitation is simple to follow. C-exciton under the application of such high energy pump can be generated through dual channels: it can be photogenerated directly as the pump energy is sufficient enough or it can also be formed from the B-exciton. Regarding its formation from B exciton, in such a scenario the incident pump excites the electrons into very high energy levels of the L valley, *i.e.* the E_L^{High} region so the photoexcited carriers can very easily tunnel to the electronic states lying at X, rendering the formation of C exciton. For 2.95 eV pump excitation however, there is no such likelihood of the C-exciton forming directly; instead, one of the following two scenarios may be in play: i) there is a chance for direct IV transfer because the carriers may be landing into sufficiently high energy electronic states after photoexcitation in such a situation, or ii) there may be an energy offset encountered that needs to be overcome by either probe-mediated or phonon-mediated excitation of the carriers prior to IV transfer. Asserting the definite process involved is difficult. Even if there is an energy offset that needs to be transcended it may be quite modest, so the PIA/probe absorption process for transferring the carriers from E_L^{Low} to E_L^{High} region to facilitate IV transfer may be nearly instantaneous, explaining the resemblance observed in the bleach growth times.

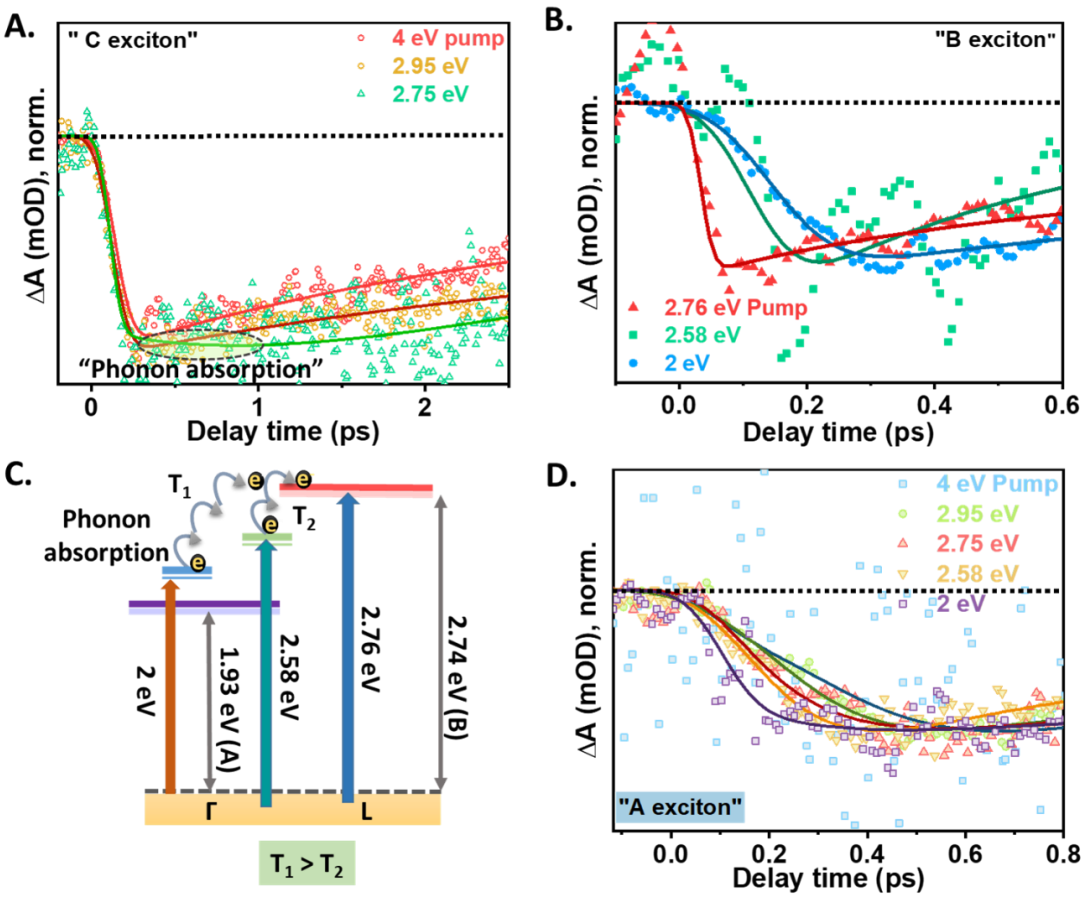

Figure 7.7 Transient bleach profiles for Cs_2SnI_6 NCs irradiated with different pump energies. **(A)** C-exciton dynamics showing the difference in the bleach rise time under different color pumps. **(B)** Bleach dynamics for B-exciton under varied excitations. **(C)** Schematic depicting the pump dependent contribution of phonon absorption processes in the formation of B exciton (2.74 eV bleach). For 2 eV pump, due to the existence of large energy offset (0.74 eV), the photogenerated carriers take long time to advance from the initially excited state to the B-exciton band edge because they require to absorb a significant number of phonons to beat this energy barrier (T_1); however, for higher energy pump like 2.58 eV, this offset is relatively reduced (0.16 eV) so relatively less number of phonons are required to counter this mismatch, resulting in the faster formation of B-exciton (T_2). **(D)** Comparative kinetics displaying the difference in the bleach growth times of A- exciton with pump energies varying between 4 eV and 2 eV.

The role of PIA/probe absorption in the generation of the C exciton is better potrayed in the kinetics probed for 2.76 eV pump. The bleach growth is found to be quite retarded ($\tau_{gC(2.76)}$ ~ 0.8 ps) in contrast to that witnessed for relatively higher energy pumps. This is because the rise time measured here includes the extra time it takes for electrons to reach high energy states

by crossing the large energy offset through the probe/phonon mediated routes before they can tunnel from L to X-valley for C-exciton formation. Further between the two possibilities, the probe absorption mediated channel that causes the photoinduced excitation of the charge carriers cannot alone be sufficient. This is owing to the fact that such probe mediated processes are quite spontaneous and thus cannot account for the lag in the relaxation process. On the other hand, the alternative route of phonon reabsorption takes a while because it requires a plentitude of phonons to be absorbed by the electrons to translate from E_L^{Low} to E_L^{High} region. This delays the subsequent IV transfer and consequently the formation of the C-exciton, rendering it liable and a likely explanation for such an observation.

Figure 7.7 B displays the pump dependent kinetics observed at the site of B exciton. The rising time of the B-exciton bleach is seen to increase monotonously as the pump energy is reduced from 2.76 eV to 2 eV. The schematic depiction in **Figure 7.7 C** assists in understanding such a finding. Since 2.76 eV excitation implies resonant excitation of exciton-B, so it develops instantly and thereby the bleach growth kinetics is fairly fast ($\tau_{gB(2.76\ eV)}$ = <100 fs). However, for lower energy pumps such as 2.58 eV and 2eV, the growth kinetics is relatively retarded. This is due to the fact that in such circumstances, migration of charge carriers excited in low energy electronic states to states matching excitonic B characteristic is mandatory for the formation of B-exciton. This can happen only through probe assisted absorption process or through reabsorption of the emitted phonons. The bleach growth kinetics' pattern displayed in **Figure 7.7 B** is strongly pump energy dependent, which points to the phonon-absorption process as the primary mechanism at work. Infact, if the process had been mediated by probe photon absorption, the bleach growth time would not have been reliant on excitation energy. This can be explained in the following manner: The originally photogenerated carriers in the case of the 2eV pump excitation are positioned in lower states than those in the case of the 2.58 eV pump. Therefore, in the earlier scenario (0.74 eV), more phonons must be absorbed in order to excite the carriers over the energy offset than in the latter scenario (0.16 eV). As a result, more time is required in the formation of C-exciton, which explains the slow bleach growth as excitation energy is decreased. ($\tau_{gB(2.76eV)}$ = <100 fs, $\tau_{gB(2.58\ eV)}$ = 220 fs, $\tau_{gB(2\ eV)}$ = 330 fs). It should be further noted that owing to such large energy offsets, phonon absorption may alone not suffice. Substantial number of phonons may be required in such a situation because the available phonons are very low in energy.[37] Rather it may be a joint venture of both probe induced and phonon absorption processes. Probe induced excitation of the charge carriers may

help transverse some fraction of the energy offset while the rest may be circumvented by absorption of phonons.

Following our understanding of the formation mechanisms of both C and B excitons, we then looked into the evolution of exciton A **(Figure 7.7 D)**. For all of the pump excitations used, we found that mono-exponential fitting parameters best suit the A- exciton bleach growth dynamics. As is clearly depicted in **Table 7.1**, the bleach rising time decreases steadily as the pump energy is reduced from 4 eV (700 fs) to 2eV (450 fs). Thus the bleach growth patterns are mainly in line with the conventional anticipations. It is typically expected that when NCs are excited with high energy pump, the hot charge carriers are placed much above the band edge thereby there is long intraband relaxation time involved for these carriers to reach the band edge. The time manifested in the bleach growth is a measure of this intraband relaxation time. However, for excitations closer to the band edge i.e. when there is less excess energy, intraband relaxation occurs quickly, resulting in a rapid rise time for the bleach.

Table 7.1 Fitting parameters for A-exciton bleach growth dynamics.

Excitation pump energy (eV)	Bleach growth time τ_g (fs)
4	700
2.95	550
2.75	540
2.58	440
2	450

Until now, we had our primary focus laid on tracing the formation of each of the three excitons individually. Nevertheless, contrasting the bleach growth and decay dynamics of all three excitons together can indeed give us a better understanding of how the dynamics of these excitons are interconnected. Among all the excitons, bleach recovery is the slowest for the exciton C and fastest for exciton B, as evident from the normalised kinetic plots for all those pump energies ($E > E_B$) that enable the formation of C exciton. The bleach decay pattern may thus be summarised as $\tau_{dB} < \tau_{dA} < \tau_{dC}$, as justified by the time constants obtained during multi exponential fitting of the signal decay profile **(Tables 7.2 A-C) (Figure 7.8 A-C)**. In such cases, the growth of the bleach signal, on the other hand, follows the $\tau_{gB} < \tau_{gC} < \tau_{gA}$ pattern. These collective inferences drawn from tracking the bleach dynamics may be explicated through the following series of events:

The sole plausible mechanism for the generation of the B exciton is intraband relaxation starting from an excited state and since the injected charge carriers carry only just a little amount of extra energy, so this relaxation time is pretty small ($\therefore$small τ_{gB}). However, once generated, the B exciton has three competing decay channels: i) IV scattering process, which is responsible for the generation of C exciton ii) direct recombination iii) and the other recovery channel is mediated through the A exciton states.

Also in the other scenario, when the high-energy C exciton fails to emerge and only the A and B exciton are seen in the spectral data **(Figure 7.8 D-E)**, the B exciton bleach again displays faster decay than A exciton. Same is reflected in the time constants provided in the **Tables 7.2 D and E**. Understanding the sequence of events in this situation is reasonably easy, and it can help identify the most likely mechanism of decay for the B exciton in the previous circumstance where C exciton is also involved. Since IV scattering-mediated decay is no longer possible, the two remaining alternatives for decay is either through the A exciton or through direct recombination. Due to the independent intraband relaxation occurring in the Γ valley for the formation of A exciton and the fact that the IB edge states at Γ-point are already occupied results in Pauli blocking of these states. Another issue that can slow down the decay of the A-exciton is the fact that this transition is parity-forbidden and it is very well known that the decay processs for parity forbidden transitions is much slower than the allowed transitions. In case if this channel had been active mode of decay, it should have slowed the decay of the B exciton more than that of the A exciton. To put it another way, the B exciton decay ought to have started after the A-exciton decay had finished, however this is not the case. Therefore, the most justifiable mode of B exciton decay for $E < E_B$ excitations is through direct recombination while for other situation when $E > E_B$, there is an additional decay mechanism feasible for B exciton, *i.e.* IV transfer.

Regarding the decay of C exciton, it can either undergo direct (only for 4eV excitation) or indirect recombination or it can also decay through the A exciton states. As already pointed that the A exciton mediated decay channel is sealed because of Pauli blocking. This later argument can explain the exceedingly sluggish C exciton bleach recovery, which is even slower than the A exciton, certifying that A exciton decay is the primary pathway for C exciton decay. A simple schematic illustration potraying the most probable pathways involved in the decay of these three excitons is provided in **Figure 7.8 F**.

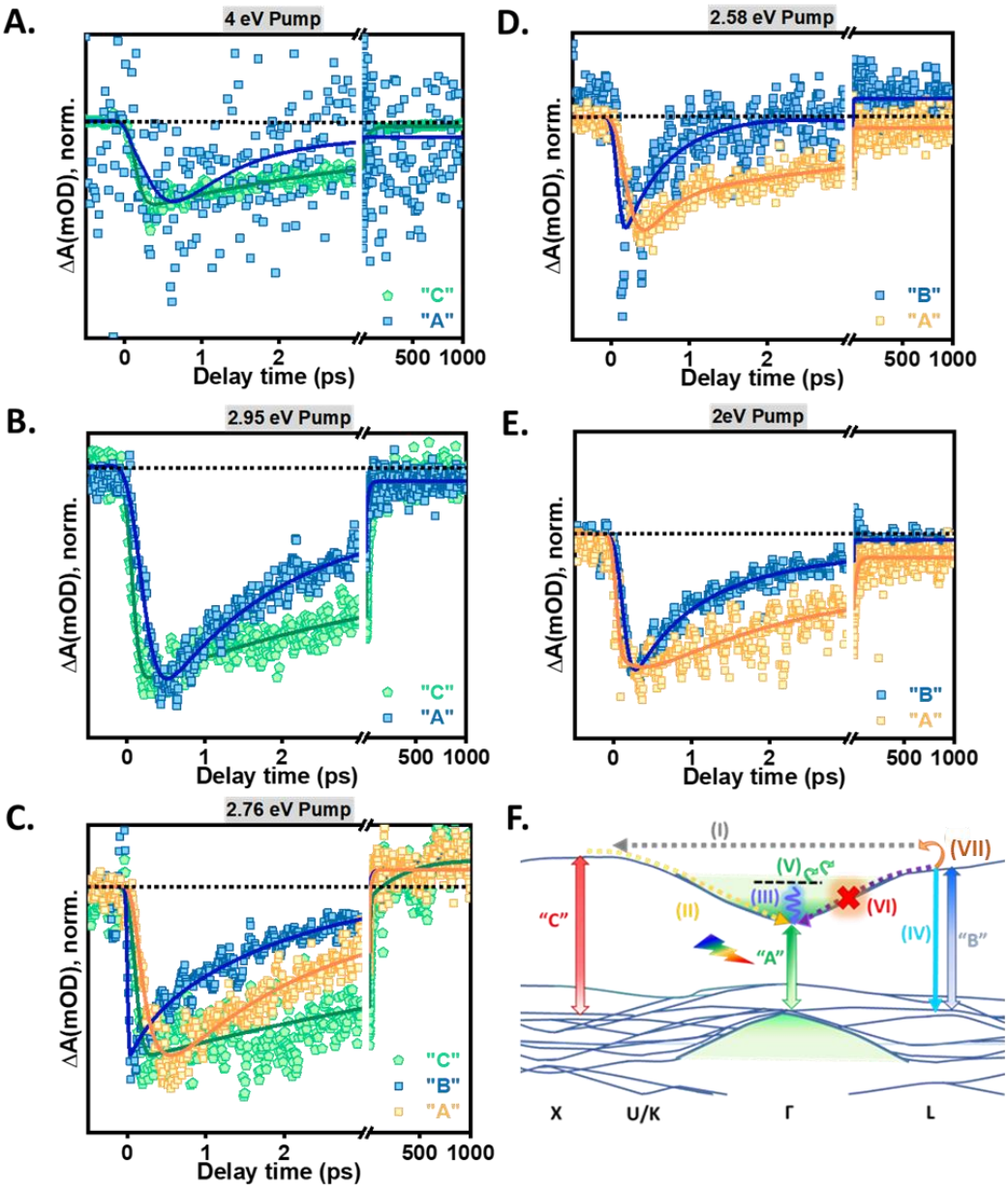

Figure 7.8 (A-E) Normalised kinetic traces comparing the time dependent behaviour of the three excitons dominating the photo-physics of Cs_2SnI_6 under different pumps. The probe energies corresponding to monitored electronic transitions have been denoted by the nomenclature adopted throughout this writing, **(F)** Schematic portrayal of the most probable processes involved in the formation and decay of these excitons (I- IVS mechanism involved in the formation of C exciton from B exciton, II- decay of C exciton through A exciton at Γ valley, III- intraband relaxation of the hot carriers at Γ point (A-exciton formation), IV-decay of B-exciton through radiative recombination, V- phonon absorption by the excited carriers in the Γ valley for the formation of B exciton, VI- decay of B exciton through A exciton, VII phonon absorption by the charge carriers injected into the low energy electronic states to reach the high energy levels.

Table 7.2 Time constants obtained upon multi exponential fitting of the signal growth and decay profiles for different excitons under different energy pump excitations.

A. Pump energy = 4 eV

Exciton bleach	Growth time τ_g (ps)	Decay time τ_{d1} (ps)	Decay time τ_{d2} (ps)	Decay time τ_{d3} (ns)
A	0.7 (100%)	4.72 (-80.2%)		>1 (-19.8%)
C	0.35 (100%)	10.1 (-74%)	210 (-20%)	>1 (-6%)

B. Pump energy = 2.95 eV

Exciton bleach	Growth time τ_g (ps)	Decay time τ_{d1} (ps)	Decay time τ_{d2} (ns)
A	0.55 (100%)	61.9 (-92.5%)	>1 (-7.5%)
C	0.35 (100%)	39 (-79%)	>1 (-21%)

C. Pump energy = 2.76 eV

Exciton bleach	Growth time τ_g (ps)	Decay time τ_{d1} (ps)	Decay time τ_{d2} (ns)
A	0.54 (100%)	63.4 (-100%)	> 1 (100%)
B	<0.1 (100%)	7.1 (-100%)	> 1 (100%)

D. Pump energy = 2.58 eV

Exciton bleach	Growth time τ_g (ps)	Decay time τ_{d1} (ps)	Decay time τ_{d2} (ns)
A	0.440 (100%)	9 (-100%)	>1 (100%)
B	0.220 (100%)	18.6 (-88.75%)	>1 (-11.25%)

E. Pump energy = 2 eV

Exciton bleach	Growth time τ_g (ps)	Decay time τ_{d1} (ps)	Decay time τ_{d2} (ns)
A	0.450(100%)	11.4(-60%)	>1 ns(-40%)
B	0.330 (100%)	13.7(-95%)	>1 ns (-5%)

7.2.5 Carrier mobility measurements

Apart from carrier relaxation, carrier mobility is another crucial aspect of carrier transportation that contributes to the observed device performance. It is well known that carriers photo-generated in high-energy electronic states, referred to as hot carriers, have very different transport properties than carriers injected near the band edge, termed as cold carriers. In conventional semiconductors, hot carriers are noticed to be less mobile than the cold ones. This is because they experience more carrier-phonon scatterings.[38] Excitation energy dependent photoconductivity measurements are undoubtedly the best tool for examining this perspective. To figure out such difference in carrier behaviour for Cs_2SnI_6, we conducted optical pump terahertz (THz) probe (OPTP) spectroscopic investigations. While carrier density and relaxation control TA dynamics, time resolved photoconductivity (σ) dynamics derived from optical pump terahertz (THz) probe OPTP measurements are proportional to the product of carrier population (n) and short range effective mobility φμ (φ is the photon to free carrier conversion ratio): [39]

$$\sigma = n.\, e.\, \varphi\mu \ldots\ldots\ldots\ldots\ldots\ldots \quad \textbf{Eq.(7.1)}$$

The OPTP investigations fundamentally record the pump induced relative attenuation of the terahertz electric field i.e. -ΔE/E. The instantaneous photoconductivity of the sample is further linearly proportional to this relative change -ΔE/E (t_p) in the thin film approximation as apparent from the following equation: [40]

$$\Delta\sigma(t_p) = \frac{\varepsilon_0 c(n_a+n_b)}{d}\left[\frac{-\Delta E(t_p)}{E_0}\right]\ldots\ldots\ldots\ldots\ldots \quad \textbf{Eq. (7.2)}$$

Here, ε_0 is the permittivity of the free space, η_a and η_b are the refractive index of air and quartz (substrate) respectively, c is the speed of light in vacuum, d is the film thickness, $\Delta E = E_{pump} - E_0$ and E_{pump}, E_0 are the transmitted terahertz pulse in the presence and absence of pump, respectively. [41,42] It can thus be stated from Eq.7.1 and Eq.7.2 that there is linear dependency prevalent among these three quantities -ΔE/E, σ and μ.

By carrying out OPTP measurements employing energetically different pumps (2.95 eV-far band gap which ensures the photogeneration of hot carriers and 2 eV-near band gap excitation for injecting the cold carriers), we attempted to explore the effect of varied excess energies on the carrier mobilities (μ). Similar charge carrier density "n" was injected onto the sample at both the excitation energies. In order to evaluate the trend in carrier mobility, we used **Eq. 7.1 and Eq. 7.2** to extract effective mobility plots (φμ) from -ΔE/E (tp) curves plotted at the peak of THz pulses **(Figure 7.9 A)**. Interestingly, we observed dramatic changes in time resolved mobility curves at the two different pumps **(Figure 7.9 B)**. When the pump energy is tuned to 2.95 eV, the effective mobility curve shows a quick and progressive rise for a duration of 3.7 ps before dropping off to a constant mobility after a time lapse of 10 ps. However on lowering the pump photon energy to 2 eV, this rise is observed to be rather slow. The growth of the signal in close band gap excitation case is prolonged to 5 ps and it further remains saturated for sometime just like in the case of 2.95eV excitation. Similar slow growth of dynamics has been previously observed has been previously associated with polaron formation.[43] Moreover, recent investigations have also demonstrated polaron formation in Cs_2SnI_6 in accordance with this hypothesis**.**[26,44] Furthermore, looking at the peak mobilities, it is inferred that the mobility of the hot carriers is ~1.6 times enhanced than the cold ones. The results in the present finding are completely in line with a recent research on $Cs_2AgBiBr_6$, where Bonn *et al.* witnessed unusually enhanced mobility for hot carriers owing to their Ballistic transport and similarly slow rising photoconductivity for low energy excitations.[43] The slow rise can thus be explained in the following way: The process of polaron formation on one hand increases the effective mass of the charge carriers, which eventually restricts the charge carrier mobility but at the same time it also reduces the carrier-phonon scattering processes which improve the carrier mobility. As a result, anytime polaron formation happens, there are competing mechanisms at work.[45] However unlike $Cs_2AgBiBr_6$,[43] we encountered huge difference in the saturated mobility magnitudes (~1.2 times) for Cs_2SnI_6 which implies that although for both cases of excitation there is polaron indulgence, yet the final polaron states attained are not same. The mobility measurements overall are thus suggestive that the carriers in Cs_2SnI_6 irrespective of being hot or cold are highly mobile and in addition also encounter reduced scatterings with phonons. Both these aspects are the prerequisites for good functionality of a hot carrier solar cell.

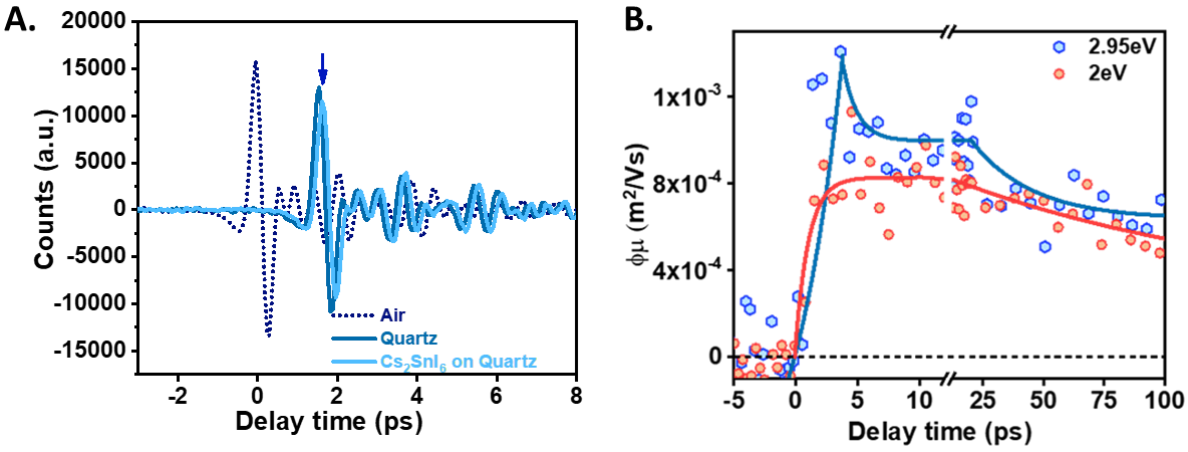

Figure 7.9 (A) THz-TDS waveform transmitted through air, quartz and Cs_2SnI_6 spincoated over quartz substrate **(B)** Effective mobility plots depicting the difference in trends for the rise in the mobility observed under two distinct types of pump excitations: far above band gap excitation (2.95 eV pump) and close to band gap (2 eV) excitation.

7.3 Summary

In this present chapter, we first inferred the electronic structure of Cs_2SnI_6 and assigned the likely positions of the high energy excitons in its Brillouin zone using theoretical calculations. Then, using the time resolved transient absorption (TA) spectroscopy, we investigated the temporal evolution of these excitons by exciting them selectively with varied energy pumps and keeping track of their formation and decay. In this way, we propose the most plausible mechanisms playing role for the formation and decay of these excitons. Upon closely watching the transient dynamics, we mapped out that among all the three excitons perceptible in the TA spectra, the highest energy exciton shows the slowest decay. Such observation implies that the decay of the highest energy exciton is not through direct recombination rather it is mediated through the low energy excitons. Surprisingly, we also found that generation of certain excitons takes place even when the input photon energy was inadequate to directly photogenerate them. The explanation for such an unusual finding is that in such instances, the high energy excitons emerge from the low energy excitons by negotiating the energy offset via absorption of phonons and IV scattering processes. Apart from carrier relaxation, carrier mobility is another vital figure of merit in carrier transportation. So, we also examined the difference in the transport behaviour exhibited by the carriers photogenerated in the high energy electronic states and those injected near the band edge employing OPTP studies. The obtained mobility plots indicate that the hot carriers photogenerated in the high energy states of Cs_2SnI_6 are more mobile than the band edge carriers which is a less encountered observation. Furthermore, in

the case of near band gap excitation, a slow rise is noticed in the early time dynamics, followed by saturation in the long time scales, indicating the possibility of polaron formation in the carrier dynamics of Cs_2SnI_6. Thus in entirety, according to the data acquired in the present study, Cs_2SnI_6 exhibits slowly decaying high energy excitons and highly mobile charge carriers. Both these characteristics are well established as the prerequisites for a hot carrier solar cell absorber layer. Hence, because of the coexistence of these two traits, Cs_2SnI_6 can be envisioned to have the potential for being a future hot carrier solar cell contender.

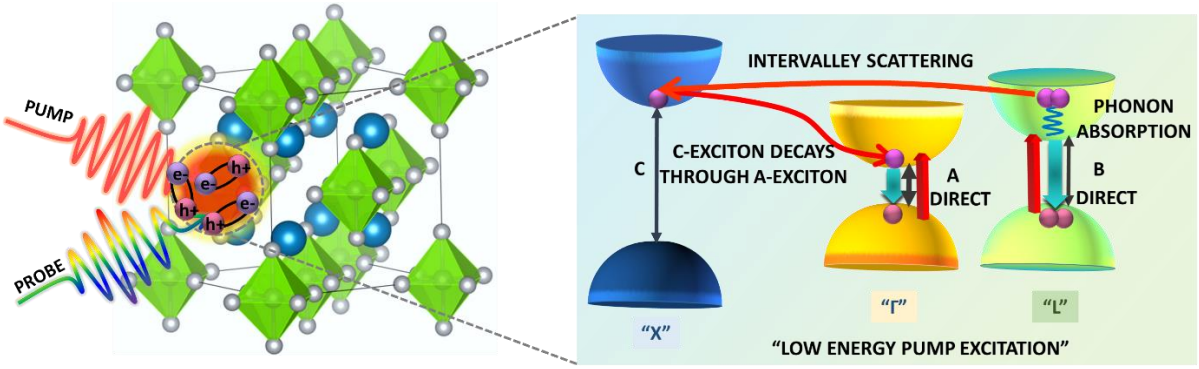

"Graphical representation of the formation and decay mechanisms followed by the excitons in Cs_2SnI_6 when the employed pump energy is low"

7.4 References

(1) Li, J.; Cao, H.L.; Jiao, W.B.; Wang, Q.; Wei, M.; Cantone, I.; Lü, J.; Abate, A. Biological Impact of Lead from Halide Perovskites Reveals the Risk of Introducing a Safe Threshold. *Nat Commun* **2020**, *11* (1), 310.

(2) Schileo, G.; Grancini, G. Lead or No Lead? Availability,Toxicity, Sustainability and Environmental Impact of Lead-Free Perovskite Solar Cells. *J Mater Chem C* **2021**, *9* (1), 67–76.

(3) Green, M. A.; Ho-Baillie, A.; Snaith, H. J. The Emergence of Perovskite Solar Cells. *Nat Photonics* **2014**, *8* (7), 506–514.

(4) Grätzel, M. The Light and Shade of Perovskite Solar Cells. *Nat Mater* **2014**, *13* (9), 838–842.

(5) Ju, M.G.; Chen, M.; Zhou, Y.; Dai, J.; Ma, L.; Padture, N. P.; Zeng, X. C. Toward Eco-Friendly and Stable Perovskite Materials for Photovoltaics. *Joule* **2018**, *2* (7), 1231–1241.

(6) Zong, Y.; Zhou, Y.; Zhang, Y.; Li, Z.; Zhang, L.; Ju, M.G.; Chen, M.; Pang, S.; Zeng,

X. C.; Padture, N. P. Continuous Grain-Boundary Functionalization for High-Efficiency Perovskite Solar Cells with Exceptional Stability. *Chem* **2018**, *4* (6), 1404–1415.

(7) Slavney, A. H.; Hu, T.; Lindenberg, A. M.; Karunadasa, H. I. A Bismuth-Halide Double Perovskite with Long Carrier Recombination Lifetime for Photovoltaic Applications. *J Am Chem Soc* **2016**, *138* (7), 2138–2141.

(8) Hoye, R. L. Z.; Brandt, R. E.; Osherov, A.; Stevanović, V.; Stranks, S. D.; Wilson, M. W. B.; Kim, H.; Akey, A. J.; Perkins, J. D.; Kurchin, R. C.; et al. Methylammonium Bismuth Iodide as a Lead-Free, Stable Hybrid Organic–Inorganic Solar Absorber. *Chem – A Eur J* **2016**, *22* (8), 2605–2610.

(9) Koedtruad, A.; Goto, M.; Amano Patino, M.; Tan, Z.; Guo, H.; Nakamura, T.; Handa, T.; Chen, W.T.; Chuang, Y.C.; Sheu, H.S.; et al. Structure–Property Relations in Ag–Bi–I Compounds: Potential Pb-Free Absorbers in Solar Cells. *J Mater Chem A* **2019**, *7* (10), 5583–5588.

(10) Krishnamoorthy, T.; Ding, H.; Yan, C.; Leong, W. L.; Baikie, T.; Zhang, Z.; Sherburne, M.; Li, S.; Asta, M.; Mathews, N.; et al. Lead-Free Germanium Iodide Perovskite Materials for Photovoltaic Applications. *J Mater Chem A* **2015**, *3* (47), 23829–23832.

(11) Shao, S.; Liu, J.; Portale, G.; Fang, H.-H.; Blake, G. R.; ten Brink, G. H.; Koster, L. J. A.; Loi, M. A. Highly Reproducible Sn-Based Hybrid Perovskite Solar Cells with 9% Efficiency. *Adv Energy Mater* **2018**, *8* (4), 1702019.

(12) Jokar, E.; Chien, C.-H.; Tsai, C.-M.; Fathi, A.; Diau, E. W.-G. Robust Tin-Based Perovskite Solar Cells with Hybrid Organic Cations to Attain Efficiency Approaching 10%. *Adv Mater* **2019**, *31* (2), 1804835.

(13) Hao, L., Li, T., Ma, X. *et al.* A Tin-Based Perovskite Solar Cell With an Inverted Hole-Free Transport Layer to Achieve High Energy Conversion Efficiency By SCAPS Device Simulation. *Opt Quant Electron* **53**, 524 (2021).

(14) Ke, W.; Stoumpos, C. C.; Kanatzidis, M. G. "Unleaded" Perovskites: Status Quo and Future Prospects of Tin-Based Perovskite Solar Cells. *Adv Mater* **2019**, *31* (47), 1803230.

(15) Xiao, Z.; Lei, H.; Zhang, X.; Zhou, Y.; Hosono, H.; Kamiya, T. Ligand-Hole in $[SnI_6]$ Unit and Origin of Band Gap in Photovoltaic Perovskite Variant Cs_2SnI_6. *Bull Chem Soc Jpn* **2015**, *88* (9), 1250–1255.

(16) Lee, B.; Stoumpos, C. C.; Zhou, N.; Hao, F.; Malliakas, C.; Yeh, C.-Y.; Marks, T. J.; Kanatzidis, M. G.; Chang, R. P. H. Air-Stable Molecular Semiconducting Iodosalts for Solar Cell Applications: Cs_2SnI_6 as a Hole Conductor. *J Am Chem Soc* **2014**, *136* (43), 15379–

(17) Dang, T. C.; Le, H. C.; Pham, D. L.; Nguyen, S. H.; Nguyen, T. T. O.; Nguyen, T. T.; Nguyen, T. D. Synthesis of Perovskite Cs_2SnI_6 Film via the Solution Processed Approach: First Study on the Photoelectrochemical Water Splitting Application. *J Alloys Compd* **2019**, *805*, 847–851.

(18) Amaya Suazo, F. J.; Shaji, S.; Avellaneda, D. A.; Aguilar-Martínez, J. A.; Krishnan, B. Solar Cell Using Spray Casted Cs_2SnI_6 Perovskite Thin Films on Chemical Bath Deposited CdS Yielding High Open Circuit Voltage. *Sol Energy* **2020**, *207*, 486–495.

(19) Qiu, X.; Cao, B.; Yuan, S.; Chen, X.; Qiu, Z.; Jiang, Y.; Ye, Q.; Wang, H.; Zeng, H.; Liu, J.; et al. From Unstable $CsSnI_3$ to Air-Stable Cs_2SnI_6: A Lead-Free Perovskite Solar Cell Light Absorber with Bandgap of 1.48eV and High Absorption Coefficient. *Sol Energy Mater Sol Cells* **2017**, *159*, 227–234.

(20) Wang, A.; Yan, X.; Zhang, M.; Sun, S.; Yang, M.; Shen, W.; Pan, X.; Wang, P.; Deng, Z. Controlled Synthesis of Lead-Free and Stable Perovskite Derivative Cs_2SnI_6 Nanocrystals via a Facile Hot-Injection Process. *Chem Mater* **2016**, *28* (22), 8132–8140.

(21) Xiao, Z.; Zhou, Y.; Hosono, H.; Kamiya, T. Intrinsic Defects in a Photovoltaic Perovskite Variant Cs_2SnI_6. *Phys Chem Chem Phys* **2015**, *17* (29), 18900–18903.

(22) Cai, Y.; Xie, W.; Ding, H.; Chen, Y.; Thirumal, K.; Wong, L. H.; Mathews, N.; Mhaisalkar, S. G.; Sherburne, M.; Asta, M. Computational Study of Halide Perovskite-Derived A_2BX_6 Inorganic Compounds: Chemical Trends in Electronic Structure and Structural Stability. *Chem Mater* **2017**, *29* (18), 7740–7749.

(23) Goswami, T.; Bhatt, H.; Babu, K. J.; Kaur, G.; Ghorai, N.; Ghosh, H. N. Ultrafast Insights into High Energy (C and D) Excitons in Few Layer WS_2. *J Phys Chem Lett* **2021**, *12* (28), 6526–6534.

(24) Meng, W.; Wang, X.; Xiao, Z.; Wang, J.; Mitzi, D. B.; Yan, Y. Parity-Forbidden Transitions and Their Impact on the Optical Absorption Properties of Lead-Free Metal Halide Perovskites and Double Perovskites. *J Phys Chem Lett* **2017**, *8* (13), 2999–3007.

(25) Rasukkannu, M.; Velauthapillai, D.; Vajeeston, P. A First-Principle Study of the

Electronic, Mechanical and Optical Properties of Inorganic Perovskite Cs2SnI6 for Intermediate-Band Solar Cells. *Mater Lett* **2018**, *218*, 233–236.

(26) Maughan, A. E.; Ganose, A. M.; Almaker, M. A.; Scanlon, D. O.; Neilson, J. R. Tolerance Factor and Cooperative Tilting Effects in Vacancy-Ordered Double Perovskite Halides. *Chem Mater* **2018**, *30* (11), 3909–3919.

(27) Maughan, A. E.; Ganose, A. M.; Bordelon, M. M.; Miller, E. M.; Scanlon, D. O.; Neilson, J. R. Defect Tolerance to Intolerance in the Vacancy-Ordered Double Perovskite Semiconductors Cs_2SnI_6 and Cs_2TeI_6. *J Am Chem Soc* **2016**, *138* (27), 8453–8464.

(28) Kresse, G.; Hafner, J. Ab Initio Molecular Dynamics for Liquid Metals. *Phys Rev B* **1993**, *47* (1), 558–561.

(29) Kresse, G.; Furthmüller, J. Efficiency of Ab-Initio Total Energy Calculations for Metals and Semiconductors Using a Plane-Wave Basis Set. *Comput Mater Sci* **1996**, *6* (1), 15–50.

(30) Kresse, G.; Furthmüller, J. Efficient Iterative Schemes for Ab Initio Total-Energy Calculations Using a Plane-Wave Basis Set. *Phys Rev B* **1996**, *54* (16), 11169–11186.

(31) Li, T.; Zhao, X.; Yang, D.; Du, M.-H.; Zhang, L. Intrinsic Defect Properties in Halide Double Perovskites for Optoelectronic Applications. *Phys Rev Appl* **2018**, *10* (4), 41001.

(32) Liu, A.; Zhu, H.; Reo, Y.; Kim, M.-G.; Chu, H. Y.; Lim, J. H.; Kim, H.-J.; Ning, W.; Bai, S.; Noh, Y.Y. Modulation of Vacancy-Ordered Double Perovskite Cs_2SnI_6 for Air-Stable Thin-Film Transistors. *Cell Reports Phys Sci* **2022**, *3* (4), 100812.

(33) Kim, Y.; Yang, Z.; Jain, A.; Voznyy, O.; Kim, G.-H.; Liu, M.; Quan, L. N.; García de Arquer, F. P.; Comin, R.; Fan, J. Z.; et al. Pure Cubic-Phase Hybrid Iodobismuthates $AgBi_2I_7$ for Thin-Film Photovoltaics. *Angew Chemie Int Ed* **2016**, *55* (33), 9586–9590.

(34) Rieger, S.; Bohn, B. J.; Döblinger, M.; Richter, A. F.; Tong, Y.; Wang, K.; Müller-Buschbaum, P.; Polavarapu, L.; Leppert, L.; Stolarczyk, J. K.; et al. Excitons and Narrow Bands Determine the Optical Properties of Cesium Bismuth Halides. *Phys Rev B* **2019**, *100* (20), 201404.

(35) Lee, S.; Wang, Y.; Liu, Y.; Lee, D.; Lee, K.; Lee, D. C.; Lian, T. Exciton Dynamics in Cation-Exchanged CdSe/PbSe Nanorods: The Role of Defects. *Chem Phys Lett* **2017**, *683*, 342–346.

(36) Stanton, C. J.; Bailey, D. W. Rate Equations for the Study of Femtosecond Intervalley Scattering in Compound Semiconductors. *Phys Rev B* **1992**, *45* (15), 8369–8377.

(37) Jong, U.G.; Yu, C.J.; Kye, Y.H.; Choe, S.H.; Kim, J.S.; Choe, Y.G. Anharmonic Phonons and Phase Transitions in the Vacancy-Ordered Double Perovskite Cs_2SnI_6 from First-Principles Predictions. *Phys Rev B* **2019**, *99*(18), *184105.*

(38) Bernardi, M.; Vigil-Fowler, D.; Lischner, J.; Neaton, J. B.; Louie, S. G. Ab Initio Study of Hot Carriers in the First Picosecond after Sunlight Absorption in Silicon. *Phys Rev Lett* **2014**, *112* (25), 257402.

(39) Justice Babu, K.; Kaur, G.; Shukla, A.; Saha, R.; Kaur, A.; Sachdeva, M.; Yadav, D. K.; Ghosh, H. N. Fast Polaron Formation and Low Carrier Mobility in Defect-Free Polyhedral $CsPbBr_3$ Perovskite Nanocrystals. *ACS Photonics **2022**, 9, 3, 969–978*

(40) Glover, R. E.; Tinkham, M. Conductivity of Superconducting Films for Photon Energies between 0.3 and $40kT_c$. *Phys Rev* **1957**, *108* (2), 243–256.

(41) Ulbricht, R.; Hendry, E.; Shan, J.; Heinz, T. F.; Bonn, M. Carrier Dynamics in Semiconductors Studied with Time-Resolved Terahertz Spectroscopy. *Rev Mod Phys* **2011**, *83* (2), 543–586.

(42) Němec, H.; Kadlec, F.; Kadlec, C.; Kužel, P.; Jungwirth, P. Ultrafast Far-Infrared Dynamics Probed by Terahertz Pulses: A Frequency-Domain Approach. II. Applications. *J Chem Phys* **2005**, *122* (10), 104504.

(43) Heng, Z.; Elke, D.; Wenhao, Z.; Shuai, F.; D., V. L.; Pushpendra, K.; Mischa, B.; I., W. H. Highly Mobile Hot Holes in $Cs_2AgBiBr_6$ Double Perovskite. *Sci Adv **2021**, 7 (52), eabj9066.*

(44) Maughan, A. E.; Paecklar, A. A.; Neilson, J. R. Bond Valences and Anharmonicity in Vacancy-Ordered Double Perovskite Halides. *J Mater Chem C* **2018**, *6* (44), 12095–12104.

(45) Zhang, H.; Debroye, E.; Steele, J. A.; Roeffaers, M. B. J.; Hofkens, J.; Wang, H. I.; Bonn, M. Highly Mobile Large Polarons in Black Phase $CsPbI_3$. *ACS Energy Lett* **2021**, *6* (2), 568–573.

Chapter 8
Conclusions
&
Future Outlook

8.1 Conclusions

The primary focus of the present thesis is to address the yet unexplored fundamental photophysical aspects of few well established perovskite systems, particularly relevant from the perspective of photovoltaic applications. Keeping in mind that transient absorption spectroscopy can serve as a prospective tool for tracking such ultrafast occurances, we have deployed this differential absorption technique to monitor the time dependent excited state response of the photogenerated species in some of the noted perovskite structures. Chapter 1 that marks the beginning of the dissertation focuses on providing an overview of the perovskite domain with major emphasis laid on the metal halide perovskites- both lead based and lead free analogues, and their various derivatives. Furthermore, this chapter also brings out the various relaxation and recombination mechanisms followed by the charge carriers at different injected carrier densities as well as the underlying phonon interplay that sets in right after photoexcitation in such systems. The next chapter, Chapter 2 covers the methodologies adopted for the synthesis of the various NC systems that are the subject of this thesis work. Besides this, it also furnishes the details of the various experimental techniques deployed to affirm the successful formation of these desired NCs and their further elementary characterisations. Transient absorption spectroscopy is the most crucial investigative instrument here, as previously said in compliance with the thesis's goal, thus in this chapter we have included a thorough background and extensive description about its setup and component parts. Then in the succeeding chapters, we have covered in depth the intriguing conclusions we have drawn concerning the interrogated systems by tuning various parameters of excitation pump light, either colour or intensity and even the lattice temperature.

Talking about Chapter 3, here we investigated the charge carrier dynamics in $CsPbBr_3$@Cs_4PbBr_6 core-shell NC system, which enjoys a Type-1 band alignment and contrasted it with that typically observed in $CsPbBr_3$ NCs. Other than permitting the carriers to delocalise preferably towards the $CsPbBr_3$ states owing to Type-1 alignment, the design of this project offers added multiple advantages: Cs_4PbBr_6 lattice being quite prone to polaron formation permits the charge carriers initially photogenerated in the higher polar shell to indulge in polaron formation and it even provides an additional protection to the otherwise readily degradable core. As per the architecture inherited by this core-shell system, different relaxation pathways are anticipated to come up at different energy pump excitations. Therefore, for understanding this distinction in the relaxation routes we opted for two contrasting energy pumps. Upon monitoring the TA bleach kinetics for high energy pump excitation that ensures the simultaneous excitation of both the core and shell, we observed that the bleach signal in the core-shell system at the position of $CsPbBr_3$ bleach exhibits a slower growth in comparison to the pure $CsPbBr_3$ NCs. Such retarded bleach growth is a straightforward implication of delayed carrier cooling process in the former system. This is in contrast to the near band edge excitation case, where the kinetics for both the systems are observed to be almost analogous because of the non-indulgence of the shell. The reason accountable for this observation is validated by the investigation of the low energy PIA dynamics which reveals a clear signature of polaron formation in the core-shell structure, which on the other hand is missing in the TA response recorded for $CsPbBr_3$. Thus through this work, by harnessing the benefits endowed by growing a thin shell of Cs_4PbBr_6 we have successfully achieved further deceleration in the carrier cooling process for $CsPbBr_3$ which is already known to be an abode of slow cooling. Such deceleration in the carrier cooling is incredibly advantageous for photovoltaic domain and the integrated devices are anticipated to offer higher PCEs.

Further in Chapter 4, we highlighted the influence of lattice temperature on the process of hot carrier cooling and its conflicting contender *i.e.* polaron formation which together dictate the relaxation rate followed by the carriers in $CsPbBr_3$. Both of these processes although have opposing effects on carrier relaxation yet are fundamentally driven by the same parameter-carrier-LO phonon coupling. This coupling strength is inturn itself a strong function of temperature therefore to begin with, we performed temperature dependent PL measurements to acquire a preliminary understanding of the effect of temperature on the carrier-phonon coupling strength (300 K –5 K). The PL linewidth conclusions drawn from these investigations reveal that at temperatures between 300 K and 200 K, it is the carrier-LO phonon coupling that

pervades the picture. However as the lattice is frozen that is when the temperature is dropped down from 200 K to 5 K, the carrier-acoustic phonon coupling takes over as there is no sufficient population of LO phonons. The temperature dependent TA studies further reveal that the growth as well as the decay kinetics of the bleach are both accelerated as the temperature is lowered from 300 K to 5 K. Probing of the low energy PIA dynamics indicates the basis behind such an observation. These dynamics divulge a clear polaronic signal at 300 K however at low temperatures there is no such signal observable. It is thus due to the indulgence of this polaron that results in a retarded bleach growth *viz.* slower carrier cooling while at low lattice temperatures, the carrier opt for carrier-acoustic phonon mediated cooling pathways and thereby faster relaxation. Besides this, it is further observed that lattice temperature not only decides the onset of polaron formation but also remains pivotal in determining the pace of polaron formation. Although there is polaron formation evident from the PIA dynamics of $CsPbBr_3$ at 200 K in accordance with expectations, we did not observe any involvement of polaron in the carrier cooling process at 200 K because polaron formation is a slow process at this temperature and is conquered by hot carrier cooling. We believe that having a beforehand comprehensive knowledge of this kind can prove to be quite helpful while designing the device architecture since any device while working may be subjected to various variations in external conditions.

Chapter 5 highlights the competition in the carrier relaxation and carrier transfer processes followed by the charge carriers under different energy excitations in a perovskite/II-VI semiconductor composite system, $CsPbBr_3$- PbS (Type -1) which has already shown its excellence in phototransistor applications. Difference in the overall dynamics is expected because of the diversity in the density of states the charge carriers encounter upon being injected with different energy pumps. PL measurements executed for the two different cases of excitation-close to band gap (*w.r.t.* $CsPbBr_3$) and far band gap, together suggest of uni-directional charge transfer from $CsPbBr_3$- PbS in accordance with Type-1 design of the composite system. However in the TA studies under very high energy pump excitation, the carrier cooling dynamics monitored at the position of 1S bleach of both $CsPbBr_3$ and PbS suggest that the charge carriers undergo bidirectional transfer *i.e.* from $CsPbBr_3$- PbS and vice versa, but the transfer remains more preferential from $CsPbBr_3$ towards PbS. Then further when we had the excitation energy set resonant with $CsPbBr_3$ band gap, the TA data showcases only one direction of transfer *i.e.* from $CsPbBr_3$ towards PbS. This difference has been explained in the following manner: i) for high energy excitation, the carriers injected into the system

encounter bulk like states of both $CsPbBr_3$ and PbS, therefore there is similar density of acceptor and donor states available for transfer for the charge carriers photogenerated in both the constituent individuals. This makes the transfer process quite efficient in both directions. ii) However, when we talk of close band gap excitation, the charge carriers are although injected into high density states of PbS, for the case of $CsPbBr_3$ the initially encountered states are quite sparse. As a result, there are plenty of donor states on the PbS side to take the carriers; but, since there aren't enough donor states on the $CsPbBr_3$ side, the carriers in PbS prefer cooling to transfer, which leads to unidirectional transfer.

As opposed to the works depicted in Chapter 3-5 which are based on lead based perovskite $CsPbBr_3$, the findings presented in Chapter 6 and 7 rely on the less toxic, lead free analogue "Cs_2SnI_6". Chapter 6 sheds light on the lattice vibrational dynamics and the phonon modes supported by Cs_2SnI_6, which were only theoretically predicted but not corroborated experimentally till date. Subsequent to the preliminary investigations carried out to verify the successful formation of Cs_2SnI_6 NCs, when we executed TA studies we found oscillatory features superimposed over the otherwise exponentially decaying kinetics. In order to decipher the reason behind these oscillations, we transformed the time domain response into frequency domain which inturn revealed plentitude of peaks corresponding to the various phonon modes anticipated for Cs_2SnI_6. By analysing these frequency domain results, we then identified the origin of these periodic modulations and found the coherent emission of the fully symmetric A_{1g} mode -121 cm^{-1} responsive for such observation. Comparing with the Tellurium and Chloride counterparts, we are able to locate and identify the low frequency Raman mode (29 cm^{-1}) and one of the two predicted silent modes (14 cm^{-1}). Then further by resorting to phase analysis of the pump dependent TA data and by conducting intensity dependent measurements, the position of the other silent mode (66 cm^{-1}) is also identified. The high frequency peaks have been recognised as the overtones or the combination modes. These studies also suggest that both ISRS and DECP together are responsible for the coherent phonon generation in Cs_2SnI_6 and understanding of the probable decoupling mechanism of these coherent phonons is provided by the temperature reliant studies. Thus, our finding offers a complete description of the phonon infrastructure that makes up the Cs_2SnI_6 lattice, which was lacking up until now despite being an extremely important piece of knowledge for understanding the device performance.

Unlike the Chapter 6 which focuses on the phonon dynamics of Cs_2SnI_6, in Chapter 7 we have attempted to provide an extensive portrayal of its charge carrier dynamics. Through the

theoretical findings, firstly we have located the probable location of the different energy excitons (A,B and C) in the momentum space of Cs_2SnI_6. Subsequent to tracing them, we conducted the excitation energy dependent TA measurements which allow us to selectively excite certain excitons while at the same time monitor the formation and decay dynamics of the other remnant excitons. Upon tracking the bleach recovery kinetics of the different excitons, we found the decay of the highest energy exciton (C) to be the most retarded. Furthermore, to our surprise, we also observed the formation of certain high energy excitons even when the incident photon energy was inadequate for their direct photogeneration. By contrasting the bleach growth kinetics of the different excitons, we found that the involvement of intervalley scattering events together with phonon absorption processes (along with probable contribution from PIA as well) is the basis for such findings. Moreover, through the effective mobility investigations we found that the hot carriers in this material are more mobile than the cold charge carriers which implies that the hot carriers are subjected to lesser encounters with the emitted phonons. As a result of all the collective implications drawn from this finding, it can thus be postulated that Cs_2SnI_6, as a virtue of its traits- slowly decaying high energy exciton and highly mobile charge carriers can serve as a prospective candidate in hot carrier based solar cell devices.

8.2 Future outlook

Among the three most highlighted all-inorganic lead based MHPs, it is $CsPbI_3$ unquestionably that exhibits the slowest carrier cooling, making it the most efficient for photovoltaic applications. However its instability refrains it from being commercialised. With a few exemptions, $CsPbBr_3$, which has been a thorough subject of our study, can compete favourably with $CsPbI_3$ in all respects. By exploiting the results of the present dissertation, we can expect to alleviate some of these shortfalls in the future endeavours, and achieve equivalent or even enhanced reduction in carrier cooling rate with this bromide analogue $CsPbBr_3$, that is although far more stable but intrinsically exhibits considerably faster cooling than $CsPbI_3$. For this purpose, structures similar to the one discussed here *viz.* $CsPbBr_3@Cs_4PbBr_6$ or with more compelling properties that may delay the carrier cooling even more may be looked for in the future research. Such deceleration in cooling can expedite the easy extraction of the hot charge carriers and lead to better device efficiency. Besides this, the information furnished by the cryogenic studies carried out for $CsPbBr_3$ NCs suggests that this carrier relaxation dynamics is not persistent, rather it varies drastically with changing temperature. Nevertheless such significant change with alterations in external temperature may not be desirable. Furthermore

from the standpoint of solar panels installed in low-temperature environments, such as those proposed to be put in outer space where perovskite technology has already demonstrated promising results, the faster relaxation rate followed by carriers in $CsPbBr_3$ at cryogenic temperatures may be an obstruction. Therefore ways to retard down the cooling rate even at such low temperatures and also have a consistent relaxation rate throughout the possible temperature range should be sorted for in the near future. One workable solution in this regard can be making the process of acoustic to LO phonon up-conversion efficient.

Likewise the results also suggest that using $CsPbBr_3$ in combination with other semiconductor materials can tune the otherwise attainable properties to our advantage. In this way, designing and utilising composite systems based on $CsPbBr_3$ rather than pure $CsPbBr_3$ system can open new avenues in application domain owing to the benefits offered by both the constituting materials and can achieve functionality over a wider range of electromagnetic spectrum. Infact this strategy of preparing composites can be applied to various other MHP systems as well.

Owing to the toxicity concerns related to lead leakage, the potential future of perovskites lies in lead-free systems, especially tin-based systems. In spite of this, they are little investigated. The distinctive results obtained in this dissertation altogether indicate that Cs_2SnI_6 can be quite an outstanding material for photovoltaic applications. Therefore, efficiency close to the theoretical estimations may be achieved if more efforts are made to comprehend their opto- electronic aspects beyond that established in the present work. Despite all the plus points, one major point that needs to be addressed is that as suggested by this thesis, in comparison to lead based counterparts, the carrier cooling in Cs_2SnI_6 is relatively faster. If somehow, either through doping or through some other ways of chemical engineering we are able to bring down this carrier cooling rate in coming times, Cs_2SnI_6 withholds in itself a good future in solar applications. Future research in this direction may also take into account methods similar to the one used in the current work to slow down carrier cooling in $CsPbBr_3$. Other than Cs_2SnI_6, there are also other isostructural perovskites like Cs_2TiI_6 reported in literature that have also shown encouraging results but their underlying photophysics has not been explored at all. Such systems should be thoroughly investigated in the years ahead; who knows, if enough and properly channelised effort is put forward, these systems may catch up to or perhaps surpass the PV technology currently in use.

List of Publications included in the thesis

1. Polaron-Mediated Slow Carrier Cooling in a Type-1 3D/0D $CsPbBr_3$@Cs_4PbBr_6 Core–Shell Perovskite System. **Gurpreet Kaur**, K. Justice Babu, Nandan Ghorai, Tanmay Goswami, Sourav Maiti, and Hirendra N. Ghosh*. The Journal of Physical Chemistry Letters **2019** 10 (18), 5302-5311 (Chapter 3).
2. Temperature-Dependent Interplay of Polaron Formation and Hot Carrier Cooling Dynamics in $CsPbBr_3$ Nanocrystals: Role of Carrier–Phonon Coupling Strength. **Gurpreet Kaur**, K. Justice Babu, and Hirendra N. Ghosh*. The Journal of Physical Chemistry Letters **2020** 11 (15), 6206-6213 (Chapter 4).
3. Unravelling the Underlying Hot Carrier Transfer and Relaxation Pathways in Type-1 $CsPbBr_3$–PbS System. **Gurpreet Kaur**, Ramchandra Saha, K. Justice Babu, Ayushi Shukla, and Hirendra N. Ghosh*. The Journal of Physical Chemistry C **2021** 125 (19), 10516-10525 (Chapter 5).
4. Mapping the Real-Time Vibrational Infrastructure of Cs_2SnI_6 Nanocrystals through Coherent Phonon Dynamics. **Gurpreet Kaur**, K. Justice Babu, A. Shukla and H. N. Ghosh*. ACS Photonics **2022**, 9, 8, 2756–2766 (Chapter 6).
5. Ultrafast Glimpses of the Excitation Energy-Dependent Exciton Dynamics and Charge Carrier Mobility in Cs_2SnI_6 Nanocrystals. **Gurpreet Kaur**, Ayushi Shukla, Arijit Sinha, Koyendrila Debnath, Kaaliyamoorthy Justice Babu, Umesh V. Waghmare and Hirendra N. Ghosh*(communicated) (Chapter 7).

List of other Publications (other than that included in the thesis)

1. Fast Polaron Formation and Low Carrier Mobility in Defect-Free Polyhedral $CsPbBr_3$ Perovskite Nanocrystals. **Gurpreet Kaur**‡, K. Justice Babu‡, Ayushi Shukla‡, Ramchandra Saha, Arshdeep Kaur, Manvi Sachdeva, D.K. Yadav, and Hirendra N. Ghosh*; (‡-equal contribution). *ACS Photonics* **2022**, 9, 3, 969–978.
2. Effect of Confinement on the Exciton and Biexciton Dynamics in Perovskite 2D-Nanosheets and 3D-Nanocrystals. **Gurpreet Kaur**‡, Ayushi Shukla‡, K. Justice Babu, Nandan Ghorai, Tanmay Goswami, Arshdeep Kaur, and Hirendra N. Ghosh*; (‡-equal contribution). *J. Phys. Chem. Lett.* **2020**, 11, 15, 6344–6352.
3. Concurrent Energy- and Electron-Transfer Dynamics in Photoexcited Mn-Doped $CsPbBr_3$ Perovskite Nanoplatelet Architecture. **Gurpreet Kaur**‡, K. Justice Babu ‡, Ayushi

Shukla, Arshdeep Kaur, Tanmay Goswami, Nandan Ghorai, and Hirendra N. Ghosh*;(‡-equal contribution). *J. Phys. Chem. Lett.* **2021**, 12, 1, 302–309.

4. Probing the charge transfer mechanisms in type-II $Cs_2AgBiBr_6$-CdSe composite system: ultrafast insights. **Gurpreet Kaur**‡, Ayushi Shukla‡, Kaliyamoorthy Justice Babu, Himanshu Bhatt, Hirendra N.Ghosh*; (‡-equal contributions) *Nanotechnology 33* (48), *485406, **2022***.
5. Hot Carrier Relaxation in $CsPbBr_3$-Based Perovskites: A Polaron Perspective. **Gurpreet Kaur** and Hirendra N. Ghosh*; (Perspective) *J. Phys. Chem. Lett.* 2020, 11, 20, 8765–8776.
6. Chemically Engineered Avenues: Opportunities for Attaining Desired Carrier Cooling in Perovskites (Review article). **Gurpreet Kaur**, Ayushi Shukla, K. Justice Babu and Hirendra N. Ghosh*; *Chem. Rec.* **2022**, e202200106.
7. Insitu $CsPbBr_3$ Architecture Engineered in the Electrospun Fibers and Its Ultrafast Charge Transfer Dynamics. K. Justice Babu, **Gurpreet Kaur**, Ayushi Shukla, Arshdeep Kaur, Himanshu Bhatt, Nandan Ghorai, Goutam De and Hirendra N. Ghosh*; *Mater. Adv.*, **2022**, 3, 6566-6576.
8. Temperature-Dependent Trap-Assisted Ultrafast Carrier Dynamics in Amorphous and Crystalline Thin Films. Palwinder Singh, **Gurpreet Kaur**, Nandan Ghorai, Tanmay Goswami, Anup Thakur, Hirendra N. Ghosh*; Phys. Rev. Applied 14, 014087.
9. Defect-Interceded Cascading Energy Transfer and Underlying Charge Transfer in Europium-Doped $CsPbCl_3$ Nanocrystals. Ayushi Shukla, **Gurpreet Kaur**, K.Justice Babu, Arshdeep Kaur, D.K.Yadav and Hirendra N. Ghosh*; J. *Phys. Chem. Lett.* **2022**, 13, 1, 83–90.
10. Ultrafast Insights into High Energy (C and D) Excitons in Few Layer WS_2.Tanmay Goswami, Himanshu Bhatt, K. Justice Babu, **Gurpreet Kaur**, Nandan Ghorai, and Hirendra N. Ghosh*. *J. Phys. Chem. Lett.* **2021**, 12, 28, 6526–6534.
11. Ultrafast Charge Delocalization Dynamics of Ambient Stable $CsPbBr_3$ Nanocrystals Encapsulated in Polystyrene Fiber. K Justice Babu, **Gurpreet Kaur**, Liza Biswal, Goutam De*, Hirendra N. Ghosh*; *Chem. Eur. J. **2021**, 27, 683.*
12. Probing Ultrafast Charge Separation in CZTS/CdS Heterojunctions through Femtosecond Transient Absorption Spectroscopy. Arshdeep Kaur, Tanmay Goswami, K Justice Babu, Nandan Ghorai, **Gurpreet Kaur**, Ayushi Shukla, Sachin R Rondiya, Hirendra N Ghosh; *J. Phys. Chem. C* **2020**, 124, 36, 19476–19483.

13. Defect-Mediated Slow Carrier Recombination and Broad Photoluminescence in Non-Metal-Doped $ZnIn_2S_4$ Nanosheets for Enhanced Photocatalytic Activity. Tanmay Goswami, Dharmendra Kumar Yadav, Himanshu Bhatt, **Gurpreet Kaur**, Ayushi Shukla, K. Justice Babu, and Hirendra N. Ghosh* ; *J. Phys. Chem. Lett.* **2021**, 12, 20, 5000–5008.
14. Ultrafast Hot Electron Transfer and Trap-State Mediated Charge Carrier Separation toward Enhanced Photocatalytic Activity in g-C_3N_4/$ZnIn_2S_4$ Heterostructure. Himanshu Bhatt, Tanmay Goswami, D K Yadav, N Ghorai , Ayushi Shukla, **Gurpreet Kaur**, Arshdeep Kaur and Hirendra N. Ghosh*; *J. Phys. Chem. Lett.* **2021**, 12, 49, 11865–11872.
15. Spectroscopic Investigation of Structural Perturbations in $CsPbCl_3$ Perovskite Nanocrystals: Temperature and Excitation Energy Dependent Study. Ayushi Shukla, **Gurpreet Kaur**, Kaliyamoorthy Justice Babu, and Hirendra N. Ghosh*(communicated).
16. Temperature Driven Charge Transfer Process in Quantum Confined Two-Dimensional Mn-doped $CsPbBr_3$ Perovskite Nanoplatelets. Kaliyamoorthy Justice Babu, Ayushi Shukla, **Gurpreet Kaur**, Arshdeep Kaur, Himanshu Bhatt and Hirendra N. Ghosh* (accepted).

Permissions from Journals for reuse of content in thesis

Temperature-Dependent Interplay of Polaron Formation and Hot Carrier Cooling Dynamics in CsPbBr3 Nanocrystals: Role of Carrier–Phonon Coupling Strength

Author: Gurpreet Kaur, K. Justice Babu, Hirendra N. Ghosh

Publication: Journal of Physical Chemistry Letters

Publisher: American Chemical Society

Date: Aug 1, 2020

Unravelling the Underlying Hot Carrier Transfer and Relaxation Pathways in Type-1 CsPbBr3–PbS System

Author: Gurpreet Kaur, Ramchandra Saha, K. Justice Babu, et al

Publication: The Journal of Physical Chemistry C

Publisher: American Chemical Society

Date: May 1, 2021

Mapping the Real-Time Vibrational Infrastructure of Cs2SnI6 Nanocrystals through Coherent Phonon Dynamics

Author: Gurpreet Kaur, Ayushi Shukla, Kaliyamoorthy Justice Babu, et al
Publication: ACS Photonics
Publisher: American Chemical Society
Date: Aug 1, 2022

Conferences attended/oral and poster presentations

1. Presented a Poster entitled "*Ultrafast Charge Carrier Dynamics of Cs_2SnI_6: A promising Lead Free Perovskite*" in Perovskite Society of India Meet (PSIM-2023) held at Indian Institute of Technology, Roorkee (1^{st} – 3^{rd} March 2023).
2. Presented a Poster entitled "*Establishing the Real-Time Vibrational Framework of Cs_2SnI_6 via Coherent Phonon Dynamics*" in Ultrafast Sciences (UFS 2022) held at Indian Institute of Science Education and Research, Thiruvananthapuram (3^{rd} – 5^{th} November 2022).
3. Delivered an Oral presentation on "*Spectroscopic investigation of perovskite based materials through transient absorption measurements*", at 2^{nd} Research Scholar Day, 31^{st} March – 1^{st} April, 2022, held at Institute of Nano Science and Technology, Mohali Punjab, India.
4. Presented a Poster entitled "*Ultrafast Insights into the Temperature Dependent Conflict of Polaron Formation and Hot Carrier Cooling in $CsPbBr_3$ Nanocrystals*" in 7^{th} Theme Meeting on Ultrafast Sciences-2021 (UFS 2021), 12^{th}- 13^{th} November 2021 (Online Zoom Platform).
5. Presented a Poster entitled "*Retardation in the Charge Carrier cooling rate in Type-1 3D/0D Core-Shell $CsPbBr_3@Cs_4PbBr_6$ as a corollary of Polaron Formation*" in International Conference on Nano Science and Technology (ICONSAT 2020) held at Biswa Bangla Convention Centre, Kolkata (5^{th}-7^{th} March 2020).
6. Bagged the best Poster award for presentation of the Poster entitled "*Slow Charge Carrier cooling in Type-1 3D/0D Core-Shell $CsPbBr_3@Cs_4PbBr_6$ Perovskite system: Role of Polaron Formation*" in Ultrafast Sciences 2019 conference held at IIT Bombay, Powai, Mumbai (7^{th}-9^{th} November 2019).
7. Actively participated and attended *the Full Agenda of the DST & ACS Workshop* held at INST, Mohali (20^{th} November, 2019).